SYNOPTIC AND MESOSCALE PROCESSES ASSOCIATED WITH METEOROLOGICAL EXTREMES AT VANCOUVER, BRITISH COLUMBIA IN THE CURRENT AND FUTURE CLIMATE

by

Daniel Betancourt

A Thesis submitted to the Faculty of Graduate Studies of

The University of Manitoba

in partial fulfillment of the requirements of the degree of

DOCTOR OF PHILOSOPHY

Department of Environment and Geography

University of Manitoba

Winnipeg, Manitoba

ABSTRACT

The synoptic and mesoscale processes generating hazards in the climate of Vancouver, British Columbia are examined in this thesis. Those considered have been shown through quantitative methods to pose risk to local populations. These include heatwaves, landslides and windthrow of trees (the latter 2 are associated with antecedent heavy rain).

Landslide events are associated with moisture transport from lower latitudes, but extreme wind events preceded by heavy rain do not show such linkage. Patterns associated with extreme winds vary depending on antecedent heavy precipitation - with differences in pressure anomalies over the North Pacific versus British Columbia. Increases in landslide events are related to northwards shifting moisture sources in the Pacific, while decreases in positive pressure anomalies over this region explain decreases in purely wind events. Multiday heatwaves represent a unique process associated with upper blocking and surface West Coast Thermal Trough (WCTT) configurations. Greater occurrences in the former are increasing the intensity and duration of heatwaves. Other patterns show temporal sensitivity in prominence during multiday events.

Temporal processes regulating mesoscale circulations account for 36-38% of spatial variability in attaining heat-alert criteria between Vancouver (YVR) and Abbotsford (YXX) International airports. Considerable dynamic forcing occurs - whereas heatwaves elsewhere are typically associated with barotropic conditions. The WCTT and coastal southerlies modulate differentially the occurrence of sea-breezes at YVR and YXX.

Verification of model data for a July 2009 heatwave event suggests that magnitude and error in u-component flow are associated with v-wind intensity; and coastal southerlies are

shown to deflect and produce offshore flows at YVR. Modulation of sea-breezes occurs due to dynamic forcing rather than thermodynamic parameters such as sensible heat flux, whereas mountain-valley circulations are sensitive to Planetary Boundary Level Height. Data from a future simulation using a Pseudo-Global Warming (PGW) approach show large increases in temperature and humidex at YVR and YXX causing considerably more heat stress. Intensification of winds occurred in the future simulation driven by a stronger WCTT. Climate perturbations in geopotential height and u and v wind applied to the model in the PGW simulation did not appear to have affected changes in the WCTT.

ACKNOWLEDGEMENTS

I am very grateful to my mother and other family members for supporting me during the process of completing my doctoral degree and writing my thesis. I would like to thank Dr. Ronald Stewart for his supervision and for helping me in having a focused approach in my research. I appreciate greatly the insight from my committee member Dr. John Hanesiak on mesoscale and synoptic meteorological processes as well.

I would like to thank a former committee member Dr. Peter Rasmussen for his welcoming attitude and valuable feedback while taking courses from the Department of Civil Engineering; and Dr. Tricia Stadnyk for graciously accepting to replace Dr. Rasmussen after he passed away. Dr. Stadnyk also provided much encouragement for me to complete my degree. In addition, I would like to thank Paul Whitfield for providing data and technical expertise in statistics, and for recommending appropriate computer programs.

I would also like to thank the National Center for Atmospheric Research (NCAR) for producing and making available the pseudo-global warming (PGW) dataset used in this study; and to Kyoko Ikeda of NCAR for her feedback on these data. I am also appreciative to the University of Saskatchewan for providing the PGW data.

I am grateful to the Coastal Cities at Risk (CCaR) project led by Dr. Gordon McBean, for funding my studies, and providing me an opportunity to work in multidisciplinary environment with specialists in diverse fields such as civil engineering, economics, and medicine who are studying climate change and adaptation strategies. CCaR was an initiative of the International Development Research Centre (IDRC) to understand and characterize physical hazards confronting coastal mega-cities for several locations including Vancouver, British Columbia

under the context of climate change. It is an important aspect of addressing risk and social vulnerability in both developed and developing countries and developing adaptation strategies.

TABLE OF CONTENTS

LIST OF TABLES

LIST OF FIGURES

CHAPTER 1: THESIS INTRODUCTION AND OBJECTIVE

1.1 Background

The Vancouver, British Columbia region contains high population and diverse physiography (Fig. 1.1). It is subject to a corresponding wide array of natural hazards driven by a variety of processes including geophysical, meteorological, hydrological and oceanographic. Such hazards occur along a spatiotemporal spectrum (Burton, 1993), with pervasive and intensive events at opposite poles. Pervasive events are of long duration and have large spatial coverage, whereas intensive occurrences are more localized in spatial extent and occur on shorter timescales. Examples of hazards affecting the local population occur along this entire continuum - such as windstorms (intensive) and landslides and flooding in regions of steep terrain near the Coast Mountains due to multi-day rainfall events (moving towards the pervasive end of the spectrum).

Many studies have shown that trends in extreme meteorological events responsible for natural hazards are increasing, and many future projections show further increases due to Anthropogenic Warming (IPCC, 2018). Chapter 3 reviews such trends and projections over the Northern Hemisphere and locally and reviews some future projections. Given this background, the Coastal Cities at Risk (CCaR) project was formed as an initiative of the International Development Research Centre (IDRC) to understand and characterize natural hazards affecting coastal mega-cities including Vancouver under the context of climate change. CCaR provided the funding and motivation for this thesis - which focuses solely on meteorologically (purely atmospheric processes) and hydro-meteorologically (interaction of precipitation and hydrologic processes) driven events affecting the region (see the subsequent section below).

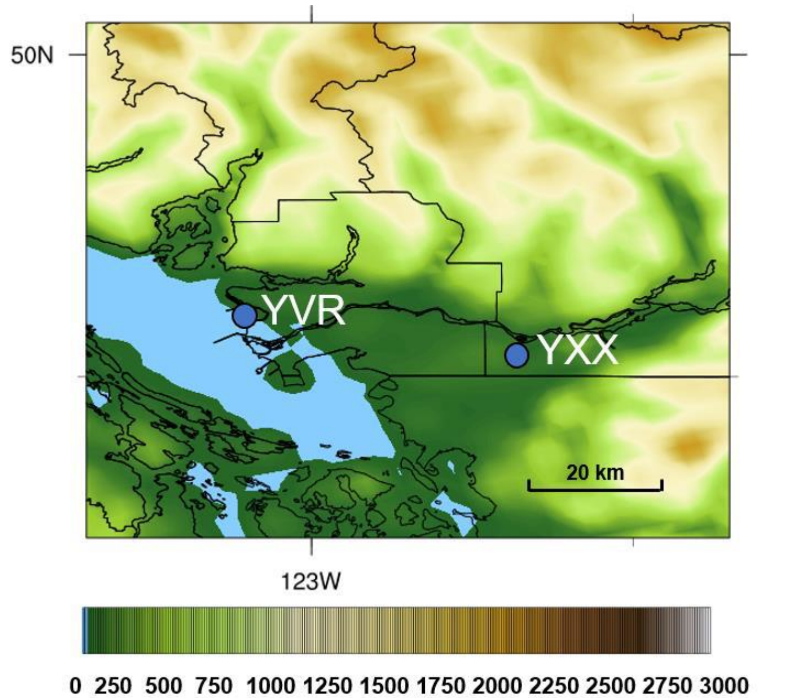

Figure 1.1: Physiography of the Vancouver, British Columbia region. Circles represent the locations of Vancouver (YVR) and Abbotsford International Airports (YXX). The vertical scale (m) is indicated by the shading. Lines represent political boundaries.

1.2 Objective

Given the wide range of physical hazards affecting the Vancouver, British Columbia region and the potential for increased extremes, characterizing synoptic and mesoscale interactions is key to understanding modulation of future extremes and is critical to addressing risk for the region.

Specifically, the objective of this thesis is to better understand the synoptic and mesoscale meteorological processes associated with surface phenomena that have been shown through quantitative methodologies and rigorous scientific procedures to pose risk to populations in the region in the current and future climate. Examples include property damage and risk of injury during landslides or windthrow events; and an increased burden on public health care systems during heatwaves.

1.3 Outline

The objective will be met through analysis organized into three separate papers as part of a manuscript thesis as outlined below. The first paper deals with a range of hydro-meteorologically driven hazards. The latter two focus on heatwaves exclusively due to the high risk that heat extremes pose on human health locally (Kosatsky et al., 2012). These three papers are specifically as follows:

(i) Betancourt, D., and R.E. Stewart. *Synoptic Typing, Empirical Orthogonal Function (EOF) Analysis and Trends in Hydrometeorological Extremes.*

Extreme heat events (using Henderson and Kosatsky (2012) to identify thresholds), major wind events and heavy precipitation events (using BGC Engineering (2006) to identify thresholds) at Vancouver are linked with synoptic types and EOFs representing key meteorological processes. Trend analyses of these synoptic types and EOF coefficients are also conducted to understand any changes in associated processes. This work has been prepared for submission to a major atmospheric science journal.

(ii) Betancourt, D., and R.E. Stewart. *Relating Spatial and Temporal Variability in Extreme Maximum Temperature During Heatwaves in the Vancouver, British Columbia Region.*

Patterns in co-occurrence and spatial variability of near heat-alert criteria (using Henderson and Kosatsky (2012) to identify thresholds) are examined to determine driving mechanisms. Multiple Correspondence Analysis (MCA) and compositing are used to relate spatial variability to temporal evolution of mesoscale flows during multiday heatwave events at Vancouver. This work has been prepared for submission to a major atmospheric science journal.

(iii) Betancourt, D., and R.E. Stewart. *Changes in Thermodynamic Forcing During the July 2009 Heatwave using a Pseudo-global warming (PGW) Approach.*

Data from a 4 km resolution PGW experiment (Liu et al., 2017) using the Weather Research and Forecasting (WRF) model are examined to study changes in future heatwaves at Vancouver, British Columbia. Synoptic regimes, storm tracks and dynamic forcing were maintained relatively constant (via spectral nudging) to isolate the impacts of thermodynamic drivers (projected changes in parameters related to heat and moisture as applied to the initial and lateral boundary conditions of the WRF simulation) on the 2009 heatwave event. This work has been prepared for submission to a major atmospheric science journal.

Chapter 2 will provide a review of the synoptic and mesoscale mechanisms and processes which are important component to the extreme events over the region being considered in Chapters 4-6. Chapter 3 will review the techniques used to establish thresholds for extreme meteorological events. As mentioned previously, it will also review trends in extreme events and future projections. Chapter 7 will summarize results from the 3 papers and provide an overall thesis conclusion.

REFERENCES

BGC Engineering Inc. (2006). *District of North Vancouver, Berkley Landslide Risk Management, Phase 1 Risk Assessment.* Report prepared for District of North Vancouver dated January 16, 2006.

Burton, I. (1993). *The Environment as Hazard* (2nd edition). New York: The Guildford Press.

Henderson S.B., and T. Kosatsky. (2012). A data-driven approach to setting trigger temperatures for heat health emergencies. *C.J. Public Health,* 103(3), 227-230.

IPCC. (2018). *Global warming of 1.5°C. An IPCC Special Report on the impacts of global warming of 1.5°C above pre-industrial levels and related global greenhouse gas emission pathways, in the context of strengthening the global response to the threat of climate change, sustainable development, and efforts to eradicate poverty.*

Kosatsky, T., S.B. Henderson, S.L. Pollock. (2012). Shifts in mortality during a hot weather event in Vancouver, British Columbia: rapid assessment with case-only analysis. *Am. J. Public Health*, 102, 2367-2371.

Liu, C., and Coauthors. (2017). Continental-scale convection-permitting modeling of the current and future climate of North America. *Climate Dyn.*, 49, 71-95. https://doi.org/10.1007/s00382-016-3327-9.

CHAPTER 2: SYNOPTIC AND MESOSCALE PROCESSES IN THE VANCOUVER, BRITISH COLUMBIA REGION

2.1 SPATIO-TEMPORAL SCALE OF METEOROLOGICAL PROCESSES

Meteorological features and processes occur across a broad range of spatial and temporal scales from micro to synoptic scale. This thesis focuses on the interaction of synoptic and mesoscale processes so defining thresholds for their scales is important to separate them and to understand their modulation on each another.

From a theoretical perspective, the threshold between synoptic and mesoscales can be characterized by a set of assumptions pertaining to physical processes at different spatial scales. These are derived from dimensional analysis to determine orders of magnitude for different variables such as the Coriolis parameter, and horizontal and vertical acceleration terms from the basic equations of motion (Atkinson, 1981). Such analyses suggest that, at synoptic scales, the horizontal acceleration in air flow is an order of magnitude smaller than the horizontal Coriolis parameter. Therefore, at this scale horizontal accelerations are small and geostrophic balance in winds between the pressure gradient force and Coriolis force can be assumed (Markowski and Richardson, 2010). Such analyses also show that the vertical component of the Coriolis parameter and vertical accelerations in air flow are several orders of magnitude smaller than gravitational acceleration (Atkinson, 1981). This allows for a simplification in the equation governing vertical airflow and for an assumption of hydrostatic balance (upward and downward forces are balanced) known as the hydrostatic equation. At the mesoscale level, assumptions regarding hydrostatic balance hold (with the exception of convective processes), but those regarding geostrophic balance in horizontal flow do not. At such scales, the Coriolis parameter (which is proportional to wind speed) has the same magnitude as at synoptic scales, but the pressure gradient force can be up to several orders of magnitude greater (Markowski and Richardson, 2010). This results in considerable horizontal accelerations of air and ageostrophic circulations at the mesoscale level.

Additionally, the distinction between synoptic and mesoscales can be estimated by the Rossby number (Lin, 2007). The Rossby number is given by the equation:

$$Ro = \frac{U}{f \cdot L} \tag{2.1}$$

Where U is the wind speed, f is the Coriolis parameter and L is the horizontal scale of a meteorological phenomenon. Those processes with a Ro greater than 1 can be considered as mesoscale phenomena.

Both Atkinson (1981) and Lin (2007) adopt a classification system wherein mesoscale phenomena occur between 2 and 2000 km in spatial scale corresponding as 1 h to 1 week in temporal scale. This includes many processes such as thunderstorms, sea-breezes, and low-level jets. Synoptic processes occur at scales above the upper threshold to over 10 000 km spatially and up to monthly time-scales. These processes include mid-latitude cyclones and long waves in the upper air pattern.

2.2 SYNOPTIC PROCESSES

2.2.1 Seasonal Cycle

The West Coast of North America experiences considerable precipitation during the winter months. The region is impacted by frequent cyclonic activity from the Pacific Ocean when the storm track is situated at mid latitudes (Oke and Hay, 1994) and baroclinicity is enhanced. A semi-permanent area of low pressure in the Gulf of Alaska known as the Aleutian Low can often draw moisture from semi-tropical regions of the Pacific. Disturbances moving across the basin therefore often have access to deep moisture. In certain cases, moisture advection can be sustained for several consecutive days leading to considerable precipitation. This pattern is often referred to as a Pineapple Express (Lackmann and Gyakum, 1999; Roberge et al., 2009).

It is during the October to April period that intensive events such as extreme precipitation and wind occur most frequently. These events are driven by powerful cyclones in the winter season when temperatures gradients and the jet stream are strongest. This is in spite of the fact that, in summer, systems can contain more moisture, but lack synoptic forcing and have less flow and vapour flux associated with them (Neimann et al., 2008). Warner et al. (2012) showed that heavy precipitation and precipitable water are strongly associated with each other during the winter months but display very little relationship to one another in the warm season. These synoptic patterns can lead to flash flooding, landslides and windthrow of trees in the Vancouver area from an interaction of heavy antecedent precipitation, intense 24 h precipitation and extreme winds.

During the warmer season, the storm track weakens and shifts north. At the same time, a large anticyclone from the Pacific region extends its influence on the West Coast. This often yields long stretches of clear, tranquil weather (Oke and Hay, 1994). If the pattern and jet stream become more amplified, high pressure builds in aloft and at the surface - setting the stage for periods of above normal temperature or even a heatwave to affect the region. This is modulated by mesoscale mechanisms further discussed in Section 2.3. At the same time, convection can also occur during the summer months leading to intense, but more localized heavy precipitation. Modulation from the sea-breeze front (Section 2.3) may play a role in these convective events for coastal regions.

2.2.2 Synoptic Patterns and Hydrometeorological Extremes

There has been considerable study of synoptic patterns associated with extreme precipitation over the region, but not for extreme winds. Lackmann and Gyakum (1999) showed that extreme precipitation events associated with flooding over the Pacific Northwest were characterized by positive 500 hPa geopotential height (GPH) anomalies over the Bering Sea and Southwestern United States, and strong negative pressure anomalies (which were multi-centred) over the Gulf of Alaska. The associated southwest upper flow assisted in advecting considerable moisture into the region.

Other studies have shown similar patterns such as Warner et al. (2012) and Roberge et al. (2009) for which "south-west type" events were associated with intense poleward water vapour transport over the West Coast of North America. Roberge et al. (2009) also showed that intense vapour transport into the region could be associated with more zonal configurations or "west type" events. This varying meridionality in upper flow as it relates of to the interaction of extreme wind and heavy antecedent precipitation is discussed in Chapter 4.

In terms of extreme wind events in the region, the majority are also caused by intense synoptic lows during the winter season. In particular, the strongest winds occur along and behind occluded fronts extending equatorward from synoptic systems moving onshore to the north of the region (Mass and Dotson, 2010). Winds are enhanced initially due to ageostrophic accelerations from terrain blocking in the more stable air (see Section 2.3) preceding the front; and then due to momentum transfer in the unstable air behind this feature. See Chapter 4 for more discussion on the processes associated with extreme winds over the region.

2.2.3 Modulation from Large-scale Atmosphere-Ocean Systems

Large scale modes of variability in parameters such as sea-surface temperatures (SST) over the Pacific Basin have a large effect on the local climate – particularly in the winter season. They vary in temporal scale from interseasonal - such as the El Nino/ Southern Oscillation (ENSO) to decadal - like the Pacific Decadal Oscillation (PDO). These are in turn coupled to atmospheric modes of variability in surface pressure and 500 hPa GPH like the Pacific North America pattern (PNA) (https://www.esrl.noaa.gov/psd/forecasts/reforecast2/teleconn/pna.html), the North Pacific Oscillation (NPO)

(https://www.esrl.noaa.gov/psd/forecasts/reforecast2/teleconn/wpo.html) and East Pacific Oscillation (EPO) (https://www.esrl.noaa.gov/psd/forecasts/reforecast2/teleconn/epo.html); and in tropical convection and associated parameters at intraseasonal timescales such as the Madden-Julian Oscillation (MJO).

Both the positive phases of PDO and ENSO (Stahl et al., 2006) are associated with below normal precipitation occurrence during winter over most of the region. In terms of extreme winds, their frequency has been shown to be associated with both negative PDO and ENSO phases (Abeysirigunawardena et al., 2009). The specific modulation on extreme winds and precipitation events from these systems will be discussed in Chapter 4. The atmospheric indices describing variation in atmospheric pressure at the surface and aloft are shown in Fig 2.1. The PNA is well correlated with ENSO and PDO (Stahl et al., 2006), but displays greater internal variability since it is an atmospheric index rather than oceanic (see Chapter 4). The EPO and WPO are similar but with the center of the modes shifted zonally from each other somewhat (Fig 2.1). Due to the similarity, only the WPO is considered in Chapter 4; and it is associated with above average precipitation in the region. The MJO in certain phases as it propagates eastward has been shown to be associated with precipitation extremes over the region (Zhang, 2005) and is also considered in Chapter 4.

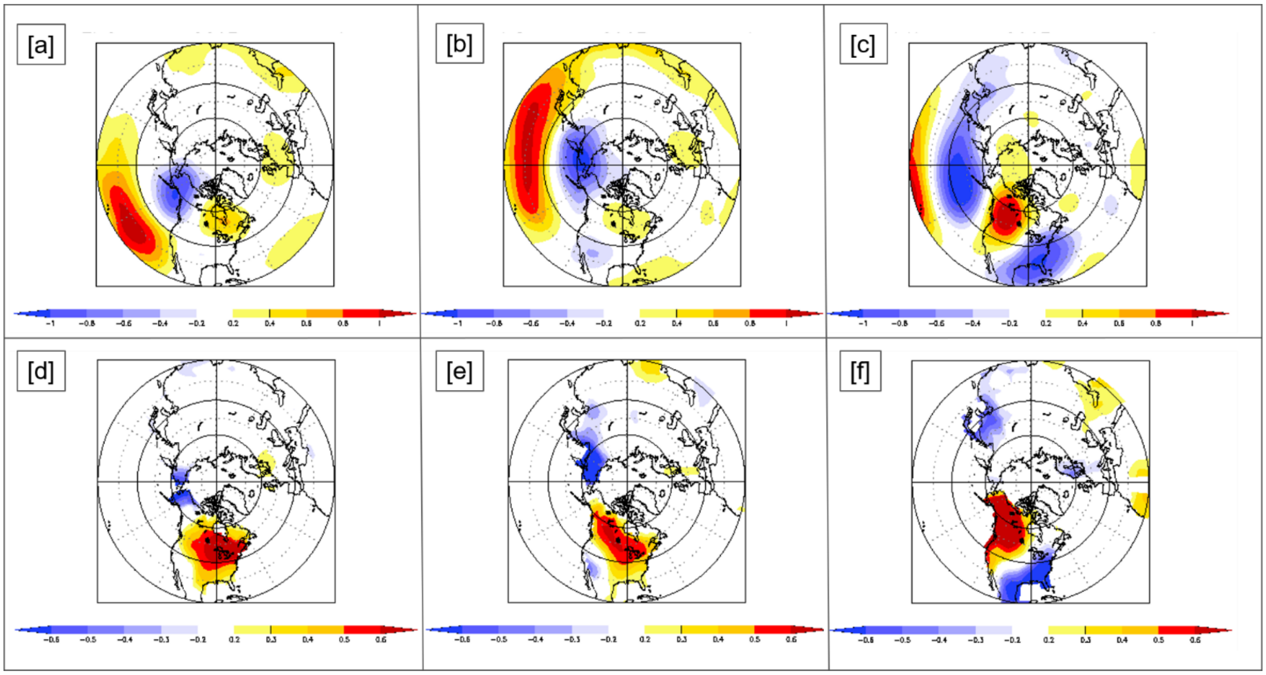

Figure 2.1: Standardized 500 hPa GPH (top row or [a]-[c]) and surface pressure anomalies associated with the EPO (left column or [a] and [d]), WPO (middle column or [b] and [e]), and PNA (right column or [c] and [f]). Reproduced from *https://www.esrl.noaa.gov/psd/forecasts/reforecast2/teleconn*

2.2.4 Synoptic Patterns Associated with Heatwaves

As mentioned previously, heatwaves in the region are associated with highly meridional or blocked upper air patterns (Bumbaco et al., 2013). This was also typical of several major heatwaves in the midlatitudes recently such as Europe in 2003, and Russia in 2010 (discussed further in this section). However, at lower levels - mesoscale modulating mechanisms are more particular to the region (Section 2.2).

Such an amplified pattern allowed the subtropical ridge over the Azores to move further north than usual during August of 2003 leading to the major heat wave over Europe (Black et al., 2006). The circulation pattern was mirrored at lower levels and was consistent through a large depth of the atmosphere. This suggested an equivalently barotropic environment with little shear, and with most dynamic forcing displaced pole ward. The resulting lack of clouds and precipitation allowed for deep mixing of the lower atmosphere and strong surface heating, feeding back and stabilizing the large-scale pattern. In other words, a positive feedback loop existed where physical and thermodynamic parameters strengthened the large-scale flow anomaly and dynamics. Della-Marta et al. (2007) also found the significance of anticyclonic influence for two different types of heat wave patterns centered over Iberia and northern Europe, with additional input from sea surface temperature anomalies and the Atlantic Multidecadal Oscillation. Likewise, Dole et al. (2011) described the upper air pattern as a blocking configuration, specifically an omega block during the 2010 Russian heat wave. It was found to be similar to a composite of the top 10 warmest Julys for western Russia. It is also likely that severe drought also brought on by the blocking pattern provided additional surface feedback.

2.3 MESOSCALE PROCESSES

2.3.1 Orographic Processes

<u>2.3.1.1</u> <u>General Mechanisms</u>

Orographic effects play an important role in modulating precipitation over the region even though the Coast Mountains in the vicinity of Vancouver are relatively low (< 1500 m). This is in part due to the orientation of the Coast Mountains, which run from west-northwest to east-southeast across the area, and therefore generate a normal incidence of flow in a southerly wind regime. Such flows (associated with warm air and moisture advection) can be quite strong ahead of large frontal systems during the winter as mentioned previously and leads to the potential for orographically enhanced precipitation. Locations near the mountains experience considerably more precipitation than areas away from them such as Vancouver International Airport (YVR) (Oke and Hay, 1994). This makes studying extremes in precipitation challenging across the region since there are relatively few stations that have a long duration of data (see Section 4.2 for an approach on adjusting precipitation in accordance with elevation across the region).

Orographic enhancement results from one of several, interacting mechanisms (Houze, 1993). It can occur simply from the lifting of thermodynamically stable air over a physical barrier which cools adiabatically until it becomes saturated. In other cases, moisture may be provided by higher level clouds that are not influenced by orographic effects, but which supply lower level clouds formed from orographic forcing. Precipitation is then triggered through a variety of warm rain or cold cloud processes in the orographically produced cloud. Additionally, air parcels ascending mountainous terrain may become destabilized (even if initially stable) as they reach the lifted condensation level (from which point the air cools at a moist adiabatic rate), and the level of free convection (the point at which an air parcel becomes more buoyant than its surrounding environment). This allows for an acceleration of air parcels resulting in convective precipitation.

2.3.1.2 Terrain Blocking

The previous discussion assumes that a flow of air encountering a mountain barrier will ascend over it, but this is not always the case. In situations of high stability and weaker cross-barrier flow, air may be blocked from ascending the terrain (Houze, 1993). The likelihood of low-level blocking as an airflow reaches a mountain barrier is given by the Froude number (Atkinson, 1981):

$$Fr = \frac{U}{N \cdot H_m} \tag{2.2}$$

Where Fr is the Froude number (dimensionless), U is the cross-barrier wind speed ($m \cdot s^{-1}$), N is the Brunt-Vaisala frequency ($rad \cdot s^{-1}$) and H_m is the mountain height (m). Values of Fr < 1 are typically associated with blocked low-level flows.

Such situations can occur when the flow of retreating, cool air-masses is impeded by mountain ranges; and advancing warm air may be lifted and produce precipitation relatively far away from any mountains. James and Houze (2005) used radar data to study the characteristics of orographically enhanced precipitation over the coast of northern California and determined that there were two main regions of intense rainfall. One was situated over the inland mountain ranges, but the other was situated offshore. It is theorized that the observed maxima in precipitation intensity over the ocean was in response to cases of blocked flow. Previously, Houze et al. (2001) discussed the effect of stability and blocking on the position of maximum precipitation when conducting a similar study over the Mediterranean side of the Alps. It was found that the greater the stability and inferred blocking during an event, the further the displacement of the intense precipitation away from the mountains. Such occurrences may enhance low level frontogenesis and precipitation rates.

Conditions favorable to low-level blocking occur in the region during arctic outflow periods - when cold, stable air from the interior moves through gaps and valleys in the mountains (Jackson and Steyn, 1994; Stewart et al., 1995). Any enhanced precipitation bands associated with an incoming system will be displaced further south away from areas with any significant orography (personal communication with meteorologists at the Pacific Storm Prediction Centre in Vancouver). The strong gradient in isohyets of average annual precipitation also occur in areas of flatter terrain and not solely in the mountains or in close proximity to them (Oke and Hay, 1994).

2.3.2 West Coast Thermal Trough

Past studies such as McKendry (1994) have noted the importance of low-level troughing during periods of above normal temperatures over the region in summer. This feature is known as the West Coast Thermal Trough (WCTT), and is an important mesoscale phenomenon affecting the area during the summer months (Brewer et al., 2012). It represents an inverted trough extending northwards along the West Coast from the thermal low over the southwestern United States (Brewer et al., 2012). It results from an interaction of the background synoptic pressure pattern and low-level warming (Mass et al., 1986). Brewer et al. (2013) showed that its formation is highly sensitive and largely attributable to adiabatic warming generated by easterly, down-slope flows. Brewer et al. (2013) also found that contributions from thermodynamic parameters (such as sensible heat flux) and temperature advection were not as important to its formation.

The composite surface pressure pattern for the summer months generates a northerly pressure gradient along the West Coast between the Pacific High and southwestern United States thermal low (Mass and Albright, 1987); it does not show the WCTT since it is a transient feature (Brewer et al., 2012). However, a WCTT-like structure extending northwards towards Oregon is the leading mode of surface pressure anomalies during the summer months (see Chapter 4). The movement of a synoptic surface pressure ridge onshore - and the development of upper ridging aloft - allows for a low-level easterly or offshore flow to develop. This leads to low-level warming and pressure decreases manifested as a northward extension of the WCTT (Mass et al., 1986). As the synoptic ridge (aloft and at the surface) move eastwards, there is an attenuation in down-slope flow locally as the WCTT moves across various coastal mountain ranges and evolves into a thermal low over interior regions (Mass et al., 1986). This allows for an influx of cool, marine air to move into the region (this process is discussed in the subsequent section).

Climatologies for the WCTT developed by Brewer et al. (2012) show that the WCTT has a high frequency of occurrence near the Oregon and California coast, but is much less common farther north towards the British Columbia coast. The mode of surface pressure variability related to the WCTT and synoptic ridge (see Chapter 4) also displays a sharp gradient near the Oregon/California coastal region - suggesting that the extension of the WCTT north of this region is uncommon. In addition to the further discussion in Chapter 4 of the WCTT and its relation to surface pressure anomalies and heatwave processes; its specific modulation on local flow patterns during such events is discussed in Chapters 5 and 6.

2.3.3 Coastal Southerlies

As mentioned in the previous section, the region typically experiences northerly flows during the summer time due to the prevailing synoptic pressure pattern. However, the region is subject to abrupt reversals in meridional flow associated with the influx of cool, moist marine air which propagate northwards along the West Coast of North America (Mass and Albright, 1987). These coastal southerlies are associated with the end of periods of above normal temperature.

Such meridional wind anomalies are generated by the interaction of decelerating onshore flows and orography oriented parallel to the coast (Reason, 1994). The advection of these cool and stable air-masses by a synoptic feature results in low-level blocking (discussed in Section 2.2.1.2) as they encounter the mountainous terrain. This causes convergence and pressure increases as a mesoscale ridge forms. Under certain conditions, the blocking is sustained long enough such that imbalances occur between the pressure gradient force and the Coriolis parameter (due to deceleration), and an ageostrophic flow develops parallel to the coast which propagates to the left of the mountain barrier (northwards). This occurs when the ratio of the Rossby number to the Froude number is considerably greater than one (in cases of a small

Rossby number) or if the Froude number is less than one (in cases of a large Rossby number). The ratio is given by the following formula (Reason, 1994) :

$$\frac{Ro}{Fr} = \frac{N \cdot H_m}{f \cdot L_m} \tag{2.3}$$

Where Ro is the Rossby number (dimensionless), Fr is the Froude number (dimensionless), N is the Brunt-Vaisala frequency ($rad \cdot s^{-1}$), f is the Coriolis parameter ($rad \cdot s^{-1}$), H_m is the mountain height (m), and L_m is the half-width of the mountain (m). Under those conditions, blocking will persist for a period of time defined by the reciprocal of the Coriolis parameter.

The rate at which coastal southerlies propagates northwards can be estimated using an empirical relation in accordance with the following formula (Mass and Albright, 1987):

$$V = 0.79 \cdot \sqrt{\frac{\Delta P}{\rho}} \tag{2.4}$$

Where V is the speed of propagation ($m \cdot s^{-1}$), ΔP is the pressure difference (Pa) ahead and behind the coastal southerlies, and ρ is the air density ($kg \cdot m^{-3}$).

2.3.4 Sea-breeze Circulations

Differential heating between land and ocean induces thermal circulations, with warm air rising over land and sinking over the relatively cool water surfaces (Atkinson, 1981). Rising, convergent airflows over land draw in cooler air which is subsiding and diverging out over the water. This results in a sea breeze and mesoscale front of marine air which moves inland. The thermal pattern and flow reverses itself during the night-time hours when the land cools faster than the surrounding ocean surfaces. A diurnal cycle of onshore versus offshore flows occurs if there is no over-riding forcing from the synoptic pattern and subsequent surface pressure gradient.

The characteristics and climatology of the local sea breeze for the region were described by Steyn and Faulkner (1986). The mean velocity of the sea breeze was found to be 3 $m \cdot s^{-1}$, and its occurrence was found to diminish considerably farther inland. The authors developed specific criteria for assessing days when sea breezes were likely to occur using a modified sea breeze index. This took into account inertial and buoyant forces by incorporating wind speed and land-sea temperature difference respectively. Sea breeze occurrence at Vancouver International Airport (YVR) is considerably greater than at Abbotsford International Airport (YXX) with an average of 85.9 sea breeze days per year occurring at YVR versus only 47.6 per year at YXX. This is due to greater distance and shielding from the ocean and its moderating effects at YXX.

Further studies by Steyn (1998) used observational data for key meteorological variables such as vapour pressure, potential temperature, and wind direction to provide further insight into the vertical structure of sea-breezes over the region. The sea-breeze was found to have the same depth as the local atmospheric boundary layer over the ocean (around 400-500 m). This study utilized turbulent fluxes including surface sensible heat flux to estimate thermal forcing and sea-breeze strength.

Recently, additional studies have utilized a time-integrated sensible heat flux to develop relationships used for determining sea-breeze intensity rather than land-sea temperature difference (Porson et al., 2007; Wichink et al., 2004). Porson et al. (2007) represents the sea-breeze velocity scale as the formula:

$$u_{sscale=} \sqrt{\frac{g \cdot H}{T \cdot \omega}} \tag{2.5}$$

Where u_{sscale} is the u-component flow generated by the sea-breeze ($m \cdot s^{-1}$), g is the gravitational acceleration ($m \cdot s^{-2}$), H is the time-integrated surface sensible heat-flux since sunrise ($W \cdot m^{-2}$), T is the surface temperature (K), and ω is the period of time since sunrise (s). The sea-breeze depth from Porson et al. (2007) is represented as:

$$z_{sscale=} \sqrt{\frac{g \cdot H}{T \cdot \omega}} \cdot \frac{1}{N} \tag{2.6}$$

Where z_{sscale} is the depth of the sea-breeze and N is the Brunt-Vaisala frequency ($rad \cdot s^{-1}$).

Sea-breeze intensity is subject to modulation from synoptic scale pressure gradients which can suppress or enhance its movement onshore (Atkinson, 1981). The interaction between mesoscale and synoptic scale flows as it relates to sea-breezes and their modulation from the WCTT is discussed in (Chapters 5 and 6). Sea-breeze velocity is calculated from high resolution model data simulating the July 2009 heatwave in Chapter 6.

2.3.5 Mountain-valley Circulations

Local wind fields in the region are further regulated by mountain-valley circulations. These circulations arise from differences in thermal forcing on slopes and air between the slopes at the same height above sea-level (Atkinson, 1981). The slopes experience heating due to sensible heat transfer from the ground, while the area between slopes receives much less heat from this process. This causes air to rise over the slopes due to buoyancy effects, and also generates lower pressure. This in turn causes a pressure gradient force from the area between slopes (high pressure) to the slopes themselves (low pressure) which causes air to move in that direction.

This upwards motion of air is therefore driven purely by thermodynamic mechanisms unlike the synoptically induced upslope flows considered in Section 2.2.1.1. In some cases, a return downwards movement or recirculation can develop in which air flow is balanced. Such recirculations occur when the depth of the Planetary Boundary Layer (PBL) is low in relation to overall ridge height.

Over some sections of the region, mountain-valley circulations can be difficult to distinguish from sea-breezes (Steyn and Faulkner, 1986). However, Reuten et al. (2005) determined that on calm clear days with minimal synoptic forcing, upslope flows of 6 $m \cdot s^{-1}$ as high as 800 m above ground level can develop over the Coast Mountains. These can be closed by re-circulation when the PBL height is lower – specifically when the ratio of ridge height and PBL depth is greater than 2 (Reuten et al. 2005). This can lead to a re-circulation of pollutants down towards the surface. The typical south-westerly sea-breezes which develop over the region in summer can transport pollutants eastwards (Steyn and Faulkner, 1986) towards the Coast Mountains where they are incorporated into upslope flows and either vented out into the free atmosphere or recirculated back towards the surface. Recirculation also can arise from diurnal cycles in horizontal advection of air (onshore and upslope during the day and offshore and downslope at night) which can bring pollutants back onshore and lead to stratification of the low-level atmosphere (McKendry et al., 1997). These processes are further discussed in Chapter 6 - specifically in relation to PBL depth during the July 2009 heatwave.

REFERENCES

Abeysirigunawardena, D.S., E. Gilleland, D. Bronaugh, P. Wong. (2009). Extreme wind regime responses to climate variability and change in the inner south coast of British Columbia, Canada. *Atmos.-Ocean,* 47(1), 41-62.

Atkinson, B.W. (1981). *Meso-scale atmospheric circulations.* London, England: Academic Press.

Black, E., Blackburn, M., Harrison, G., Hoskins, B., Methven, J. (2004). Factors Contributing to the Summer 2003 European Heatwave. *Weather*, 59(8), 217-223.

Brewer, M.C., C.F. Mass, B.E. Potter. (2012). The West Coast thermal trough: climatology and synoptic evolution. *Mon. Weather Rev.,* 140, 3820-3843.
_______(2013). The West Coast thermal trough: mesoscale evolution and sensitivity to terrain and surface fluxes. *Mon. Weather Rev.*, 141, 2869-2896.

Bumbaco, K.A., K.D. Dello, N.A. Bond. (2013). History of Pacific Northwest heat waves: synoptic pattern and trends. *J. Appl. Meteor. Clim.,* 52, 1618-1631.

Della-Marta, P.M., et al. (2007). Summer heat waves over western Europe 1880-2003, their relationship to large-scale forcings and predictability. C*lim. Dyn,* 29, 251-275.

Dole, R. et al. (2011). Was there a basis for anticicipating the 2010 Russian heat wave? *Geophys. Res. Lett.*, 38, L06702, doi:10.1029/2010GL046582.

Houze, R.A. (1993). *Cloud Dynamics.* Oxford, UK: Academic Press.
______, C. N. James, and S. Medina, 2001: Radar observations of precipitation and airflow on the Mediterranean side of the Alps: Autumn 1998 and 1999. *Quart. J. Roy. Meteor. Soc.*, 127, 2537–2558.

Jackson, P.L. and D.G. Steyn. (1994). Gap winds in a Fjord: observations and numerical simulation. *Mon. Wea. Rev.,* 122, 2645-2665.

James, C. N. and R.A. Houze (2005). Modification of precipitation by coastal orography in storms crossing Northern California. *Mon. Wea. Rev.*, 133, 3110-3131.

Lackmann, G. M. and Gyakum, J. R. (1999). Heavy cold-season precipitation in the northwestern United States: Synoptic climatology and an analysis of the flood of 17–18 January 1986. *Weather Forecasting*, 14, 687–700.

Lin, Y. (2007). Mesoscale Dynamics. Cambridge University Press, Cambridge, NY

Markowski, P., and Y. Richardson. (2010). Mesoscale Meteorology in Midlatitudes. John Wiley & Sons, Ltd. West Sussex, UK.

Mass, C.F., M.D. Albright, D.J. Brees. (1986). The onshore surge of marine air into the Pacific Northwest: a coastal region of complex terrain. *Mon. Weather Rev.*, 114, 2602-2627.
______, M.D. Albright. (1987). Coastal southerlies and alongshore surges of the West Coast of North America: evidence of mesoscale topographically trapped response to synoptic

forcing. *Mon. Weather Rev.,* 115, 1707-1738.

______, B. Dotson. (2010). Major extratropical cyclones of the northwest United States: historical review, climatology and synoptic environment. *Mon. Weather Rev.,* 138, 2499-2527.

McKendry, I.G. (1994). Synoptic circulation and summertime ground-level ozone concentrations at Vancouver, British Columbia. *J.Appl. Meteor.*, 33, 627-641.

______, D.G. Steyn, J. Lundgren, R.M Hoff, W. Strapp, K. Anlauf, F. Froude, J.B. Martin, R.M Banta, L.D. Olivier. (1997). Elevated ozone layers and vertical down-mixing over the Lower Fraser Valley. *Atmos. Environ.*, 31(14), 2135-2146.

Neiman, P.J., Ralph, F.M., Wick, G.A., Lundquist, J.D., Dettinger, M.D. (2008). Meteorological characteristics and overland precipitation impacts of Atmospheric Rivers affecting the West Coast of North America based on eight years of SSM/I satellite observations. *J. Hydrometeorol.,* 9(1), 22-47.

Oke, T.R., and Hay, J. (1994). *The Climate of Vancouver.* B.C. Geographical Series 50. UBC.

Porson, A., D.G. Steyn, G. Schayes (2007). Sea-breeze scaling from numerical model simulations. *Boundary-Layer Meteorol.,* 122:17–29.

Reason, C.J.C. (1994). Orographically trapped disturbances in the lower atmosphere: scale analysis and simple model. *Meteorol. Atmos. Phys.,* 53, 131-136.

Reuten, C., D.G. Steyn, K.B. Strawbridge, P. Bovis. (2005). Observations of the relation between upslope flows and the convective boundary layer in steep terrain. *Boundary-Layer Meteorol.,* 116, 37-61.

Roberge, A., Gyakum, J.R., Atallah, E.H. (2009). Analysis of intense poleward water vapor transports into high latitudes of western North America. *Weather Forecasting*, 24, 1732-1747.

Stahl, K., R.D. Moore, I.G. McKendry (2006). The role of synoptic-scale circulation in the linkage between large-scale ocean-atmosphere indices and winter surface climate in British Columbia, Canada. *Int. J. Climatol.* 26, 541–560.

Stewart, R.E. and co-authors. (1995). Winter storms over Canada. *Atmos.-Ocean,* 33(2), 223-247.

Steyn, D.G., and D.A. Faulkner. (1986). The climatology of sea-breezes in the Lower Fraser Valley, B.C. *Climatol. Bull.,* 20, 21-39.

______, (1998). Scaling the vertical sctructures of sea breezes. *Boundary-Layer Meteorol.,* 86, 505-524.

Warner, M.D., Mass, C.F., Salathe, E.P. (2012). Wintertime extreme precipitation events along the Pacific Northwest Coast: climatology and synoptic evolution. *Mon. Wea. Rev.* 140, 2021-2043.

Wichink Kruit, R.J., A.A.M. Holtslag, A.B.C. Tijm. (2004). Scaling of the sea-breeze strength with observations in the Netherlands. *Boundary-Layer Meteorol.*, 112, 369-380.

Zhang, C. (2005). Madden-Julian oscillation. *Rev. of Geophysics,* 43(2), 1-36, RG2003, doi:10.1029/2004RG000158.

CHAPTER 3: TECHNIQUES TO ESTABLISH THRESHOLDS FOR EXTREME METEOROLOGICAL EVENTS AND TREND ANALYSIS

3.1 Introduction

Identifying meteorological extremes is sometimes challenging. Common thresholds are based on the 90th, 95th or 99th percentile for a particular meteorological variable. A percentile represents the value below which that proportion of observations or samples within the distribution of a variable occurs. A probability density function (PDF) describes the relative frequency distribution for the different values of the variable from which percentiles are derived. PDFs for different meteorological variables take different forms such as normal (daily maximum and minimum temperatures) and exponential (hourly and daily rainfall, daily maximum wind gust, mean hourly wind speed). Often, cumulative distribution functions (CDFs) are used which describe the cumulative frequency distribution for values of a variable. Quantiles within a CDF give the probability that a variable will be at least as high as specified value.

Empirical distributions of meteorological data such as those for temperature and precipitation can be fitted to statistical models corresponding to normal, exponential and other distributions by solving for the associated parameters which describe their form. The disadvantage to such approaches is that the cut-off values can be somewhat arbitrary. For example a 90th percentile rain event may be statistically rare, but is unlikely to place a burden on any infrastructure or system.

3.2 Extreme Value Theory

As an alternative to the arbitrary thresholds discussed in the previous Subsection, techniques have been developed to estimate extreme values farther out in the tails of distributions using analysis based on Extreme Value Theory (Coles, 2001). These approaches involve sampling a subset of extreme events and fitting them to a new distribution - from which the magnitudes of the greatest extremes are derived. In such ways, the values for a one in 20, 50, or 100 year event are attained. BGC Engineering (2009) developed such return period intervals for intense rainfall of various durations in constructing Intensity, Duration and Frequency (IDF) curves for the Vancouver region.

Several different methodologies have been developed for sampling extreme occurrences from a broader distribution of data. In the Point Over Threshold method, points above an absolute threshold are selected and fitted to a new distribution; whereas in the Block Maxima method, relative maxima are sampled based on the annual cycle (Coles, 2001) – thus taking into account seasonal modulation of extremes. The resulting distributions are a Generalized Pareto distribution in the Point Over Threshold method, and a Generalized Extreme Value (GEV) distribution in the Block Maxima method (Coles, 2001) having different characteristics from each other. Parameters can then be solved for to estimate the value of the variable in the tails of the distribution. The Block Maxima approach involves more decision making – however, this method can more efficiently utilize the available data, and results in better estimations for the values of extremes (Kharin et al., 2007).

There are also different techniques for parameterizing the GP and GEV distributions such as the Maximum Likelihood approach and Method of L Moments. The latter technique is utilized more often, but the use of Maximum Likelihood incurs several advantages (Katz, 2013).

Covariates are incorporated into this approach which take into account periodicity or trends in the data (which can be removed). Covariates also provide insight into physical mechanisms related to teleconnection indices or ocean-atmosphere feedback mechanisms. Silmann et al. (2011), related GEV parameters to atmospheric blocking in their analysis of extreme cold outbreaks over Europe under meridional jet stream configurations. Specific to the Vancouver area, Abeysirigunawardena et al. (2009) utilized such methods to determine values for specific return period intervals associated with extreme wind events and relate their occurrence to ENSO activity.

3.3 Quantitative Methods

More recently, quantitative methodologies have been developed to determine if extreme meteorological events pose specific risk to populations. Such methods utilize rigorous scientific procedures to establish correlation between specific meteorological thresholds and risk. These methods rely on quantitative data such as randomized control trials and output from regional and global circulation models to indicate public health concerns and burdens on populations; as well as to evaluate specific public policies developed to address such concerns (Hess et al., 2014). These methodologies are referred to as evidence-based public health.

In terms of extreme heat, several studies have shown the benefit of these methodologies such as Hess et al. (2014) who used an example of this approach for New York City and found it to be a potentially useful strategy for climate change adaptation; and Zhang et al. (2014) for Detroit. The latter used modeled and observational weather data to correlate maximum temperature with mortality. A similar approach was used by Kosatsky et al. (2012) specifically for the Vancouver region to estimate that nearly 200 deaths resulted from a July 2009 heatwave.

Proposed thresholds for heat-alert advisories were developed by Henderson and Kosatsky (2012) for both Vancouver and Abbotsford in response to the impacts of the previously mentioned heatwave. Threshold temperatures for proposed heat advisories were derived by determining the lowest 2-day average temperature (with the condition that it be >= the 99th percentile) for which the distributions of daily mortality would be entirely above the 99th percentile. For Vancouver the threshold was 31˚C, while for Abbotsford it was 36˚C. These locations represent a range of afternoon maximum temperature across the region due to modulation from the afternoon sea-breeze (see Chapter 2) which typically results in cooler afternoon highs for coastal areas such as Vancouver International Airport (YVR). Since forecast temperatures for the second day would have to be used for the issuance of heat alert advisories, threshold temperatures were set to lower values (29˚C and 34˚C) to take into account the potential for model and forecast underestimation of projected afternoon maximums. These are used as selection criteria for heatwave events in Chapters 4 and 5.

The potential for advisory issuance using such approaches has extended to other natural hazards over the region as well. Jakob and Weatherly (2003) developed a graduated system of criteria and thresholds for landslide advisories in the region of North Vancouver. Using discriminant function analysis, they determined that 6 h maximum precipitation and 4-week antecedent precipitation were the most important predictors in separating landslides events from non-landslide events. The differences in discriminant function scores were then used to develop the thresholds for the advisory system. BGC Engineering (2006) developed a similar tiered landslide advisory system based on a function of storm total and 4-week antecedent precipitation to separate events from non-events (having occurred after 1972). This function is used as the basis in selection criteria for landslide events considered in Chapter 4 - with the caveat that 24 h precipitation is used since intensive rainfall events in the region average out to that duration (Jakob and Lambert, 2009).

3.4 Trends and Projections of Meteorological Extremes

3.4.1 Non-stationarity

The techniques discussed in Section 3.2 assume that statistical parameters (including the magnitude of extremes) remain constant within a time-series of data. However, as mentioned in Chapter 1, many studies show increases in the occurrence and intensity of such extremes. The temporal trends and cycles within these datasets cause them to be considered non-stationary (Coles, 2001). This provides another advantage to the quantitative methodologies used in this study (see previous sub-section).

3.4.2 Trends Over the Northern Hemisphere

Several studies for locations in the Northern Hemisphere have shown positive trends in extreme precipitation including Japan (Iwashima and Yamamoto, 1993), many regions of the United States (Karl and Knight, 1998; Kunkel et al., 1999), eastern Canada (Zhang et al., 2001), and southern and southeastern China (Zhai et al., 2005). The findings suggest a spatially consistent pattern with increases in extreme occurrences expanding out from foci representing higher precipitation regimes. With respect to Europe, a temporal pattern is noted in some studies with increases in precipitation extremes during the cold season (Osborn et al., 2000; Moburg et al., 2006); and general increases over Mediterranean regions (Brunetti et al., 2001; Alpert et al., 2002). These trends are likely being driven by increases in moisture available to precipitation-producing weather systems. Warming SSTs result in higher saturated water vapour pressure over ocean surfaces in accordance with the Clausius-Clapeyron relation, thus allowing for more evaporation and moisture advection.

Studies have also shown that heatwaves are becoming more frequent and intense. Della-Marta et al. (2007) showed that the length of summer heat-waves for western Europe doubled along with nearly a three times increase in the occurrence of hot days. Kuglitsch et al. (2010) developed heatwave indices reflecting heat wave number, length and intensity. All indices were found to be increasing in the records used which span from 1960 to 2006. Rahmstorf and Coumou (2011) developed a theoretical model for relating trends in warming with the anticipated frequency of record high temperatures. They found that the relation between the warming trend and increase in expected records was exponential, and that the projected number of new records would be much greater than if no trend were present.

Several studies have also tried to attribute heatwave intensity and probability to anthropogenic warming. For the 2003 European heatwave, Stone et al. (2004) demonstrated that validation of simulated temperature anomalies was sensitive to the inclusion of factors representing anthropogenic forcing. For the Russian heatwave of 2010, Rahmstorf and Coumou (2011) applied their model to data for Moscow in July and determined that record high temperatures are now 5 times as likely than in the past; and the probability that the event was caused by global warming was nearly 80%. Otto et al. (2012) suggested that even though the magnitude of the Moscow heat wave of 2010 may have been mainly attributable to natural variation, the likelihood of its occurrence was increased due to anthropogenic effects.

3.4.3 Local Trends at Vancouver, British Columbia

Several past studies have examined precipitation trends over the region and have noted varied results. Zhang et al. (2001) and Jakob et al. (2003) showed little if any overall trends in precipitation intensity for the region. However, at monthly timescales some trends in convective-type precipitation are apparent. Jakob et al. (2003) and PCIC (2007) showed that short duration, intense precipitation events were increasing at statistically significant rates for some stations in the region during the spring months. However, the correlation between such events and the PDO and ENSO in Jakob et al. (2003) suggested that the trends were not a result of anthropogenic warming, but rather due to a shift in the PDO regime. In terms of more pervasive hydrometeorological hazards, studies of flow rates in the region show decreases in peak flow (Morrison et al., 2002) due to decreases in snowpack.

There are also trends in warm season hazards for the region. Stewart et al. (2017) found that only lower intensity heat extremes were increasing at statistically significant rates – particularly so at YXX (which is more isolated from the effects of the sea-breeze). However, rates of increase for more intense heat extremes were considerably higher, but low sample size precluded statistical significance.

3.5 Future Projections for the Region

In terms of precipitation, most studies show greater overall precipitation for the region which will drive increases in total annual flow (Shrestha et al., 2012) (even while peak annual discharge decreases further), and increased susceptibility to landslides (Jakob and Lambert, 2009) due mainly to increases in 28 d antecedent precipitation (with lower increases in intense, short-term precipitation).

In relation to warm season hazards such as heatwaves, some studies have shown a projected increase in meridional flow patterns generally conducive to heatwave development (Francis and Vavrus, 2012). Such synoptic forcing is associated with offshore flows along the Pacific coast and drive heatwaves in the region (Brewer et al., 2013). However, Brewer and Mass (2016a) showed that synoptic variability in parameters such as geopotential height and surface pressure are projected to decrease over the region. This in turn produces reduced variability of u-component flow in the lower atmosphere and attenuates occurrences and magnitudes of offshore flows (Brewer and Mass, 2016b). As a result, projected increases in heat extremes are attenuated for areas near the ocean compared to inland.

REFERENCES

Alpert, P. and co-authors. (2002). The paradoxical increase of Mediterranean extreme daily rainfall in spite of decrease in total values. *Geophys. Res. Lett,* 29(11), doi.org/10.1029/2001GL013554

Abeysirigunawardena, D.S., E. Gilleland, D. Bronaugh, P. Wong. (2009). Extreme wind regime responses to climate variability and change in the inner south coast of British Columbia, Canada. *Atmos.-Ocean,* 47(1), 41-62.

BGC Engineering Inc. (2009). *Regional IDF Curves, Metro Vancouver Climate Stations: Phase 1.*

_______(2006). *Landslide Risk Management for Berkely-Riverside Escarpment.*

Brewer, M.C., C.F. Mass. (2016a). Projected changes in western U.S. large-scale summer synoptic circulations and variability in CMIP5 models. *J. Climate,* 29, 5965-5978.

_______(2016b). Projected changes in heat extremes and associated synoptic- and mesoscale conditions over the northwest United States. *J. Climate*, 29, 6383-6400.

Brunetti, M., L. Buffoni, M. Maugeri, T. Nanni (2000). Precipitation intensity trends in northern Italy. *International Journal of Climatology,* 20, 1017–1031.

Coles, S. (2001). *An Introduction to Statistical Modeling of Extreme Values.* London, England: Springer-Verlag.

Della-Marta, P.M., M.R. Haylock, J. Lutebacher, H. Wanner (2007). Doubled length of Western European summer heat waves since 1880. *J. Geophys. Res.*, 112, doi:10.1029/2007JD008510.

Francis, J.A.,and S.J. Vavrus (2012). Evidence linking Arctic amplification to extreme weather in mid-latitudes. *Geophys. Res. Lett.,* 39, L06801, doi:10.1029/2012GL051000.

Jakob, M., and H. Weatherly. (2003). A hydroclimatic threshold for landslide initiation the North Shore Mountains of Vancouver, British Columbia. *Geomorph.,* 54, 137-156.

_______and S. Lambert. (2009). Climate change effects on landslides along the southwest coast of British Columbia. *Geomorph.,* 107, 275-284.

______, McKendry, I., Lee, R. (2003). Long term changes in rainfall intensities in Vancouver, British Columbia. *Can. Water Resources Jour.,* 28(4), 587-604. DOI:10.4296/cwrj2804587.

Karl, T.R. and R.W. Knight (1998). Secular trends of precipitation amount, frequency, and intensity in the United States. *Bull. Am. Meteorol. Soc.,* 79**,** 231–241.

Katz, R.W. "Statistical Methods for Relating Temperature Extremes to Large-Scale Meteorological Patterns." US CLIVAR: Analyses, Dynamics, and Modeling of Large

Scale Meteorological Patterns Associated with Extreme Temperature and Precipitation Events. Lawrence Berkeley National Laboratory, Berkeley, CA, Aug 20-22, 2013.

Kharin, V.V., F.W. Zwiers, X. Zhang, G.C. Hegerl. (2007). Changes in temperatures and precipitation extremes in the IPCC ensemble of global coupled model simulations. *J. Climate*, 20,1419-1444.

Kosatsky, T., S.B. Henderson, S.L. Pollock. (2012). Shifts in mortality during a hot weather event in Vancouver, British Columbia: rapid assessment with case-only analysis. *Am. J. Public Health,* 102, 2367-2371.

Kuglitsch, F.G. et al. (2010). Heat wave changes in the eastern Mediterranean since 1960. *Geophys. Res. Lett,* 37, L04802, doi:10.1029/2009GL041841.

Kunkel, K.E., K. Andsager, D.R. Easterling (1999). Long-Term Trends in Extreme Precipitation Events over the Conterminous United States and Canada. *J. Climate*, 12(7), 2515–2527.

Henderson S.B., and T. Kosatsky. (2012). A data-driven approach to setting trigger temperatures for heat health emergencies. *C.J. Public Health,* 103(3), 227-230.

Hess J.J., and co-authors. (2014). An evidence-based public health approach to climate change adaptation. *Environ. Health Perspect.* 122, 1177–1186

Iwashima, T. and R. Yamamoto (1993). A statistical analysis of the extreme events: Long-term trend of heavy daily precipitation. *J. Meteor. Soc. Japan,* 71**,** 637–640.

Moberg A. and co-authors. (2006). Indices for daily temperature and precipitation extremes in Europe analyzed for the period 1901–2000. *J. Geophys. Res*., 111, D22106, doi:10.1029/2006JD007103.

Morrison, J., M. C. Quick, and M. G. G. Foreman, 2002: Climate change in the Fraser River watershed: Flow and temperature projections. *J. Hydrol.*, 263, 230–244.

Osborn, T.J., M. Hulme, P.D. Jones, T. A. Basnett, (2000). Observed Trends in the Daily Intensity of United Kingdom Precipitation. *Int. J. Climatol*., 20, 347–264.

Otto, F.E.L., N. Massey, G.J. van Oldenborgh, R.G. Jones, M.R. Allen, (2012). Reconciling two approaches to attribution of the 2010 Russian heat wave. *Geophys. Res. Lett.*, 39, L04702, doi:10.1029/2011GL050422.

Pacific Climate Impacts Consortium. (2007). *GVRD Historical and Future Rainfall Update.*

Rahmstorf, S., and D. Coumou (2011). Increase of extreme events in a warming world. *Proceedings of the National Academy of Sciences of the United States of America,* 10.1073/pnas.1101766108.

Shrestha, R. R., M. A. Schnorbus, A. T. Werner, A. J. Berland (2012). Modeling spatial and temporal variability of hydrologic impacts of climate change in the Fraser River basin, British Columbia, Canada. *Hydrol. Processes*, 26, 1840–1860.

Sillmann, J., M. Croci-Maspoli, M. Kallache, R.W. Katz, (2011). Extreme cold winter temperatures in Europe under the influence of North Atlantic atmospheric blocking. *J. Climate*, 24, 5899-5913.

Stewart, R.E., D. Betancourt, J.B. Davies, D. Harford, E. Joakim, Y. Klein, R. Lannigan, L. Mortsch, K. Tang and P.H. Whitfield, 2017: A multi-perspective examination of heat waves affecting Metro Vancouver: Now into the future. Natural Hazards. DOI: 10.1007/s11069-017-2793-7.

Stone, D.A., P.A. Stott, M.R. Allen (2004). Human contribution to the European heatwave of 2003. *Nature*, 432, 610-614.

Zhai, P. M., X. Zhang, H. Wan, and X. Pan (2005). Trends in total precipitation and frequency of daily precipitation extremes over China. J. Climate, 18, 1096–1108.

Zhang K. and co-authors. (2014). Using forecast and observed weather data to assess performance of forecast products in identifying heat waves and estimating heat wave effects on mortality. *Environ. Health Perspect.*, 122, 912–918.

Zhang, X., W.D. Hogg, E. Mekis (2001). Spatial and temporal characteristics of heavy precipitation events over Canada. *J. Clim*., 14, 1923–1936.

CHAPTER 4: SYNOPTIC TYPING, EMPIRACAL OTRTHOGONAL FUNCTION ANALYSIS AND TRENDS IN HYDROMETEOROLOGICAL EXTREMES AT VANCOUVER, BRITISH COLUMBIA

4.1 INTRODUCTION

4.1.1 Overview of Physical Hazards

The Vancouver, British Columbia region of Canada represents a diverse landscape with complex terrain and a corresponding wide array of physical hazards across the annual cycle. Many of these are associated with meteorologically driven extremes which have been shown through quantitative methods to pose risk to populations in the region.

There have been several such high-impact events over the region recently - namely the July 2009 heatwave (Kosatsky et al., 2012), multiday rainfall events resulting in a landslide in January 2005 (BGC Engineering, 2006), and the Stanley Park Windstorm of December 2006 (Worcester, 2010). Heatwaves are mainly limited to summer months (July to August) as the Jetstream moves north in response to a polewards shifting Hawaiian High (Oke and Hay, 1994). Ridge extensions allow for periods of clear air, insolation, and advection of subtropical airmasses (Bumbaco et al., 2013) – they can also facilitate downslope, offshore circulations in the lower atmosphere locally and can lead to extreme maximum temperatures (Brewer et al., 2012, Brewer et al., 2013; Brewer and Mass 2016a). Some studies have shown an increase in the frequency of heatwaves (Kuglitsch et al., 2010) and projected increases in the future climate (Rahmstorf and Coumou, 2011). However, Stewart et al. (2017) found that increases in the most extreme cases were not statistically significant for the local region, and that future increases in heatwaves over the Pacific Northwest may be attenuated in near-coastal zones (Brewer and Mass 2016a; Brewer and Mass 2016b).

During the winter months, the storm track retreats south allowing multiple synoptic frontal systems to come onshore. These systems are capable of producing heavy precipitation due to orographic forcing and severe winds as well (Oke and Hay, 1994). Studies in trends of precipitation over the region show mixed results with most agreement being on increases of short duration, intense rainfall events during spring (Jakob et al., 2003; PCIC 2007). Such convective types of systems can have localized effects and lead to flash flooding and local landslides; however widespread heavy precipitation region-wide is dependent on persistent synoptic patterns during the winter-time that supply abundant moisture (Lackmann and Gyakum 1999; Roberge et al., 2009) particularly near the North Coast Mountains. For example, Neimann et al. (2008) found that land-falling moisture plumes contained more water vapor during the summer, but in the absence of synoptic systems, flow and vapor flux is weaker. Similarly, Warner et al. (2012) showed that heavy precipitation and precipitable water are strongly associated with each other during the winter months, but displayed very little relationship to one another in the warm season.

Heavy antecedent precipitation can lead to favourable conditions for landslides in areas of steep terrain in the Vancouver region (Jakob and Weatherly, 2003; BGC Engineering, 2005; BGC Engineering, 2006) and windthrow of trees in certain soil types. The interplay of hydrometeorological variables such as intense short duration precipitation, heavy antecedent precipitation and winds associated with synoptic weather systems during the winter season therefore are critical to understanding physical risk during this season.

4.1.2 Objectives

Specifically, the objective of this paper is to better understand the meteorological processes behind a variety of hydrometeorological hazards related to extreme heat, wind, and precipitation across the annual cycle which have been shown to pose risk to the Vancouver, British Columbia region using quantitative or evidence-based approaches.

Empirical Orthogonal Function (EOF) analysis and synoptic typing will be used to characterize key synoptic and mesoscale processes associated with heatwaves, landslides, and windthrow events over the region.

Trend analysis of these synoptic types and EOF coefficients will also be conducted to understand any changes in associated processes.

4.2 METHODS

4.2.1 Data

4.2.1.1 Station Data

Daily meteorological data from several weather stations over the Vancouver region were acquired from Environment and Climate Change Canada (ECCC). Data pertaining to heatwaves were obtained for Vancouver International Airport (YVR) and Abbotsford International Airport (YXX), whereas data pertaining to winter-time hydrometeorological extremes were acquired for West Vancouver Automatic (WWA), West Vancouver Cypress Park (WVC) and North Vancouver Holyrood (NVH) in addition to YVR.

Data from 1950 to 2015 were extracted for YVR and YXX, but time periods for the other stations were variable due to limited availability. Data for WWA were acquired for the period 1992 to 2015; for WVC from 1958 to 1963; and for NVH from 1960 to 1968. Stations closer to the mountains represent a different climatological regime in terms of average annual precipitation – with much higher values due to orographic effects (Oke and Hay, 1994). Therefore, even though precipitation data for YVR extends for a long period, it does not accurately reflect values for regions most at risk from landslide events. These stations were selected because they are at a similar elevation to the station in North Vancouver used by studies to establish thresholds for landslide events (Jakob et al., 2003; Jakob and Lambert 2009); and a strong correlation between the average annual precipitation and elevation exists across the area (BGC Engineering 2009).

4.2.1.2 Cumulative Distribution Function Transfer Method for Precipitation

To assess the feasibility of extending the period of data relevant to hydrometeorological extremes, distributions were compared of daily, 7 d, and 28 d antecedent precipitation between YVR and WWA for 1992 to 2015; YVR and WVC for 1958 to 1963; YVR and NVH for 1960 to 1968.

Distributions for the 3 additional stations were similar to each other for each parameter, as were the distributions from YVR between the different time periods (Fig. 4.1). A cumulative distribution function (CDF) transfer method similar to that used in Stewart et al. (2017) was implemented for each station by mapping the YVR distribution onto the others and looking up corresponding percentiles or quantiles - thereby adjusting daily precipitation and 28 d antecedent precipitation for YVR for the period of 1950-2015 by taking an average of the 3.

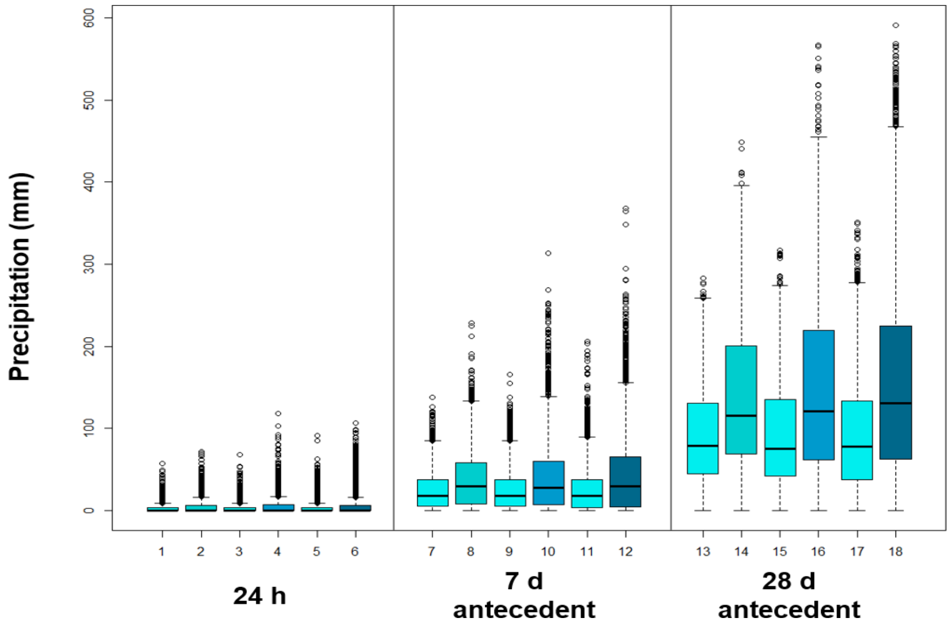

Figure 4.1: Boxplot for distributions of 24 h (left panel), and 7 and 28 d antecedent precipitation (centre and right panel respectively) between YVR (light cyan) and WVC (dark cyan) for the period 1958-1963; NVH (blue) for the period 1960-1968; and WWA for the period 1992-2015. Boxes extend between the 25th – 75th percentiles; while solid horizontal lines represent median values; vertical dashed lines extend to the 5th and 95th percentile respectively; and points represent outlying values. All subsequent boxplot will have the same formatting.

4.2.1.3 Reanalysis Data

Additionally, 6-hourly NCEP/NCAR Reanalysis Project (NNRP) data (Kalnay et al., 1996) were attained for the period 1950-2015 for a domain covering the West Coast of North America and a section of the northeast Pacific Basin bounded by the latitudes 30˚ N to 65˚ N and longitudes 210˚ W to 250˚ W. This was selected to have a large enough area to gain insight into synoptic processes while limiting computational demand. Variables acquired were sea-level pressure (SLP) and 500 hPa Geopotential Height (GPH). These data were used for the EOF analysis and synoptic typing.

The period of June to August was utilized for heatwave events, while the months of October to April were used for hydrometeorological extremes.

4.2.2 Selection Criteria

A catalogue of extreme events was generated for each class in accordance with specific criteria derived from evidence-based approaches whenever possible. The respective datasets were scanned exceedances of such thresholds to compare with EOF and other data.

4.2.2.1 Heatwaves

The proposed thresholds for heat alert criteria in the Vancouver region developed by Henderson and Kosatsky (2012) were used to identify heatwave events. These were based on an average of observed maximum same day temperature and forecast high temperature the subsequent day – 29˚C for YVR and 34˚C for YXX. The candidate triggers were based on the lowest temperature recorded on all days which were at or above the 99th percentile for daily mortality coincident with 2-day average maximum temperature also greater than or equal to the 99th percentile. These triggers were higher – 31˚C and 36˚C for Vancouver and Abbotsford respectively. For the purposes of identifying individual extreme heat days in this study, the lower thresholds were utilized because occurrences of temperatures greater than candidate values are very rare in the data period for YVR and YXX.

Single day maximum temperatures were used as selection criteria in this study, as any mesoscale processes occurring require compositing at a high temporal resolution, and conflation may become an issue at 2-day intervals. Occurrence of heat advisory days were estimated using both approaches and Pearson coefficients showed moderate correlation and statistical significance for both Vancouver and Abbotsford.

Near advisory heat alert criteria were met a total of 54 times for Abbotsford and 41 for Vancouver; giving a total of 95 cases and 70 heat wave days when criteria were met at either location. There were 18 multiday events when criteria were met at one or both stations consecutively representing 40 total days (36 times at Abbotsford, and 22 at Vancouver for a total of 58 cases).

4.2.2.2 Landslide Events

A variety of studies have attempted to develop triggers for landslide initiation over the local region. Variables typically include recent, intense (or storm total) precipitation and some measure of antecedent precipitation over a longer period prior to the occurrence.
BGC Engineering (2005) determined 24 h precipitation and 4-week antecedent precipitation as determining factors for landslide initiation over northern coastal regions of British Columbia.

With respect to the North Coast Mountains in the Vancouver region, Jakob and Weatherly (2003) used discriminant function analysis to establish 6 h maximum precipitation and 4-week antecedent precipitation as important predictors in separating events which produced landslides from those that did not. The difference in the discriminant function scores between the two outcomes were used to develop a graduated system of thresholds and alert criteria. Similarly, BGC Engineering (2006) established a tiered landslide advisory methodology for North Vancouver. All landslide events having occurred after 1972 were above the highest threshold as a function of storm total precipitation and 4-week antecedent precipitation. The threshold selected for this study follows the system developed by BGC Engineering (2006) based on those two variables for the lowest alert criteria. The 24 h precipitation amount was used as the storm total here since most periods of intense precipitation average to around 24 h (Jakob and Lambert 2009). Specifically, landslide alert events were considered to be triggered if: daily precipitation is greater than 150 mm; or the daily precipitation is greater than 40 mm and the 28 d antecedent precipitation is greater than 225 mm; or if the daily precipitation is between 40-150 mm, and the antecedent precipitation is between 150-225 mm. A total of 350 cases between 1950 to 2015 occurred using the above criteria.

4.2.2.3 Windthrow Events

Threshold criteria for windthrow events are not as clear as for other extremes. Various studies have attempted to determine critical wind speeds for tree breakage using mechanical models and empirical relations, but these models have limitations in terms of calibration and verification (Gardiner et al. 2008). Recently, an absolute threshold for tree breakage has been proposed by Virot (2016) of 42 $m \cdot s^{-1}$. More generally, the enhanced Fujita scale used by the National Weather Service includes estimates of tree breakage and toppling for a ranging from wind speeds of 32.5 $m \cdot s^{-1}$ to 52.8 $m \cdot s^{-1}$. A traditional index of wind damage – the Beaufort Wind Scale -suggests tree toppling can occur at lower wind velocities with a threshold of 24.7 $m \cdot s^{-1}$ (https://www.canada.ca/en/environment-climate-change/services/general-marine-weather-information/understanding-forecasts/beaufort-wind-scale-table.html). Specific to the region, toppling of trees affecting power lines increases exponentially towards this threshold (Read, 2015).

These discrepancies arise due to different processes which cause tree damage (apart from tree health, structural integrity, etc). Certain soil types lose their cohesiveness when saturated which can lead to tree toppling and uprooting at lower wind velocities. Therefore, considerations of antecedent precipitation are important to establishing any threshold for windthrow occurrence rather than just precipitation intensity or storm total precipitation (Read, 2015). This process is mutually exclusive with trunk breakage in that if a tree topples at a lower wind velocity, the trunk cannot break at a higher one. For the purposes of the study therefore, the lowest threshold from the Beaufort Wind Scale (daily maximum wind gusts greater than or equal to 24.7 $m \cdot s^{-1}$ at YVR) was used to identify windthrow events constrained by 28 d antecedent precipitation of greater than the 90th percentile. To establish a more concise threshold, a catalogue of tree damage for Vancouver could be developed from which important variables and respective thresholds could be better understood through statistical procedures. Occurrences of greater than or equal to 90 km/h daily maximum wind gusts at YVR were also considered to understand the processes representing extreme wind represent not constrained by precipitation. Overall 35 occurrences of extreme wind occurred over the period – 19 not constrained by antecedent precipitation and 16 that were (Tables B-1 and B-2).

4.2.3 Multilevel Synoptic Classification and Empirical Orthogonal Function Analysis

Previous studies have utilized both compositing and synoptic typing for the region relating large scale patterns to extremes - Bumbaco et al. (2013) for heatwaves over the Pacific Northwest; McKendry (1994) for episodes of above normal temperature and elevated ground level ozone concentration at Vancouver; and Stahl et al. (2006) to examine the role of ocean-atmosphere coupling on winter SLP patterns over British Columbia. As in the latter study, McKendry et al. (2006) used a combination of Principal Component Analysis (PCA) and k-means synoptic to validate mean SLP patterns from a Global Climate Model for the Pacific Northwest of North America.

PCA is a dimensionality reduction technique which converts potentially correlated observations from different variables into uncorrelated, linearly independent combinations representing separate modes of variability. These are knowns as Principal Components (PCs). When used with time-series of gridded data in meteorological and oceanographic applications, the technique is typically referred to as EOF analysis. The reduction of the time-space field in the data results in i) spatial patterns representing the different modes of variability referred to as EOFs, and ii) a time-series in the magnitude of occurrence for each of the EOFs referred to as PCs, PC scores, or PC coefficients. In this study, the terms PC and PC coefficient are used.

K-means sorting is a method of non-hierarchical cluster analysis in which data or observations are assigned to one of a user-defined number clusters (k) by minimizing the size of the centroid (cluster mean) and reducing the with-in cluster sum of squares (minimizing point-centroid distance within each group). The algorithm re-calculates the optimal position of the centroids and points relative to each centroid after each data are processed in a number of iterations based on centroid stability or a user-defined threshold. Synoptic types based on the centroids (means) are similar to standard weather maps unlike EOFs which represent orthogonal or independent modes of variability and have lower physical interpretability (Grotjahn et al., 2016).

Here, a methodology similar to McKendry et al. (2006) and Stahl et al. (2006) was taken combining PC or EOF analysis with k-means clustering to derive several synoptic types for the warm season (June to August) and cold season (October to April) using a newer version of the software used in those studies. In McKendry et al. (2006) and Stahl et al. (2006), scores of the retained unrotated EOFs were passed to a k-means sorting algorithm to produce clusters or synoptic types. In this study, EOFs for both SLP and 500 hPa GPH gridded anomalies were rotated using the Varimax technique to derive a multilevel synoptic classification system.

For the warm season, 21 rotated EOFs were retained for SLP and 8 for 500 hPa GPH. While for the cold season, 14 rotated EOFs were retained for SLP and 15 for 500 hPa GPH. Threshold for retention of EOFs was selected to retain all PCs which explained at least 5% of the total variability (eigenvalues greater than 5) for the associated parameter (Fig. 4.2) or for any local maxima below this threshold. This was considered after rotation so EOFs whose eigenvalues are less than 5 are included for the case of sea-level pressure anomalies. In fact, rotation of certain EOFs had a large impact on their respective eigenvalues.

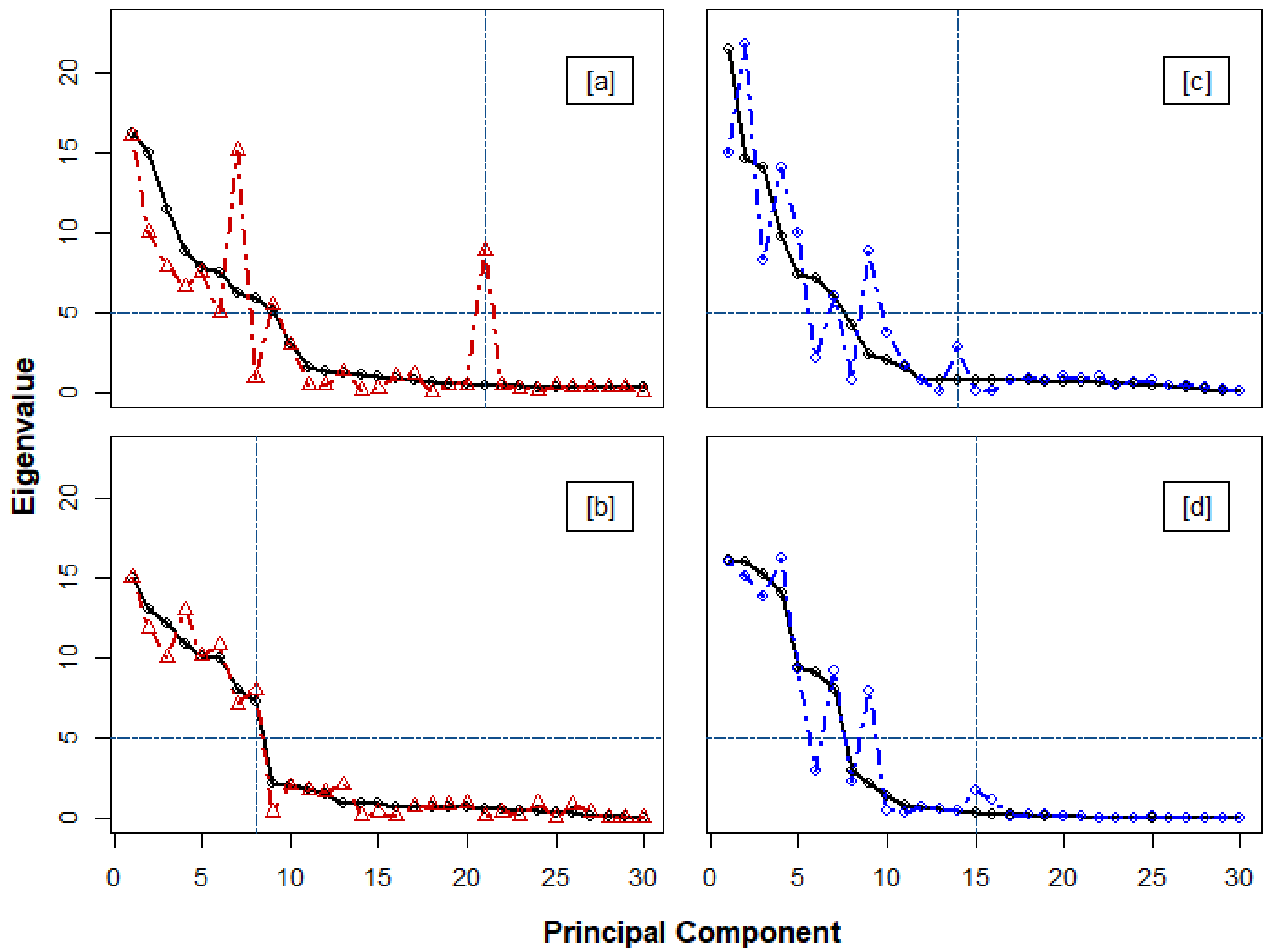

Figure 4.2: Eigenvalues for: June-August unrotated (black lines with round markers) and rotated (dashed red lines with triangular markers) PCs of (a) surface pressure anomalies and (c) 500 hPa GPH anomalies; and October-April unrotated (black lines with round markers) and rotated (dashed blue lines with circular markers) PCs of (b) surface pressure anomalies and (d) 500 hPa GPH anomalies. Horizontal dashed lines represent the 5% threshold for retention of principal components, and vertical dashed lines represent number of retained principal components after rotation.

A quantitative framework was developed to select the appropriate number of synoptic clusters (or the value of k) in the sorting algorithm for the warm season period. To start with, an approach following that of Smith (2012) was employed wherein the dispersion of all different synoptic types occurring on heat-alert days was measured against the maximum occurrence of certain synoptic types on heat-alert days. Ideally, the former should be minimized and the latter maximized – in this scenario one would see a large amount of heat-alert days as represented by a few synoptic types. Related to this, the relationship of within cluster and between-cluster variability was considered. With an increasing number of clusters (or value of k) for the sorting algorithm, the synoptic types should become more different from each other, while at the same time more similar to other members of their respective cluster. This results in sharper, better defined synoptic patterns which would be advantageous for identifying synoptic and mesoscale mechanisms related to heatwave occurrence. At the same time however, the dispersion of different synoptic types occurring during heat-alert days increases as more and more clusters are present, and the maximum occurrence of heat-alert days pertaining to one particular cluster would decrease. Since this study is concerned with potentially temporally evolving patterns, some measure of partitioning of different synoptic types as a function of time from observed heat-alert days should also be considered.

Therefore, three parameters were derived in order to determine the appropriate value of k (number of synoptic clusters). Parameter α represents the ratio of maximum occurrence of a specific synoptic type during heatwave days to the total number of synoptic types occurring on heat-alert days (a measure of dispersion). Parameter β represents the ratio of between-cluster variation for all clusters and within-cluster variation of the maximum occurring synoptic type. Parameter γ an index related to the partitioning of synoptic types between all events and multiday events, first and last days of multi-day events, and days prior and days subsequent to multi-day events. The distributions of the variables were standardized by dividing all values by their respective means so that each of the 3 parameters had similar weight. A composite index was derived by adding α and β and scaling (multiplying) them by γ.

Maximum occurrence of synoptic type is highest for lower values of k as expected for most cases (not shown). However, for days pertaining to multiday events, maximum occurrence peaks at a k value of 54 compared with 11 for all days combined (not shown). In terms of α, most cases show a steep decline and exponential decay as k increases, although less so for days prior to, and days subsequent to multiday events (Fig. 4.3a,b,d,e,g,h). For β, trends show an approximately linear increase with k (Fig. 4.3a,b,d,e,g,h), while γ shows a logarithmic increase (Fig. 4.3c,f,i).

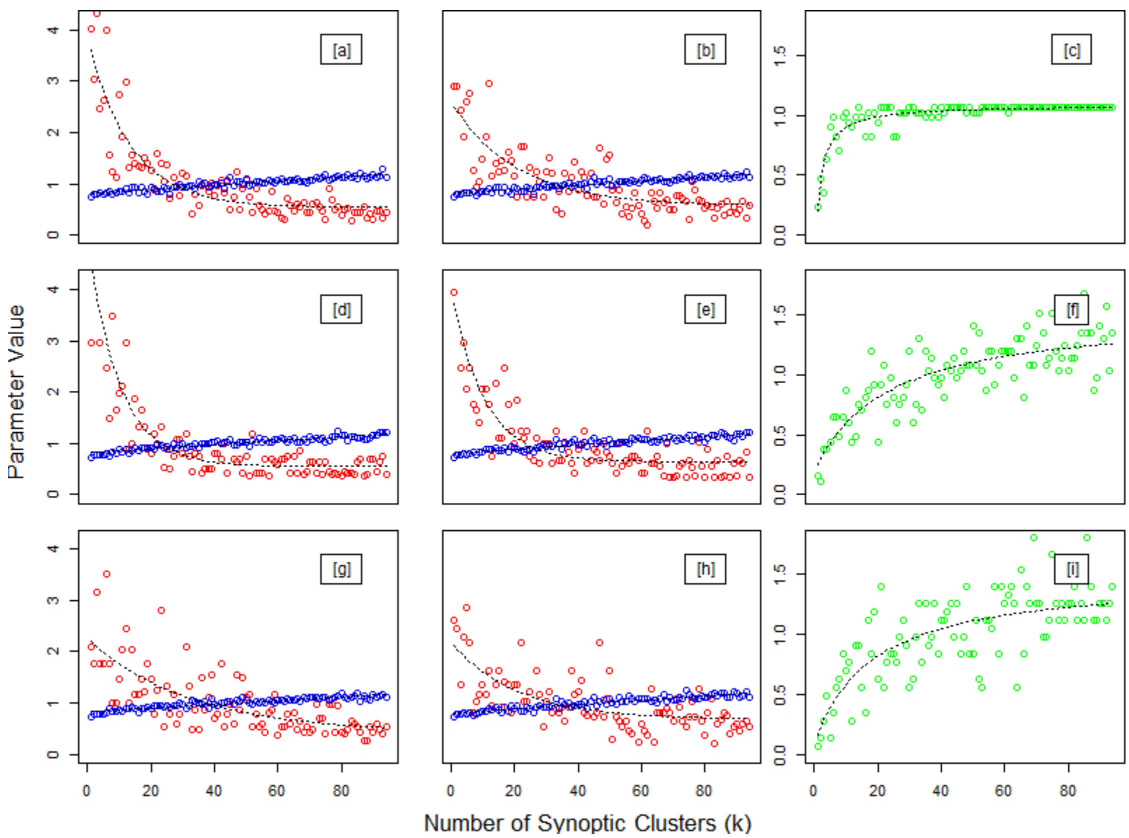

Figure 4.3: Parameters α (red circles), β (blue circles), and γ (green circles) for: [a] single day and [b] multiday events (top row), [d] first and [e] last day of multiday events (middle row), [g] day prior to and [h] day subsequent to multiday events (bottom row). Fitted curves for all parameters are represented by dotted lines.

When examining the composite index for determining the optimal number of synoptic clusters to retain for all days, multiday events, first days, last days, days prior and days subsequent to heatwave occurrence, it is clear that the appropriate value for k depends on the category of interest. For all events (Fig. 4.4a), the optimal number for k is reached early on, while multiday events (Fig. 4.4b) show a bi-modal peak in the composite index extending to much higher values of k. Both of these variables show a convergence in the index inferred through the lowering standard deviation as k reaches higher values. Meanwhile, for first days, and last days (Fig 4.4c,d), the index shows signs of continually increasing with little evidence of convergence. This suggests the k-means sorting algorithm is still resolving patterns associated with such days as the maximum value of k is reached. For days prior to, and days subsequent to multiday heatwave occurrence (Fig 4.4d,e), multimodal peaks are reached at mid to high range values of k and begin decreasing as the maximum number of synoptic clusters is reached. This implies that a lower value of k is needed to differentiate synoptic types between days prior and days subsequent to heatwaves. This is to be expected since there is larger time separation between these days than there is between first and last days of heatwaves; and therefore a stronger signal for differing synoptic types is present.

Since this study is interested with temporally evolving patterns associated with heatwaves, k-means clustering was ultimately not used as an approach due to limitations in differentiating synoptic types between first and last days of multiday events. Instead, individual EOFs were assessed in importance to heatwave occurrence; as were the physical mechanisms they represented. Using EOFs allows for interpretation of discrete, independent processes important to extreme events (Grotjahn et al., 2016). This also incurred advantages for winter-time events and synoptic clustering was not used for these events either. However, the methodology of k-means clustering is included in this work because: i) it represents an example of an approach for selecting the number of synoptic clusters which is typically arbitrary (Grotjahn, 2016); and ii) the parameters and composite index provide insight into the sensitivity of synoptic typing with respect to temporally evolving patterns.

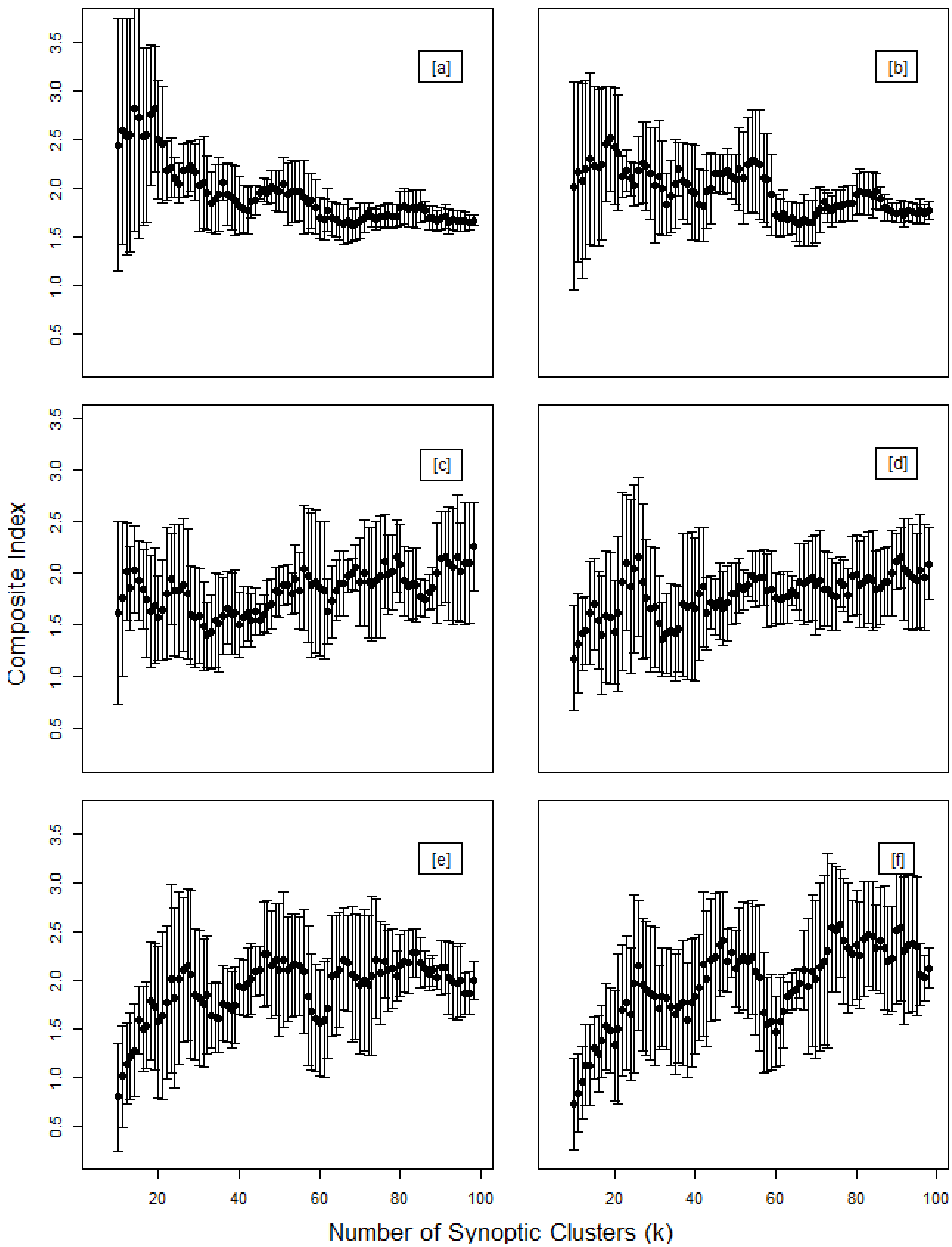

Figure 4.4: Mean composite index for determining appropriate number of clusters (k) in a multilevel synoptic classification system of heatwave days. Panels represent indices for: [a] all heatwave days, [b] days belong to multiday events; and [c] first day of, [d] last day of, [e] day prior to, and [f] day subsequent to multiday events. Error bars represent running standard deviation of index values

4.2.4 Regression Analysis

Linear regression was conducted to analyze trends in large scale atmosphere-ocean indices to understand any changes in the occurrence of extreme events; and for trends in several dynamic and thermodynamic parameters over the Pacific basin to gain insight into potential causal mechanisms. Logistic regression was conducted on: trends in occurrence of PC coefficient values greater than the 90^{th} , 99^{th}, and 99.9^{th} percentiles (count data) for each EOF/PC using the R project for statistical computing; and on trends in occurrence (counts) of the different types of extreme events. A logistic regression model was also used to understand the relationship between atmosphere-ocean indices and monthly probability of occurrence for the different events being considered.

In logistic regression, the odds ratio represent the exponentiated coefficients for parameters in the model. The product of a given y-value and the odds ratio gives the new value of y for a 1 unit increase in x. Since they are exponentiated, odds ratios cannot be negative; values less than 1 represent a decrease in odds, whereas values greater than 1 represent an increase.

RESULTS

4.3.1 Summer-time PCs and EOFs

The distributions of coefficients for all PCs occurring during single day and multiday heatwave events is shown in Fig. 4.5. The PCs are ordered by SLP first and then 500 hPa GPH (prior to rotation for both variables). For single day events, PCs 7 (although only with a median near 0.5) and PCs 28 have the highest positive distributions during single day events and are therefore important processes during these occurrences. Looking at the corresponding warm season EOFs (or eigenvectors, loading patterns, etc.) (see Figs. A-1 and A-2), EOF 7 represents an atypical surface pressure pattern with a trough oriented northeastwards from the subtropical Pacific basin rather than a classic West Coast Thermal Trough (WCTT) along the Pacific coast which is associated with heatwave events over the region (Brewer et al. 2013). EOF 28 depicts a classic upper ridge elongation over the west coast of North America which typical of west coast heatwaves (Bumbaco et al. 2013).

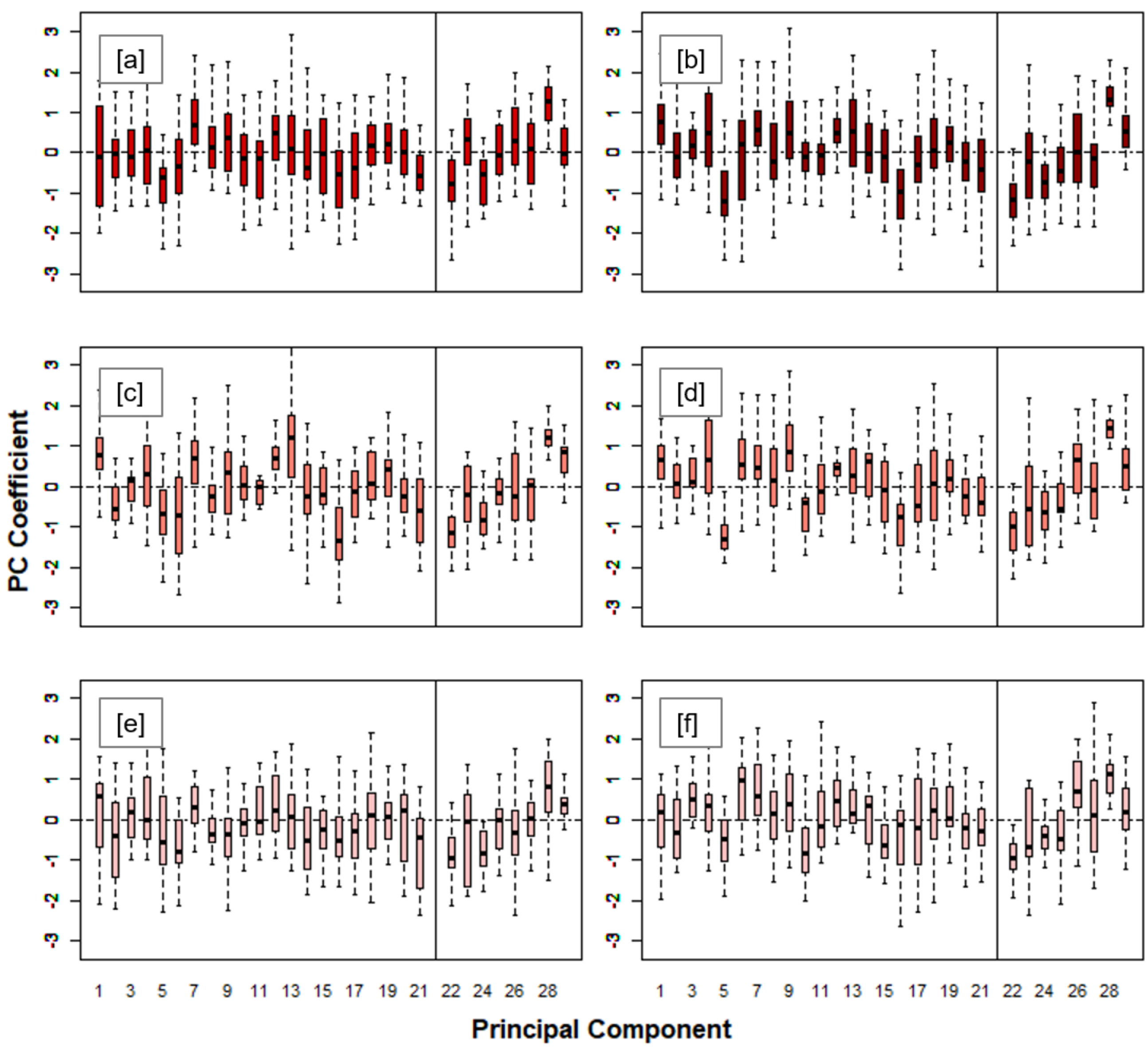

Figure 4.5: Boxplot for distributions of June-August SLP and 500 hPa GPH PC coefficients for a) single day events, b) multiday events; and for c) days preceding, d) first days, e) last days, and f) days

subsequent to multiday events. Formatting follows Fig. 1. Vertical line delineates SLP (left) and 500 GPH (right) PCs.

When multiday events are considered, the most important SLP PC represents both the leading mode of summer-time variability and the classic SLP configuration for heatwaves in the region. Namely, the interaction of a northwards displaced Pacific high approaching the west coast of North America (Mass et al., 1986; Mass and Albright, 1987) and the WCTT extending northwards from the thermal low over the Southwestern U.S. (Brewer et al., 2012). However, the negative pressure anomalies do not fully extend into British Columbia, so that WCTT extensions further poleward do not contribute as much to summertime SLP variability within the domain – and are therefore rarer. As in the case for single day events, EOF 28 shows high importance for multiday heatwaves.

There are also differences apparent in the distribution of coefficients for certain PCs. In particular, PC 1 (as already mentioned) has a positively shifted distribution for multiday events – particularly initially – which implies the WCTT extension from the Oregon coastal region in EOF 1 is a key process for such occurrences (Fig. 4.6a). There is also considerable difference in the distributions of PC 29 - being also positively distributed for multiday events when compared with single day events (Fig. 4.6b). EOF 29 represents a complex blocking structure - with 500 hPa GPH anomalies poleward of negative pressure anomalies. This can be interpreted as a Rex Block configuration – adding stability and longevity to the pattern for multiday events.

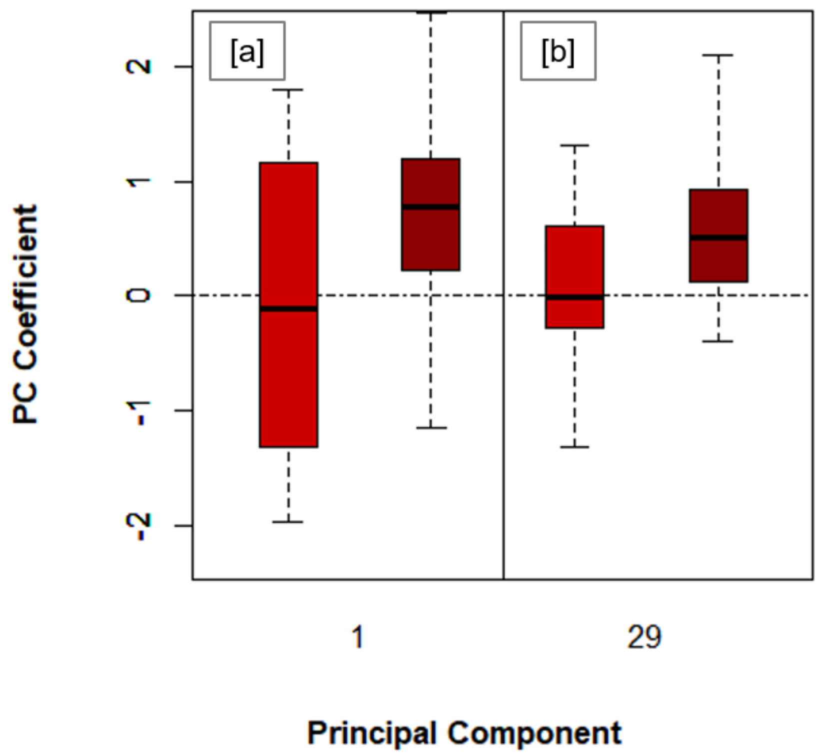

Figure 4.6: Boxplots for differences in distributions of June-August PC coefficients between single day events (left plot) and multiday events (right plot) for a) PC 1, and b) PC 29. Formatting follows Fig. 1.

From Fig. 4.5, it is also apparent that certain PC distributions display temporal sensitivity. In particular, PCs 3,6,9, and 26. These temporal trends in the distribution of PC coefficients are shown in Fig. 4.7. The distributions for all generally increase with time, and the first 3 corresponding EOFs depict low pressure anomalies at various foci inland. This can be interpreted as the movement of the WCTT inland and across the Coastal Mountains which occurs at the end of heatwave events (Brewer et al., 2012; Brewer et al., 2013; Brewer and Mass 2016a). EOF 9 also shows weak high pressure anomalies along the coast south of British Columbia which is interpretable as a mesoscale ridge generating coastal southerlies - which bring a cessation to heatwave events in the region (Mass et al., 1986; Mass and Albright, 1987; McKendry et al., 1997). EOF 26 shows high pressure anomalies at 500 hPa displaced eastwards – this implies the motion of upper ridge eastwards which in a feedback process with surface processes brings an end to the heatwave pattern.

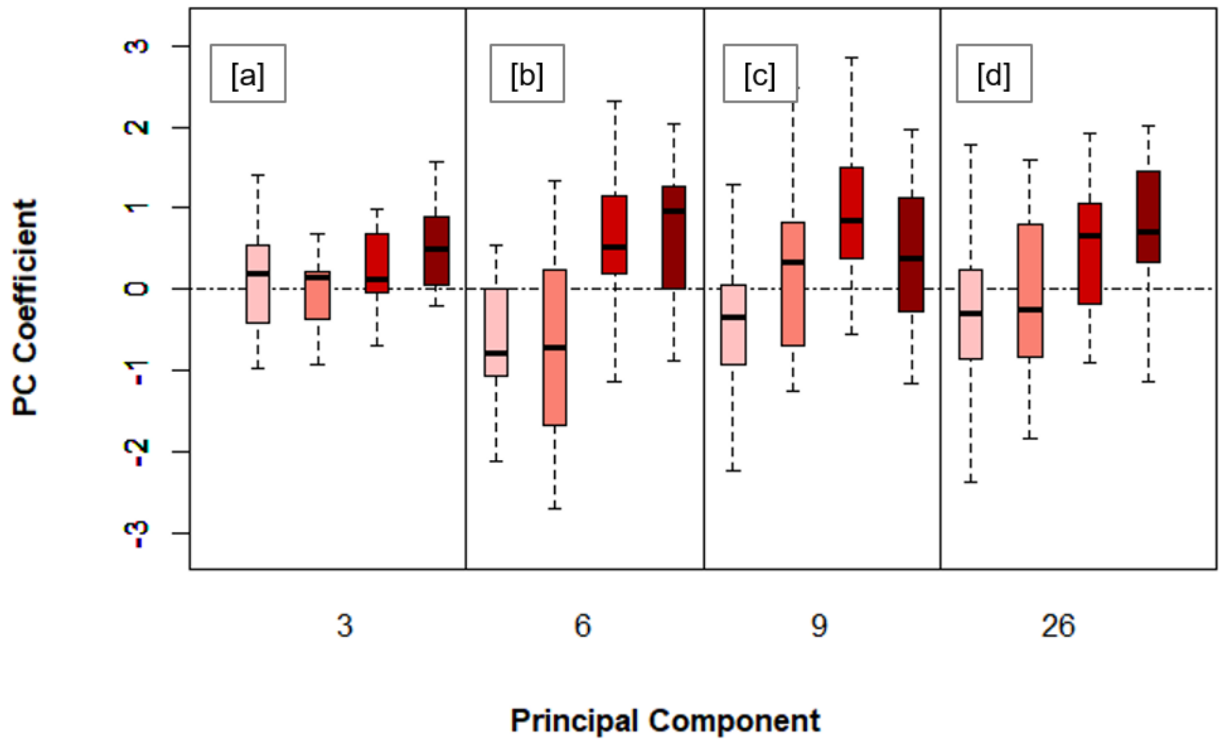

Figure 4.7: Boxplots from left to right of PC coefficient distributions: the day preceding, first day, last day, and day subsequent to multiday heatwave events for PCs: a) 3, b) 6, c) 9, and d) 26. Formatting follows Fig. 1.

4.3.2 Winter-time PCs and EOFs

The mean distributions of PC coefficients for the 28 d period preceding landslide and windthrow events (not constrained and constrained by 28 d antecedent precipitation respectively) are shown in Fig. 4.8. When considering antecedent conditions prior to landslide events, the signals are weak (median values are between 0 and 1), but distributions are highest for PCs 8 and 11 (SLP); and PCs 18 and 19 (500 hPa GPH). EOF 8 depicts low pressure anomalies in the Gulf of Alaska, whereas EOF 11 represents high pressure anomalies in the central U.S. The pattern of pressure anomalies in EOFs 11 and 19 suggests that they associated with each other. EOF 19 shows a northwest flow over the central U.S descending around an upper high further west corresponding to the location of surface high pressure anomalies in EOF 11. EOF 18 in particular represents a well known mechanism where-by deep moisture transport is facilitated; as is interaction with tropical and subtropical moisture in the Pacific (Lackmann and Gyakum 1999; Roberge et al., 2009) in a phenomenon often referred to as a Pineapple Express. These are associated with land-falling Atmospheric Rivers (Ralph et al., 2005) aligned perpendicular to the North Coast Mountains in the Vancouver region which enhances orographic forcing and precipitation totals over that region. It resembles "southwest-type events" from Roberge et al. (2009). EOF 19 implies a more zonal flow aloft with not as much linkage to the subtropics implied, but still allowing for considerable moisture advection and resembles "west- type" events from Roberge et al. (2009).

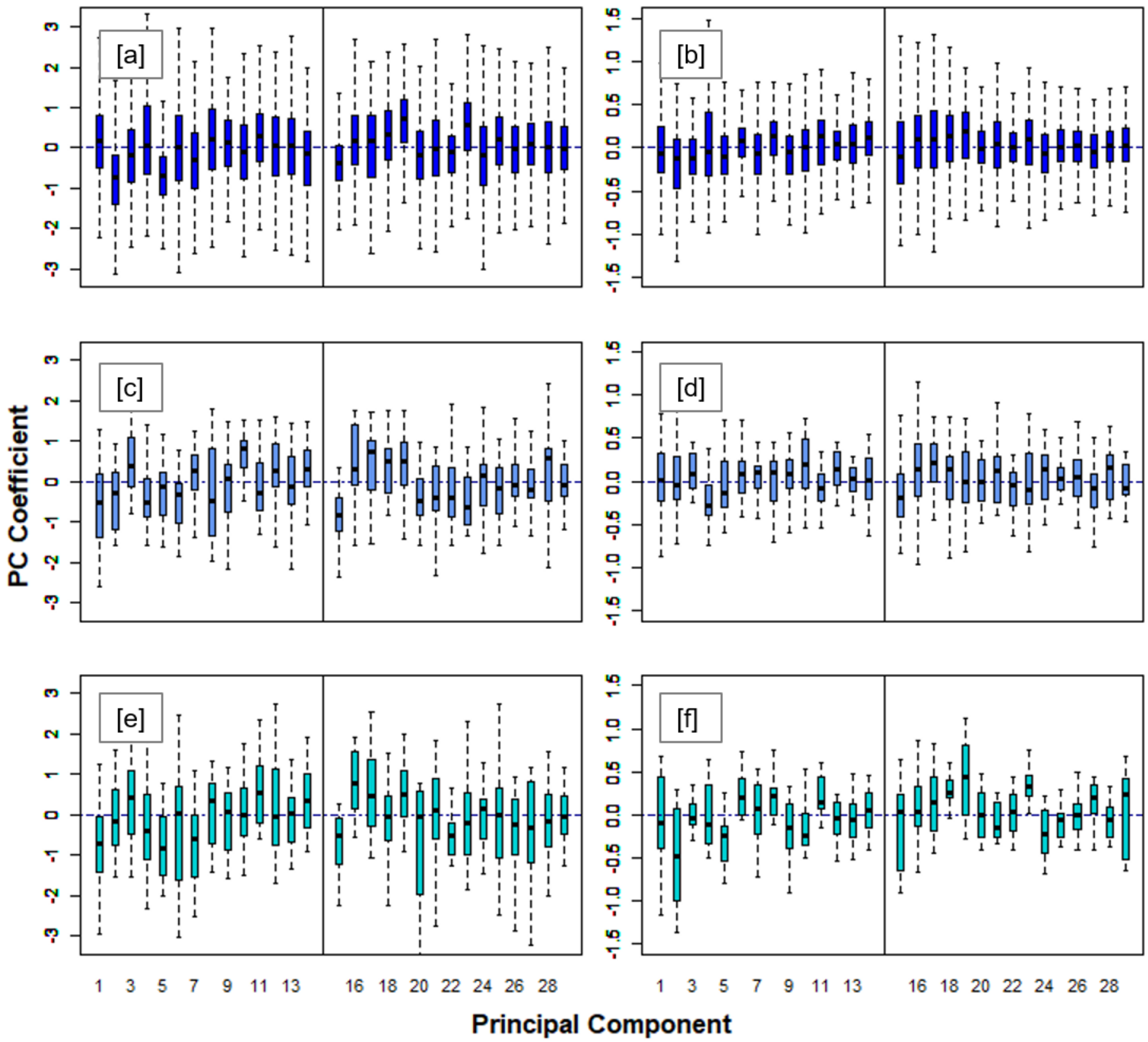

Figure 4.8: Boxplot of October-April SLP and 500 hPa GPH PC coefficients for: the day of (left column) and the period 28 d antecedent to (right column) landslide events (top row, dark blue); wind events not constrained by precipitation (middle row, light blue); and windthrow events constrained by antecedent precipitation (bottom row, turquoise). Formatting follows Fig. 1. Vertical line delineates SLP (left) and 500 GPH (right) PCs.

PC distributions the day of landslide events show PCs 19 and 23 (both pertaining to 500 hPa GPH) to be most important. EOF 19 has already been discussed, whereas EOF 23 is an anomaly pattern consistent with a positive Pacific North America (PNA) mode (see Section 3.3.4). This mode is generally associated with negative precipitation anomalies for the region (Stahl et al., 2006), but given the function used for estimating landslide events, some of theses occurrences are driven much more by antecedent precipitation and EOFs which are associated with above average precipitation. It is also characterized by a strong Aleutian Low which has been discussed as an important mechanism for heavy precipitation.

With regards to wind events not constrained by antecedent precipitation, PC distributions for the day of the event are highest for SLP PCs 3, 7, and 10 and 500 hPa GPH PCs 17, 18, 19 and 28. The corresponding SLP EOFs (Fig. A-1) all represent high pressure anomalies at various foci in the Pacific Basin – typical of a negative PNA mode. EOFs 3 and 10 also show negative pressure anomalies along the northern British Columbia coast or further inland setting a strong northwest geostrophic flow and implies cool advection over relatively warm water which assists in destabilization and momentum transfer downwards in the form of wind gusts. EOF 17 represents the upper reflection of a negative PNA pattern consistent with SLP EOFs 3,7,10. EOFs 18 and 19 as mentioned previously represent high precipitation processes – however, some Pacific Basin typhoons which have transitioned extra-tropically can approach the British Columbia coast from the southwest – as was the case with Typhoon Freda which produced the second highest maximum daily wind gust recorded at YVR and the highest with a southerly component). Southwest flow configurations would be conducive to steering them towards the region therefore conflating the distributions of PC coefficients as would other EOFs such as 1,5, 20 and 22. In case of Typhoon Freda, EOFs 24 and 26 show considerably positively shifted distributions for their PCs (not shown) even though they contribute very little to overall variability (Fig. 4.2). These systems can generate a very strong southerly flow and a minority of the wind events did show a southerly component to the maximum wind gust (Tables B-1 and B-2). Further study is required to characterize the synoptic processes for the subset of southerly extreme wind events at YVR and to assess if they are dominated by such transitioning extratropical systems, or if yet other diverse mechanisms are contributing as much.

PCs for antecedent conditions prior to windthrow events not confined by precipitation are generally similar, but PC 17 dominates as the most important, and PCs 18 and 19 have reduced importance.

Distributions for the day of wind events constrained by prior precipitation were highest for SLP PCs 3, 8, and 11, and for 500 hPa GPH PCs 16 and 17. EOF 16 represents the upper configuration of a generally positive PNA pattern; and with a displaced Polar Vortex over the Hudson Bay region (also implying a negative Arctic Oscillation (AO) in this process). All other EOFs are a combination of processes associated with landslide and wind events not constrained by antecedent precipitation – suggesting a conflation of these different processes. The differences in distributions between wind events constrained by prior precipitation and those that are not are summarized in Fig. 4.9.

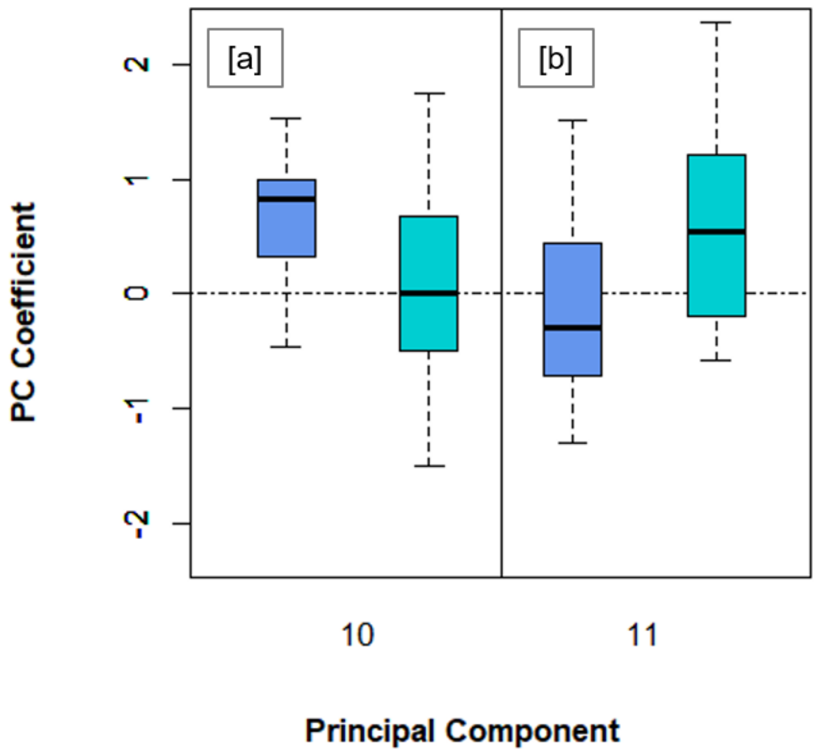

Figure 4.9: Differences in coefficient distributions for the day of wind events not constrained by antecedent precipitation (left) and those that are (right) for PCs: a) 10 and b) 11. Formatting follows Fig. 1.

In terms of antecedent conditions for wind events constrained by precipitation, SLP PCs 6 and 8 had the highest distributions for coefficients whereas 500 hPa GPH PCs 19 and 23 were the highest. EOF 6 represents an arctic outbreak scenario suggesting that snow and rain-on snow events play an important role preceding these types of windthrow events. EOFs 19 have already been discussed – with the implication here being that a west-southwest upper flow rather than a deep SW upper flow is sufficient to advect moisture for the necessary precipitation; and that, again, a positive PNA mode (as represented by EOF 23) is an important pattern to such events. This is summarized in Fig. 4.10.

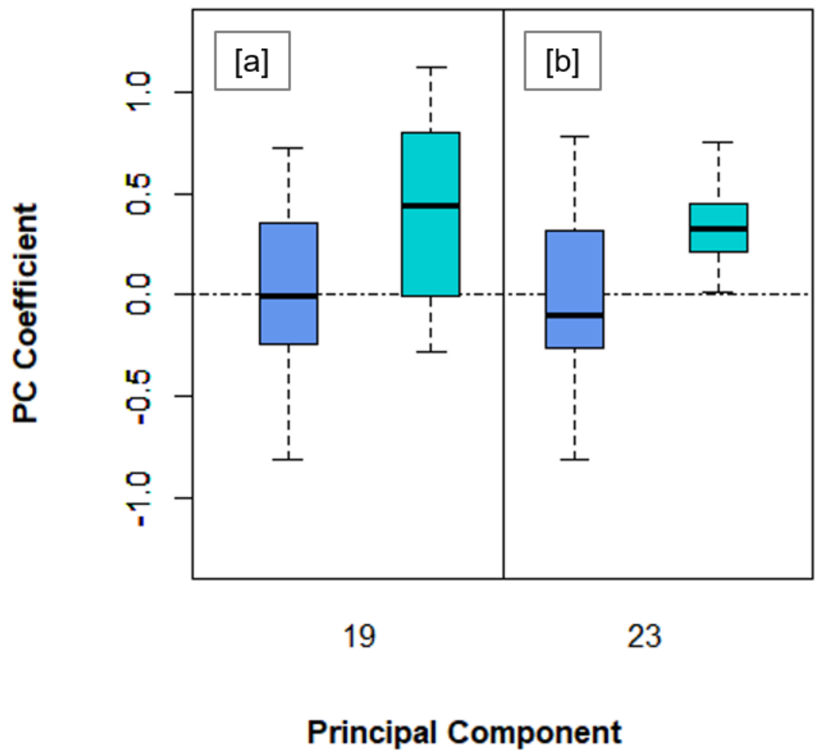

Figure 4.10: Differences in coefficient distributions for the 28 d period antecedent to wind events not constrained by antecedent precipitation (left) and those that are (right) for PCs: a) 19, and b) 23. Formatting follows Fig. 1.

4.3.3 Trend Analysis

4.3.3.1 Heatwaves

Trend analysis for intensity and duration of heatwaves at YVR and YXX from Stewart et al. (2017) is summarized in Fig 4.11. The change in odds of individual days and the maximum length of multiday events above particular temperatures was greatest for the highest temperature classes. However, these trends were not statistically significant due to small sample size.

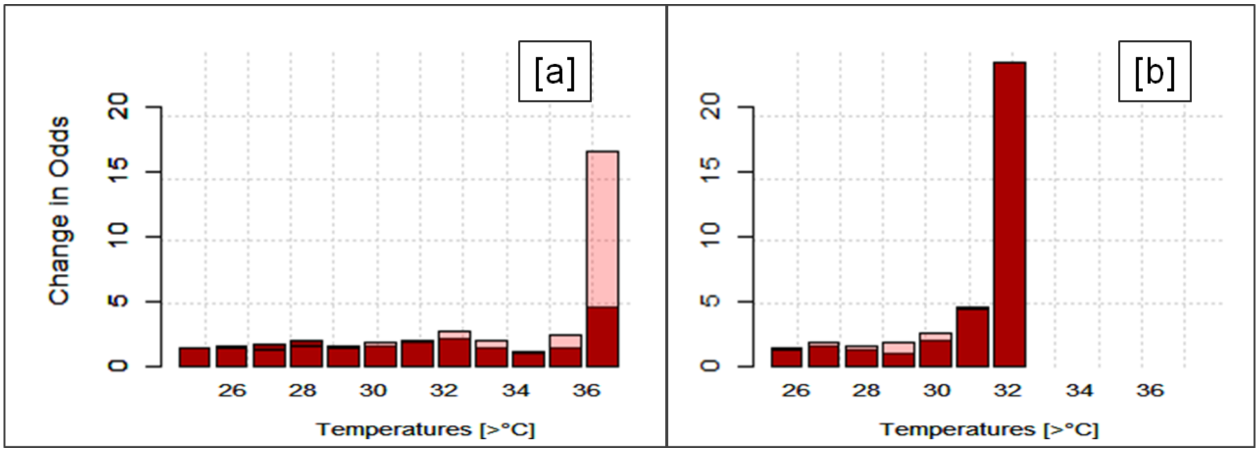

Figure 4.11: Change in odds in occurrence of individual days (dark red), and maximum length of consecutive days (light red) at or above specific temperatures thresholds for a) YXX and b) YVR. Adapted from Stewart et al. (2017).

4.3.3.2 Landslide and Windthrow Events

The results for the logistic regression carried out on hydrometeorological extreme events shows that only landslide events are increasing in probability (Fig. 4.12, top panel) – with a p-value of 0.11 for the odds ratio (Table 4.1). The odds of windthrow events not constrained by antecedent precipitation were decreasing considerably - at a nearly statistically significant rate (p-value of 0.09), whereas windthrow events constrained by prior 4-week precipitation were decreasing very slightly, but the odd ratio is not statistically significant. However, occurrences of both types of wind events appear to show a cyclical pattern.

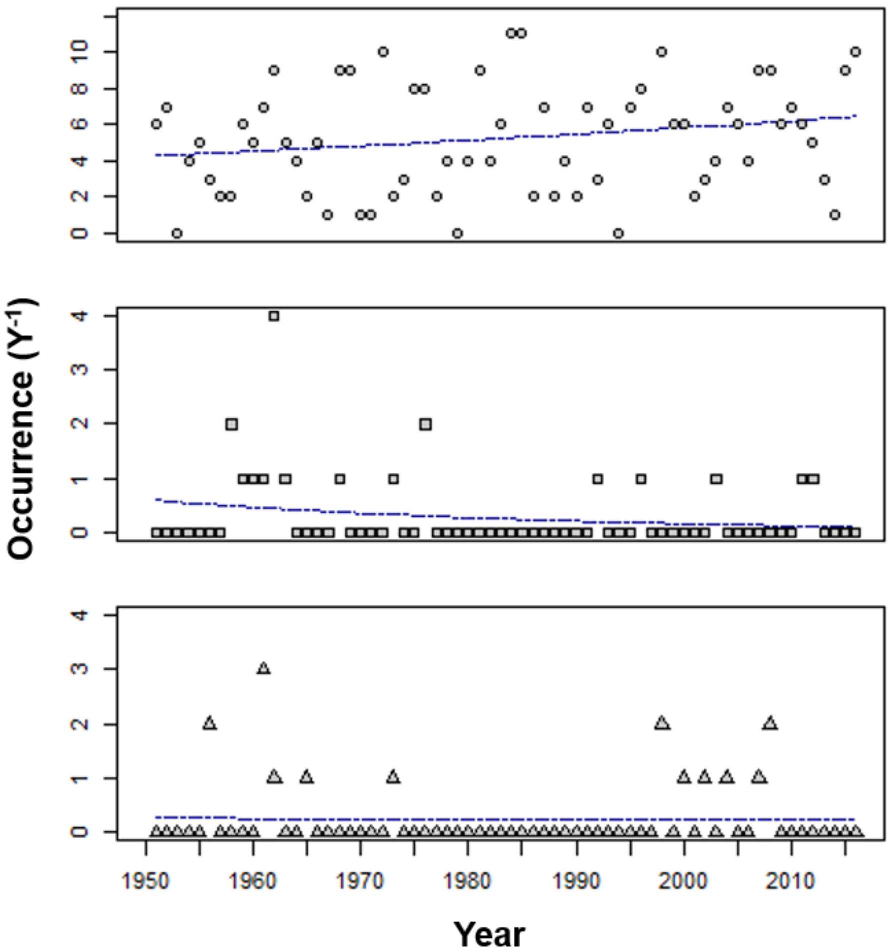

Figure 4.12: Logistic regression on counts of: landslide events (top row), wind events not constrained by antecedent precipitation (middle row), and wind events constrained by antecedent precipitation (bottom row). Regression line is denoted by dashed blue line.

Table 4.1: Logistic regression model for trends in landslide, wind only, and wind and precipitation events.

	Odds Ratio	P-Value
Landslide	1.006	0.107
Wind Only	0.974	0.082
Wind & Precipitation	0.997	0.882

4.3.3.3 Trends in PCs and EOFs

The logistic trend analysis for selected PCs which were shown to be important to heatwave events are summarized in Table 4.2. For heatwave related PCs/EOFs only two show statistically significant changes in the yearly occurrences of exceedances of either the 90th, 99th or 99.9th percentile for the coefficients. PC 3 shows a statistically significant negative trend for the 99th percentile. EOF 3 is important in the latter stages of heatwaves and implies possible delays in the movement of the WCTT across the Coast Mountains. PC 29 shows statistically significant increases for the 90th percentile. EOF 29 is a blocking pattern which shows increased importance during multiday events – and combined with decreases in EOF 3 may be driving increases in the probability of multiday events explaining the results of Stewart et al. (2017).

Table 4.2: Results for logistic regression on yearly counts of selected June-August PC coefficients at or above the 90th, 99th, and 99.9th percentile. Statistically significant values are in bold.

Parameter	Odds Ratio	Change in Odds	p-value
EOF_1_PCT90	1.001874	1.129392	0.5751365
EOF_1_PCT99	1.004899	1.373921	0.6138039
EOF_1_PCT99_9	0.9815638	0.2292984	0.5623417
EOF_3_PCT90	0.9955435	0.748022	0.1185491
EOF_3_PCT99	**0.9778132**	**0.2326131**	**0.0094815**
EOF_3_PCT99_9	0.9915289	0.5752397	0.6705279
EOF_6_PCT90	0.9963277	0.7873076	0.2295133
EOF_6_PCT99	0.9917495	0.5836187	0.2211388
EOF_6_PCT99_9	1.026329	5.415446	0.3311108
EOF_9_PCT90	1.004684	1.354921	0.114101
EOF_9_PCT99	1.006053	1.480348	0.4151988
EOF_9_PCT99_9	1.022931	4.36529	0.3187716
EOF_28_PCT90	0.9973476	0.8414427	0.4116747
EOF_28_PCT99	0.9945869	0.7027133	0.4376229
EOF_28_PCT99_9	0.9771767	0.2229727	0.2712828
EOF_29_PCT90	**1.007779**	**1.654762**	**0.0412952**
EOF_29_PCT99	0.9996149	0.9752722	0.9782895
EOF_29_PCT99_9	0.978187	0.2384646	0.4062566

For winter-time PCs and EOFs (Table 4.3), PC 6 shows statistically significant declines in occurrences above the 99th percentile, and PC 10 at the 90th percentile. Both of the corresponding EOFs are related to positive surface pressure anomalies and negative PNA configurations which typify wind events not constrained by antecedent precipitation. The coefficient of PC 19 is increasing statistically significantly in occurrences exceeding the 99th percentile. EOF 19 is important to both landslide events and windthrow events constrained by prior precipitation; and may be driving increases in the latter given that trends in extreme coefficient values for EOF 18 are actually decreasing (Fig. A-17).

Table 4.3: As in Table 4.2, but for October-April PC coefficients

PC	Odds_Rt_90	Odds_Rt_99	Odds_Rt_99.9	P_val_90	P_val_99	P_val_99.9
6	0.9973108	**0.9868621**	0.1940168	0.0777387	**0.00478708**	0.4265593
8	0.9976851	0.9939734	0.9967938	0.1940168	0.1732265	0.8350603
10	**0.9953828**	0.9895959	0.9908936	**0.0248158**	0.06051337	0.5035915
16	0.996474	0.9898417	0.9778617	0.3052176	0.1380903	0.1475246
18	0.9963708	0.9953871	0.9767259	0.1794332	0.4431017	0.159963
19	1.003425	**1.01331**	1.015998	0.1631625	**0.03259856**	0.2985771
23	0.9972624	0.9914986	0.9947323	0.1722313	0.1266296	0.7039433

4.3.4. Relation to Winter-time Large-scale Atmospheric and Oceanic Indices over the Pacific Basin

Several of the October-April EOFs from this study bear relation to modes of SLP and 500 hPa GPH variability for the entire North Pacific domain – the leading modes being the PNA (https://www.esrl.noaa.gov/psd/forecasts/reforecast2/teleconn/pna.html), the West Pacific Oscillation (WPO) (https://www.esrl.noaa.gov/psd/forecasts/reforecast2/teleconn/wpo.html), and the East Pacific Oscillation (EPO) (https://www.esrl.noaa.gov/psd/forecasts/reforecast2/teleconn/epo.html). The WPO is also known as the North Pacific Oscillation (NPO) and will be referred to as such in this study. The same modes are not reflected in this study because the domain being utilized is considerably smaller due computation requirements and constraints. It is well understood that atmospheric processes over the North Pacific are coupled to variations in sea-surface temperatures (SST) across inter-seasonal temporal scales – such as the El Nino Southern Oscillation (ENSO); to interdecadal – such as the Pacific Decadal Oscillation (PDO) – the first leading mode for the North Pacific domain. There is further modulation from intra-seasonal teleconnection patterns of enhanced tropical convection - such as the Madden-Julian Oscillation (MJO) which propagates eastwards across lower latitudes. All of these are especially important during the winter season (Stahl et al., 2006). Therefore, the impact of these large-scale indices relating atmospheric pressure patterns and SSTs over the greater Pacific Basin on landslide and windthrow events is examined. The EPO is not considered in this study as it is similar to the NPO (which has the high latitude pole of anomalies shifted further west than for the EPO).

Fig. 4.13 summarizes the distribution of the monthly PDO, PNA, NPO, and ENSO indices as a function of monthly counts for landslide and windthrow events. For landslide events, the PDO and PNA show generally neutral tendencies until the highest classes are encounter where they show positive values. However, the top two class represent only one occurrence, so sample size precludes much confidence in any kind of relationship. Both the NPO and ENSO indices show generally negative associations with landslide occurrences. The negative phase the NPO has been linked with above average precipitation across the region (Nigam, 2003) as has ENSO (Stahl et al., 2006).

For wind events not constrained by antecedent precipitation, the PDO shows neutral tendencies, but the PNA becomes negatively skewed with greater than one occurrence of such events per month. This reaffirms the negative correlation between the PNA pattern and only wind driven events. For windthrow events with antecedent precipitation, what is most noticeable is the negative tendencies in PDO indices, and positive tendencies related to NPO values. This suggests that such events represent a unique mechanism and not simply a conflation of purely wind events and heavy antecedent precipitation occurrences.

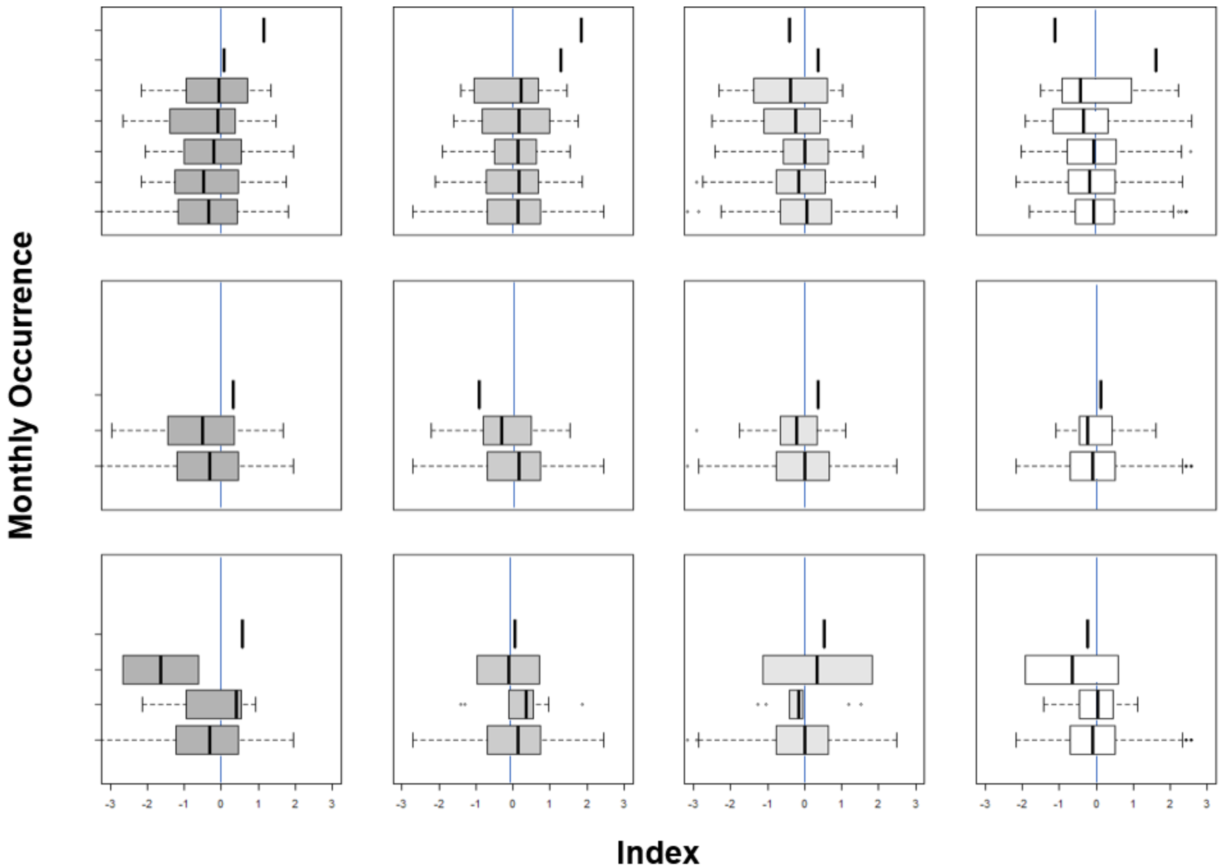

Figure 4.13: Boxplots for monthly distribution of the PDO (dark grey), PNA (grey), NPO (light grey), and ENSO (white) indices by monthly count in occurrences of: landslide events (top row), wind events not constrained by precipitation (middle row), and wind events constrained by antecedent precipitation (bottom row). Single observations are denoted by a simple vertical line. Formatting follows Fig. 1, but plots are horizontal instead of vertical.

4.4 DISCUSSION

4.4.1 Summary of Heatwave Processes

As shown in previous sections, certain EOFs display differences between multiday and single day events which provide insight into which mechanisms are crucial to longer lived heatwaves.

In particular, EOF 1 which represents the extension of the WCTT northwards from the U.S Pacific Coast to British Columbia is key to multiday events and generates a downslope, offshore flow generally for the Vancouver region in a relatively stable configuration. EOF 29 is also more important during multiday events and is a stable Rex Block pattern. The upper low off of the coast of California acts to inhibit the eastward motion of the upper ridge over British Columbia and the WCTT across the coastal mountain ranges.

Several EOFS were also shown to display temporal sensitivity in importance during multiday events. They represent an evolution of mesoscale flows relating the westward motion of the upper ridge over British Columbia with corresponding motion of the WCTT at the surface which allows for the arrival of coastal southerlies at the end of the event.

Statistically significant trends in EOFs 3 and 29 are likely contributing to more prolonged and possibly more intense heatwaves over the region. This provides a physical interpretation for the large increases in the most extreme events from Stewart et al. (2017) which were not statistically significant due to small sample size. More on the physical basis and driving mechanisms of trends will follow in a subsequent section.

4.4.2 Atmospheric processes related to Landslide and Windthrow Events

As was discussed earlier, not only are landslide and purely wind-driven events quite distinct processes, even windthrow events constrained with antecedent precipitation may represent a distinct mechanism as well. To further explore, results from a multiple logistic regression model relating occurrences of each type of event are shown in Table 4.4. The predictive value for the models are low – only one variable (coefficient) in the model for landslide events was statically significant (a negative correlation with the NPO). In fact, the variables with 3 lowest p-values all are from the landslide model due to its larger sample size. Even though there is no statistical significance for other variables it provides more robust support for explaining the differing processes which are occurring. Particularity the negative correlation with the PNA for only wind driven events which has the next lowest p-value. Even though the PDO and PNA are positively correlated (Stahl et. al, 2006) and connected through patterns of ocean-atmosphere coupling – the PNA displays higher internal variability to the lower heat capacity and quasi-chaotic processes of turbulence, convection, and mixing being more efficient in the atmosphere than the ocean than the PDO (see Fig. 19 in Section 4.4.2).

The model for windthrow events constrained by antecedent precipitation provides insight into the unique processes which are likely occurring. In particular, a positive correlation with the NPO in contrast with the other two types of events, and a negative relation to ENSO.

Table 4.4: Results from multiple logistic regression models on occurrence of landslide, wind only, and wind with antecedent precipitation events. Statistically significant values are in bold.

Landslide	**Coefficient**	**Odds Ratio**	**P-value**
PDO	0.09	1.09	0.14
PNA	-0.00	1.00	0.99
NPO	**-0.13**	**0.88**	**0.01**
ENSO	-0.11	0.90	0.12
Wind Only			
PDO	-0.08	0.93	0.78
PNA	-0.36	0.70	0.16
NPO	-0.14	0.87	0.53
ENSO	0.25	1.29	0.37
Wind and Antecedent Precipitation			
PDO	0.03	1.03	0.91
PNA	0.07	1.07	0.80
NPO	0.25	1.28	0.33
ENSO	-0.24	0.78	0.45

4.4.3 Relation to MJO

From the results of previous sections, one can infer that a unique process is occurring which drives windthrow events constrained by antecedent precipitation. To further explore, the relation of the 3 types of events to the MJO phase is considered. Fig. 4.14 shows the mode of the highest occurring MJO phase for 28 d antecedent period and the day of the 3 types of events.

When comparing the modes of MJO phase for antecedent versus day-of conditions, a clear transition is apparent for landslide and purely wind events (left 2 columns). The mode with the highest occurrence for both those events is for phase 3, with generally lower occurrences of phase 6-8 for landslide events and 5-8 for wind only events. This is suggestive of a westward propagating MJO wave across the tropical and subtropical Pacific Basin. The MJO is known to have various teleconnection pattern related to temperature and precipitation anomalies over North America related to its phase and as it traverses the different zones or phases of its cycle. Particularly with a negative NPO phase which facilitates linkage with subtropical convection by enhancing meridional upper flow patterns (Nigam 2003). When a passing MJO wave is modulated by the PNA pattern in its negative phase, it possibly results in a teleconnection pattern related to extreme winds over the region and suppresses precipitation below extreme levels.

For windthrow events with antecedent precipitation, there is no clear progression in the mode for the various MJO phases. Although the sample size is very small, one can infer that such events are not linked with the MJO given the positive correlation with the NPO. The positive phase of the NPO inhibits interaction and linkage between the mid-latitudes and the tropics and therefore likely isolates these types of events from MJO modulation. Of note is the negative correlation with ENSO – the negative phase of ENSO corresponds with positive precipitation anomalies over the region as mentioned previously. Therefore, the antecedent precipitation necessary to trigger the conditions of precipitation constrained windthrow events may be generated by inter-seasonal mechanisms such as Jetstream configurations which supply moisture and storms to the Pacific Northwest and British Columbia during the negative ENSO phase rather than intra-seasonal teleconnections with the MJO.

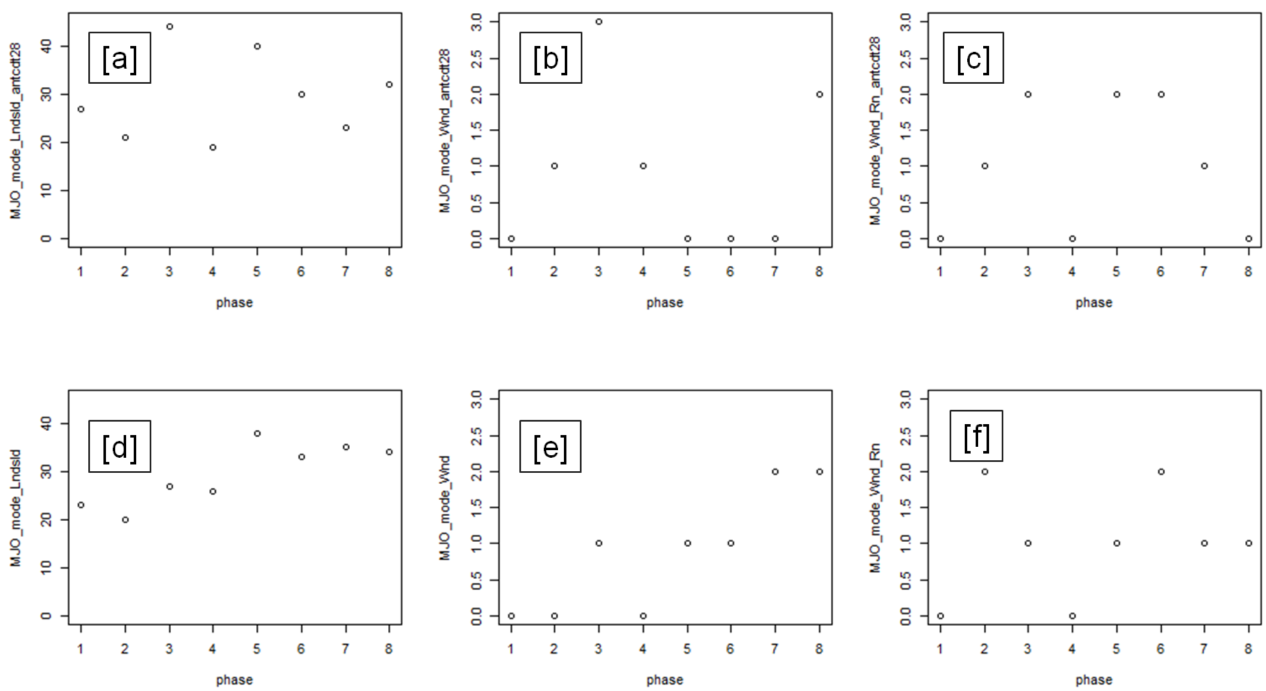

Figure 4.14: Mode of most frequently occurring MJO phase during the 28 d antecedent period (a-c or top row) and day of (d-f or bottom row): landslide events (a,d or left column), wind events not constrained by precipitation (b,e or middle column), and wind events constrained by antecedent precipitation (c,f or right column).

4.4.4 Driving Mechanisms for Trends

4.4.4.1 Dynamic-Thermodynamic Feedback or Coupling

As previously discussed, ocean-atmosphere coupling is important to some of the major indices over the Pacific Basin. More specifically, the feedback between thermodynamic variables related to SST, latent and sensible heat flux, and specific humidity; and dynamics pertaining to synoptic weather patterns responsible for extremes is critical to understanding such events.

Therefore, trends in certain monthly thermodynamic parameters are examined for both the summer and winter season (Figs. 4.15 and 4.16) using NNRP data for the period 1950-2015 for all variables except sea-surface temperature – which were calculated using the COBE dataset at 1° x 1° resolution for the same time period.

During the summer, a weak, but spatially coherent pattern is apparent in the trends of monthly net latent heat flux, SST, and net sensible heat flux off of the southern coast of California. Locally greater increases in SSTs appear to be driving corresponding increases in net latent heat flux (greater evaporation and potentially cloud cover) and sensible heat flux to the atmosphere above. These maxima are located in the vicinity and eastern flank of the low pressure anomalies from EOF 29 which are important to multiday heatwave events. Therefore, it appears likely that thermodynamic-dynamic feedback is increasing the probability in the occurrence of the 500 hPa GPH low seen in EOF 29 and may explain the trends seen in that mode of variability.

At the same time, basin-wide increases are occurring in specific humidity at 1000 hPa in response to warmer SSTs as anticipated by the Clausius-Clapeyron relation (higher saturated water vapour pressure with higher temperatures). Note that increases in latent heat flux are more limited in coverage likely due to the atmosphere above warming faster than the ocean below (due to lower heat capacity and more efficient convective and mixing processes) resulting in a net lowering of latent heat flux while still allowing for increased moisture or greater moisture advection from lower latitudes.

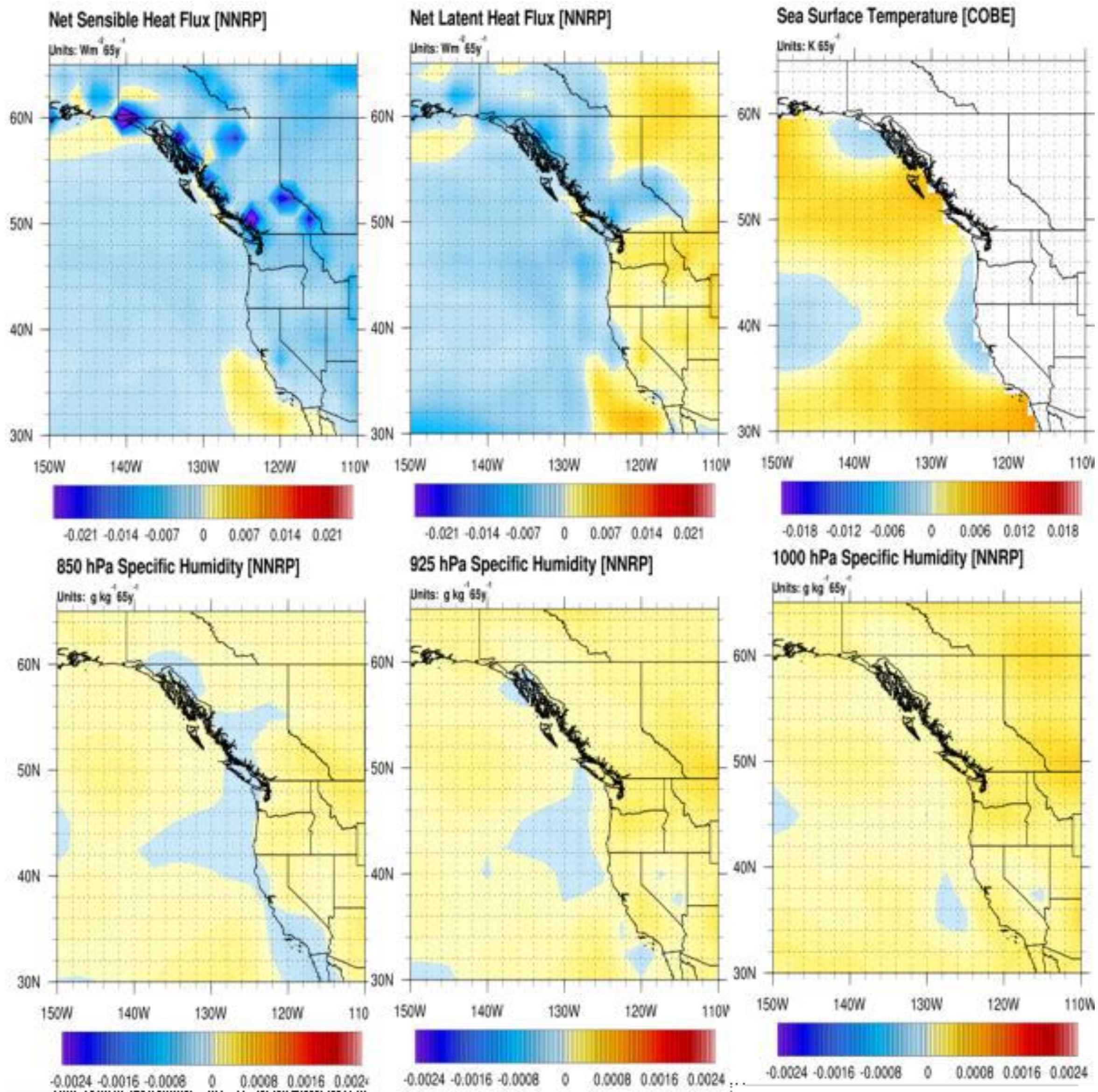

Figure 4.15: Linear regression coefficients for trends in various thermodynamic parameters for the period June-August 1950-2015 from NNRP and COBE datasets.

During the winter season, a large area of warming SSTs is noticeable over the Pacific between approximately 42˚ N and 52˚ N. This pattern is similar to the second leading mode of SST variabilities in the North Pacific Basin – the North Pacific Gyre Oscillation (NPGO) (DiLorenzo, 2008). Much like the PNA and PDO are coupled, the NPO and the NPGO are linked in that positive NPO values are negatively correlated with NPGO mode (Li Yi et al., 2018). In particular, the SST trend pattern seen here suggests positive trends in atmospheric feedback from the NPO (more on the trend analysis of major Pacific indices in the subsequent section). As with the summer season, broad increases are seen in 1000 hPa specific humidity across the entire basin but around 50° N in particular providing more moisture for precipitation bearing systems moving onshore. There is also an increasing moisture source or region of evaporation somewhat equatorward when looking at the pattern of trends in latent heat flux. Evaporated moisture from these source regions could be incorporated by passing weather systems and steered towards the region by the flow regime in EOF 19 – which is increasing in occurrence.

Trends are small and were not tested for statistical significance adding uncertainty to the findings. However, the patterns for several of the trends in the parameters during summer are spatially coherent with each other increasing confidence in the interpretation provided.

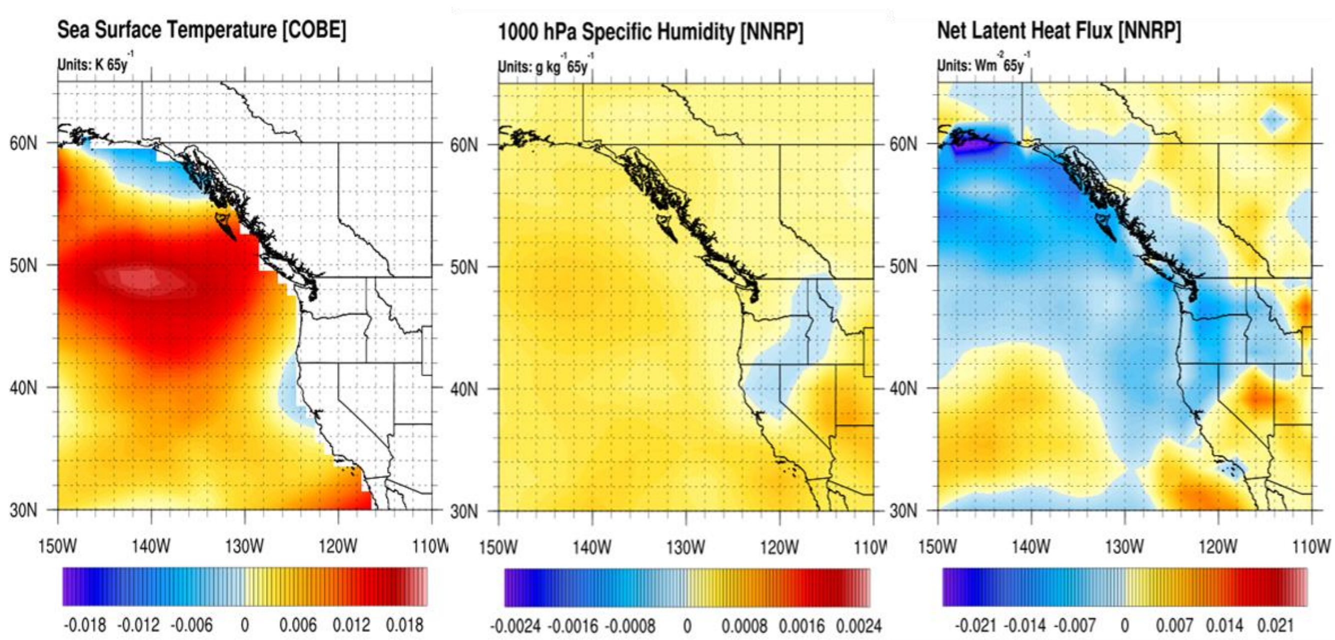

Figure 4.16: As in Fig. 6 but for the period October-April.

4.4.4.2 Changes in Forcing from Ocean-Atmosphere Indices over the Pacific Basin

Given the relation of large scale atmospheric and oceanic SST variability to landslide and windthrow events, the linear regression in trends of such indices provides more insight into the driving mechanisms seen in the trends of those events. From Fig. 4.17, all of the indices considered in this study are increasing, however only trends for the PNA are statistically significant (Table 4.5). This is the likely driving factor behind decreases seen in EOF 3 and statistically significant declines in purely wind events which are associated with that EOF.

Slightly increasing values for the NPO (consistent with the pattern of warming SSTs) are likely being offset by increases in EOF 19 and increases in moisture sources from the Pacific outlined in the previous section to produce slight increases in the occurrence of landslide events. It is possible that EOF 19 is becoming more important in terms of supplying sufficient antecedent precipitation to such events given the upstream patterns of increased SSTs and latent heat flux and decreases in EOF 18 all related to NPO/NPGO coupling and trends. Given this, one might expect increases in windthrow events constrained by precipitation to also be increasing, however, increases in ENSO are likely inhibiting these events somewhat as they appear to be linked with negative phases of ENSO rather than MJO teleconnections like the other 2 events.

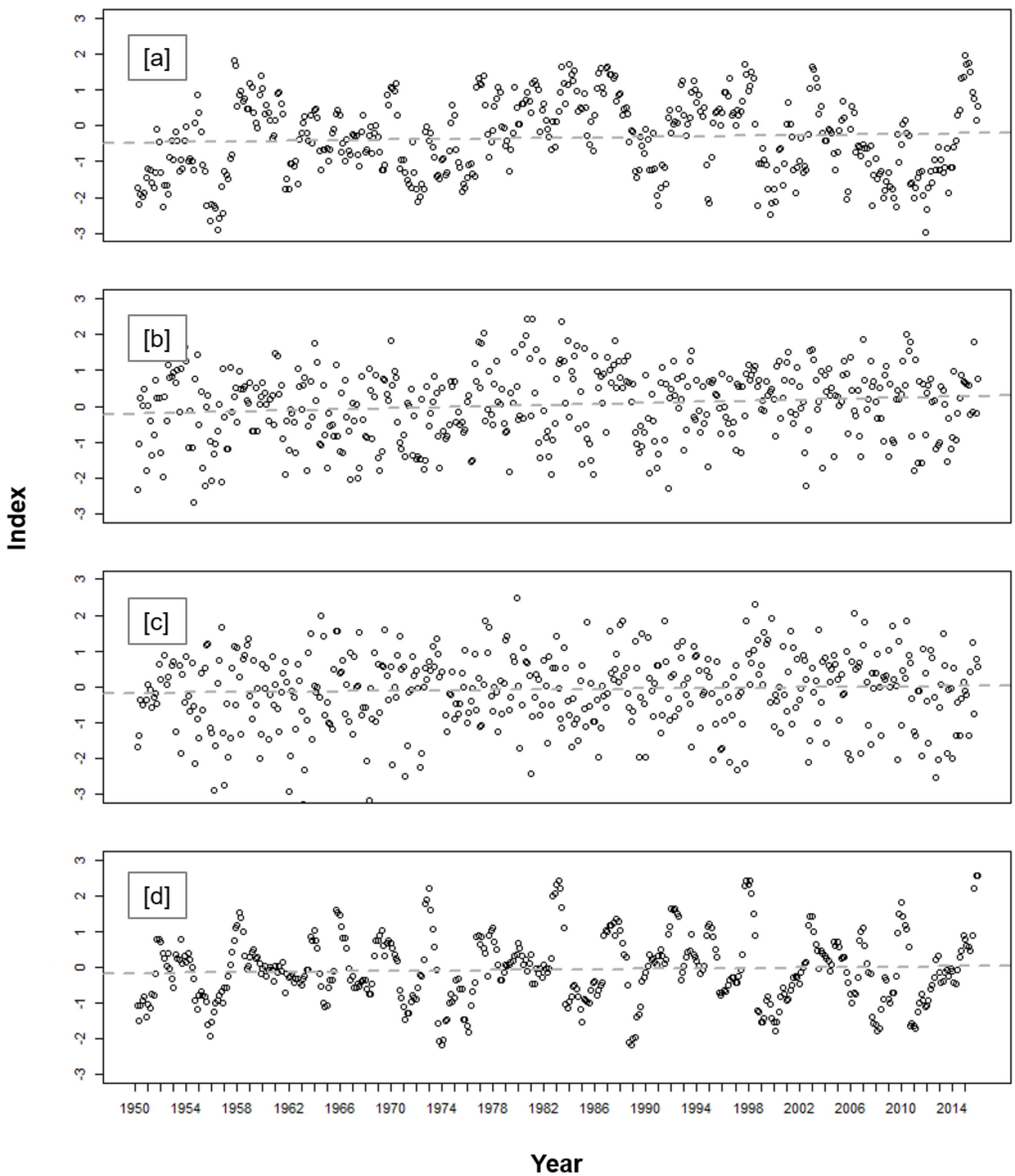

Figure 4.17: Linear regression of trends in the October-April indices of the a) PDO, b) PNA, c) NPO, and d) ENSO. Trend line is denoted by dashed grey line.

Table 4.5: Results for linear regression on trends of Atmosphere-Ocean indices.

	Coefficient	P-Value
PDO	0.0006	0.1310
PNA	**0.0011**	**0.0018**
NPO	0.0004	0.2391
ENSO	0.0004	0.1883

4.5 CONCLUSIONS

4.5.1 Summary

An analysis has been carried out for the winter and summer periods to examine meteorological processes associated with heatwave events, and landslide and windthrow events respectively for the Vancouver region. An EOF based approach was used examining PC coefficient distributions to assess which processes are important to the different extremes. For the latter 2 types of events, relation to large scale indices characterizing modes of SST and atmospheric variability over the Pacific Basin were also considered. Logistic and linear regression were conducted to analyze trends in the different events, EOFs, large scale indices, and thermodynamic parameters to understand changes in these events and possible driving mechanisms.

Several summertime EOFs show differences in terms of importance between single day and multiday heatwave events – in particular EOFs 1 and 29, which suggest multiday events may represent a unique process. Many of the EOFs also display temporal sensitivity and explain many of the shifting mesoscale circulation during the evolution of multiday events. Winter EOFs related to negative phases of the NPO and a deep Aleutian Low (18 and 19) are important to landslide events, while EOFs related to positive pressure anomalies over the Pacific basin and negative PNA modes contribute strongly to purely wind-driven events. EOFs and teleconnection indices suggest that windthrow events constrained by antecedent precipitation represent a unique process – without implied linkage to the subtropics and the MJO; and not just a conflation of the processes driving the previous two types of events. They show a relation to negative ENSO phases rather than negative PNA configurations. Past studies have statistically related extreme wind occurrence to both negative ENSO and PDO phases. However, this study demonstrates that the physical processes associated with extreme winds - and their association with either ENSO and PNA - are sensitive to the occurrence of heavy antecedent precipitation.

Trends in selected EOFs for summertime show statistically significant decreases in EOF 3 and increases in EOF 29, which are likely contributing to increases in the intensity and duration of heatwave events. The latter is connected to patterns of dynamic and thermodynamic feedback off the south coast of California. Changes in the occurrence of landslide and windthrow events are explainable by the relationship of statistically significant increases in EOF 19, increasing and northwards shifting moisture sources in the Pacific Basin, and increases in all large-scale ocean- atmosphere indices.

4.5.2 Limitations

As mentioned in the Methodology, a more precise threshold is needed for antecedent precipitation or other variables associated with windthrow events and possible approaches are outlined in that section.

Further study is required to address several issues. It is important to examine the likely rare processes associated with southerly extreme wind events – including those such as Typhoon Freda which affect the Vancouver region periodically. Further study is required to explore the linkage of landslide and windthrow events to the atmosphere-ocean indices (given the lack of statistical significance for most variables in the logistic regression models due to small sample size) as well as the relationship of negative ENSO phases and apparent lack of modulation from the MJO exerted on windthrow events constrained by precipitation.

REFERENCES

BGC Engineering Inc. (2005). *Hydro-meteorological Thresholds for Landslide Initiation and Forest Operations Shutdowns in the Kalum and North Coast Forest Districts.*

______(2006). *Landslide Risk Management for Berkely-Riverside Escarpment.*

______(2009). *Regional IDF Curves, Metro Vancouver Climate Stations: Phase 1.*

Brewer, M.C., C.F. Mass. (2016a). Projected changes in western U.S. large-scale summer synoptic circulations and variability in CMIP5 models. *J. Climate*, 29, 5965-5978.

_______(2016b). Projected changes in heat extremes and associated synoptic- and mesoscale conditions over the northwest United States. *J. Climate*, 29, 6383-6400.

______, B.E. Potter. (2012). The West Coast thermal trough: climatology and synoptic evolution. *Mon. Weather Rev.*, 140, 3820-3843.

______, B.E. Potter. (2013). The West Coast thermal trough: mesoscale evolution and sensitivity to terrain and surface fluxes. *Mon. Weather Rev.*, 141, 2869-2896.

Bumbaco, K.A., K.D. Dello, N.A. Bond. (2013). History of Pacific Northwest heat waves: synoptic pattern and trends. *J. Appl. Meteor. Clim.*, 52, 1618-1631.

Di Lorenzo, E., and co-authors. (2008). North Pacific Gyre Oscillation links ocean climate and ecosystem change. *Geophys. Res. Lett.*, 35, L08607, DOI:10.1029/2007GL032838.

Gardiner, B., and co-authors. (2008). A review of mechanistic modelling of wind damage to forests. *Forestry*, 81(3), 447-462.

Grotjahn, R., and co-authors. (2016). North American extreme temperature events and related large scale meteorological patterns: a review of statistical methods, dynamics, modeling, and trends. *Clim. Dyn.*, 46, 1151-1184.

Jakob, M., McKendry, I., Lee, R. (2003) Long term changes in rainfall intensities in Vancouver, British Columbia. *Can. Water Resources Jour.*, 28(4), 587-604. DOI:10.4296/cwrj2804587.

Jakob, M., and H. Weatherly. (2003). A hydroclimatic threshold for landslide initiation the North Shore Mountains of Vancouver, British Columbia. *Geomorph.*, 54, 137-156.

Jakob, M., and S. Lambert. (2009). Climate change effects on landslides along the southwest coast of British Columbia. *Geomorph.*, 107, 275-284.

Kosatsky, T., S.B. Henderson, S.L. Pollock. (2012). Shifts in mortality during a hot weather event in Vancouver, British Columbia: rapid assessment with case-only analysis. *Am. J. Public Health*, 102, 2367-2371.

Kuglitsch, F.G. et al. (2010). Heat wave changes in the eastern Mediterranean since 1960. *Geophys. Res. Lett.*, 37, L04802, doi:10.1029/2009GL041841.

Lackmann, G.M. and Gyakum, J.R. (1999). Heavy cold-season precipitation in the northwestern United States: Synoptic climatology and an analysis of the flood of 17–18 January 1986. *Weather Forecasting*, 14, 687–700.

Li Yi, D. and co-authors. (2018). The North Pacific Gyre Oscillation and mechanisms of its decadal variability in CMIP5 models. *J. Climate*, 31, 2487-2509.

Mass, C.F., M.D. Albright, D.J. Brees. (1986). The onshore surge of marine air into the Pacific Northwest: a coastal region of complex terrain. *Mon. Weather Rev.*, 114, 2602-2627.

______, M.D. Albright. (1987). Coastal southerlies and alongshore surges of the West Coast of North America: evidence of mesoscale topographically trapped response to synoptic forcing. *Mon. Weather Rev.*, 115, 1707-1738.

McKendry, I.G. (1994). Synoptic circulation and summertime ground-level ozone concentrations at Vancouver, British Columbia. *J.Appl. Meteor.*, 33, 627-641.

______, D.G. Steyn, J. Lundgren, R.M Hoff, W. Strapp, K. Anlauf, F. Froude, J.B. Martin, R.M Banta, L.D. Olivier. (1997). Elevated ozone layers and vertical down-mixing over the Lower Fraser Valley. *Atmos. Environ.*, 31(14), 2135-2146.

______, K. Stahl, R.D. Moore (2006). Synoptic sea-level pressure patterns generated by a general circulation model: comparison with types derived from NCEP/NCAR re-analysis and implications for downscaling. *Int. J. Climatol.*, 26, 1727–1736.

Neiman, P.J., and co-authors. (2008). Meteorological characteristics and overland precipitation impacts of Atmospheric Rivers affecting the West Coast of North America based on eight years of SSM/I satellite observations. *J. Hydrometeorol.*, 9(1), 22-47.

Nigam, S., 2003: Teleconnections. *Encyclopedia of Atmospheric Sciences*, J. R. Holton et al., Eds., Academic Press, 2243–2269.

Oke, T.R, and J.E. Hay. (1994). *The Climate of Vancouver.* Vancouver, British Columbia: University of British Columbia Press.

Pacific Climate Impacts Consortium. (2007). *GVRD Historical and Future Rainfall Update.*

Rahmstorf, S., and Coumou, D. (2011). Increase of extreme events in a warming world. *Proc. Natl. Acad. Sci. U.S.A.*, 10.1073/pnas.1101766108.

Ralph, F. M., Rotunno, R., Neiman, P.J. (2005). Dropsonde observations in low level jets over the northeastern Pacific Ocean from CALJET-1998 and PACJET-2001: Mean vertical-profile and atmospheric-river characteristics. *Mon. Wea. Rev.*, 133, 889–910.

Read, W.A. (2015). The climatology and meteorology of windstorms that affect southwest British Columbia, Canada, and associated tree-related damage to the power distribution grid (doctoral thesis). University of British Columbia, Department of Forestry, Vancouver, BC.

Roberge, A., Gyakum, J.R., Atallah, E.H. (2009). Analysis of intense poleward water vapor transports into high latitudes of western North America. *Weather Forecasting*, 24, 1732 -1747.

Smith, R. (2012). Relationships between synoptic circulation patterns and freezing rain in Churchill, Manitoba (1953-2009) (Unpublished master's thesis). University of Manitoba, Department of Environment and Geography, Winnipeg, MB.

Stahl, K., R.D. Moore, I.G. McKendry (2006). The role of synoptic-scale circulation in the linkage between large-scale ocean-atmosphere indices and winter surface climate in British Columbia, Canada. *Int. J. Climatol.* 26: 541–560.

Stewart, R.E., D. Betancourt, J.B. Davies, D. Harford, E. Joakim, Y. Klein, R. Lannigan, L. Mortsch, K. Tang and P.H. Whitfield, 2017: A multi-perspective examination of heat waves affecting Metro Vancouver: Now into the future. Natural Hazards. DOI: 10.1007/s11069-017-2793-7.

Virot, E., and co-authors. (2016). Critical wind speed at which trees break. *Phys. Rev.,* E 93, 023001.

Warner, M.D., Mass, C.F., Salathe, E.P. (2012). Wintertime extreme precipitation events along the Pacific Northwest Coast: climatology and synoptic evolution. *Mon. Wea. Rev.* 140, 2021-2043.

Worcester, R. (2010). *State of the Park Report for the Ecological Integrity of Stanley Park.*

CHAPTER 5: RELATING SPATIAL AND TEMPORAL VARIABILITY IN EXTREME MAXIMUM TEMPERATURE DURING HEATWAVES IN THE VANCOUVER, BRITISH COLUMBIA REGION

5.1 INTRODUCTION

Heatwaves are extreme meteorological events which have public health impacts everywhere including the mid-latitudes. Several major heatwave events have occurred in recent years - notably at Chicago, United States in 1995; Paris and Europe in 2003; Moscow and Russia in 2010. However, such events have also taken place in regions not typically associated with extreme heat. One example of this is in Vancouver and the lower mainland of British Columbia, Canada in July 2009. During this event, an estimated 200 heat-related deaths occurred (Kosatsky et al., 2012).

There are different metrics by which heatwave occurrence and duration are measured, some of which can be arbitrary or subjective. Exact qualifications vary from jurisdiction to jurisdiction. For example, the definition used by Environment and Climate Change Canada (ECCC) is the occurrence of three consecutive days with maximum temperatures greater than or equal to 32˚C, but temperatures greater than 30˚C are rare at Vancouver International Airport (Stewart et al., 2017). More recently, evidence based approaches have been used to develop thresholds for identifying extreme events (Hess et al., 2014; Zheng et al., 2014). Specific to the Vancouver region, Henderson and Kosatsky (2012) related 99th percentiles of daily mortality and afternoon maximum temperature at Vancouver and Abbotsford International Airports to develop a threshold for issuing heat alert advisories. By using both a coastal station and a more inland site – which is more sheltered from the effect of sea breezes which commonly affect the area (Steyn and Faulkner, 1986) - a range of thresholds region-wide can be established. Identification of such parameters is critical to assessing trends and future impacts of heatwaves in the region.

Several past studies of heatwaves have been focused over the adjacent Pacific Northwest region of the United States which shares several physiographic commonalities with the study area; and even contains a small portion of the Lower Fraser Valley. Those focused further north in the Lower Fraser Valley itself have been related to episodes of high ground level ozone concentration - which has a close association to above normal temperature occurrence. Both have been linked with upper and surface ridging, and associated clear conditions allowing for considerable insolation. However, the heat alert criteria used by Henderson and Kosatsky (2012) likely represents a small subset of days with above normal temperature and surface ozone concentration.

Studying heatwaves in the Vancouver region is challenging because of the complex physiography. Thermally driven mesoscale processes that result from differential heating modulate afternoon maximum temperatures and produce local variations. In addition to afternoon sea breezes, other local patterns include mountain valley circulations (Steyn and Faulkner, 1986; McKendry et al., 1997) and urban heat island effects (Oke, 1973; Oke and Maxwell, 1975; Oke and Hay, 1994) due to Vancouver's large population and high urban density. Other mesoscale features have also been linked with heat waves along the west coast including the West Coast Thermal Trough (WCTT) (Brewer et al., 2012, Brewer et al. 2013), and onshore coastal surges (Mass et al., 1986; Mass and Albright, 1987; Reason and Dunkley, 1993; McKendry et al., 1997).

Several studies have also suggested a specific temporal pattern associated with periods of above normal temperatures in the region: (i) the movement of surface high pressure onshore (ii) subsequent sharpening and northwards migration of the WCCT, (iii) the eventual weakening and eastward shift of the WCTT and, (iv) the arrival of a mesoscale ridge and coastal southerlies which heralds the end of the heatwave episode. Such evolutions are modulated by the interaction and oscillation of the WCTT and the onshore coastal push or surge. Many of the Canadian studies have also suggested a temporal pattern of shifting flows and regimes during such periods (McKendry et al., 1997; Snyder and Strawbridge, 2004; Ainslie and Steyn, 2007). The mesoscale response to such changing flows is further regulated by the highly variable terrain, and may produce local effects not reflective of the larger pattern (Lange, 1999). An example is the offshore flow that was noted at Vancouver International Airport during the July 2009 heatwave (Stewart et al., 2017).

Given the substantial health impacts of such events it is important to understand the underlying mechanisms and processes driving variability in the occurrence of extreme maximum temperature. Specifically, the objective of this paper is to examine potential causes for this variability, and to demonstrate the temporal evolution of synoptic and mesoscale flows as at least one important source.

5.2 METHOD

5.2.1 Selection Criteria

Daily station data for Vancouver International Airport (YVR) and Abbotsford International Airport (YXX) were acquired from ECCC. Records YVR extend back to 1939, whereas those for YXX extend back only to 1944. The dataset was scanned for occurrences of maximum temperatures greater than or equal to 29˚C at YVR and 34˚C at YXX for the period in which data were available at both locations. These represent the proposed thresholds for heat alert criteria (Henderson and Kosastsky, 2012), based on an average of observed maximum same day temperature and forecast high temperature the subsequent day. Candidate triggers developed by Henderson and Kosastsky (2012) were based on the lowest temperature recorded on all days which were at or above the 99^{th} percentile for daily mortality coincident with 2-day average maximum temperature also greater than or equal to the 99^{th} percentile. These triggers were higher – 31°C and 36°C for YVR and YXX respectively. For the purposes of identifying individual extreme heat days in this study, the lower thresholds were utilized because occurrences of temperatures greater than candidate values are very rare in the data period for YVR and YXX.

Only single day maximum temperatures were used as selection criteria in this study (rather than a 2-day average), as the various mesoscale processes being investigated require compositing at a high temporal resolution, and may become conflated at 2-day intervals. Occurrence of heat advisory days were estimated using both approaches and Pearson correlation coefficients showed moderate correlation and statistical significance for both YVR and YXX. When considering cases occurring solely within multiday events defined by the criteria used in this study - Pearson coefficients increased for YVR, but decreased for YXX and lost statistical significance. The implications of these discrepancies as related to temporal variability and evolution of heatwaves is discussed later.

Near advisory heat alert criteria were met a total of 54 times for YXX and 41 for YVR; giving a total of 95 cases and 70 heat wave days when criteria were met at either location. There were 18 multiday events when criteria were met at one or both stations consecutively representing 40 total days (36 times at YXX, and 22 at YVR for a total of 58 cases).

5.2.2 Compositing

In order to understand the mechanisms driving spatial variability of heatwave events in the region, daily composites of vector wind, u and v component wind, and dewpoint were generated for days when heat-alert criteria were met at YVR and YXX. Hourly station data for both locations were acquired from Environment and Climate Change Canada (ECCC) and extracted for heatwave days to generate composite time-series of surface meteorological parameters.

To further understand and characterize what temporally varying processes may be driving this spatial variability during multiday events, composites of several lower tropospheric meteorological fields were made through acquisition of North American Regional Reanalysis (NARR) data from the National Centers for Environmental Prediction (NCEP). NARR is described by Mesinger et al. (2006) and is available at 3 hourly intervals and 32 km resolution from 1979 onwards (the commencement of the satellite era). Only 9 multiday heatwave events occurring after the beginning of the dataset could be sampled using this product. However, it was considered a superior approach than using the more coarsely resolved NCEP/National Center for Atmospheric Research (NCAR) Reanalysis Project (NNRP) data, which is a global product available at 6 hourly intervals and 209 km resolution (Kalnay et al., 1996). This is because the coarse resolution of this product – even though it extends back to 1948 – precludes the ability to capture potentially critical mesoscale processes which drive heatwave events over the region.

5.2.3 Multiple Correspondence Analysis

To estimate what portion of spatial variability in the exceedance of heat alert criteria was attributable to temporal processes in the data, multiple correspondence analysis (MCA) was run for data pertaining to multiday events. MCA is a statistical method for analysing patterns of variability analogous to PCA (see Chapter 4), but for categorical variables (Le Roux and Rouanet, 2011). This includes binary categorical variables such as those being analysed (either the heat-alert criteria were met or not). Specifically, the package FactoMineR in the R project for statistical computing (Le et al., 2008) was used to compute the MCA. Patterns or modes of variability comparable to eigenvectors from PCA were examined to assess which of these modes contributed most to spatial variability (versus co-occurrence), and how they compared to the variability generated from single day events occurring at one location versus the other.

5.3 RESULTS

5.3.1 Pattern and Relation of Co-occurrence

There were 25 heat wave days when criteria were met concurrently at both locations (35.2%), which yielded a moderate and statistically significant Pearson correlation coefficient of occurrences between the locations. 18 such occurrences were during multiday events, while 7 occurred as single day events. Therefore, the majority of single day events represented situations in which criteria were met at only one location (82.9%), whereas that was less likely to occur on days which were part of multiday events (53.8%). The single day events were approximately equally distributed at both sites with 22 at Abbotsford (31.0%), and 19 at Vancouver (26.8%). A higher proportion of all heat-alert cases at Vancouver occurred as single day events (53.7%) versus during multiday events (46.3%); and Vancouver had a higher probability of occurrence (63.3%) on single days than during multi-day events (55.0%).

There were many multiday events for which the advisory criteria are met at Abbotsford on the first day either with co-occurrence at YVR or exclusively at YXX (94.4% overall; 83.3% exclusively), while much less so for Vancouver (22.2% overall; 5.5% exclusively). Conversely, criteria were more likely to be reached at Vancouver on the last day of a multiday event (72.2% overall; 16.7% exclusively); which was comparable to probabilities at Abbotsford (77.7% overall; 22.2% exclusively). As a proportion of the total multiday cases for each location however, Vancouver had a greater likelihood of meeting criteria (50.0%) on the last day than Abbotsford (38.9%). This is because there were more overall cases of Abbotsford reaching the criteria during multiday events (38) than for Vancouver (22). This also likely explains why the correlation coefficients between the Henderson and Kosatsky (2012) method, and the approach used here to identify heatwave days decreases for Abbotsford during multiday events. Since the former method utilizes a 2-day average and Abbotsford has a greater likelihood of meeting the criteria on the first day, such occurrences are filtered out.

5.3.2 Daily Composites

In this section, some of the mechanisms responsible for the spatial variations in achieving the proposed threshold temperatures are considered. The composites imply considerable differences in terms of synoptic forcing and pressure gradient at the surface despite similarities in 500 hPa geopotential height (not shown). Given the magnitude of flow at YVR when the criteria are reached at exclusively at YXX, the presence of a considerable surface pressure gradient can be inferred (Fig 5.1). Onshore flow from the Georgia Strait is enhanced in such cases, implying an influx of cooler marine air which limits daytime heating. U component flow remains positive or onshore the entire day, and any land breeze is completely suppressed. This amount of synoptic enhancement contrasts with the barotropic or equivalently barotropic patterns generally associated with heat waves (Feudale and Shukla, 2011; Black et al., 2004). This is likely developed by the movement and intensification of the WCTT in relation to a dipole region of high pressure affecting the West Coast of North America. This sets up a northeasterly pressure slope over the region, and the subsequent flow is funnelled and deflected along the Georgia Strait (which is oriented northwest to southeast).

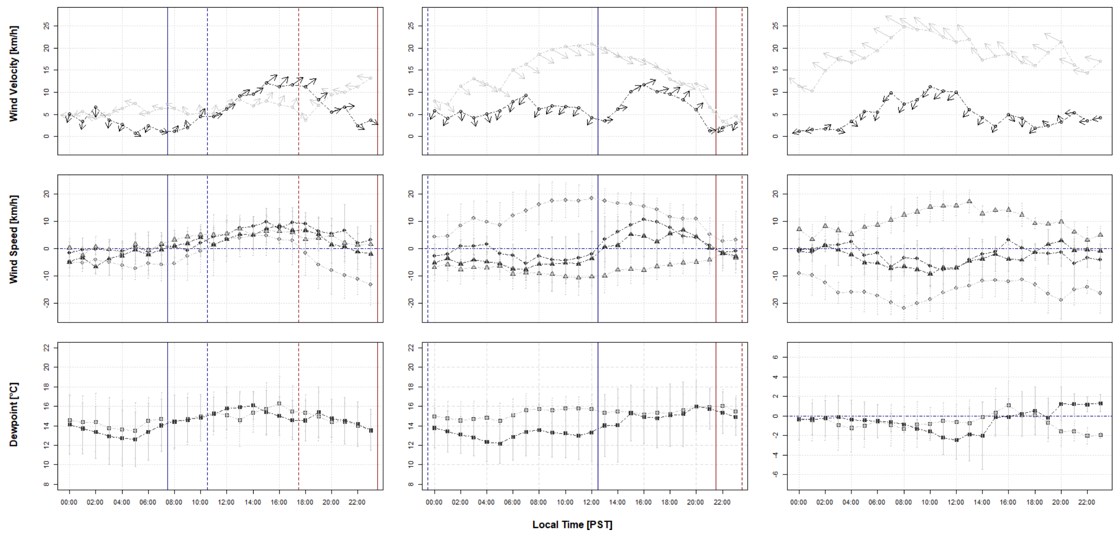

Figure 5.1: Composites of vector wind (arrows) (top row), u (circles) and v (triangles) component flow (middle row), and dewpoint (squares) (bottom row) at YVR (grey) and YXX (black) for all occurrences when criteria is met at YVR exclusively (left column), YXX exclusively (middle column) and the difference between them (right column). Vertical lines represent the onset of the sea-breeze (blue) and land-breeze (red) at YVR (solid) and YXX (dashed).

It is also clear in such cases that at YXX there is a preponderance of northerly to north-easterly flow with a large downslope/offshore component (negative u values), and inferred adiabatic warming. A southwesterly sea-breeze only reaches YXX between 14:00 – 15:00 local time allowing for considerable warming due to both solar insolation and sensible heat transfer from the ground surface, along with vertical warm air advection from the downslope flow. This is consistent with the major mechanism for heat wave occurrence over the Pacific Northwest in which the normal maritime regime is suppressed in favour of a downslope, offshore (continental) one (Brewer and Mass, 2016a; Brewer and Mass, 2016b).

For cases in which the criteria are reached at YVR only, a more relaxed pressure gradient and a weaker WCTT is implied in the vector wind composites with overall lighter wind speeds (<15 km/h). This allows local winds to be controlled more by diurnally driven and thermally induced flows due to differential heating (sea and land- breezes). It is also apparent that onshore flows or sea-breezes arrive much earlier at YXX in such occurrences, and later at YVR – with evidence of a land-breeze re- establishing an off-shore wind direction during the evening at YVR. V-component winds at YVR also have a tendency to positive (poleward) values during such days, while they are entirely negative for cases when criteria are reached at YXX.

When examining the changes in the u and v wind components between cases, it is clear that for YXX, changes in the u and v component flow are similar to one another while they oppose each other at YVR. This implies a negative correlation between zonal and meridional wind components at YVR and a positive one at YXX. That is – within the context of heatwave mechanisms, offshore flows at YVR appear to be regulated strongly by occurrences of positive v-component winds. This is likely to be associated with the arrival of the onshore coastal surge.

Therefore, spatial variability in attaining heat-alert criteria over the region is largely controlled by the modulation of land and sea-breezes across a range of synoptic and mesoscale forcing regimes. This forcing could be caused from varying, discrete synoptic patterns, but also from the temporal evolution of mesoscale flows previously noted such as interaction and oscillation of the WCTT and the onshore coastal push. The mesoscale response to such changing flows is further regulated by the highly variable terrain, and may produce local effects such as the offshore flow that was noted at YVR during the July 2009 heatwave (Stewart et al., 2017). In the subsequent section, an attempt is made to understand how much these processes are responsible for the observed variability.

5.3.3 Contribution from Temporal Processes

By examining the weights of the variables (first 8 rows of Fig. 5.2) for each eigenvector (or mode of variability) from MCA, a large driver of variability (or anomalies) is non- occurrence at YXX on the first day of such events. In other words, all eigenvectors feature occurrence of heat-alert criteria on the first day at YXX. Conversely, another large contributor to variability and anomalies is occurrence of heat-alert criteria at YVR during the first day of multiday events for 2 of the first and fourth eigenvector (columns 1 and 4, Fig. 5.2). Therefore, for those modes of variability, YVR does not attain heat- alert criteria on the first day of such events.

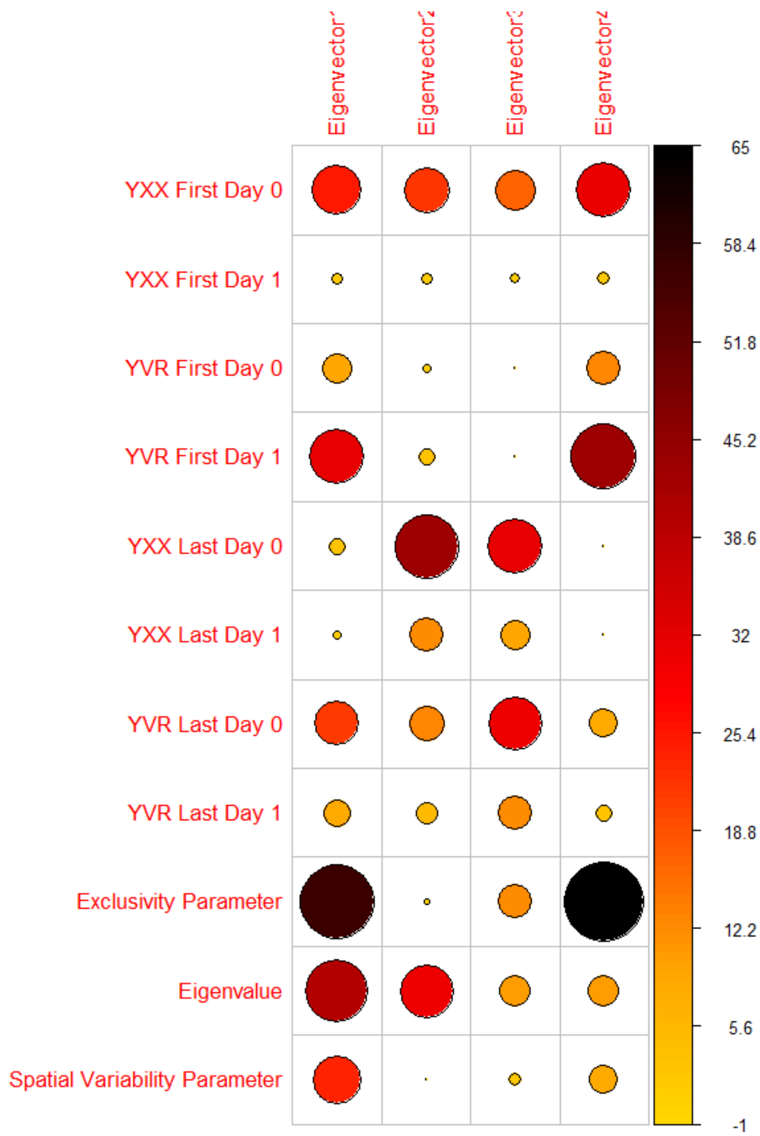

Figure 5.2: Results from MCA with coloured circles indicating: weights of variables within each eigenvector (1 denotes occurrence, whereas 0 denotes non-occurrence); exclusivity and spatial variability parameters, and eigenvalue associated with each eigenvector.

In order to help interpret the results of the MCA, a further matrix plot is presented (Fig. 5.3) to represent the likelihood of occurrence and non-occurrence at each location during multiday events. Representations of likelihoods were derived by finding the difference in weights for each outcome of the variables at YVR and YXX for each eigenvector. The results show similar patterns of occurrence/non-occurrence for the first and fourth eigenvector, when there is a high likelihood of non-occurrence at YVR on the first day. The second eigenvector represents a multiday event where there is a high probability of occurrence at YXX on the first day and co-occurrence of heat-alert criteria at both YVR and YXX on the last day. The third eigenvector represents multiday events when there is a high probability of occurrence at both YVR and YXX on the first and last days of multiday heatwave events.

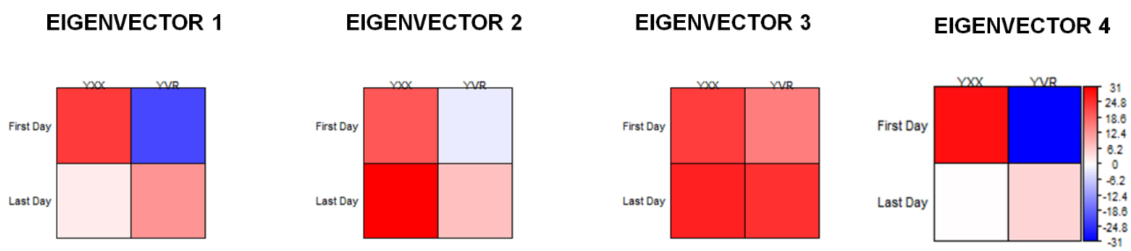

Figure 5.3: Matrix plot representing likelihood of heat-alert criteria during multiday events at YVR and YXX for each eigenvector from MCA. Red shading denotes likelihood of occurrence, whereas blue shading represents likelihood of non-occurrence.

To try to quantify the amount of spatial variability that is driven by temporal processes, an exclusivity parameter was derived by summing all the differences of weights in occurrence versus non-occurrence between YVR and YXX for each eigenvector (row 9, Fig. 5.2). This was then scaled (multiplied) by the amount of overall variability each eigenvector contributed to (i.e. the eigenvalue) in the MCA (row 11, Fig. 5.2). The results suggest there are two eigenvectors which contribute to spatial variability in attaining heat-alert criteria during multi-day events – eigenvectors 1 and 4.

This spatial variability parameter was then weighted against the total number of cases for multiday events (40) and compared with the spatial variability occurring from single day events (weighted by 26 cases of single day events). The results suggest that 38% of the total spatial variability in the dataset can be attributed to temporal processes during multiday events. As an alternative approach to estimate how much spatial variability is linked with multiday events, negative correlation was assessed between YVR and YXX for single day events and between the weights of the variables for YVR and YXX within each eigenvector. The values were scaled in the same way as for the previous method and showed a similar result of 36%. Therefore, it appears that temporal processes occurring during multiday events has a considerable impact in producing spatial variability of heat alert criteria at YVR and YXX.

In order to examine what may be driving spatial variability during single day events, temperature distributions at both YVR and YXX were examined when criteria were met at YVR or YXX (Fig. 5.4). The results show a similar temporal pattern in higher temperatures for YVR after single day occurrences at YXX than before. Temperatures are considerably lower after single day occurrences at YVR than after single day occurrences at YXX itself. This suggests that the same temporally evolving processes which govern spatial variability during multiday events also play an important role in single day events, but factors such as cloud cover, smoke, sea-surface temperature anomalies may prevent the full expression of the pattern.

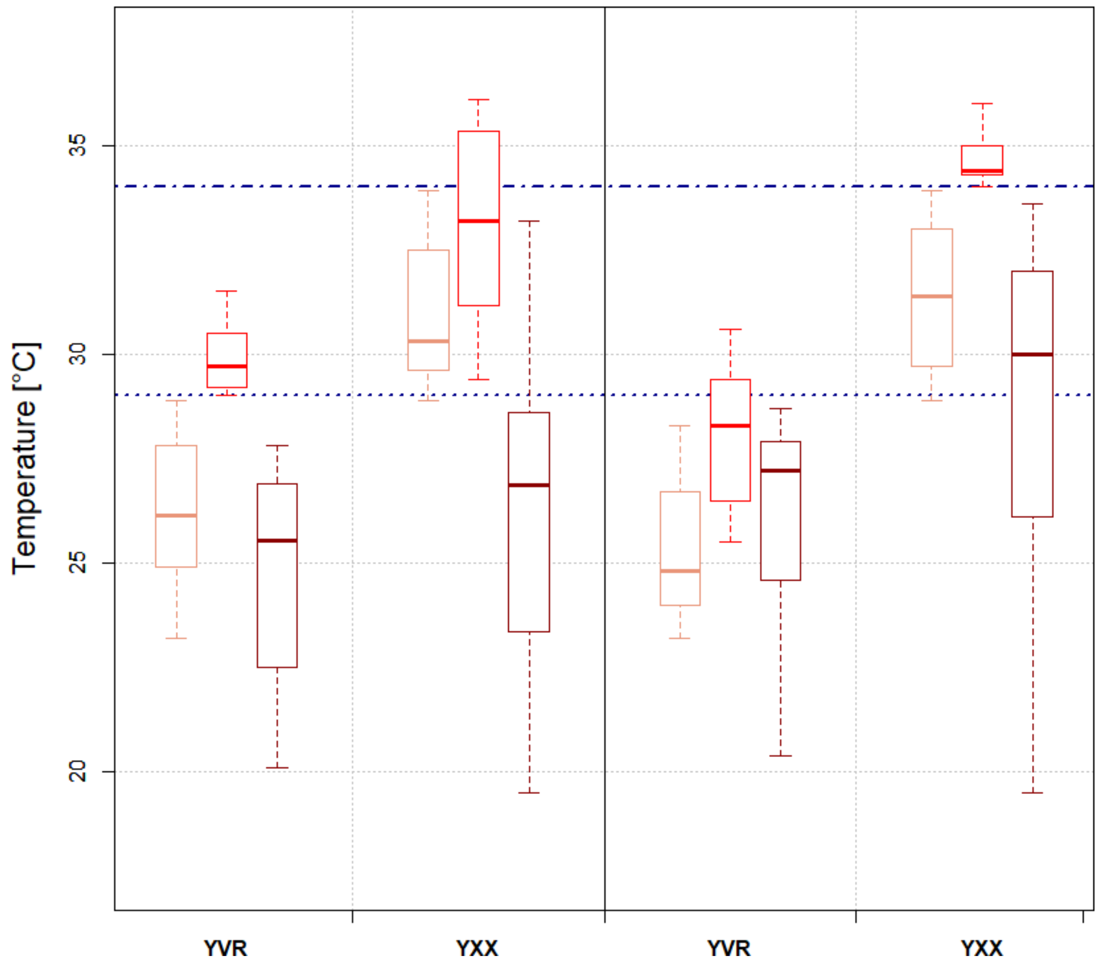

Figure 5.4: Boxplot showing distributions of maximum temperatures at YVR and YXX for days prior to (salmon), days subsequent to (dark red), and during single day events (red) when heat alert criteria are reached at YVR (left panel) and YXX (right panel)

Given the importance of temporally varying processes during heatwave events, the subsequent section will discuss more in detail the evolution and interaction of these mechanisms in modulating extreme temperature occurrences in the region.

5.4 DISCUSSION

5.4.1 Temperature and Zonal Wind Anomalies

As mentioned previously, a key feature dictating flows through the course of a heat wave event is the WCTT. Those circulations are in turn modulated by local physiographic effects and result in the evolution of flow regimes observed over the region. As the WCTT moves northwestwards in the earlier stages of a heat wave episode (Fig. 5.5), it extends off the west coast of Vancouver Island, and establishes a north-easterly pressure slope on the eastern side of the WCTT; and a west- northwesterly pressure slope on the west side of the WCTT over the Pacific Ocean). However, due to the orientation and channelling effect of the Georgia Strait, the north-easterly oriented pressure slope results in north-westerly flow over the strait and adjacent onshore regions of Vancouver (Lange, 1999).

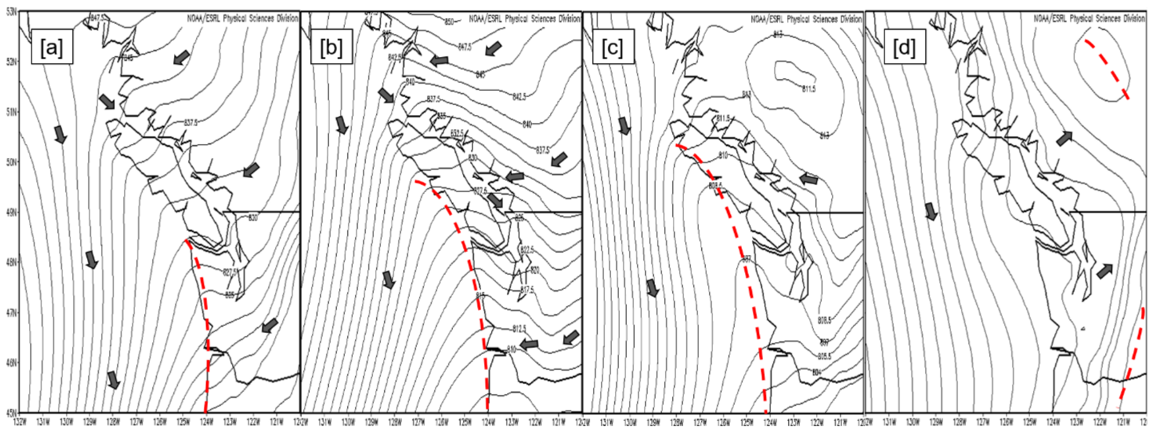

Figure 5.5: NARR daily composites of 925 hPa geopotential height (m) and 1000 hPa generalized vector wind schematic (arrows) for: [a] preceding day, [b] first day, [c] last day, and [d] subsequent day of a heatwave event. Broken red line represents position of WCTT.

Therefore, even though heatwave events in the region are generally associated with offshore flow anomalies in the lower troposphere, there is an absence of negative zonal flow anomalies at the surface during the onset of heatwave events over the Georgia Strait and adjacent onshore areas. Lange (1999) noted that sea-breezes typically develop on these types of onshore flows through the day as differential heating between land and ocean intensifies. This results in a backing of the local pressure slope to a more westerly orientation around Vancouver and southwesterly farther south – conforming to the contours of the local coastline and causing a deceleration of winds since they are no longer favourably aligned with the Georgia Strait. However, it has also been noted that stronger northwest flows over the Georgia Strait can resist the tendency towards backing and weakening (Pottier et al., 1997). This type of forcing regime – which is consistent with a stronger and more intense WCTT in the early stages of heat wave events – therefore suppresses the propagation of the afternoon sea-breeze (noted by westerly or south-westerly flow component) further inland up the Fraser Valley towards Abbotsford. The suppression of this cooler, denser air instead facilitates mixing and down sloping of air associated with a northerly or north-easterly trajectory off the Coast Mountains as seen in composites for the Abbotsford cases.

The absence of negative zonal flow anomalies over the Georgia Strait is demonstrated in Fig. 5.6. Offshore flow anomalies are relegated above altitudes of 900 metres and higher, with a near-surface region of neutral or non-anomalous u-component flows over the Georgia Strait

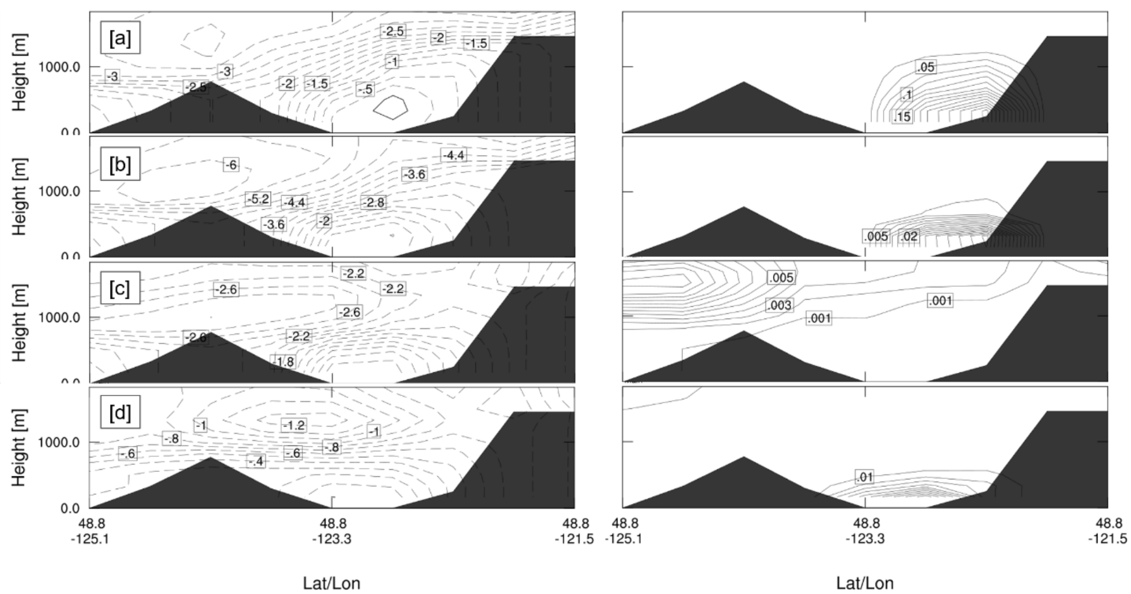

Figure 5.6: Cross-section over the Georgia Strait showing zonal wind anomalies (compared to 1981- 2000 average from NARR) (left column) and associated probability values (right column) in the lower troposphere for a) day prior, b) first day, c) last day, and d) day subsequent to multiday heatwave events.

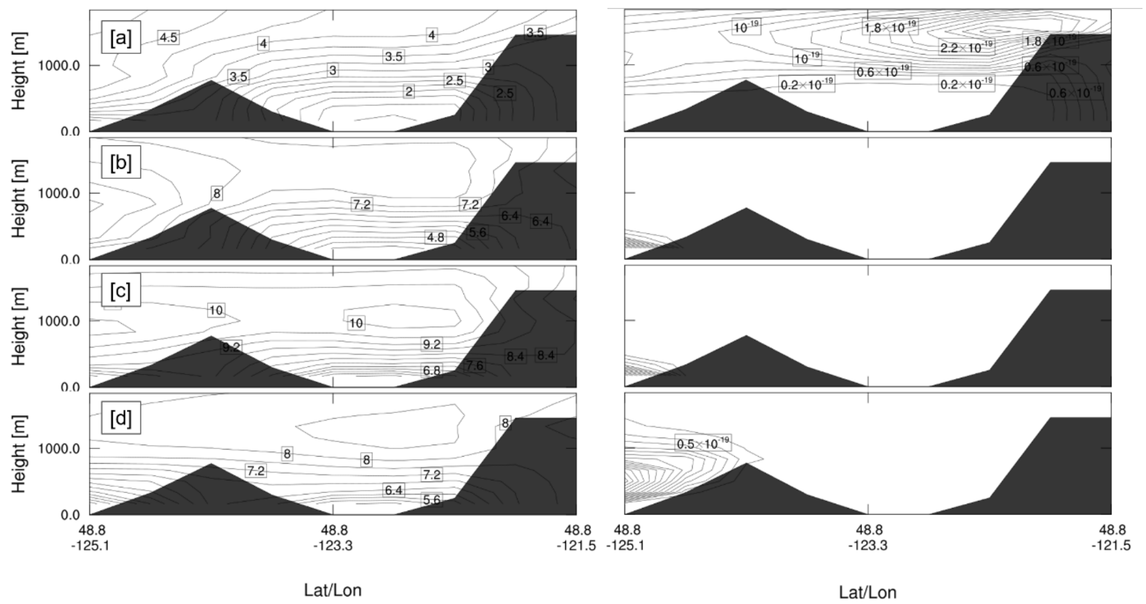

Figure 5.7: Temperature anomalies in the lower troposphere during multiday heatwave events. Formatting follows previous figure.

5.4.2 Coastal Southerlies and Meridional Wind Anomalies

As the heatwave pattern evolves and the WCTT shifts further east, the pressure slope becomes oriented more towards the west-southwest (west of the WCTT), which generally allows more marine air inflow into the Fraser Valley (Snyder and Strawbridge, 2004). This represents the arrival of coastal southerlies (Fig. 5.8), and associated mesoscale coastal ridging. It is reflected in the increase of positive surface meridional wind anomalies in the last day composite for heat wave events, and the attenuation of negative zonal wind anomalies for the same corresponding time. However, the negative zonal flow anomalies also extend further west around Vancouver on the last day (not shown), which is consistent with the delayed onset of the sea-breeze seen in cases where the criteria are reached solely at Vancouver International Airport. Therefore, there is generally a greater influx of marine cooled air entering the Fraser Valley on the last day of heatwave events, but at the same time there is a local suppression of the sea-breeze for the airport station and western sections of the Vancouver.

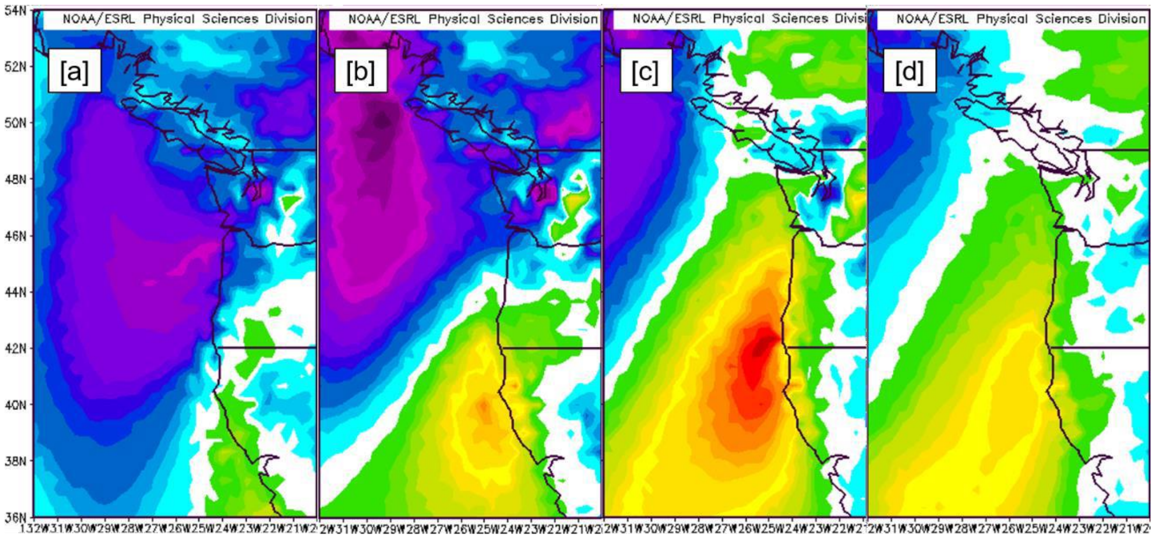

Figure 5.8: NARR meridional wind anomalies (compared to 1981-2000 average) for a) day prior, b) first day, c) last day, and d) day subsequent to multiday heatwave events.

5.4.3 Temperature and Moisture Anomalies

The pattern of temperature anomalies largely corresponds with the zonal and meridional flow anomalies observed. Positive temperature anomalies extend well out into the Pacific Ocean associated with the offshore flows at 925 and 850 hPa (not shown). However, similar to the case for zonal winds near the surface, the temperature anomalies are attenuated at low levels over the Georgia Strait (Fig. 5.7) due to the marine influence. Therefore, the Georgia Strait has a considerable buffering capacity against warming from offshore, continental outflows – and this influence spreads inland through the development of afternoon sea-breezes.

Henderson and Kosatsky (2012) did not consider the effects of humidity in their study of heat related deaths during the July 2009 heatwave, however it has been found to exacerbate heat related stress considerably. High dewpoints occurred during the July 2009 event, but the source of the moisture was unclear (Stewart et al., 2017). Bumbaco et al. (2013) considered moisture as a variable for their heatwave composites using NNRP reanalysis, and demonstrated a region of positive specific humidity anomalies at 1000 hPa under the ridge over the Pacific Ocean. Here, higher resolution NARR data are used to show an additional area of positive specific humidity anomalies which develop locally (Fig. 5.9), in contrast with the tropical moisture being advected by the ridge in the Pacific. Under the upper ridge, conditions favoring strong insolation such as lack of clouds, and generally lighter winds in the lead up to the heatwave episode, cause warming of the shallower waters in the Georgia Strait. This leads to greater evaporation and an increase in moisture and dewpoint. With the arrival of the coastal surge, this higher moisture gets pushed up the Fraser Valley where it can linger even several days after the end of heat alert criteria. Therefore, lower temperatures are somewhat offset by higher dewpoints at the end of heat wave events in the region.

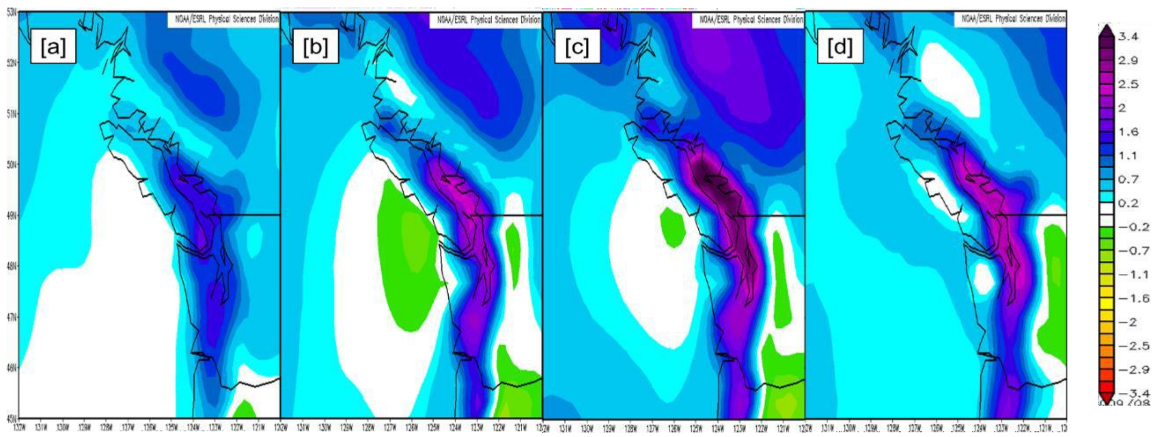

Figure 5.9: NARR specific humidity anomalies (compared to 1981-2000 average) for a) day prior, b) first day, c) last day, and d) 2 days subsequent to multiday heatwave events.

5.5 SUMMARY AND CONCLUSIONS

A review of the synoptic and mesoscale processes associated with events meeting near heat advisory criteria has been carried out. Particular attention has been paid to those mechanisms responsible for producing spatial variability in temperatures exceeding proposed thresholds in the region. Temporal variability of synoptic-mesoscale interactions during multiday events are demonstrated as a considerable source of this spatial pattern and variation (36-38%) – particularly the relationship between the WCTT and the onshore coastal ridge.

Even though the WCTT is situated just offshore at the beginning of such events, a pronounced northwest flow develops at low levels over the Georgia Strait in response to a north-easterly oriented pressure slope east of the WCTT. This cooler, denser airstream acts much like a density current and undercuts the general easterly and offshore flow above. The strength of this flow suppresses the normal weakening and backing of northwest winds off the Georgia Strait. As such, the occurrence of westerly and south westerly sea-breezes is reduced; and the eastward progress of the afternoon sea-breeze front is impeded. This allows adiabatically warmed, continental air to dominate much of the metropolitan region in a way classically understood to produce heat waves in the Pacific Northwest.

As the WCTT progresses eastward and weakens, a coastal southerly flow propagating from Oregon and California arrives in response to a building mesoscale ridge. The effect is to weaken the offshore regime for most of the, except the western regions of Vancouver including YVR. Positive moisture anomalies were found to be locally generated from the Georgia Strait which can exacerbate heat stress even after air temperatures have dropped below near heat alert criteria levels.

The resulting variability in parameters related to heat and moisture during the course of a heat wave can present challenges to implementing public health and planning policies, however there is value in knowing spatially where the greatest probabilities of exceedance in thresholds will occur. For the case of the city of Vancouver and the airport, occurrences there are often preceded by exceedance of thresholds at Abbotsford the day prior; and the two-day average of observed or forecast (for the second day) high at this location may also trigger the original heat alert criteria from Henderson and Kosatsky (2012). This is informative to officials because Vancouver has the highest population density in the entire region, and anticipating reductions in natural cooling mechanisms such as sea-breezes is critically important.

REFERENCES

Ainslie, B., D.G. Steyn. (2007). Spatiotemporal trends in episodic ozone pollution in the Lower Fraser Valley, British Columbia, in relation to mesoscale atmospheric circulation patterns and emissions. *J. Appl. Meteor. Climatol.*, 46, 1631-1644.

Black, E., Blackburn, M., Harrison, G., Hoskins, B., Methven, J. (2004). Factors Contributing to the Summer 2003 European Heatwave. *Weather,* 59(8), 217 223.

Brewer, M.C., C.F. Mass. (2016a). Projected changes in western U.S. large-scale summer synoptic circulations and variability in CMIP5 models. *J. Climate*, 29, 5965-5978.

______(2016b). Projected changes in heat extremes and associated synoptic- and mesoscale conditions over the northwest United States. *J. Climate*, 29, 6383- 6400.

______, B.E. Potter. (2012). The West Coast thermal trough: climatology and synoptic evolution. *Mon. Weather Rev.,* 140, 3820-3843.

______, B.E. Potter. (2013). The West Coast thermal trough: mesoscale evolution and sensitivity to terrain and surface fluxes. *Mon. Weather Rev.*, 141, 2869-2896.

Bumbaco, K.A., K.D. Dello, N.A. Bond. (2013). History of Pacific Northwest heat waves: synoptic pattern and trends. *J. Appl. Meteor. Clim.*, 52, 1618-1631.

Della-Marta, P.M., Haylock, M.R., Lutebacher, J., Wanner, H. (2007). Doubled length of Western European summer heat waves since 1880. *J. Geophys. Res.*, 112, doi:10.1029/2007JD008510.

Feudale, L., and J. Shukla. (2011). Influence of seas surface temperature on the European heat wave of 2003 summer. Part I: an observational study. *Climate Dyn.*, 36(9), 1691-1703.

Henderson S.B., and T. Kosatsky. (2012). A data-driven approach to setting trigger temperatures for heat health emergencies. *C.J. Public Health*, 103(3), 227-230.

Kalnay, E., and co-authors. (1996). The NCEP/NCAR 40-year reanalysis project. *Bull. Am. Meteorol. Soc.*, 77(3), 437-471.

Kosatsky, T., S.B. Henderson, S.L. Pollock. (2012). Shifts in mortality during a hot weather event in Vancouver, British Columbia: rapid assessment with case-only analysis. *Am. J. Public Health*, 102, 2367-2371.

Kuglitsch, F.G. et al. (2010). Heat wave changes in the eastern Mediterranean since 1960. *Geophys. Res. Lett.*, 37, L04802, doi:10.1029/2009GL041841.

Lange, O. (1999). *The wind came all ways: a quest to understand the winds, waves and weather in the Georgia Basin.* Environment Canada.

Le, S., J. Josse, F. Husson. (2008). FactoMineR: an R package for multivariate analysis. *J. Stat. Software*, 25(1), 1-18.

Le Roux, B., and H. Rouanet. (2011). *Multiple Correspondence Analysis.* Sage Publications: Thousand Oaks, CA.

Mass, C.F., M.D. Albright. (1987). Coastal southerlies and alongshore surges of the West Coast of North America: evidence of mesoscale topographically trapped response to synoptic forcing. *Mon. Weather Rev.*, 115, 1707-1738.

___, M.D. Albright, D.J. Brees. (1986). The onshore surge of marine air into the Pacific Northwest: a coastal region of complex terrain. *Mon. Weather Rev.,* 114, 2602-2627.

Mesinger, F. and coauthors. (2006). North American Regional Reanalysis. *Bull. Am. Meteorol. Soc.*, 87(3), 343-360.

McKendry, I.G. (1994). Synoptic circulation and summertime ground-level ozone concentrations at Vancouver, British Columbia. *J.Appl. Meteor*., 33, 627-641.

_____, D.G. Steyn, J. Lundgren, R.M Hoff, W. Strapp, K. Anlauf, F. Froude, J.B. Martin, R.M Banta, L.D. Olivier. (1997). Elevated ozone layers and vertical down-mixing over the Lower Fraser Valley. *Atmos. Environ.*, 31(14), 2135-2146.

Oke, T.R. (1973). City size and the urban heat island. *Atmos. Environ.*, 7, 769-779.

_____, G.B. Maxwell (1975). Urban heat island dynamics in Montreal and Vancouver. *Atmos. Environ.,* 9, 191-200.

_____, J.E. Hay. (1994). *The Climate of Vancouver.* Vancouver, British Columbia: University of British Columbia Press.

Pottier, J.L., S.C. Pryor, R.M. Banta (1997). Synoptic variability related to boundary layer and surface features observed during Pacific '93. *Atmos. Environ.*, 31(14), 2163-2173.

Rahmstorf, S., and Coumou, D. (2011). Increase of extreme events in a warming world. *Proc. Natl. Acad. Sci. U.S.A.,* 10.1073/pnas.1101766108.

Smith, R. (2012). Relationships between synoptic circulation patterns and freezing rain in Churchill, Manitoba (1953-2009) (Unpublished master's thesis). University of Manitoba, Department of Environment and Geography, Winnipeg, MB.

_____, R. Dahni, D. Blair. (2013). *Synoptic Typer Tools.*

Snyder, B.J., K.B. Strawbridge. (2004). Meteorological analysis of the Pacific 2001 air quality field study. *Atmos. Environ.*, 38, 5733-5743.

Steyn, D.G., and D.A. Faulkner. (1986). The climatology of sea-breezes in the Lower Fraser Valley, B.C. *Climatol. Bull.,* 20, 21-39.

Stone, D.A., Stott, P.A., Allen, M.R. (2004). Human contribution to the European heatwave of 2003. *Nature,* 432, 610-614

CHAPTER 6: CHANGES IN THERMODYNAMIC FORCING DURING THE JULY 2009 HEATWAVE USING A PSEUDO-GLOBAL WARMING (PGW) APPROACH

6.1 INTRODUCTION

6.1.1 Background

The Vancouver, British Columbia area is a region of complex physiography and its population faces a wide array of meteorologically driven physical hazards. The region is often subjected to heavy rains and winds during the cold season as large-scale disturbances move across the Pacific (Oke and Hay, 1994). However, heatwaves during the warm season have proven to be a considerable hazard with as many as 200 deaths attributed to such an event during July 2009 (Kosatsky et al., 2012). The region is not accustomed to extremes in heat (Stewart et al., 2017) and is therefore more vulnerable to its impacts. The event resulted in proposed thresholds for public safety interventions; specifically - the issuance of heat-alert advisories in order to mitigate future health impacts (Henderson and Kosatsky, 2012).

Globally, trends show heat extremes are increasing due to anthropogenic forcing (Kuglitsch et al., 2010), and studies also show the potential for further increases in both the intensity and frequency of heatwaves in the future climate (Rahmstorf and Coumou, 2011). More locally however, some uncertainty exists in terms of trends and future projections of heat extremes in the Vancouver region. Stewart et al. (2017) found that, while heat extremes are generally increasing across the region, results were more statistically robust for lower grade occurrences at inland sites. This is suggestive of a potential buffering capacity from the afternoon sea-breeze in attenuating heat extremes along coastal zones; and also of the smaller sample size for the most extreme events (which were increasing at the highest rate both in terms of intensity and duration).

As seen from Chapter 5, temperatures during heatwave events are modulated by a complex interaction of several mesoscale processes such as the West Coast Thermal Trough (WCTT) (Brewer et al., 2012, Brewer et al., 2013) onshore coastal surge, afternoon sea-breeze (Steyn and Faulkner, 1986), mountain-valley circulations (Reuten et al., 2005). This is compounded by the size and density of urban infrastructure in Vancouver which exacerbates heat extremes via the heat island effect (Oke and Maxwell, 1975).

Brewer and Mass (2016) showed that extreme offshore flow events in the lower troposphere below 700 hPa - which precede heatwaves in the region - are projected to decrease in occurrence in the future climate due to an overall reduction in the variability of u-component winds. However, in Chapter 4, it was shown that extreme values for an Empirical Orthogonal Function (EOF) or eigenvector important to multiday events was increasing at a statistically significant rate. It was characterized mainly by a large negative pressure anomaly at 500 hPa off the southern coast of California and appears to be increasing due to dynamic-thermodynamic feedback related to increasing SSTs and latent heat flux in that region. The upper low would have a stabilizing effect - slowing down the progression of the poleward upper ridge and WCTT in the lower atmosphere. Therefore, a mechanism exists to offset future reductions in offshore flows – and may be driving the increases in the most extreme heatwave parameters from Stewart et al. (2017).

6.1.2 Objectives

Given the uncertainty in dynamic forcing of any future increases in heat extremes over the region – and that future occurrences in heatwaves may be enhanced by changes in purely thermodynamic variables such as: changes in land to sea temperature contrast; increases in sensible heat flux due to drier topsoils; and warmer sea-surface temperatures leading to higher extreme maximum temperatures. Additionally, the broad increases in June-August 1000-850 hPa specific humidity across the northeast Pacific basin from specific source regions of higher net latent heat flux; along with increased local sources of evapotranspiration in the Fraser Valley and Puget Sound (see Chapter 5) – may lead higher humidex and heat index values during future heatwaves.

Specifically, the objective of this article is to examine the role of thermodynamic forcing on changes to key meteorological parameters at Vancouver and Abbotsford and on the evolution of associated mesoscale circulations. This will be accomplished by analyzing the results from a high-resolution model simulation - in which projected changes to temperature and moisture are applied to historical synoptic patterns which occurred during the July 28-30, 2009 heatwave event discussed by Kosatsky et al. (2012) and Stewart et al. (2017).

6.2 METHODOLOGY

6.2.1 Pseudo-global Warming Approach

In the context of global warming; it is of great interest to understand how the magnitude and frequency of events like the July 2009 heatwave would change given projected changes in key parameters of temperature and moisture. Such an approach has been referred to as a Pseudo-Global Warming (PGW) technique. In this approach, changes in the initial and lateral boundary conditions of a high resolution climate model are forced by increases in mixing ratios and temperatures (Rasmussen et al., 2011; Liu et al., 2017; Hara et al., 2008; Kawase et al., 2013) in line with those established by the Intergovernmental Panel on Climate Change (IPCC).

Thermodynamic modifications on the initial and boundary conditions of models were first proposed by Schaar et al. (1996), but changes were applied uniformly across model domains. This is known as a surrogate global warming approach. Sato et al. (2007), along with Kimura and Kitoh (2007), implemented modifications based on spatially varying GCMs output to estimate changes to thermodynamic parameters. The PGW was then further established by Rasmussen et al. (2011) who utilized climate change perturbations derived from the Community Climate System Model (CCSM) run under the IPCC Special Report on Emissions Scenarios (SRES) A2 climate change assumption for the period 2045-2055. Spatial perturbations fields were calculated by subtracting monthly climatologies for the 2045-2055 projection from a 1995-2005 base simulation (also from the CCSM) for a number of key parameters related to temperature and moisture. The climatological perturbations were then added to the data fields driving the WRF model and the lateral boundary conditions were altered.

Subsequently, the PGW experiment was expanded to a larger domain covering the continental United States and southern Canada (as far north as approximately 55° N) and run for a longer integration period from 2000-2013 (Liu et al., 2017). Similar approaches have also been utilized by Hara et al. (2008) and Kawase et al. (2013) to examine the effects of climate change on snow fall in Japan.

Independently, a similar approach was implemented by Hill and Lackmann (2011) and Mallard et al. (2013), in which temperature changes solely from adiabatic processes are used. This approach does allow for preservation of wind fields and shear. However, moisture changes are not directly applied and must be estimated from the temperature perturbations.

6.2.2 Data

6.2.2.1 Control and PGW Datasets

High resolution data from the Weather Research and Forecasting (WRF- described in the subsequent section) were acquired from the National Center for Atmospheric Research (NCAR) for the Continental United States (CONUS) domain, and from the University of Saskatchewan for a western Canadian (WC) domain. The data were being made available to several universities and research institutions across North America.

To compare the effect of climate change, variables for both a control (CTRL) and PGW simulation conducted by NCAR were attained. Data were acquired in formats for both 2 dimensional and 3 dimensional variables. The 2-dimensional hourly data were acquired to examine the evolution of surface weather conditions at fine temporal resolution during the selected events. The 3- dimensional variables (for a variety of pressure levels to develop vertical profiles) were acquired at a coarser temporal resolution (daily) to assess synoptic and upper-air patterns and forcing during the event. Additional daily output was acquired when antecedent conditions with respect to parameters such as daily maximum temperature or precipitation were necessary. The CTRL and PGW CONUS runs were both iterated from October 2000-October 2013 (Liu et al., 2017). For the WC domain, CTRL data were available from October 2000-October 2013, while for the PGW run, the time period available was for October 2000-December 2006.

Lateral and initial boundary conditions for the CTRL run were provided by the ERA-Interim reanalysis dataset. Rasmussen et al. (2011) used the NCAR and National Centers for Environmental Prediction (NCEP) North American Regional Reanalysis (NARR) data in the initial PGW experiment to serve as the initial and lateral boundary condition on the WRF-ARW model. It is available at 32 km resolution and 45 vertical levels at 3 hourly intervals (Mesinger et al., 2006). ERA-Interim has a spatial resolution of only 80 km, but greater vertical resolution with 60 levels (Dee et al., 2011). These data are produced by the European Centre for Medium Range Weather Forecasting (ECMWF) and were used by NCAR as the basis for the lateral and initial boundary conditions on the WRF model in the PGW experiment.

For the PGW run, mean monthly climate perturbations were derived from an ensemble of models from the Coupled Model Inter-comparison Project 5 (CMIP5) using Representative Concentration Pathway 8.5 (RCP 8.5) for the period 2071-2100 by NCAR. These were subtracted from values for a base period simulation run from 1976-2005; and were re-gridded and added on to the ERA-Interim dataset (Liu et. al, 2017). This was done for a number of meteorological variables such as air temperature, specific humidity, zonal and meridional winds, and served as the initial and lateral boundary conditions for the PGW integration period.

Monthly means for several variables were also acquired for the CTRL and PGW datasets. These were used to infer the mean monthly climate perturbations from the 2071-2100 CMIP5 simulations dynamically downscaled by the WRF model to 4 km resolution. This allowed for an examination of how the lateral and initial boundary conditions in the PGW simulation were being influenced with respect to the perturbed variables.

6.2.2.2 Data Interpolation

Vertical cross-sections and horizontal sections of geopotential height (GPH) for specific pressure levels aloft were interpolated from the 3-dimensional CTRL and PGW data using the NCAR Command Language and NCAR Graphics (NCL). GPH of specific pressure levels are in part a function of the thickness of the atmospheric layer from the surface up to that pressure level. Any thermal expansion of that layer introduced by the 2071-2100 climate perturbations is proportional to this thickness layer. Therefore, where the layer is deepest (near sea level) - the expansion will be greater; and where the height of the pressure level is closer to the surface (higher terrain) - the increases will be lower. These terrain effects were evident when comparing the monthly climatologies and differences in GPH fields between the CTRL and PGW simulations for the lower atmosphere (not shown). Increases in the GPH of the 925, 850, and 700 hPa level diminished over higher elevations. This imparts a bias of lower geopotential height field increases over higher terrain in the PGW simulation. This is relevant since the 925 hPa GPH field was used to examine any changes in dynamic forcing related to the WCTT between the CTRL and PGW simulations. The WCTT shows best definition at this level (Brewer et al., 2013). Special interpolation would be required to estimate these GPH fields over mountainous terrain and to remove the previously mentioned effects. See section 6.4.1 for further discussion.

6.2.2.3 Station Data

Additionally, data from Environment and Climate Change Canada (ECCC) at hourly time intervals corresponding to the period of July 28-30, 2009 were acquired for a coastal site – Vancouver International Airport (YVR); and an inland location – Abbotsford International Airport (YXX). These are same locations used to derive the heat-alert criteria utilized in Chapters 4 and 5.

The data for key meteorological variables such as u and v-component wind, vector wind, temperature, and dewpoint which characterize the various processes on-going during the heatwave were acquired for the purposes of validation against the CTRL dataset.

6.2.2.4 Humidex

The humidex was developed by Masterton and Richardson (1979) and represents a dimensionless index used to quantify heat stress by combining the effects of temperature and dewpoint. Station data from ECCC already included humidex as a parameter. For the WRF CTRL and PGW datasets, humidex values were derived in accordance with the following formula:

$$H = T + (0.5555) * (6.11 * (exp\ (5417.7530 * ((\frac{1}{273.16}) - (\frac{1}{273.16 + T_d}))) - 10))\ (6.1)$$

Where T represents air temperature (˚C) and T_d represents dewpoint temperature (˚C).

6.2.3 Model

The model used to generate the data from NCAR and University of Saskatchewan is the Weather Research and Forecasting Model (WRF) version 3.1, run at 4 km resolution with the advanced research WRF (ARW) core. WRF-ARW 3.1 is composed of 45 vertical levels. Further details on the WRF-ARW are described by Skamarock et al. (2008). Rasmussen et al. (2011) outlined the various parameterization schemes implemented in the model. They include the Noah land surface model, Mellor–Yamada–Janjic boundary layer scheme, Community Atmosphere Model's radiative forcing scheme for shortwave and longwave, and a cloud microphysical scheme developed by Thompson et al. (2008). Information on the specific schemes chosen to run the model for the PGW experiment are provided by Liu et al. (2017).

The model iterated at hourly time-steps with initial and lateral boundary conditions applied every 3 hours, and spectral nudging every 6 hours to maintain the synoptic pattern. This was done for the entire integration period for both the CTRL and PGW runs. This study utilizes a subset of this data for the CTRL and PGW runs corresponding to the occurrence of the Vancouver heatwave from July 28-30, 2009.

In spite of the spectral nudging, some dynamic changes are introduced by virtue of the monthly perturbations to mean u and v component flow. The introduction of zonal and meridional flow perturbations cannot be avoided to maintain thermal wind balance within the WRF model (personal communication with Kyoko Ikeda). This introduces some uncertainty in isolating purely thermodynamic factors during the July 2009 heatwave. Brewer and Mass (2016) also utilized an ensemble of CMIP5 models to show that variability in u-component flow in the lower atmosphere will decrease in the future climate over the region. The mean u-component flow for the region is positive during summer - with northwest winds around the semi-permanent Hawaiian High in the Pacific Basin. Changes in monthly means of zonal winds could impart dynamically induced offshore flow tendencies during the July 28-30, 2009 period. Consequently, changes to u-component flow in the monthly climatologies were examined in addition to the GPH fields previously mentioned. These limitations and alternative approaches will be discussed in section 6.4.1.

6.2.4 Error Calculations

6.2.4.1 Bias

Model bias was quantified on an hourly basis for surface parameters such as temperature, dewpoint, humidex, and u and v-component wind at YVR and YXX as follows:

$$Bias = CTRL - Obs \tag{6.2}$$

Where Obs are the hourly observational data for each station from ECCC and CTRL are the hourly modeled values from the WRF control run.

6.2.4.2 Root Mean Square Error

To assess model performance the Root Mean Square Error (RMSE) was calculated on a daily basis for YVR and YXX. RMSE represents the square root of the mean of squared biases over a particular number of data points in accordance with the following formula:

$$RMSE = \sqrt{\sum_{1}^{n} \frac{(CTRL - Obs)^2}{n}} \tag{6.3}$$

Where Obs are the observational data for each station from ECCC and CTRL are the modeled values from the WRF control run, and n is the number of data points (hourly) for the observational and control model datasets. Since RMSE is the mean of the bias squared it gives greater weight to larger errors.

6.2.5.3 Mean Bias Error

RMSE can only be positive since the biases are squared in the formula. To get a sense if error is positive or negative over certain periods, the Mean Bias Error (MBE) was calculated with the following formula:

$$MBE = \sum_{1}^{n} \frac{CTRL - Obs}{n} \tag{6.4}$$

Where Obs are the observational data for each station from ECCC and CTRL are the modeled values from the WRF control run, and n is the number of data points (hourly) for the observational and control model datasets. Positive and negative values can cancel each other out when calculating the mean, so MBE can be misleading without using another error metric like RMSE.

6.2.4.4 Bias-adjusted Model Change

Bias correction were applied to the CTRL dataset on an hourly basis for the surface variables at YVR and YXX to take into account model error when analyzing changes in the PGW values. The model change was calculated in accordance with the formula:

$$Model\ Change\ = PGW - Bias \tag{6.5}$$

Model changes were then added to the CTRL data to derive the bias-adjusted values.

6.2.5 Sea-breeze Calculation

Given some uncertainty in dynamic forcing, the estimated strength of the afternoon sea-breeze during the July 2009 heatwave in the CTRL and PGW simulations was calculated to isolate the effects of thermal forcing on local circulation patterns. Several sea-breeze scaling studies have utilized time-integrated surface sensible heat flux to assess such forcing rather than land-sea temperature difference (Porson et al., 2007; Wichink et al., 2004). Specifically, the sea-breeze velocity scale from Porson et al. (2007) was calculated to estimate the u-component or onshore flow generated by a pure sea-breeze in accordance with the following formula:

$$u_{sscale=}\sqrt{\frac{g \cdot H}{T \cdot \omega}} \tag{6.6}$$

Where u_{sscale} is the u-component flow generated by the sea-breeze ($m \cdot s^{-1}$), g is the gravitational acceleration ($m \cdot s^{-2}$), H is the time-integrated surface sensible heat-flux since sunrise ($W \cdot m^{-2}$), T is the surface temperature (K), and ω is the period of time since sunrise (s).

6.3 RESULTS

6.3.1 Overview of the July 2009 Heatwave

An extensive meteorological overview of the July 2009 heatwave at Vancouver was provided in Stewart et al. (2017). Here a brief summary will be provided as background for this study. The event featured 3 consecutive days above the threshold temperature criteria derived from Henderson and Kosatsky (2012) (see Chapters 4 and 5); and the all time maximum high for Vancouver International Airport (YVR).

Aloft the period was characterized by an amplified pattern featuring an upper ridge over British Columbia at 500 hPa - which is typical of heatwaves over the region (Bumbaco et al., 2013). At the same time, a cut-off low circulation developed off the south coast of California. This resembles the pattern of negative pressure anomalies in the 500 hPa geopotential height (GPH) EOF associated with multiday heatwave events (Chapter 4), which serve to stabilize the blocking structure responsible for the heatwave pattern.

At the surface, a WCTT was situated along the West Coast for the first two days (July 28-29) and passed through the Vancouver region on the third day (July 30). This had the differential effect of accelerating the afternoon sea-breeze towards YXX, while producing a local off-shore flow at YVR – contributing to the all-time record high at that location.

6.3.2 Model Verification

Liu et al. (2017) performed considerable model verification against observation-based data to gauge model performance. A sensitivity analysis was also conducted to assess the various parameterization schemes available in the WRF model in terms of validation. Model output for several meteorological variables was verified against the parameter-elevation regressions on independent slopes (PRISM) model. Overall results suggested that the model performance remained consistent throughout the entire integration period with no evidence of increasing error or drift. In terms of temperature, model error was reduced in summer compared to winter. However, considerable warm biases were detected for the central and western interior sections of the United States during the summer months. At the same time, cool biases were detected along the West Coast over California, Oregon, and Washington. Such a pattern has considerable implications for heatwave simulations over the Vancouver region – given the interplay of coastal influences and offshore flows bringing warm air from interior sections of western North America, which are so important to such occurrences.

Further verification is therefore presented in this article due to these biases, and also because verifications were not conducted for locations outside the United States in Liu et al. (2017); and the verifications were not conducted versus actual station data.

6.3.2.1 Thermodynamic Variables

Comparison of observational and model data show several caveats with temperature (especially YVR) and dewpoint (both YVR and YXX). In terms of temperature there is a warm bias at both sites – more apparent at YVR than YXX (see Fig.1), and least pronounced at both locations on the afternoon of the last day. Both sites show positive MBEs for all days (Table 1) with YXX show lower RMSEs on all days. At YVR, performance is best in the early morning hours but with substantial underestimation of temperatures during the afternoon hours and evening hours when large negative biases occur on days 1 and 2 (Fig. 3) On day 3, underestimation of temperatures is reduced at YVR during peak heating, but increases substantially during the evening (Fig. 3). Overall, RMSE actually increases on day 3 at YVR due to the substantial underestimation of temperatures that evening (Table 1). At YXX, underestimation of temperatures is more uniformly distributed, but is greatest during the time of afternoon maximum temperature on the first 2 days and on the evening of the day 3 - with negative biases being largest then (Fig. 3). RMSE is lowest on day 3 at YXX, with the MBE closest to 0 (Table 1) with the arrival of the coastal southerlies.

Dewpoint temperature is considerably underestimated at both locations – especially days 1 and 2 (Fig. 1). Underestimation is reduced by the late on day 3 for both sites with negative biases lowest on that day (Fig. 3). Modeled dewpoints actually increase with the arrival of the onshore push, while actual values decrease. This suggests the model is underestimating local sources of evapotranspiration (see Chapter 5), and increases moisture values only with the arrival of the marine airmass on the last day.

Humidex takes into account both temperature and dewpoint, so that at YVR the substantial underestimation of dewpoint and overestimation at temperature largely cancel each other out - although generally the parameter is slightly underestimated (Fig 6.1). At YXX, the temperature overestimations are not as large while the dewpoint underestimations are – leading to almost complete error cancelation between temperature and dewpoint in the humidex formula (Fig 6.1).

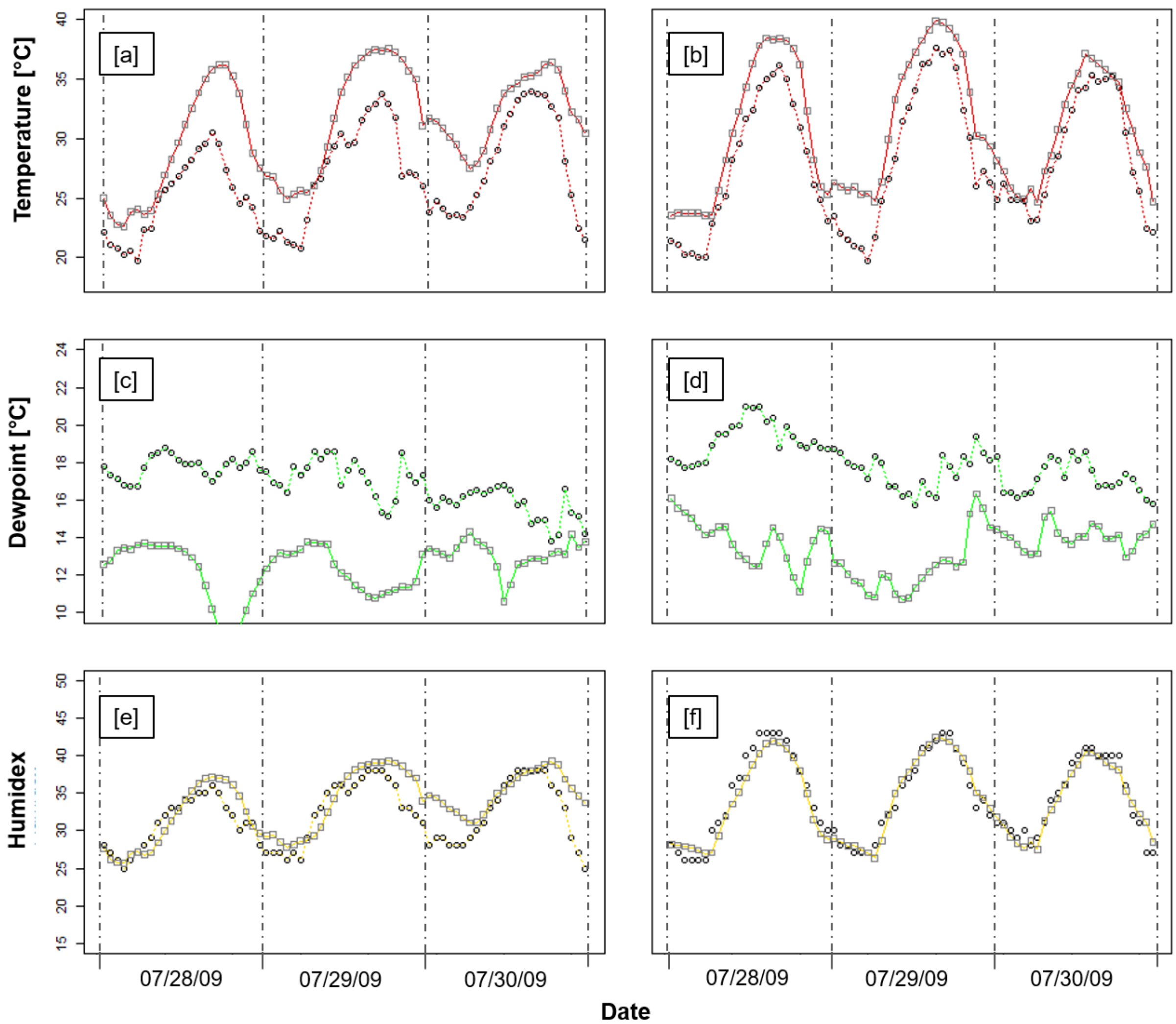

Figure 6.1: Comparison of station data (dotted line) and WRF CTRL data (solid line) at the gridpoint nearest to YVR (left column or [a], [c], and [d]) and YXX (right column or [b], [d], and [f]) for air temperature denoted by a red lines (top row or [a] and [b]), dewpoint temperature denoted by green lines (middle row or [c] and [d]) and humidex denoted by gold lines (bottom row or [e] and [f]).

6.3.2.2 Surface Flows

WRF-ARW considerably underestimates the magnitude of the onshore, northwest flow the first 2 days at YVR (Fig. 6.2). The u-component flow for those afternoons are underestimated and v-component flow are overestimated at YVR (Fig. 3) – particularly the first day. There is a diurnally driven pattern to model bias for both u and v-component wind the first 2 days as during the night-time biases are reversed (Fig. 6.3). Overall, MBEs are negative for both days at YVR (Table 1) - likely due to more undefined or missing values during the night-time. The pattern suggests that WRF is not accurately resolving the relatively strong NW flows in the Georgia Strait seen in the first day composites of multiday heatwave events (see Chapter 5). These flows result from the deflection and channeling of a generally northeast pressure slope (Lange, 1999), that is typical of the synoptic pattern during the initial phases of heatwave events; and can obscure the pattern of sea to land-breeze reversal which the CTRL displays for YVR. During day 3, u-component flow is overestimated at YVR (Fig. 6.3) when actually the offshore flow persisted all day (Fig. 6.2). This implies that WRF is not resolving the local off-shore flow event that can occur at YVR with the arrival of coastal southerlies (Stewart et al., 2017). The v-component flow itself actually verifies relatively well on day 3 at YVR, and RMSEs for the parameter are lower on all days than for u-component flow (Table 6.1). This suggests that the interaction of coastal southerlies with the local terrain is key to reproducing offshore flows at YVR, not the modeling of the southerlies themselves.

At YXX, afternoon winds are only slightly underestimated, but more importantly, the arrival of the sea-breeze as suggested by a southwest flow (Steyn and Faulkner, 1986) is slightly delayed in the model data. This is most obvious when looking at the u-component flow (Fig. 6.2) which shows the slight offset on all 3 days. On the evening of day 3, a large error occurs in the model data with WRF generating a strong easterly flow (Fig. 2) and negative u-component biases (Fig. 3). This causes RMSE for u-component flow to be considerably higher than for any other day and direction for both locations (Table 1). V-component flow at YXX also shows a diurnal pattern with afternoon maxima both underestimated and delayed (associated with the arrival of the sea-breeze). On the evening of day 3, there is a moderate underestimation of v-component flow corresponding to the strong easterly bias seen in the u-component data at the same time. Overall, WRF appears to over-estimate the value of offshore, down-slope flow at YXX which delays the arrival of the sea-breeze on all 3 days, and generates a strong easterly flow on the evening of day 3.

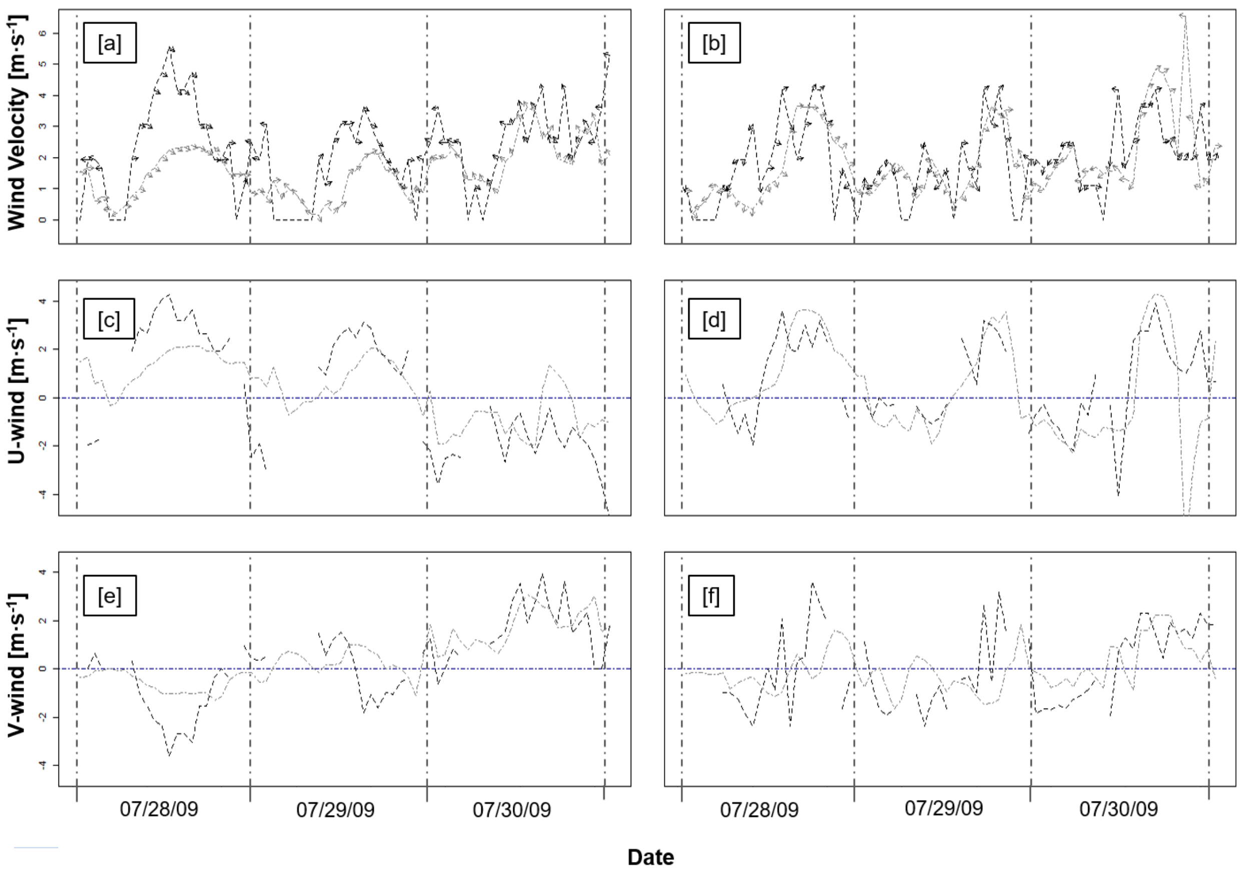

Figure 6.2: Comparison of station data (dotted line) and WRF CTRL data (solid gray line) at the gridpoint nearest to YVR (left column or [a], [c], and [d]) and YXX (right column or [b], [d], and [f]) for vector wind (arrows point in the direction towards air is moving) (top row or [a] and [b]), u-component flow (middle row or [c] and [d]), and v-component flow (bottom row or [e] and [f]).

6.3.2.3 Relationship Between Temperature and Flow Verification

A relationship between error in flow and temperature occurs at both sites on the first 2 days – most apparent at YVR. At that location, underestimation of NW flow is associated with considerable overestimation of afternoon maximum temperature. (Fig. 6.3). At YXX there is a modest increase (reduced bias) in temperature verification after the delayed arrival of the sea-breeze in the model data. Therefore, temperature bias in large part is driven by error in onshore flow intensity and sea-breeze propagation on the first 2 days. The relationship is not as clear by the evening of day 3 however. Temperature verification is generally better at both sites in the afternoon likely due to the arrival of the coastal southerlies and their local modulating effects discussed previously, but decreases substantially during the evening when strong onshore and offshore biases in u-component flow occur at YVR and YXX respectively. Therefore WRF-ARW model verification during the heatwave is sensitive to the temporal evolution of mesoscale processes during the event – both in terms of the NW flows off the Georgia Strait initially; and how u-component flow errors are modulated by the effects of positive v-component winds which arrive later.

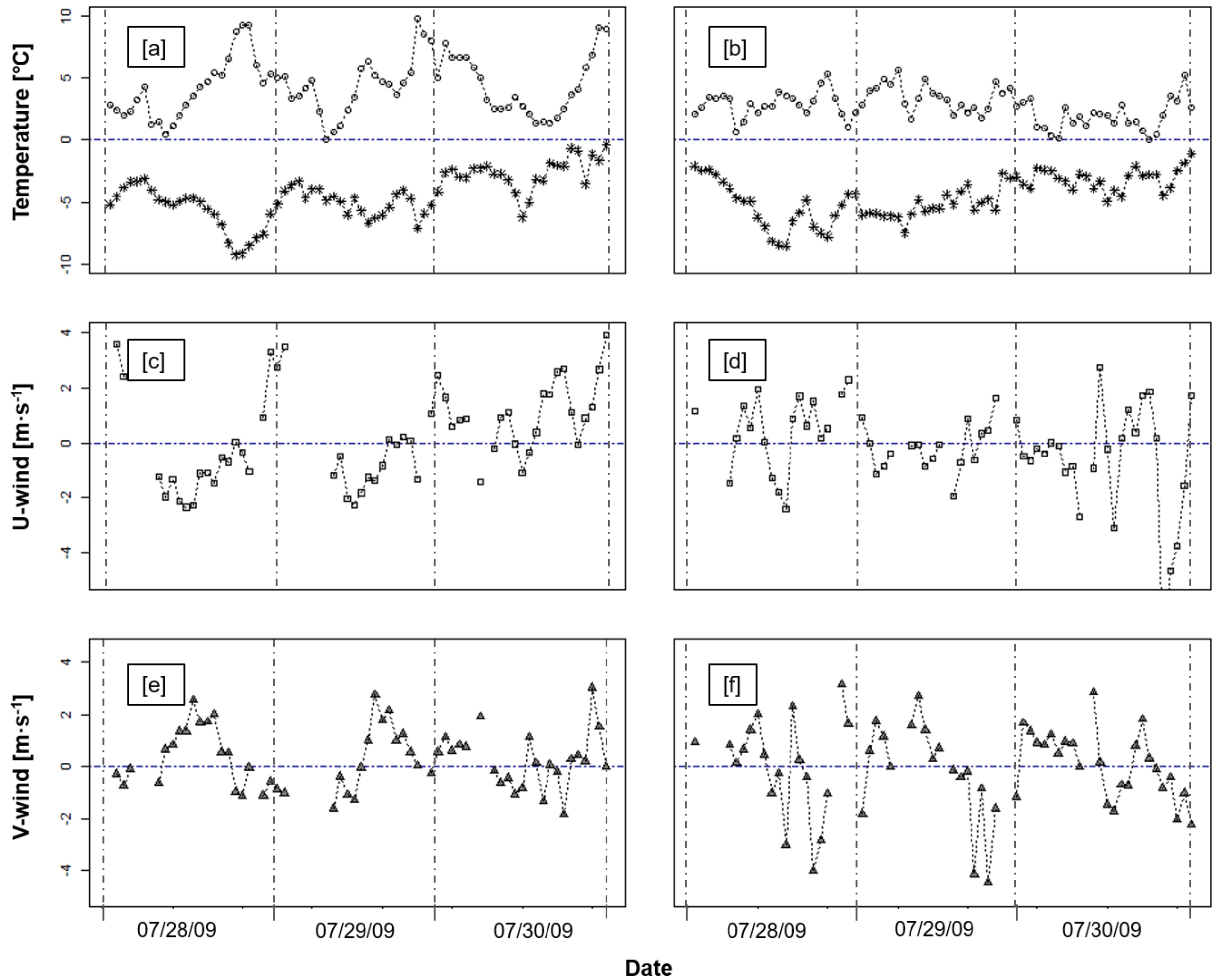

Figure 6.3: Model bias for YVR (left column or [a], [c], and [d]) and YXX (right column or [b], [d], and [f]) for air temperature (dotted line with circles) and dewpoint temperature (dotted line with asterisks) (top row or [a] and [b]), u-component flow (dotted line with grey squares) (middle row or [c] and [d]), and v-component flow (dotted lines with triangles) (bottom row or [e] and [f]).

Table 6.1: Daily RMSE and MBE values for WRF CTRL data at YVR and YXX.

	YVR						**YXX**					
	RMSE			***MBE***			***RMSE***			***MBE***		
	Day 1	**Day 2**	**Day 3**	**Day 1**	**Day 2**	**Day 3**	**Day 1**	**Day 2**	**Day 3**	**Day 1**	**Day 2**	**Day 3**
Temp. (°C)	4.84	5.06	5.01	4.17	4.52	4.40	3.07	3.58	2.22	2.90	3.43	1.86
Dewpoint (°C)	5.97	5.08	2.90	-5.69	-4.98	-2.60	5.73	5.22	3.25	-5.39	-5.08	-3.11
U-wind ($m \cdot s^{-1}$)	1.85	1.66	1.60	-0.26	-0.15	0.99	1.39	0.84	2.40	0.43	0.15	0.77
V-wind ($m \cdot s^{-1}$)	1.18	1.26	1.11	0.40	0.27	0.25	1.85	1.85	1.25	0.06	0.16	0.06

6.3.3 Bias-adjusted Model Changes in PGW Dataset

By applying the model bias to the PGW data, an adjusted hourly dataset can be used to examine changes in key meteorological variables at YVR and YXX under the PGW scenario during the July 2009 heatwave.

6.3.3.1 Changes to Thermodynamic Parameters

There are considerable increases in all thermodynamic variables at both YVR and YXX for all 3 days in the PGW scenario (Fig. 6.4). Given the large model bias during afternoon and early evening hours at YVR the first 2 days, adjusted PGW temperature increases are highest for morning and early afternoon hours and are attenuated during late afternoon and early evening. Temperatures exceed the heat alert criteria derived from Henderson and Kosatsky (2012) (see also Chapter 4 and 5) by mid-morning, extending the period of heat stress to considerably earlier in the day. This reduces the period of time below heat-alert criteria - which serve as a break from the extreme heat. The pattern is somewhat different for day 3, in that temperature increases during mid-morning to midday are minimal, however low temperatures the previous night stay near or just below the 29˚C threshold for YVR. This again would considerably add to heat stress. Afternoon maximum temperatures on days 2 and 3 would reach near 40˚C at YVR under the adjusted PGW scenario, although the increase is actually lowest for day 3 (when an offshore flow is present at YVR).

At YXX, adjusted temperature increases are greatest for the afternoons of days 1 and 2 and the evening and overnight of day 1 (Fig. 6.4). Temperatures on the afternoon of day 2 would approach 45˚C – an increase of almost 7˚C due to lower model overestimation in the CTRL run than for YVR. This would approach the current record high maximum temperature in Canada (45˚C). Overnight lows most nights would be near 25˚C. Temperature increases are attenuated on the afternoon of day 3 with the arrival of the coastal southerlies and onshore surge.

In terms of dewpoint, large increases are seen in the adjusted PGW output for YVR and YXX for the entire period as was the case for temperature. This is particularly true at YVR during the afternoon of day 1, and on day 2 near midday with values near 24˚C (Fig. 6.4). At YXX, increases are not as large at any given hour, but values would be higher – near 25˚C on day 1. These are values that the region is not accustomed to, and currently only occur within Canada over the eastern Prairies and southern portions of Ontario and Quebec (Mekis et al., 2015). Henderson et al. (2012) and Henderson and Kosatsky (2012) did not take into account dewpoint into their estimations and proposed heat-alert criteria, but the adjusted PGW data would suggest that in the future they may have to be incorporated. The adjusted increases in dewpoint generally decrease throughout the course of the event – following the improving model performance in dewpoint by day 3. Again, this is suggestive that local sources of evapotranspiration are more important than evaporation from relatively cooler and deeper oceans farther offshore in contributing to high moisture values during the heatwave.

The combined increases in air and dewpoint temperature also would lead to considerable increases in humidex at all times during the heatwave period. Humidex values at YVR would exceed 40˚C on all afternoons. This represents the threshold for humidex advisories issued by ECCC. At YXX, humidex values would be at or above 50˚C on days 1 and 2 – this approaches the all-time record high for humidex values in Canada of 53˚C (https://www.canada.ca/en/environment-climate-change/services/seasonal-weather-hazards/warm-season-weather-hazards.html#toc7).

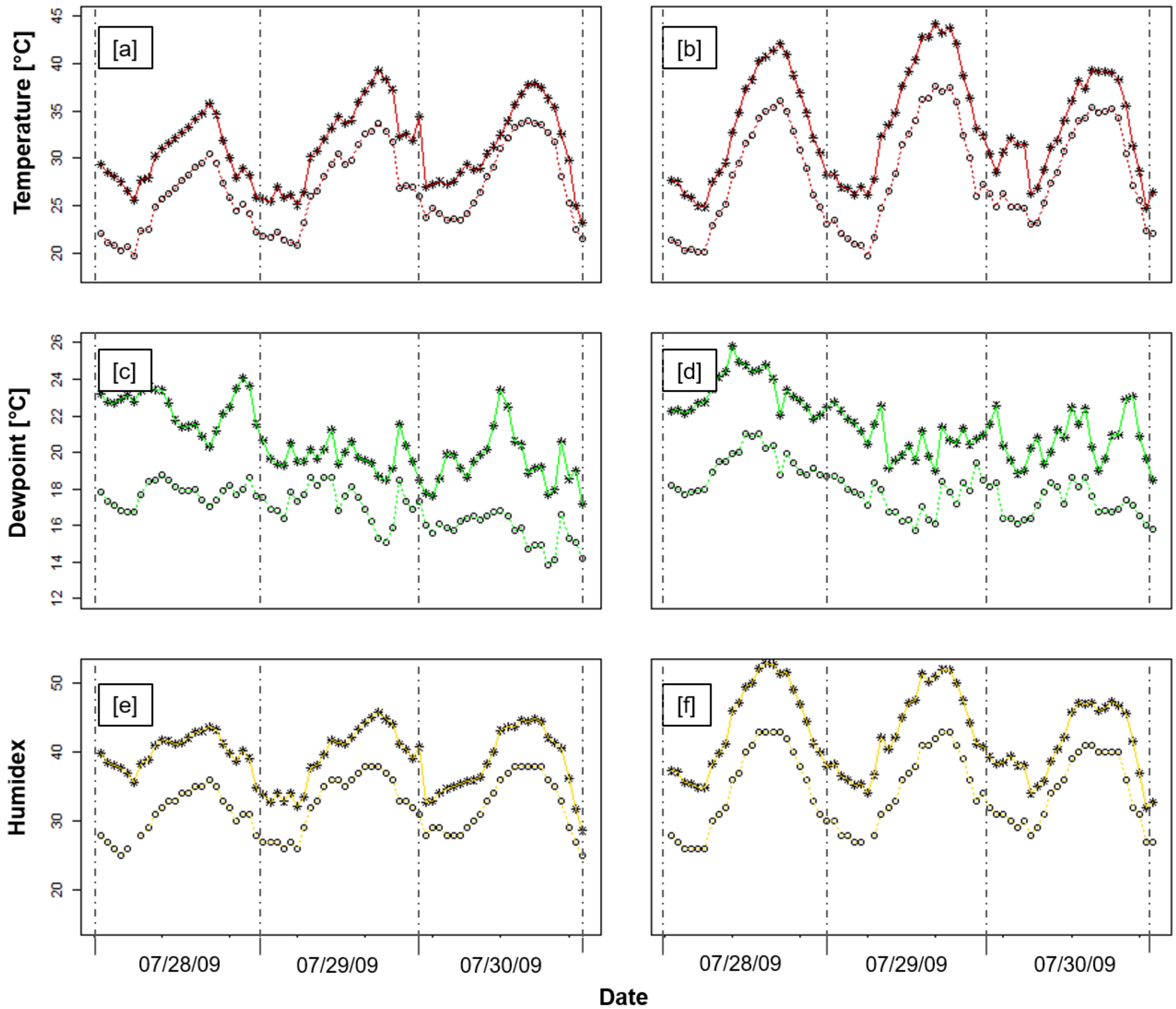

Figure 6.4: Comparison of station data (dotted line with circles) and bias-adjusted WRF PGW data (solid line with asterisks) at the gridpoint nearest to YVR (left column or [a], [c], and [d]) and YXX (right column or [b], [d], and [f]) for air temperature denoted by a red lines (top row or [a] and [b]), dewpoint temperature denoted by green lines (middle row or [c] and [d]) and humidex denoted by gold lines (bottom row or [e] and [f]).

6.3.3.2 Changes to Surface Flow

Much like model error was different between the first 2 days and day 3, so is the pattern of adjusted surface flows at YVR and YXX. At YVR, there is an increase in the NW flow off Georgia Strait on the first 2 afternoons (especially day 2) (Fig. 6.5). This is seen most clearly in the increases in onshore (u-component flow) and decreases in southerly (v-component flow) on the first 2 afternoons. On day 3 the pattern for u-component winds are reversed implying greater offshore component to the flow. On all 3 afternoons there is general increase in wind magnitude.

At YXX, what is most clear is an increase in the adjusted u-component flows beginning on the evening of day 2 (and a particularly large increase on the evening of day 3) and lesser increases in the v-component flow starting at the same time (Fig. 6.5). This implies a greater onshore flow and stronger sea-breeze at YXX on day 3. There is a general increase in wind magnitude at YXX most clearly seen on days 2 and 3.

One can therefore infer an intensification in the temporal cycle of flows affecting both locations. The stronger flows off Georgia Strait act as a buffer in attenuating temperature increases the first 2 afternoons (even though the increases are greater than for day 3 due to model underestimation of the offshore flow at YVR during day 3); while temperature increases are attenuated considerably at YXX with an increasing onshore component to the flow. While model error appeared to be more sensitive to zonal rather than meridional flow on day 3, the largest changes are also for u-component flow on the same day. This implies an intensification in the WCTT and/or mesoscale ridge (generating the coastal southerlies) which modulates the relationship between zonal and meridional flow on day 3 of the heatwave. A broader perspective on mesoscale circulations over the region during the event will be provided in section 6.3.4.

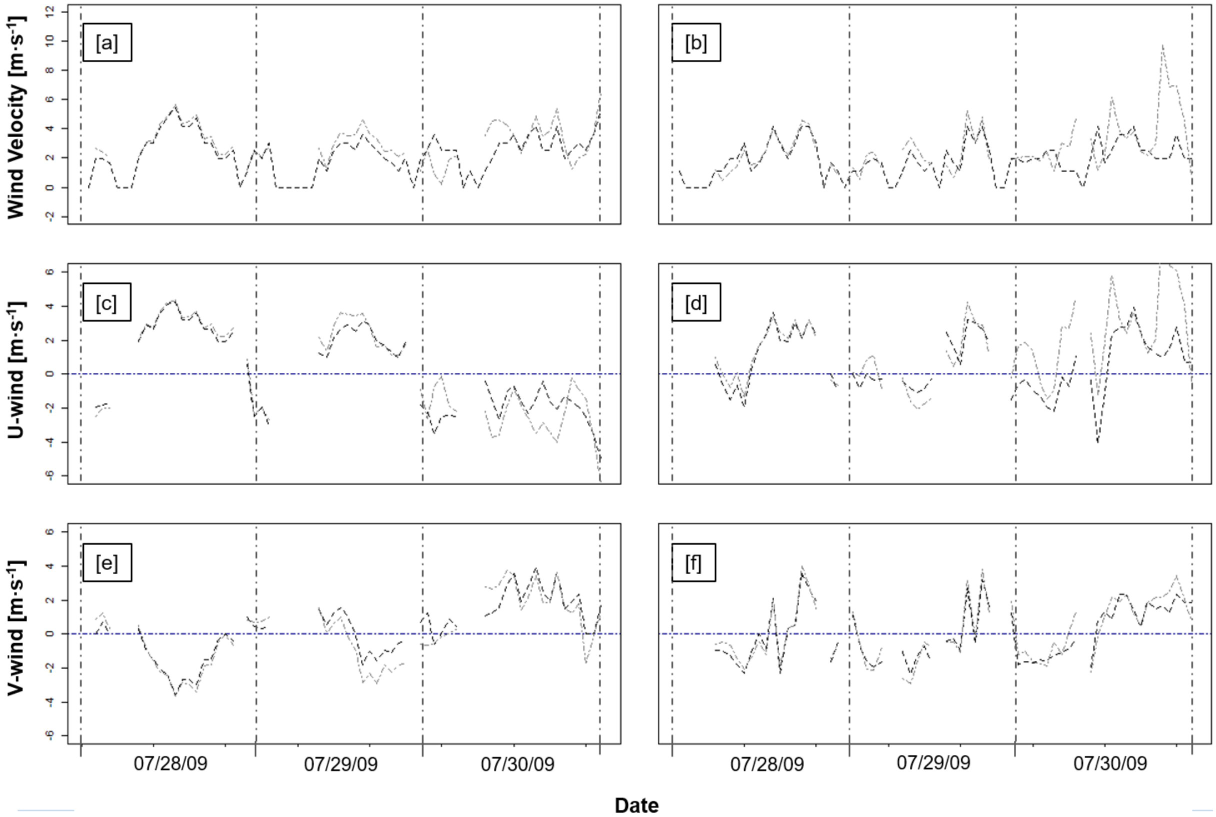

Figure 6.5: Comparison of station data (dotted line) and adjusted WRF PGW data (dotted gray line) at the gridpoint nearest to YVR (left column or [a], [c], and [d]) and YXX (right column or [b], [d], and [f]) for vector wind (formatting of wind vectors follows Fig. 6.2) (top row or [a] and [b]), u-component flow (middle row or [c] and [d]), and v-component flow (bottom row or [e] and [f]).

6.3.4 Regional Changes in Mesoscale Characteristics of the Heatwave

Looking at data for particular stations and corresponding gridpoints is useful from the perspective of verification and bias correction, but does not provide enough insight on the mesoscale circulations or any evolution in their characteristics during the heatwave period. Therefore, an overview of such processes is provided in this section.

<u>6.3.4.1 Overview</u>

Regionally, when examining the CTRL data the various mesoscale effects mentioned in the introduction are apparent. For example, temperatures are highest over land versus ocean; valleys are warmer than the surrounding mountain slopes; and the urban core of the metropolitan

Vancouver region and Abbotsford show higher temperatures averaged out over the entire period in both the CTRL and PGW runs (Fig. 6.6).

To study if the magnitude of winds increased in the PGW run; the mean scalar wind was calculated for both runs (not considering direction which could cancel out magnitudes). Not surprisingly, wind magnitudes are highest over the ocean (due to lack of surface resistance) and on ridgetops across the area (compared to the sheltering effects of valleys and lower elevations; and urban areas).

When examining changes between the CTRL and PGW datasets, temperature increases averaged over the event ranges from 2˚C to 6˚C over the area (Fig. 6.6). Increases were attenuated over the Georgia Strait, and the southwestern metropolitan area of Vancouver (including YVR and Richmond); and over high elevations. Increases in temperature were maximized over the Gulf Islands and interior valleys.

The reason for the attenuation in the Georgia Strait is due to an increase in wind magnitude over the area and increased sea-breeze propagation on land. The reason for the large increases is not clear. A reduction in wind magnitude may imply less synoptically forced down-sloping and adiabatic warming - and increased de-coupling of winds and more intense local valleys circulations (which produce their own adiabatic warming). Increases in sensible heat flux from drier soils may also be contributing to increased heating in these sheltered valleys. For the Gulf Islands, increased NW flow off Georgia Strait caused downwind areas to: i) be shielded from effects of sea-breeze; and ii) receive adiabatic warming due to downslope flow on first 2 days (see Figs. 6.8 and 6.11). The opposite pattern occurred on day 3 with a southeasterly flow over the Georgia Strait (see Figs. 6.9 and 6.12).

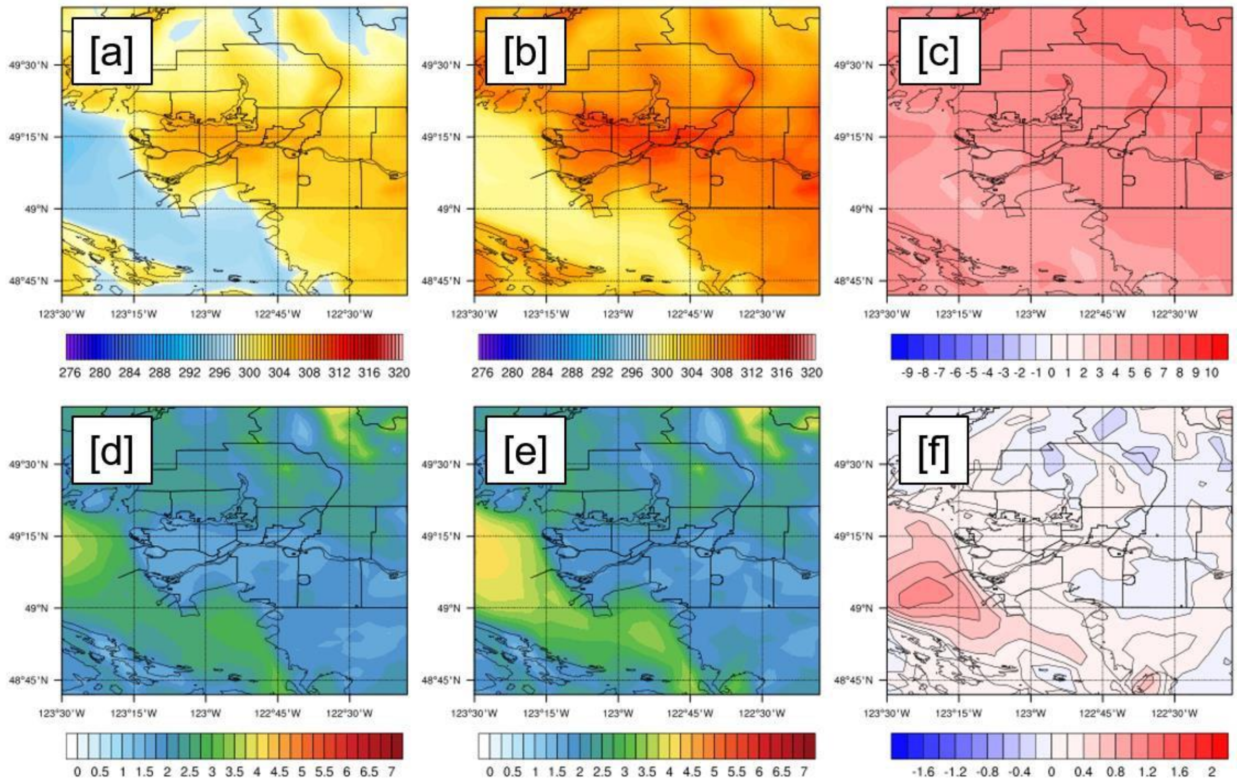

Figure 6.6: Mean temperature (K) (top row, or [a] to [c]), and mean wind magnitude ($m \cdot s^{-1}$) (bottom row, or [d] to [f]) for the CTRL simulation (left column, or [a] and [d]), the PGW simulation (middle column, or [b] and [e]), and PGW – CTRL (right column, or [c] and [f]) over the region during the July 2009 heatwave.

6.3.4.2 Diurnal Cycle and Temporal Evolution of Mesoscale Processes

The various mesoscale processes produce circulations and wind directions (in response to thermal forcing) which cancel each other out through the diurnal cycle. Therefore, composites of vector wind for the CTRL simulation (Fig. 6.7) were developed for nocturnal and diurnal periods.

The composites for vector wind during nocturnal and diurnal hours show strong cold drainage flows funneling down the valleys of the North Coast Mountains during night-time which reverse to an upslope direction during the day. Flow is parallel to the coast in the night-time composite, whereas it is perpendicular to the coast in the day-time composite indicating the presence of the afternoon sea-breeze. A cyclonic curvature is also apparent in the nocturnal composite over Georgia Strait south of Vancouver.

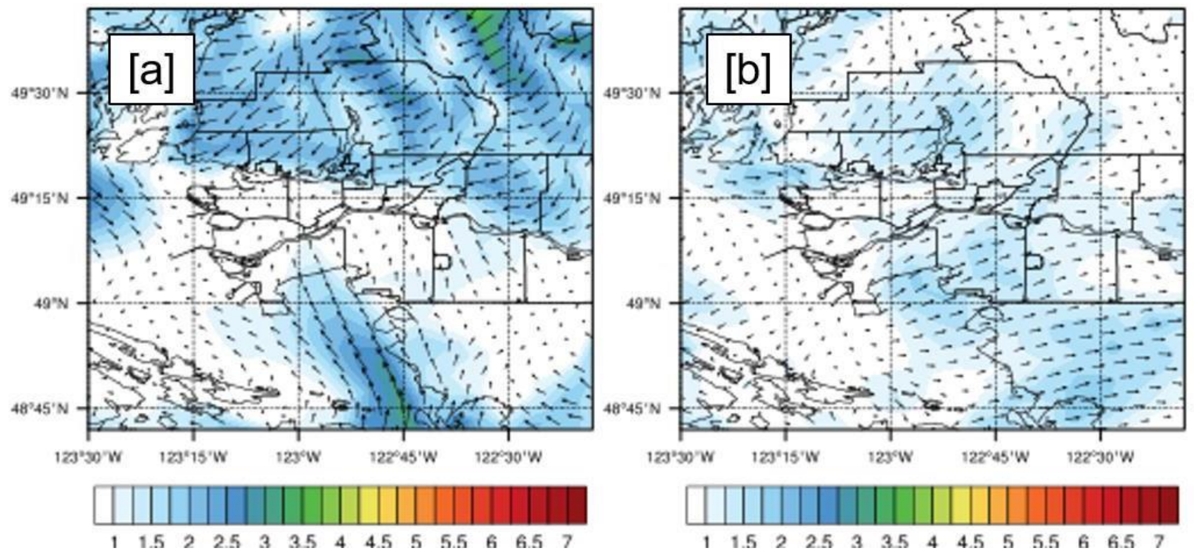

Figure 6.7: Vector wind composites for [a] nigh-time hours, and [b] day-time hours in the CTRL simulation of the July 2009 heatwave. Formatting of wind vectors follows Fig. 6.2.

Since the synoptic and mesoscale patterns were different on days 1 and 2 compared with day 3 due to the passage of the WCTT and the arrival of the coastal southerlies, temperature and vector wind composites were further divided between those 2 periods. Nocturnal composites for nights 1 and 2 in the CTRL and PGW simulations show increases in the NW Georgia Strait flows, and a reduction in the along-shore southerly jet south of Vancouver (Fig. 6.8). Day-time composites for days 1 and 2 also show increases in the NW flows off Georgia Strait, which extend considerably inland across much of Vancouver and Richmond. This increases the amount of onshore flow for those areas, and potentially inhibits the curving of flows perpendicular to the coastline which facilitates the propagation of the sea-breeze inland (Pottier et al., 1997). There is also an apparent increase in cold drainage flows into the some of the interior valleys consistent with the notion of intensifying mountain-valley circulations. The day-time composite shows a larger increase in down-sloping flows (imparted with a negative u-component given the overall synoptic pattern). This possibly represents a combination of increased offshore flow from dynamic forcing and the thermally driven changes in valley circulations previously mentioned.

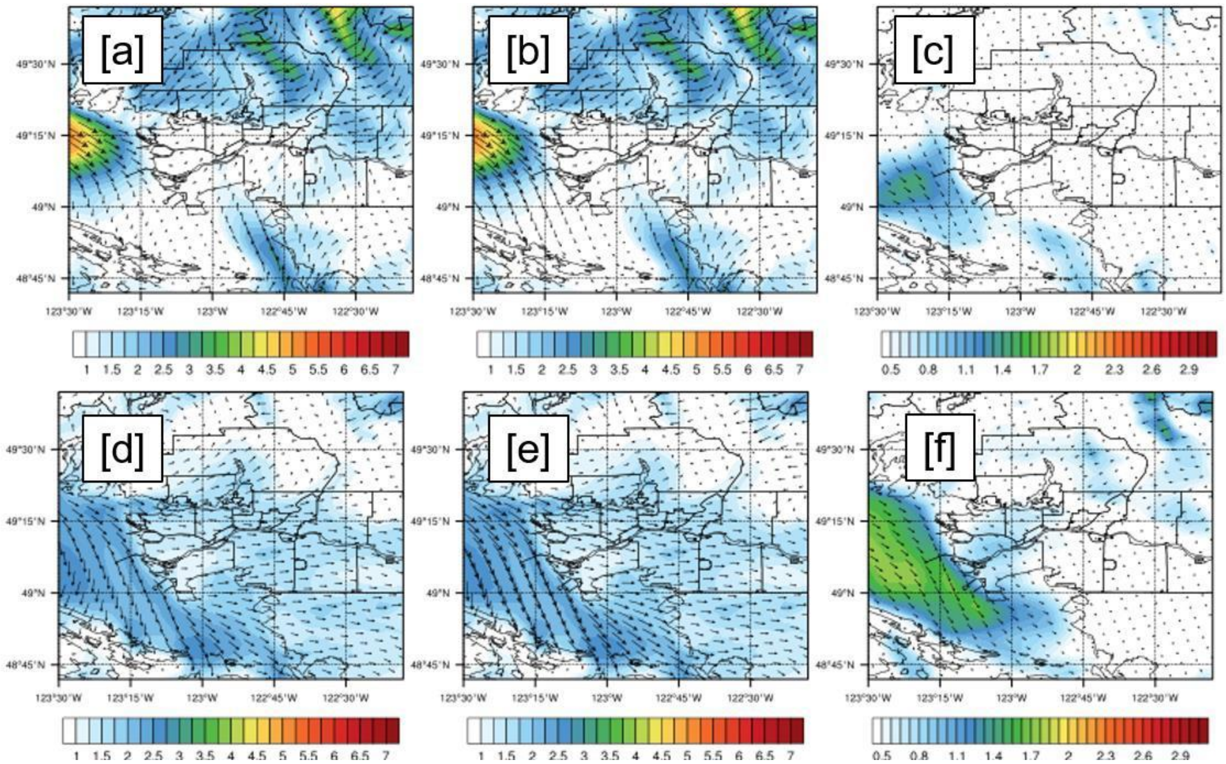

Figure 6.8: Vector wind composites for the CTRL (left column, or [a] and [d]), and PGW simulations (middle column, or [b] and [e]); and PGW – CTRL (right column, or [c] and [f]) during the first 2 nights (top row, or [a] to [c]), and first 2 days (bottom row, or [d] to [f]) of the July 2009 heatwave. Formatting of wind vectors follows Fig. 6.2.

After the passage of the WCTT, a reversal of winds is seen over Georgia Strait heralding the arrival of the coastal southerlies during the night and day 3 (Fig. 6.9). When compared with the nocturnal composites for nights 1 and 2, the along coast southerly jet is enhanced in the CTRL simulation. This is further enhanced when looking at changes between the CTRL and PGW runs. There is also an increase in the cyclonic circulation in the Georgia Strait south of Vancouver and north of the Gulf Islands. This area of vorticity acts to increases the influx of marine air for areas southeast of the Vancouver region towards Abbotsford. There is actually an increase in the onshore flow component over the Georgia Strait near Burrard Inlet due to a lessening in the cold drainage and land breeze circulation off the North Coast Mountains.

In the day 3 diurnal composite, considerable increases are seen in the SE flow over the

Georgia Strait south of the Vancouver region, easterly flow west of Vancouver, and centred over the Burrard Inlet including portion of west Vancouver, and to a lesser extent YVR. This suppresses the propagation of the sea-breeze over most of Vancouver. At the same time, an increased anticyclonic circulation develops south of the Abbotsford region and enhances the SW flow towards YXX. This facilitates the movement of the sea-breeze towards this area.

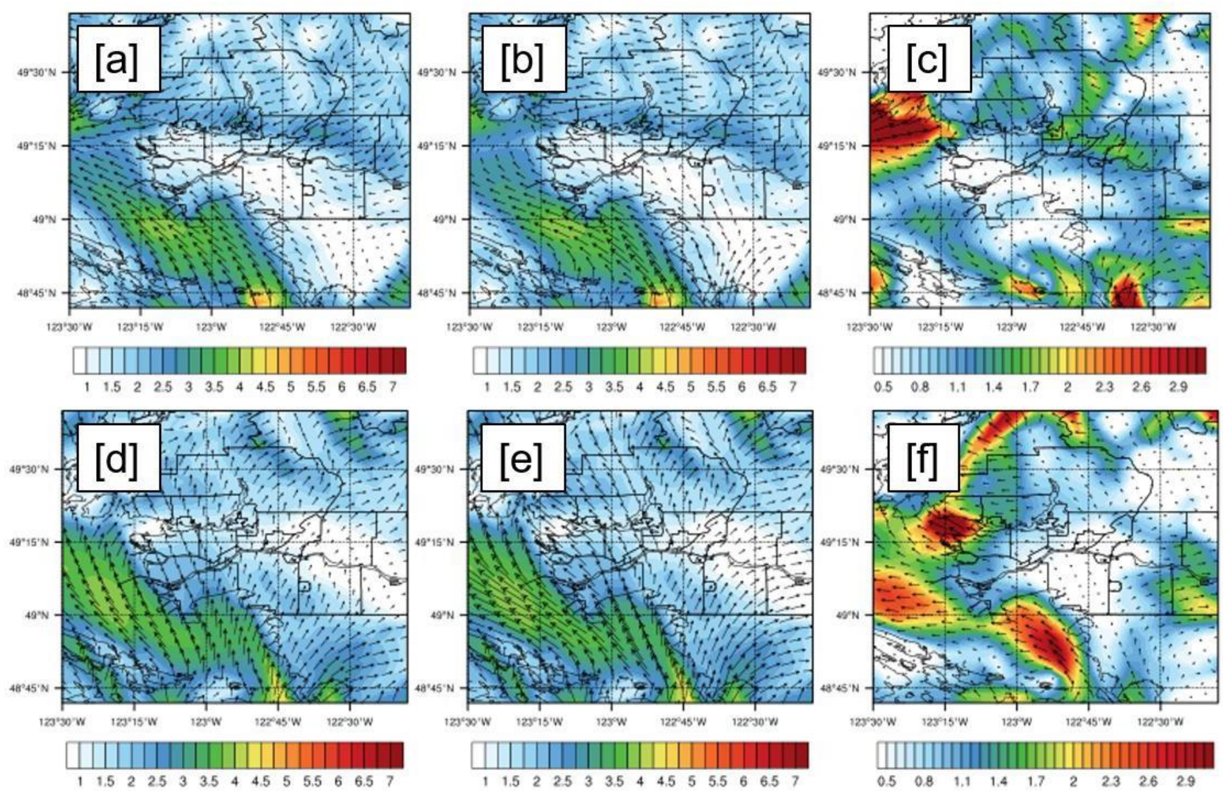

Figure 6.9: Vector wind composites for the CTRL (left column, or [a] and [d]), and PGW simulations (middle column, or [b] and [e]); and PGW – CTRL (right column, or [c] and [f]) during night 3 (top row, or [a] to [c]), and day 3 (bottom row, or [d] to [f]) of the July 2009 heatwave. Formatting of wind vectors follows Fig. 6.2.

The response of local circulations with increasing v-component flows provides insight into the mechanisms which cause the temporal varying flow patterns seen at YVR and YXX during the evolution of heatwave events. The coastal southerlies are deflected to produce offshore flows for large areas of Vancouver, and conversely an onshore circulation or jet that accelerates the sea-breeze towards YXX. This also explains the sensitivities in both u-component flow error and changes in relation to the arrival of positive v-component flows after the passage of the WCTT. The 24 h composites for days 1 and 2, and day 3 summarize these changes (Fig. 6.10).

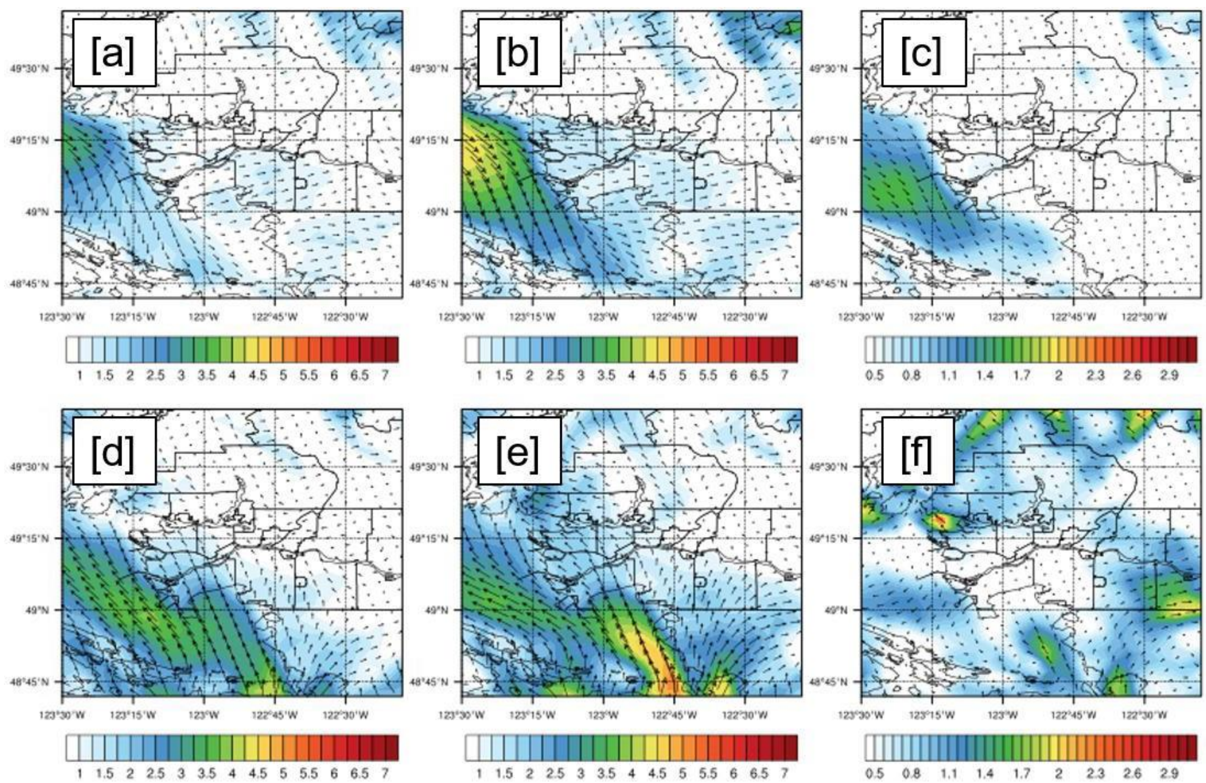

Figure 6.10: 24 h vector wind composites for the CTRL (left column, or [a] and [d]), and PGW simulations (middle column, or [b] and [e]); and PGW – CTRL (right column, or [c] and [f]) during the first 2 days (top row, or [a] to [c]), and day 3 (bottom row, or [d] to [f]) of the July 2009 heatwave. Formatting of wind vectors follows Fig. 6.2.

Diurnal and nocturnal composites for mean temperature over the region largely reflect the patterns and changes seen in the vector wind composites. Temperature changes are attenuated somewhat the first 2 nights over Georgia Strait - and to a greater degree the first 2 days with onshore areas also experiencing reduced increases (Fig. 6.11). Temperature increases are relatively homogeneous farther inland the first 2 nights, but are considerably greater from West and North Vancouver east-southeast towards the Abbotsford region during days 1 and 2. This is attributable to stronger flows off Georgia Strait and slower propagation of the sea-breeze front towards the latter regions.

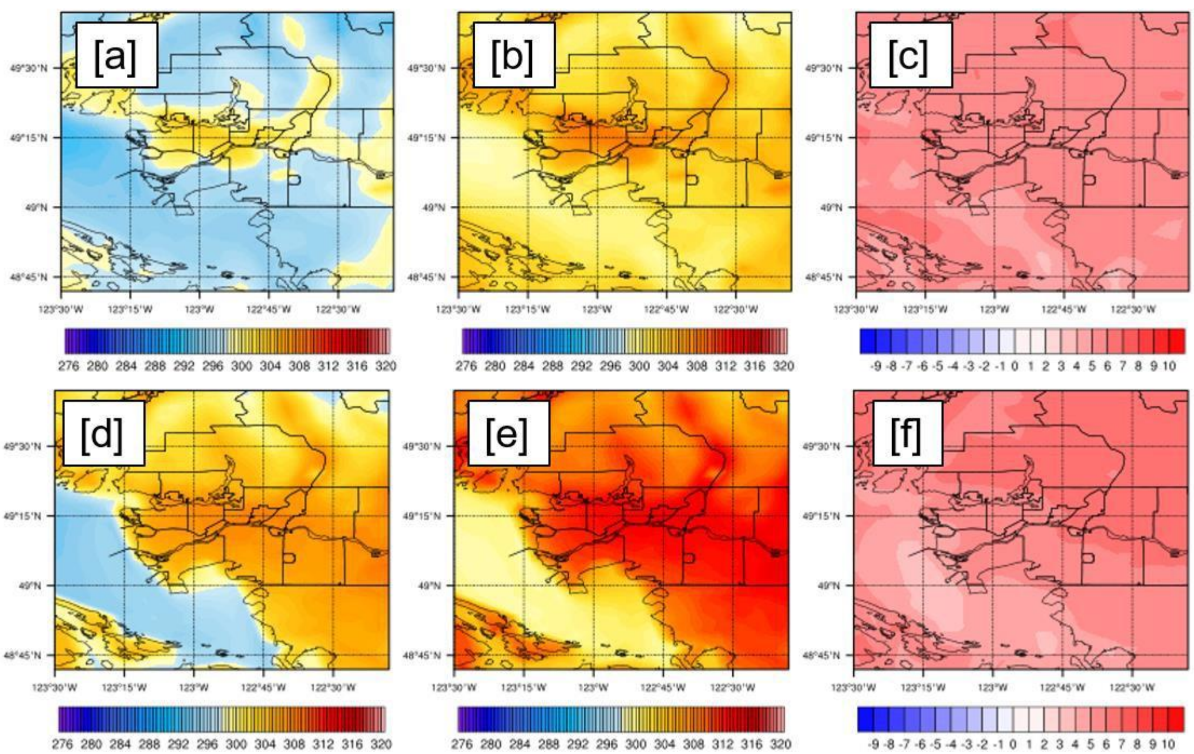

Figure 6.11: Temperature (K) composites for the CTRL (left column, or [a] and [d]), and PGW simulations (middle column, or [b] and [e]); and PGW – CTRL (right column, or [c] and [f]) during the first 2 nights (top row, or [a] to [c]), and first 2 days (bottom row, or [d] to [f]) of the July 2009 heatwave.

On night 3, temperature increases are attenuated considerably over Georgia Strait west of Vancouver due to a lessening of the offshore, land breeze circulation previously mentioned (Fig.

6.12). Conversely, there is considerable warming that occurs in some of the interior valleys due to reductions or impedance of cold drainage flows from the increased v-component flow. On day 3, considerable and widespread attenuation of temperatures increases (< 1˚C) are prevalent in those areas experiencing corridors or jets of increasing v-component flows - particularly areas south of Vancouver and southwest of Abbotsford. Temperature increases are maximized locally where increases in offshore flow occur; and farther inland away from the effects of the sea-breeze. Region-wide, temperatures are generally cooler on day 3 than on days 1 and 2 in the CTRL and PGW simulations due to the overall greater influx of marine air associated with the coastal southerlies.

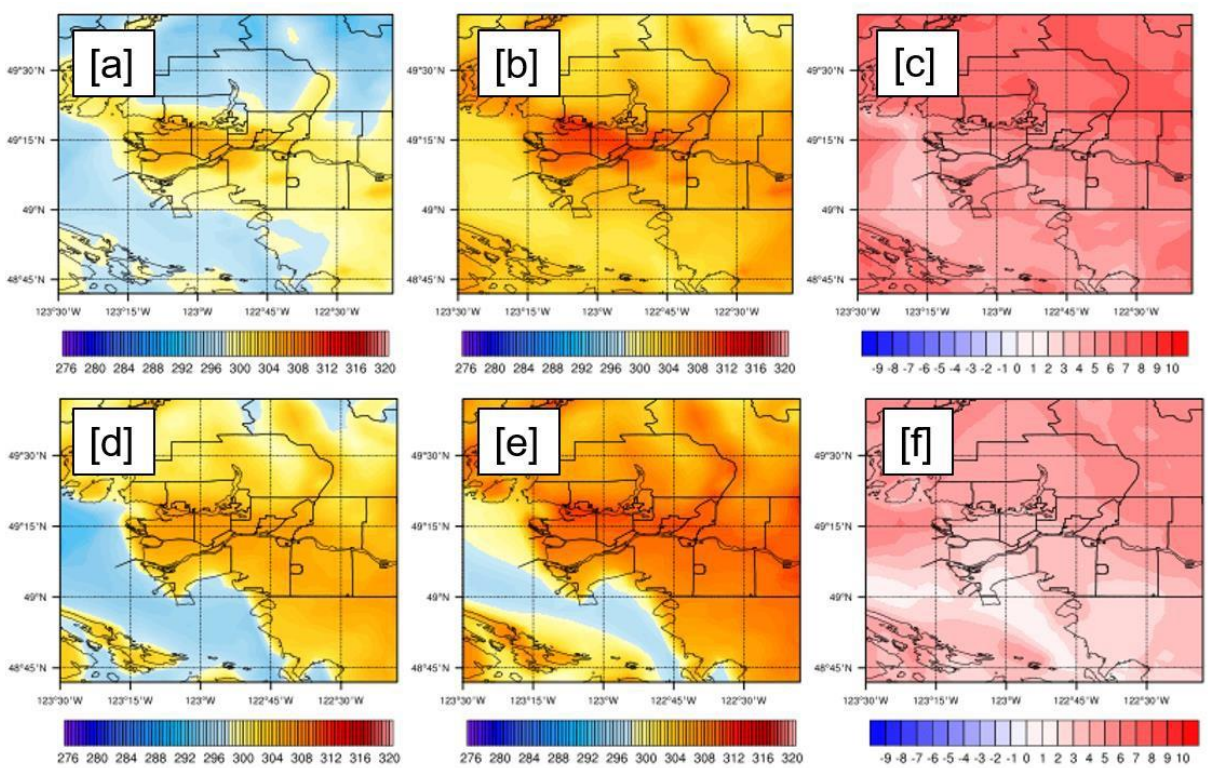

Figure 6.12: Temperature (K) composites for the CTRL (left column, or [a] and [d]), and PGW simulations (middle column, or [b] and [e]); and PGW – CTRL (right column, or [c] and [f]) during night 3 (top row, or [a] to [c]), and day 3 (bottom row, or [d] to [f]) of the July 2009 heatwave.

6.3.5 Thermally Driven Circulation Patterns

6.3.5.1 Sea-breeze Circulations

Even though sea-breeze intensity and propagation during heatwave events in the region is largely modulated by forcing from the WCTT and the onshore mesoscale ridge, the modeled effects of purely thermal forcing on this circulation were examined using the approach from Porson et al. (2007). Fig. 6.13 shows the calculated u-component sea-breeze velocity at YVR and YXX in the CTRL and PGW simulations and parameters related to thermal forcing on this process. Since this parameter is a function of time-integrated sensible heat flux since sunrise, the calculated sea-breeze strength varies largely with changes with this variable. The sensible heat flux is greater inland at YXX than at YVR on all days in the CTRL and PGW simulations. This is due to the coastal influence at YVR which lowers temperature, increases humidity and attenuates the drying of topsoil. This is particularly true during periods of above average temperatures. The sea-breeze forcing therefore is higher at YXX on all days in both simulations. It is also higher on day 3 due to the modeled sensible heat flux being highest on that day for YXX and YVR. This may be due to continued drying of the surface from extreme temperatures simulated the previous 2 days.

Increases in sea-breeze velocity are attenuated the first 2 days in the PGW simulation – particularly at YVR due to the stronger flows off Georgia Strait. Larger increases are seen on day 3. This is driven by higher cumulative sensible heat flux at both locations (even though the maximum instantaneous sensible heat flux at YVR on day 3 is approximately the same, it is higher for a long period early in the day generating a stronger sea-breeze). However, in spite of stronger thermal forcing on the sea-breeze using the approach by Porson et al. (2007) in the PGW simulation – modeled offshore flow increased at YVR on day 3 due to the of deflection of coastal southerlies which overrides any potential thermal feedback. At YXX, thermal forcing using this approach would be additive with the modulation from the coastal southerlies in accelerating the sea-breeze front towards that region.

Another measure of thermal forcing - the land-sea temperature difference (modeled SST over the Georgia Strait and simulated temperature at YXX) actually decreases on day 3. This is because temperature increases are attenuated on day 3 for many parts of the region including YXX due to the coastal southerlies entering the region; the exception being those areas where their deflection results in an increased offshore flow component (Fig. 6.12). The offshore flow at YVR also affects the calculation of sea-breeze velocity since increases in temperatures (which is inversely related to sea-breeze velocity in this method) produce negative feedback and underestimate the amount of thermal forcing – while at YXX the opposite occurs. This highlights the difficulty in isolating purely thermodynamic driving factors during heatwaves in the region and the selection of a suitable proxy variable for estimating thermal forcing during such events.

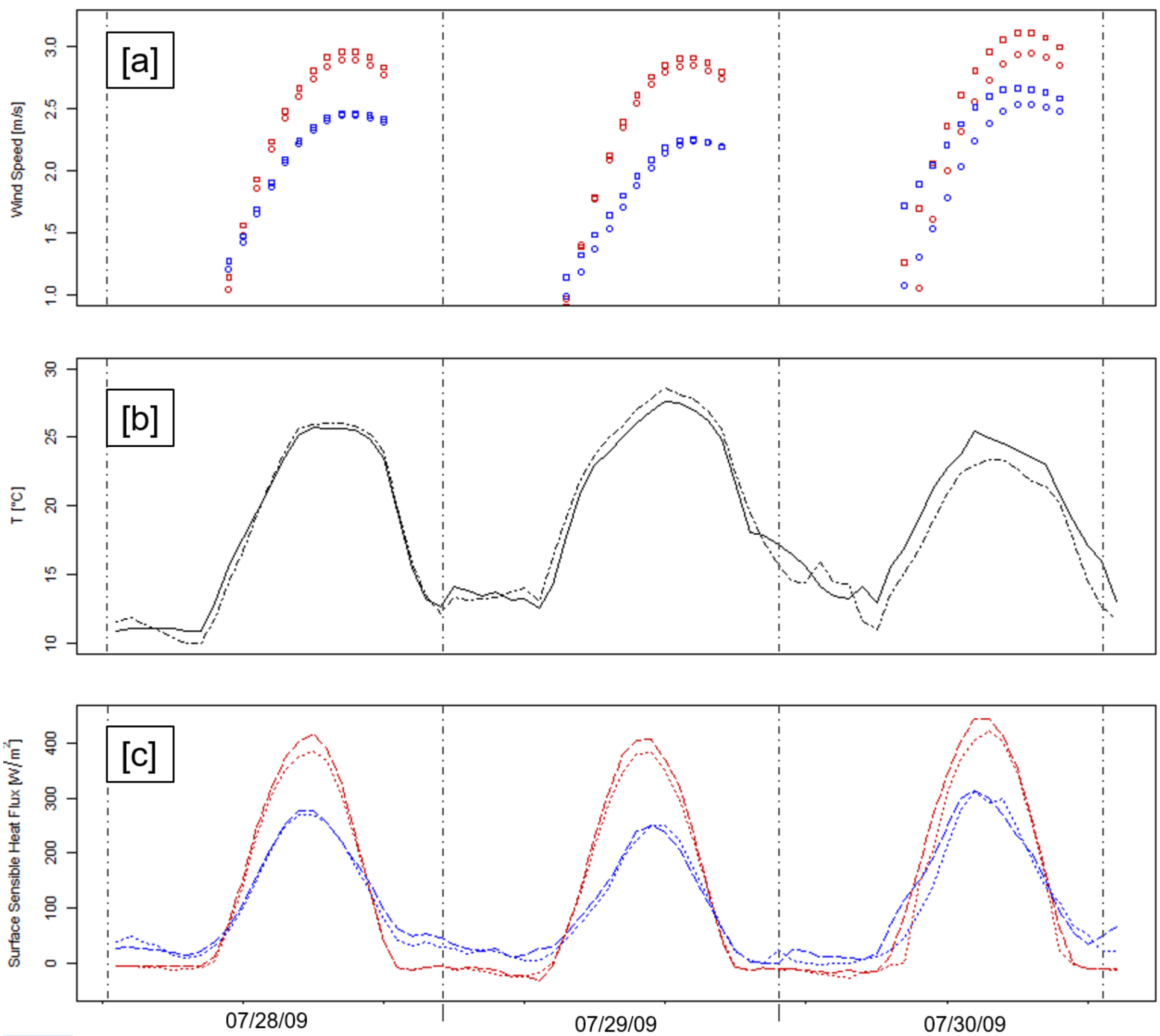

Figure 6.13: Hourly parameters related to thermal forcing on sea-breeze circulations during the July 2009 heatwave: [a] sea-breeze velocity scale at the gridpoint nearest YVR (blue) and YXX (red) for the CTRL (circles) and PGW (squares) simulations; [b] simulated land-sea temperature difference in the CTRL (solid line) and PGW (dashed line) simulations; and [c] instantaneous sensible heat flux at the gridpoint nearest YVR (blue) and YXX (red) for the CTRL (dotted line) and PGW (dashed line) simulations.

6.3.5.2 Mountain-valley Circulations

Another thermally driven process in the region is mountain-valley circulation patterns. Variability in thermodynamic forcing between the first 2 days and the third, as well as changes between the CTRL and PGW simulations in these circulations was examined. Fig 6.14 shows vertical velocity and u and w wind vectors across a transect of the Coastal Mountains. Diurnal composites for days 1 and 2 in the CTRL simulation show more intense circulation patterns than for day 3 with higher upward velocities over mountain peaks and downward velocities between. A negative (offshore) u-component flow is apparent in the days 1 and 2 composite between 1500-3000 m, whereas a positive (onshore) flow occurs on day 3. This occurs in spite of increases seen in simulated sensible heat flux both at YVR and inland on day 3.

In terms of changes, increases in circulation intensity occur for days 1 and 2 in the PGW circulations – suggestive of an increase in thermal forcing. However, at the same time there is an increase in the background offshore flow above the terrain – therefore this may also be playing somewhat of a role in the intensification. On day 3, considerable diminishment of the circulation patterns is apparent in the PGW simulation - as is the effect of a decrease in the onshore flow component which shifts the thermals westwards somewhat. This decrease in u-component flow is due to increasing flow deflection of stronger coastal southerlies which both advect a more stable, marine influenced airmass thus reducing buoyancy; and may also produce disruptive wind shear effects on the thermals. Again, increases in simulated sensible heat flux on day 3 did not have an effect of increasing overall thermal forcing. See Section 6.4.2 for more on the relationships between sensible heat flux and other measures of heating and stability in the CTRL and PGW simulations of the July 2009 heatwave.

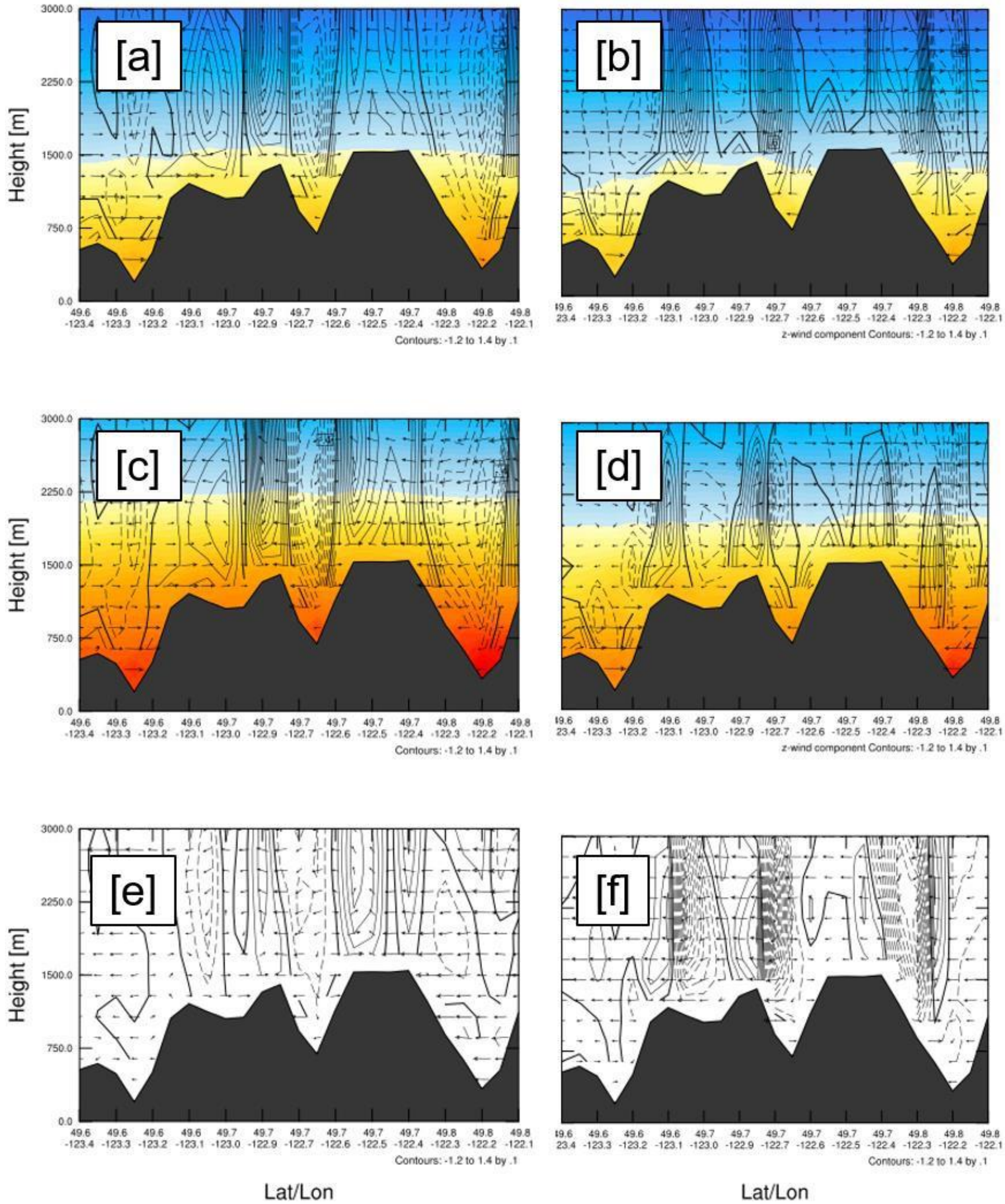

Figure 6.14: Composite vertical cross sections along a transect of the Coastal Mountains during daylight hours for temperature (C, shaded contours), vertical velocity (m·s^{-1}, contour lines), and u and w wind vectors (arrows) for the CTRL (top row or [a] and [b]), and the PGW simulations (middle row or [c] and [d]), and PGW – CTRL (bottom row or [e] and [f]) for days 1 and 2 (left column or [a], [c], [e]), and day 3 (right column or [b], [d], [f]). Formatting of wind vectors follows Fig. 6.2.

6.4 SUMMARY AND DISCUSSION

6.4.1 Dynamic Forcing

Given the increases in flow at YVR, YXX, and regionally before and after the arrival of the WCTT – intensification in dynamic forcing and the WCTT was inferred. Fig. 6.15 shows the 925 hPa GPH in the CTRL and PGW simulations and the difference between them. The CTRL simulation shows the general progression of WCTT movement northwest through the period and eventual splitting into separate lows as the onshore mesoscale ridge advances by day 3. The changes are dominated by general increases in the parameter due to the processes mentioned in section 6.2.2; and a bias towards lower increases at higher elevations as the parameter becomes undefined (where elevation is higher than the 925 hPa GPH).

In spite of these caveats, a clear pattern of both meridional and offshore variability in GPH increases is apparent (which cannot be related to these effects). On day 1, greater increases in 925 hPa GPH occur to the northwest – creating an intensified low level pressure gradient which increases the local circulations. The higher increases in 925 hPa GPH are associated with the near surface anticyclone moving onshore. On day 2, high pressure increases are attenuated inland just to the southeast of the region – suggestive of an eastward shifting WCTT. This again sets up a stronger gradient locally consistent with the flow increases seen on day 2. The terrain effects mentioned previously likely play a role most on this day, but an offshore and meridional pattern to the variability is still present. By day 3, larger increases in 925 hPa GPH are located to the southwest associated with the approaching mesoscale ridge. Taken together it is suggestive of a more intense WCTT between the synoptic ridge to the north, and the mesoscale ridge to the south. Less confidence exists in the extent of the eastward shift in the WCTT – but the effect is apparent (albeit more attenuated) even in offshore areas.

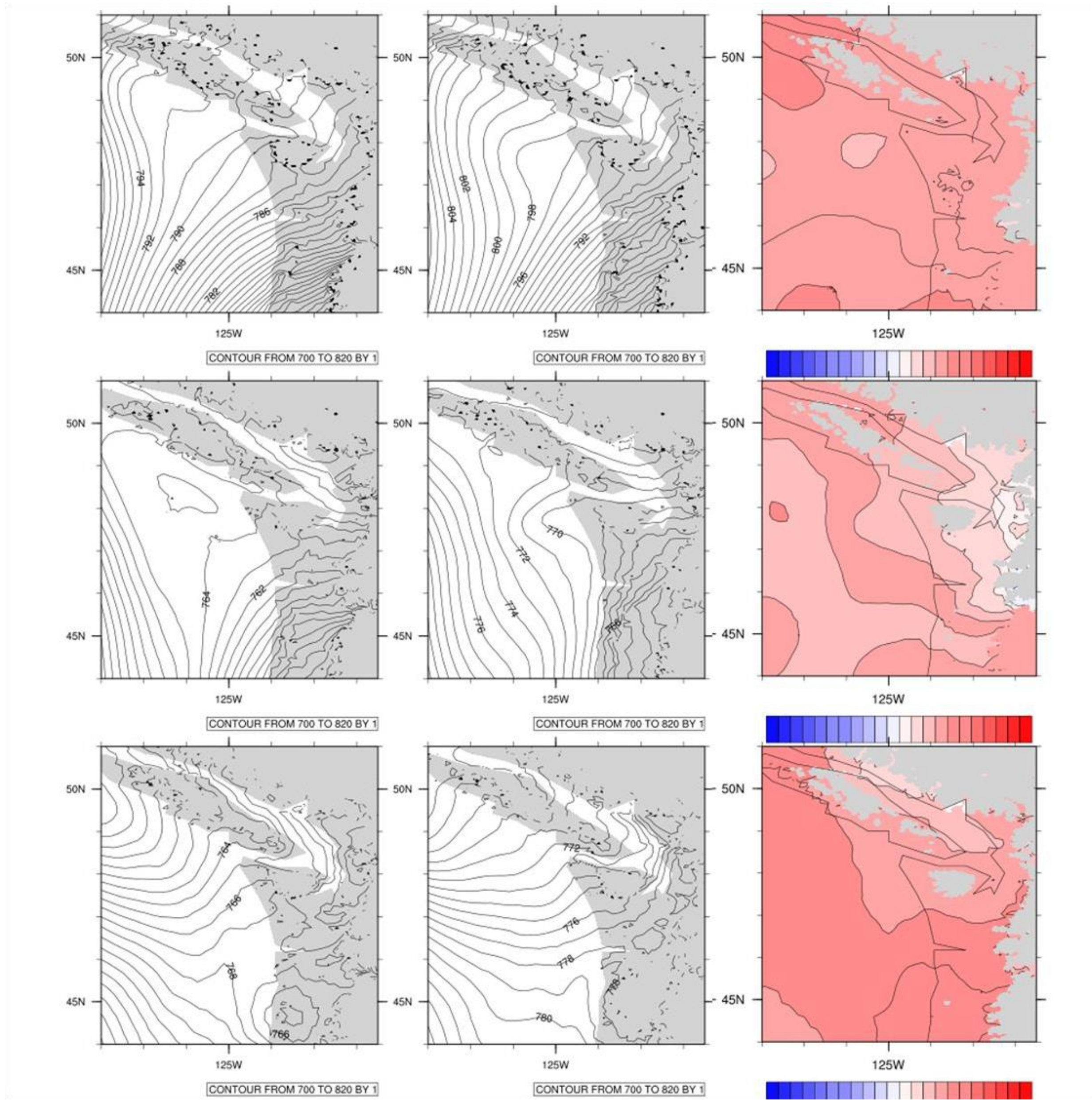

Figure 6.15: 925 hPa GPH in the CTRL (left column) and PGW (middle column) simulations, and PGW - CTRL (right column) for day 1 (top row), day 2 (middle row), and day 3 (bottom row) of the July 2009 heatwave.

As mentioned in Section 6.2.4, some dynamic forcing is introduced by the PGW approach in the form of perturbations to monthly mean u and v component flow applied to the initial and lateral boundary conditions of the WRF model. Fig. 6.15 shows mean monthly u-component climatologies at GPHs in the lower atmosphere in the CTRL and PGW simulations which are representative of the base and 2071-2100 CMIP5 simulation periods. At 925 hPa, there are small decreases in the mean u-component flow (greater offshore component), which may be slightly imparting offshore flow bias in the PGW simulation near the surface. However, heatwaves in the region are associated with offshore flows through a deeper layer of the lower atmosphere; and at these levels there are increases in the mean monthly u-component flow. Therefore, there does not appear to be significant decreases in u-component flows which may be imparting bias in the dynamics of the PGW simulation from the initial and lateral boundary conditions.

WCTT intensity has been shown to be sensitive to terrain (Brewer et al., 2013) and down-sloping flow through a considerable depth of the lower atmosphere. Consequently, changes to the lateral boundary and initial conditions related to u-component flows are not the reason for the strengthening WCTT seen in the PGW simulation; and it is possibly related to thermodynamic feedback associated and/or terrain effects. Further study is required to determine the causal mechanisms. In particular, contributions to temperature changes from individual variables in the thermodynamic equation – which represent different mechanisms of heating (diabatic versus adiabatic) - would have to be studied for changes and variations. This study did not have access to such variables in the WRF CTRL and PGW datasets.

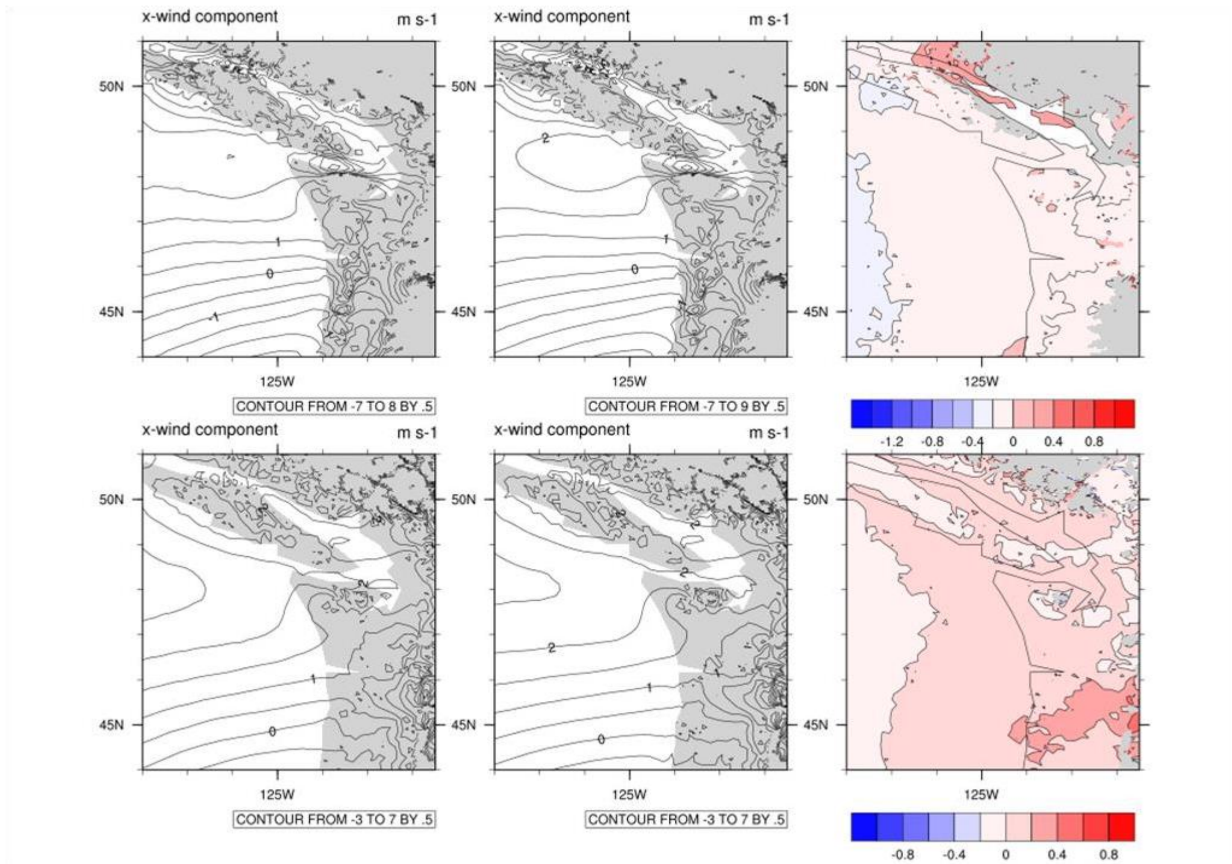

Figure 6.16: Mean monthly climatologies of u-component flow in the CTRL (left column) and PGW simulations (middle column), and PGW - CTRL (right column) at the 925 (top row) and 850 hPa GPH level.

6.4.2 Sea-breeze circulations

The disparity in thermal forcing parameters on sea-breeze circulations between days 1 and 2 and day 3 suggests that any such mechanism is more than offset by dynamic forcing and modulation from the WCTT and mesoscale coastal ridge. Porson et al. (2007) showed that a linear relationship occurred between surface sensible heat flux and temperature difference between land and sea when examining a climatology of sea-breeze days in their study. Fig 6.17, however, shows a logarithmic relation particularly on days 1 and 2 at YVR when examining modeled parameters from this study. On day 3, the relationship becomes somewhat closer to linear. The reason for non-linearity is that heatwave events do not represent days when pure sea-breezes (driven mainly by thermal forcing) occur – but rather are driven by WCTT modulation and flow deflection of coastal southerlies which change the orientation of the sea-breeze front. Since the land-sea temperature difference actually decreases in the PGW simulation while surface sensible heat flux increases – this suggests that other parameters could be utilized to estimate thermal forcing on sea-breezes and other local circulations during heatwave events (see Section 6.4.3). An additional caveat and limitation to be considered is that modeled sea-surface temperatures and sensible heat flux were not validated in this study.

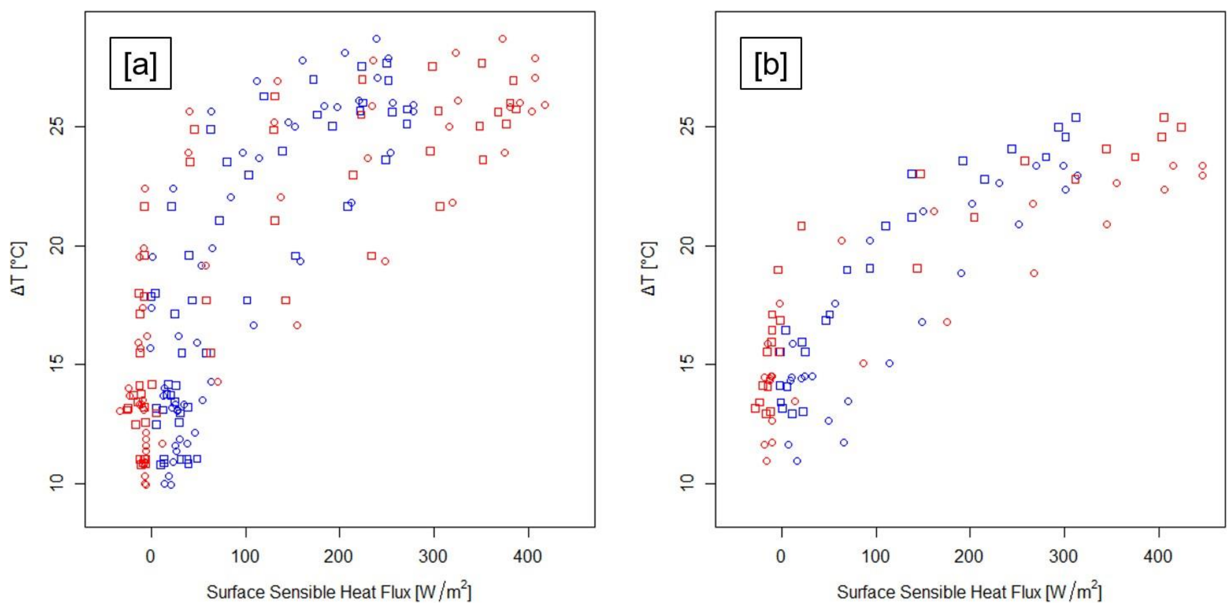

Figure 6.17: Relationship of modeled surface sensible heat flux versus land-sea temperature difference at YVR (blue) and YXX (red) for the CTRL (circles) and PGW (squares) simulations on: [a] days 1 and 2, and [b] day 3 of the July 2009 heatwave.

6.4.3 Planetary Boundary Layer Height

Planetary boundary layer height (PBLH) is sensitive to diurnal cycle and day-time heating. Mixing depth increases during the day causing PBLH height to increase in response, while the opposite occurs at night. However, PBLH is also affected by land-sea thermal differences – with lower height over the ocean due to less heating and increased stability. Since the mesoscale coastal ridge forms under a stable, stratified airmass, the associated coastal southerlies advect such boundary layer air northwards towards the region (Mass and Albright, 1987). Fig. 6.18 shows simulated PBLH during mid-afternoon on all 3 days of the heatwave in the CTRL and PGW simulations. In both simulations PBHLs are generally lower on day 3 over the region due to the advection of the lower marine boundary layer by the coastal southerlies. The lower boundary level heights prevent thermal venting of upslope flows and mountain updrafts which often occur in the region - and are apparent on days 1 and 2. This may contribute to re-circulation of pollutants down towards the surface.

Changes in PBLH on day 2 in the PGW simulation best show the contrasting effect of increasing large scale offshore flow in the region between YVR and YXX. The stronger Georgia Strait flows cause reductions in PBLH at YVR and adjacent regions, while a stronger eastwards component in winds shields regions like YXX and the North Coast Mountains from marine effects and causes a deepening of PBLHs there. On day 3, the stronger southerlies in the PGW simulation result in decreases of PBLH over most of the region - with largest decreases over the mountains. This occurs in spite of increases in surface sensible heat flux (and its contribution to low-level heating) through the course of the heatwave and also between the CTRL and PGW simulations.

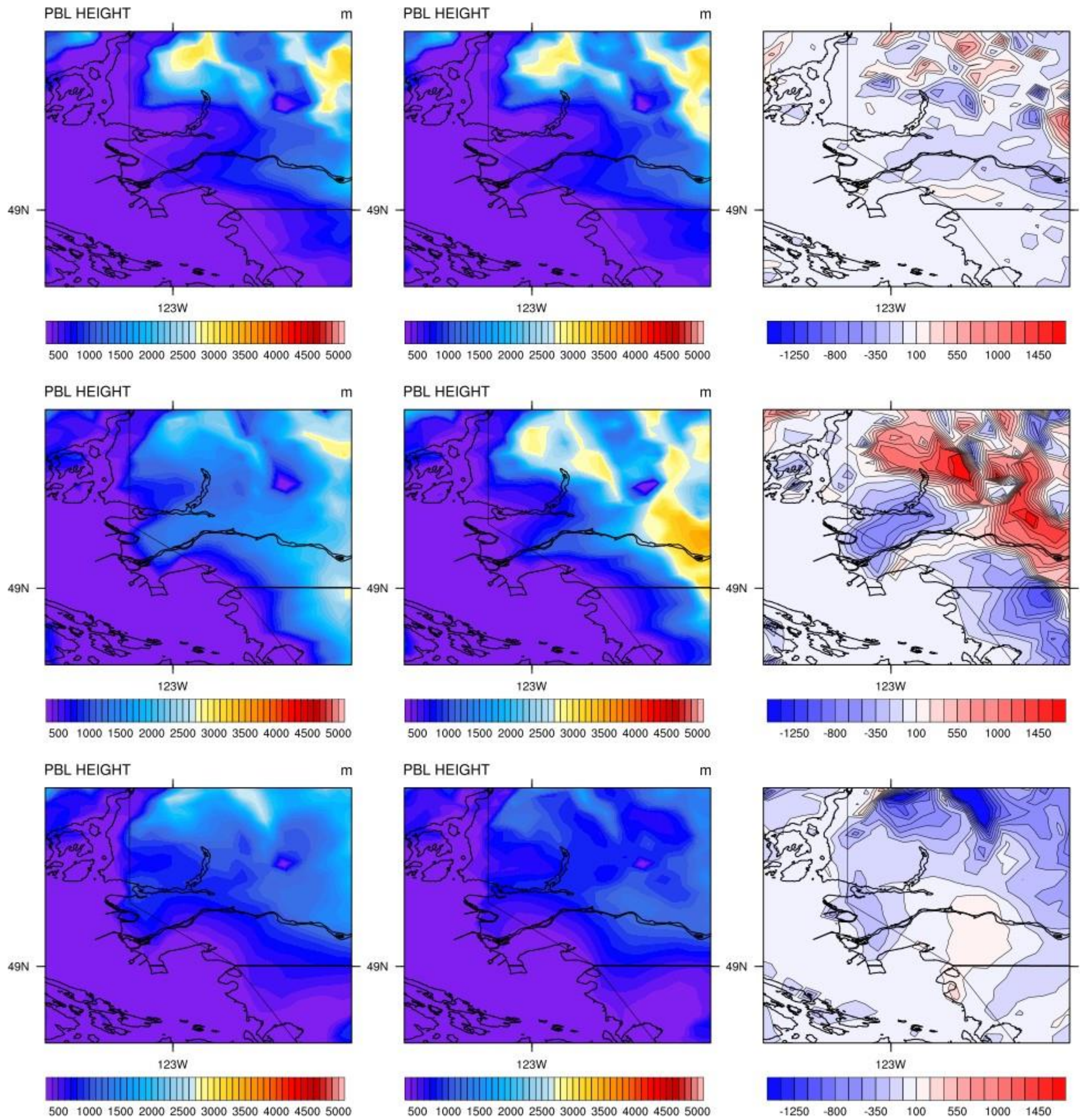

Figure 6.18: Simulated PBLH (m) over the region in the CTRL (left column), and PGW (middle column) simulations, and PGW - CTRL (right column) for: day 1 (top row), day 2 (middle row), and day 3 (bottom row) during the July 2009 heatwave.

6.4.4 Conclusions

A verification of WRF simulated parameters related to heat and moisture during the July 2009 heatwave was carried out for YVR and YXX as was an analysis of changes between the CTRL and PGW simulations for those locations. Additionally, mesoscale circulations and forcing mechanisms on such processes were examined to gain insight on possible driving factors and changes in the PGW simulation.

WRF underestimated the strength of Georgia Strait flows affecting YVR and other regions on days 1 and 2 of the heatwave causing over-estimation of temperature. Additionally, sensitivity to both error and changes in u-component flow were shown to be related to v-component flow intensity at the two locations. The high resolution of the WRF output provides insight into how flow deflection of positive v-component winds affects the position of the sea-breeze and can produce differential effects across the area. Further, it is modulation from the WCTT and mesoscale ridge which affects sea-breeze position and movement more than purely thermally driven processes like sensible heat flux. For this reason, typical relations between sensible heat flux and land-sea temperature difference did not hold in the simulation of this event. Mountain-valley circulations were shown to be sensitive to PBLH which were highest on day 2 and lowest on day 3 which in turn also reflect the arrival of the coastal southerlies.

The changes in mesoscale circulation patterns seen in the PGW simulation during the event were dominated by an intensified WCTT - which generated stronger general offshore flow initially (and stronger Georgia Strait flows), and then more intense coastal southerlies after the WCTT passed. A comparison of climatologies for u-component flow in the low levels of the atmosphere indicated that the mean monthly perturbations in u-component flow from the CMIP5 2071-2100 simulations did not likely contribute to changes in the WCTT (although some terrain effects were noted in changes to the geopotential height fields at the same levels). A more precise approach would be to re-run the PGW simulation for an integration period only enough to span the heatwave event, but to alter the boundary conditions at a 6-hourly or 24 h intervals based on a cumulative distribution function transfer method (see Section 4.2). Since heatwave events in the region are characterized by extreme offshore flows (left tail of the u-component wind distribution) - mapping changes in the variable distributions from the CMIP5 base period to the 2017-2100 simulation would allow for alterations in those parts of the distribution to be applied to the initial and lateral boundary conditions of the WRF simulation. This would be more insightful towards understanding changes in the PGW simulation than applying differences in measures of central tendency.

Reasons for the intensification of the WCTT require further study by examining individual components contributing to temperature change – in particular contributions from vertical advection or down-sloping. This would also provide more insight into any thermodynamic or terrain feedback issues.

REFERENCES

BGC Engineering Inc. (2006). *Landslide Risk Management for Berkely-Riverside Escarpment.*

Brewer, M.C. and C. F. Mass (2016). Projected changes in western U.S. large-scale summer synoptic circulations and variability in CMIP5 models. *J. Climate,* 29, 5965-5978.

_____, B.E. Potter. (2012). The West Coast thermal trough: climatology and synoptic evolution. *Mon. Weather Rev.,* 140, 3820-3843.

_____, B.E. Potter. (2013). The West Coast thermal trough: mesoscale evolution and sensitivity to terrain and surface fluxes. *Mon. Weather Rev.,* 141, 2869-2896.

Bumbaco, K.A., K.D. Dello, N.A. Bond. (2013). History of Pacific Northwest heat waves: synoptic pattern and trends. *J. Appl. Meteor. Clim.,* 52, 1618-1631.

Gutmann, E., R. M. Rasmussen, C. Liu, K. Ikeda, D. J. Gochis, M. Clark, J. Dudhia, and G. Thompson (2012). A comparison of statistical and dynamical downscaling of winter precipitation over complex terrain. *J. Climate*, 25, 262-281, doi:10.1175/2011JCLI4109.1.

Hara, M., T. Yoshikane, H. Kawase, F. Kimura (2008). Estimation of the Impact of Global Warming on Snow Depth in Japan by the Pseudo-Global-Warming Method. *Hydrol. Res. Lett.,* 2, 61-64.

Henderson S.B., and T. Kosatsky. (2012). A data-driven approach to setting trigger temperatures for heat health emergencies. *C.J. Public Health*, 103(3), 227-230.

Hill, K. A., and G. M. Lackmann (2011). The impact of future climate change on TC intensity and structure. *J. Climate*, 24, 4644–4661.

Kawase, H., M. Hara, T. Yoshikane, N. N. Ishizaki, F. Uno, H. Hatsushika, and F. Kimura (2013). Altitude dependency of future snow cover changes over Central Japan evaluated by a regional climate model, *J. Geophys. Res.-Atmos.*, 118, 12,444–12, 457, doi:10.1002/2013JD020429.

Kimura F, and A. Kitoh (2007). Downscaling by pseudo global warming method. *The final report of the ICCAP*. Research Institute for Humanity and Nature (RIHN), Kyoto, Japan.

Kosatsky, T., S.B. Henderson, S.L. Pollock. (2012). Shifts in mortality during a hot weather event in Vancouver, British Columbia: rapid assessment with case-only analysis. *Am. J. Public Health,* 102, 2367-2371.

Kuglitsch, F.G. et al. (2010). Heat wave changes in the eastern Mediterranean since 1960. *Geophys. Res. Lett,* 37, L04802, doi:10.1029/2009GL041841.

Lange, O. (1999). *The wind came all ways: a quest to understand the winds, waves and weather in the Georgia Basin.* Environment Canada.

Liu, C., and co-authors. (2017). Continental-scale convection-permitting modeling of the current and future climate of North America. C*limate Dyn.*, 49, 71-95.

Mallard, M.S., G.M. Lackmann, A. Aiyyer. (2013). Hurricanes and climate change. Part I: experimental design and isolation of thermodynamic effects. *J. Climate*, 26, 4876-4893.

Mass, C.F. and M.D. Albright (1987). Coastal southerlies and alongshore surges of the West Coast of North America: evidence of mesoscale topographically trapped response to synoptic forcing. *Mon. Weather Rev.*, 115, 1707-1738.

Masterson, J.M., and F.A. Richardson. (1979). *Humidex: a method of quantifying human discomfort due to excessive heat and humidity.* Gatineau, Quebec: Environment Canada.

Mesinger, F., and co-authors (2006). North American regional reanalysis. *B. Am. Meteorol. Soc.*, 87(3), 343.

Mekis, E., L.A. Vincent, M.W. Shephard, X. Zhang (2015). Observed Trends in Severe Weather Conditions Based on Humidex, Wind Chill, and Heavy Rainfall Events in Canada for 1953–2012. *Atmos.-Ocean*, 53(4), 383-397.

Oke, T.R. and J.E. Hay. (1994). *The Climate of Vancouver.* Vancouver, British Columbia: University of British Columbia Press.

_____, and G.B. Maxwell (1975). Urban heat island dynamics in Montreal and Vancouver. *Atmos. Environ.*, 9, 191-200.

Porson, A., D.G. Steyn, G. Schayes (2007). Sea-breeze scaling from numerical model simulations. *Boundary-Layer Meteorol.*, 122:17–29.

Pottier, J.L., S.C. Pryor, R.M. Banta (1997). Synoptic variability related to boundary layer and surface features observed during Pacific ’93. *Atmos. Environ.*, 31(14), 2163-2173.

Rahmstorf, S., and D. Coumou (2011). Increase of extreme events in a warming world. *Proceedings of the National Academy of Sciences of the United States of America,* 10.1073/pnas.1101766108.

Rasmussen, R. M., and co-authors (2011). High resolution coupled climate-runoff simulations of seasonal snowfall over Colorado: A process study of current and warmer climate. *J. Climate*, 24, 3015-3048, doi:10.1175/2010JCLI3985.1.

Reuten, C., D.G. Steyn, K.B. Strawbridge, P. Bovis. (2005). Observations of the relation between upslope flows and the convective boundary layer in steep terrain. *Boundary-Layer Meteorol.*, 116, 37-61.

Sato, T., F. Kimura, A. Kitoh (2007). Projection of global warming onto regional precipitation over Mongolia using a regional climate model. *J. Hydrol.*, 333(1), 144-154.

Schär, C., C. Frei, D. Luthi, H.C. Davies (1996). Surrogate climate-change scenarios for regional climate models. *Geophys. Res. Lett.*, 23(6), 669-672.

Skamarock, W. C., J.B. Klemp, J. Dudhia, D.O. Gill, D.M. Barker, M.G. Duda, X.Y. Huang, W. Wang, J.G. Powers. (2008). A description of the Advanced Research WRF version 3. NCAR Tech. Note NCAR/TN-4751STR, 113 pp.

Stewart, R.E., D. Betancourt, J.B. Davies, D. Harford, E. Joakim, Y. Klein, R. Lannigan, L. Mortsch, K. Tang and P.H. Whitfield, 2017: A multi-perspective examination of heat waves affecting Metro Vancouver: Now into the future. *Nat. Hazards*. DOI: 10.1007/s11069-017-2793-7.

Steyn, D.G., and D.A. Faulkner. (1986). The climatology of sea-breezes in the Lower Fraser Valley, B.C. *Climatol. Bull.*, 20, 21-39.

Thompson, G., P. R. Field, R. M. Rasmussen, W. D. Hall (2008). Explicit forecasts of winter precipitation using an improved bulk microphysics scheme. Part II: Implementation of a new snow parameterization. *Mon. Wea. Rev.*, 136, 5095–5115.

Wichink Kruit, R.J., A.A.M. Holtslag, A.B.C. Tijm. (2004). Scaling of the sea-breeze strength with observations in the Netherlands. *Boundary-Layer Meteorol.*, 112, 369-380.

CHAPTER 7: SUMMARY AND CONCLUDING REMARKS

7.1 Thesis Summary

This thesis has provided insight into the synoptic and mesoscale processes modulating meteorological extremes in the Vancouver, British Columbia region which have been shown by quantitative methods to pose risk to the local population. Due to the diverse physiography of the area, such hazards can occur throughout the annual cycle with hydrometeorological events being important in winter, and heatwaves dominating in summer. However, given the considerable risk posed by heatwaves (Henderson and Kosatsky, 2012) compared to the other hazards – much of the focus of the thesis was on such events.

Chapter 4 explored the driving processes and trends in occurrence of landslides and windthrow in association with heavy antecedent precipitation, and of summer-time heatwaves. Selection criteria for landslides events was based on BGC Engineering (2006) and took into account both 24 h and 28 d antecedent precipitation, whereas for windthrow events they were based on maximum hourly wind gust ≥ 90 km/h (following the Beaufort Windscale) and 90th percentile 28 d antecedent precipitation. Criteria for heatwaves were based on Kosatsky et al. (2012) and these were lower for YVR compared with YXX due to greater oceanic influence at the former station.

Distributions of PC coefficients derived from EOF analysis for summer and winter were used to assess processes important to the different types of events. Key differences in PC distributions for 2 EOFs suggest that multiday heatwave events represent a distinct process from single day occurrences. Multiday events are associated with the surface EOF representing the classic WCTT and ridge configuration, and with the 500 hPa GPH EOF depicting a complex blocking structure characterized by an upper low off of the California coast. Such an upper pattern impedes the westward shift of the upper ridge and associated surface features allowing for a full expression of the temporally varying mesoscale processes. The upper low may also play a role in facilitating the coastal southerlies – with negative feedback on the offshore flow mechanism associated with heatwaves, but helping to produce local offshore flows at YVR. Several EOFs also show temporal sensitivity in their PC distributions for multiday events and represent some of these evolving mesoscale circulations.

Landslide events are associated with winter-time EOFs and teleconnection indices having a strong Aleutian Low - consistent with previous studies examining heavy precipitation over the region. However, there were key differences in these parameters between windthrow events with antecedent 28 d precipitation above the 90^{th} percentile and those not above this threshold. Those without heavy antecedent precipitation were driven largely by positive pressure anomalies (both aloft and at the surface) over the North Pacific basin, whereas those with heavy antecedent precipitation were related to positive pressure anomalies shifted further east over British Columbia and did not appear to show linkage with the subtropics and MJO. The latter events therefore likely represent a unique process.

None of the trends in extreme hydrometeorological events were significant but increases in the occurrence of landslide events were nearly statistically significant and were explainable by northwards shifting and increasing moisture sources in the Pacific basin related to NPO/NPGO coupling. Increases in all of the major Atmosphere-Ocean indices over the Pacific explained the nearly statistically significant decrease in purely wind events, and stable trends in windthrow events with heavy antecedent precipitation.

Chapter 5 examined spatial variability in heat-alert criteria temperatures between YVR and YXX specifically for heatwave events. Selection criteria for heatwave days followed Kosatsky et al. (2012) as in Chapter 4. Results from MCA were used to show that 36-38% of this spatial variability is explained by temporal processes during multiday events. In particular, 2 eigenvectors contributed greatly to this variability – both showing a high probability of exceeding heat-alert criteria on the first day at YXX, whereas YVR had a greater likelihood of exceedance on the last day for both.

Hourly composites of u,v and vector wind for days in which heat-alert criteria were exceeded at YXX but not YVR, were associated with stronger flows and implied higher pressure gradients than expected for events driven mainly by barotropic processes. Onshore flow off the Georgia Strait is enhanced at YVR and persists all day in such occurrences, whereas downslope, northeasterly flows (with implied adiabatic warming) dominate the composites for YXX. This suggests considerable dynamic forcing from mesoscale features like the WCTT - in particular, a strong offshore directed flow which manifests itself farther inland at YXX, but is deflected by topography through the Georgia Strait to produce onshore flows at YVR. Cross sections showed that both temperature and u-wind anomalies were attenuated near the surface over the Georgia Strait, while being present aloft. These strong flows likely inhibit the thermally-induced backing of winds associated with initiation of the afternoon sea-breeze - which slows down the arrival of this feature at YXX.

In instances when criteria are exceeded at YVR but not YXX, a more relaxed pressure gradient is inferred with considerable offshore flows at YVR. Specifically, the sea-breeze does not arrive at YVR until just before noon (later than for YXX) on such days; and a land-breeze re-establishes by early evening. After the WCTT moves east, the deflection of coastal southerlies causes offshore flows to persist longer at YVR, while accelerating the sea-breeze front towards YXX. It was also shown that local moisture sources and evapotranspiration contribute considerably to humidity levels during heatwaves over the region.

In Chapter 6, a focused approach was taken to study future conditions associated with heatwaves over the region using WRF-CTRL and WRF-PGW simulations for the July 2009 heatwave event. Model verification of simulated parameters pertaining to heat and moisture during the event showed that Georgia Strait flows were underestimated on the first 2 days which were related to temperature overestimation at YVR. Error in u-component flow was also shown to be sensitive to v-wind intensity. Dewpoint temperatures were considerably underestimated at both locations.

The high resolution of the WRF model output provided insight into how local winds are deflected – in particular how coastal southerlies can produce offshore flows at YVR. More generally, it demonstrated the importance of modulation from the WCTT and coastal southerlies on local sea-breeze circulation rather than from purely thermal processes (like sensible heat flux). Simulated mountain-valley circulations were shown to be sensitive to PBLH which were highest on day 2 and lowest on day 3 due to the arrival of the coastal southerlies and stable, marine influenced air-mass.

Bias corrected output from the PGW simulation for YVR and YXX showed large increases in combined heat and moisture which would lead to considerably more heat stress on local populations. A general intensification of flow circulation occurred over the region in the PGW simulation driven by a stronger WCTT (and pressure gradient between the WCTT and mesoscale ridge). This in turn caused a stronger offshore flow initially and then more intense coastal southerlies as the WCTT shifted farther east. Mean monthly climate perturbations applied to the WRF model in the PGW simulation did not appear to have affected changes in the WCTT – although some terrain induced effects are possible.

7.2 Novel Contributions and Limitations

Novel contributions in this thesis to the advancement of knowledge of synoptic and mesoscale processes associated with meteorological extremes at Vancouver are listed below:

- Mechanisms associated with extreme wind events show sensitivity as to whether they are preceded by heavy antecedent precipitation or not. Previously, Abeysirigunawardena et al. (2009) related extreme wind in the region to negative phases of ENSO due to increased occurrence of synoptic systems during such periods; and with negative phases of the PDO. However in this study, events not preceded by heavy precipitation did not appear to be associated with negative phases of ENSO, but with a negative PNA, and with MJO propagation across the tropical Pacific and inferred subtropical linkage (negative NPO). Wind events constrained by heavy antecedent precipitation do not appear to be dependent on this linkage in the way that either extreme precipitation (Lackmann and Gyakum., 1999) or wind processes are. These events are associated with negative phases of ENSO and consistent with the idea of increased occurrence of synoptic systems proposed by Abeysirigunawardena et al. (2009). Antecedent precipitation relies on moisture advection from sources farther north than for extreme precipitation only. Roberge et al. (2009) has previously shown this mechanism ("west-type event") of moisture transport, but in this study, it is proposed to be related specifically to NPO and NPGO coupling. It also appears that this process is contributing more to extreme precipitation occurrences. However, these results are based on a very low sample size for wind events in particular, which reduces confidence.

- Heatwave duration over the region was shown to be sensitive to a mode of variability consisting of negative 500 hPa GPH anomalies off the California coast equatorward of positive anomalies over British Columbia. Previous studies have noted the importance of upper ridging during heatwaves, but not the negative GPH anomalies farther south. Thermodynamic-dynamic coupling as suggested by a spatially coherent pattern of trends in physical parameters are proposed to be associated with the inferred upper low off the California coast; and may be contributing to the statistically significant increases extreme values for the associated PC. The trends for physical parameters - while spatially consistent - are very small and have not been tested for statistical significance. This lowers confidence in the previously mentioned interpretation.

- Differences in coefficient distributions for several June-August EOFS representing key processes during heatwaves are used to demonstrate that these processes are temporally sensitive during the course of multi-day events.

- Previous studies have discussed this sequence of mesoscale processes that occur during periods of above normal temperatures in the region, however in this work - the amount of the spatial variability in occurrence of heat-alert criteria temperatures between YVR and YXX related specifically to these temporally sensitive processes is quantified (36-38%) using MCA. The associated features modulate onshore versus offshore flow intensity and timing at those locations during the evolution of multiday events.

- Previously, Bumbaco et al. (2013) had shown considerable moisture advection from lower latitudes during heatwave occurrences for the region. However, it is shown in this work that local sources of evapotranspiration also contribute considerably to elevated moisture levels in the area during heatwaves; and that these can linger for several days after heat-alert criteria are attained potentially prolonging heat stress.

- The high resolution CTRL and PGW WRF simulations of the July 2009 heatwave provide additional insight into temporally sensitivity mesoscale processes. Onshore versus offshore flows, PBLH, mountain-valley circulations were sensitive to dynamic forcing from the WCTT and coastal southerlies; and not to thermodynamic parameters such as sensible heat flux, or as normally would occur. Intensification of the WCTT in the PGW simulation caused an increase in Georgia Strait flows initially followed by an increase in the coastal southerlies. The reason for the intensification of the WCTT may in part be due to terrain effects and further study is required to determine its cause.

7.6 Future Work

The July 2009 heatwave was selected for study using PGW data due to its significant effects on the region. Time and resource limitations precluded the analysis of other key events such as the January 2005 multiday rainfall event and North Vancouver landslide, as well as the January 2006 Stanley Park windstorm. These additional extreme events and future impacts could be further studied using this high resolution model data and PGW scenarios as was done for the heatwave. However, the WRF model could be run at higher spatial resolution, and the climate perturbations applied to the initial and lateral boundary conditions could be derived at a higher temporal resolution using a percentile based approach (as suggested for further study of the heatwave event in Chapter 6).

Specific to the heatwave, further study as to the WCTT and associated offshore flow intensification in the PGW simulation could be conducted, along with an analysis of contributions to temperature advection from different terms in the thermodynamic equation

(Brewer et al., 2013). Similarly, contributions to flow in the horizontal momentum equation from the pressure gradient and Coriolis force could examined for any changes in the dynamics of coastal southerlies; and also for any change in their intensity and rate of propagation.

There also exist forecasting applications for the different hazards considered in this work. In terms of winter-time events, teleconnection indices could be monitored for particular patterns and combinations to establish pathways related to the occurrence of the different types of events. These could be used to enhance long range seasonal forecasts. For heatwaves, shorter term forecasting applications are possible. Specifically, a logistic regression model could be developed relating indices of standardized 700-925 hPa zonal wind anomalies (with a 1 day offset for a domain offshore of British Columbia and Washington state) and 1000 hPa meridional wind anomalies (along coastal region of California and Oregon) to the probability of exceedance of heat-alert temperatures at YVR. Critical values of the standardized anomalies for their respective domains could be derived and used within shorter term forecast data.

7.4 Concluding Remarks

This thesis highlights the complexity of interaction between mesoscale and synoptic processes in an area of varied physiography like the Vancouver, British Columbia region. Characterizing such interactions is key to understanding the mechanisms which generate extreme events and create physical risk for the local population. It is through such further study that future risk on local populations can continue to be assessed and mitigation strategies can be developed. This will be critical given the projected increases in future meteorological extremes in a diverse and densely populated area like the Vancouver, British Columbia region.

REFERENCES

Abeysirigunawardena, D.S., E. Gilleland, D. Bronaugh, P. Wong. (2009). Extreme wind regime responses to climate variability and change in the inner south coast of British Columbia, Canada. *Atmos.-Ocean*, 47(1), 41-62.

BGC Engineering Inc. (2006). *Landslide Risk Management for Berkely-Riverside Escarpment.*

Bumbaco, K.A., K.D. Dello, N.A. Bond. (2013). History of Pacific Northwest heat waves: synoptic pattern and trends. *J. Appl. Meteor. Clim.,* 52, 1618-1631.

Henderson S.B., and T. Kosatsky. (2012). A data-driven approach to setting trigger temperatures for heat health emergencies. *C.J. Public Health*, 103(3), 227-230.

Kosatsky, T., S.B. Henderson, S.L. Pollock. (2012). Shifts in mortality during a hot weather event in Vancouver, British Columbia: rapid assessment with case-only analysis. *Am. J. Public Health*, 102, 2367-2371.

Lackmann, G.M. and Gyakum, J.R. (1999). Heavy cold-season precipitation in the northwestern United States: Synoptic climatology and an analysis of the flood of 17–18 January 1986. *Weather Forecasting*, 14, 687–700.

Roberge, A., Gyakum, J.R., Atallah, E.H. (2009). Analysis of intense poleward water vapor transports into high latitudes of western North America. *Weather Forecasting*, 24, 1732-1747.

APPENDIX A: SUPPLEMENTAL FIGURES

This section contains supplemental figures for Chapter 4 including summer-time and winter-time EOFs, and trend analysis for counts of associated PC coefficient values greater than the 90th, 99th and 99.9th percentiles.

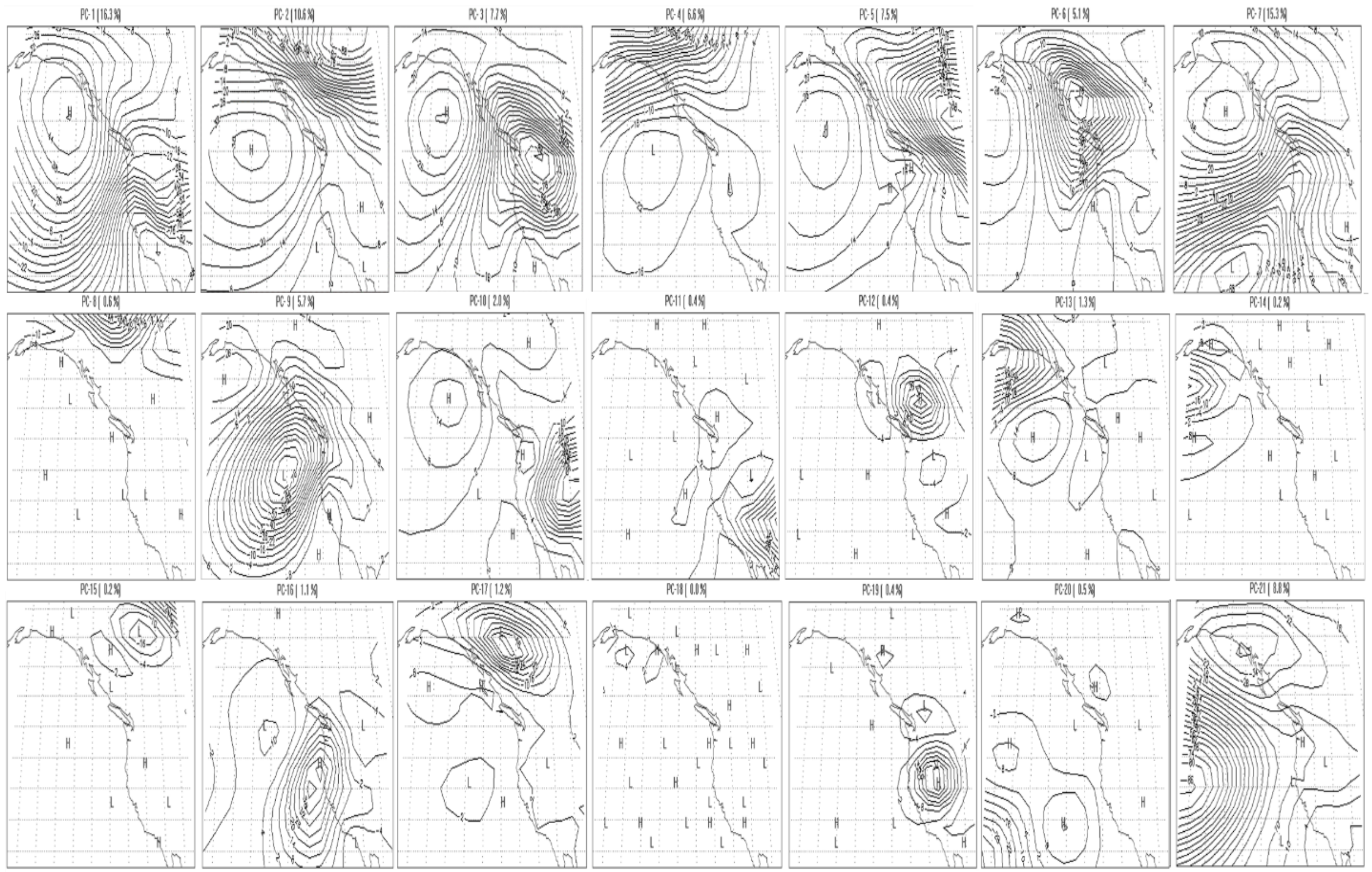

Figure A-1: June-August EOFs of SLP anomalies for the period 1950-2015 (hPa).

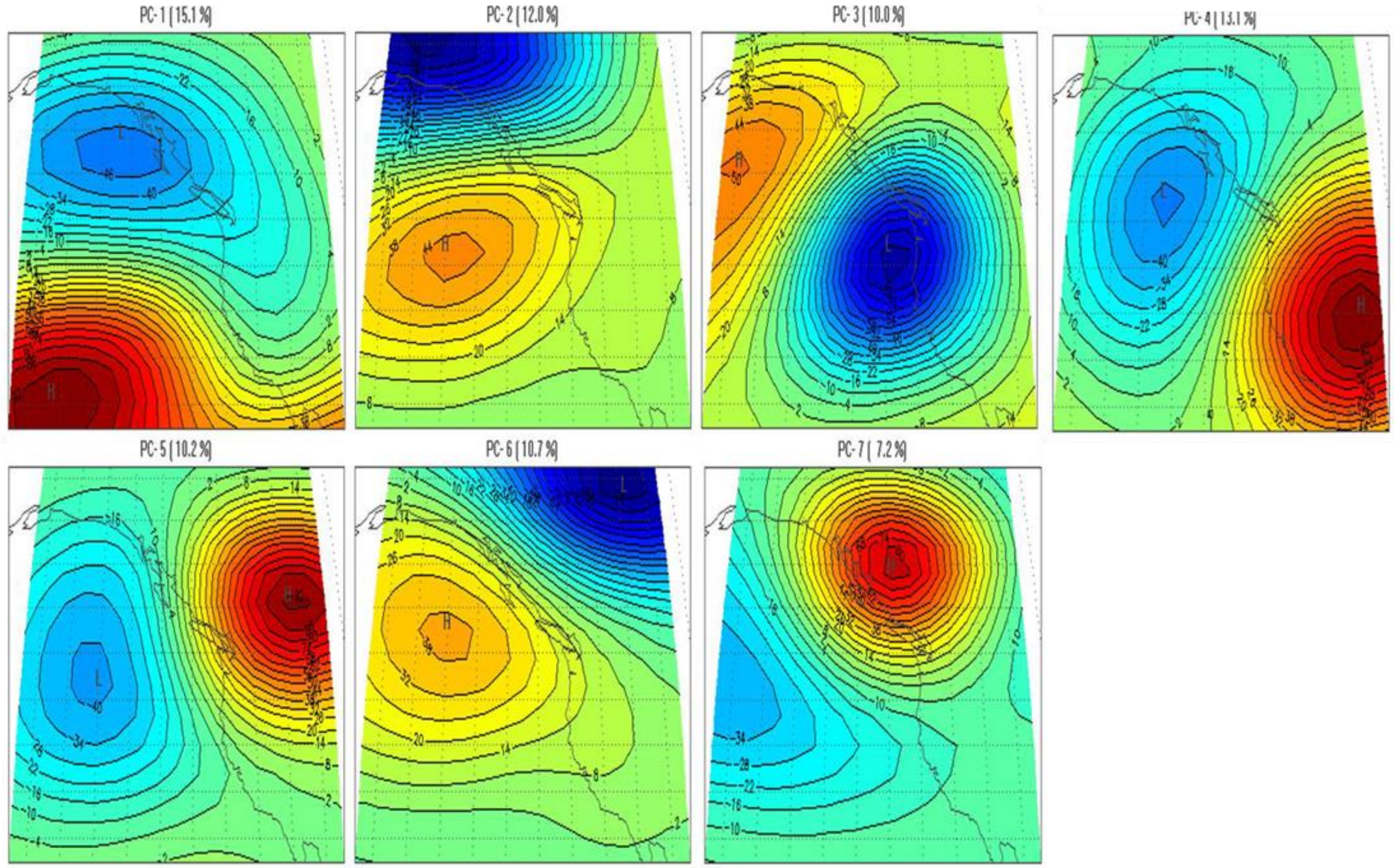

Figure A-2: June-August EOFs of 500 hPa geopotential height anomalies for the period 1950-2015 (hPa).

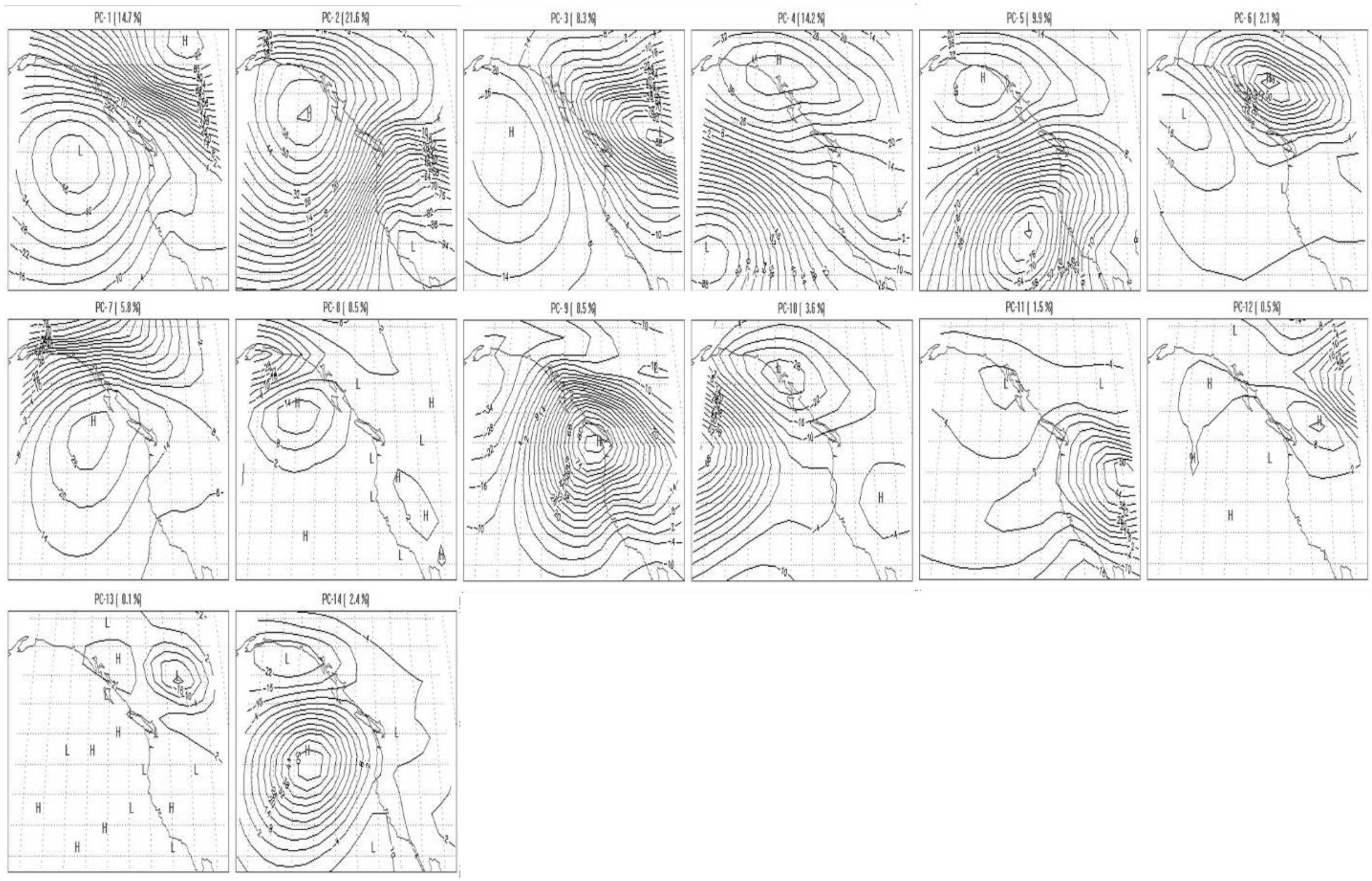

Figure A-3: October-April EOFs of SLP anomalies for the period 1950-2015 (hPa).

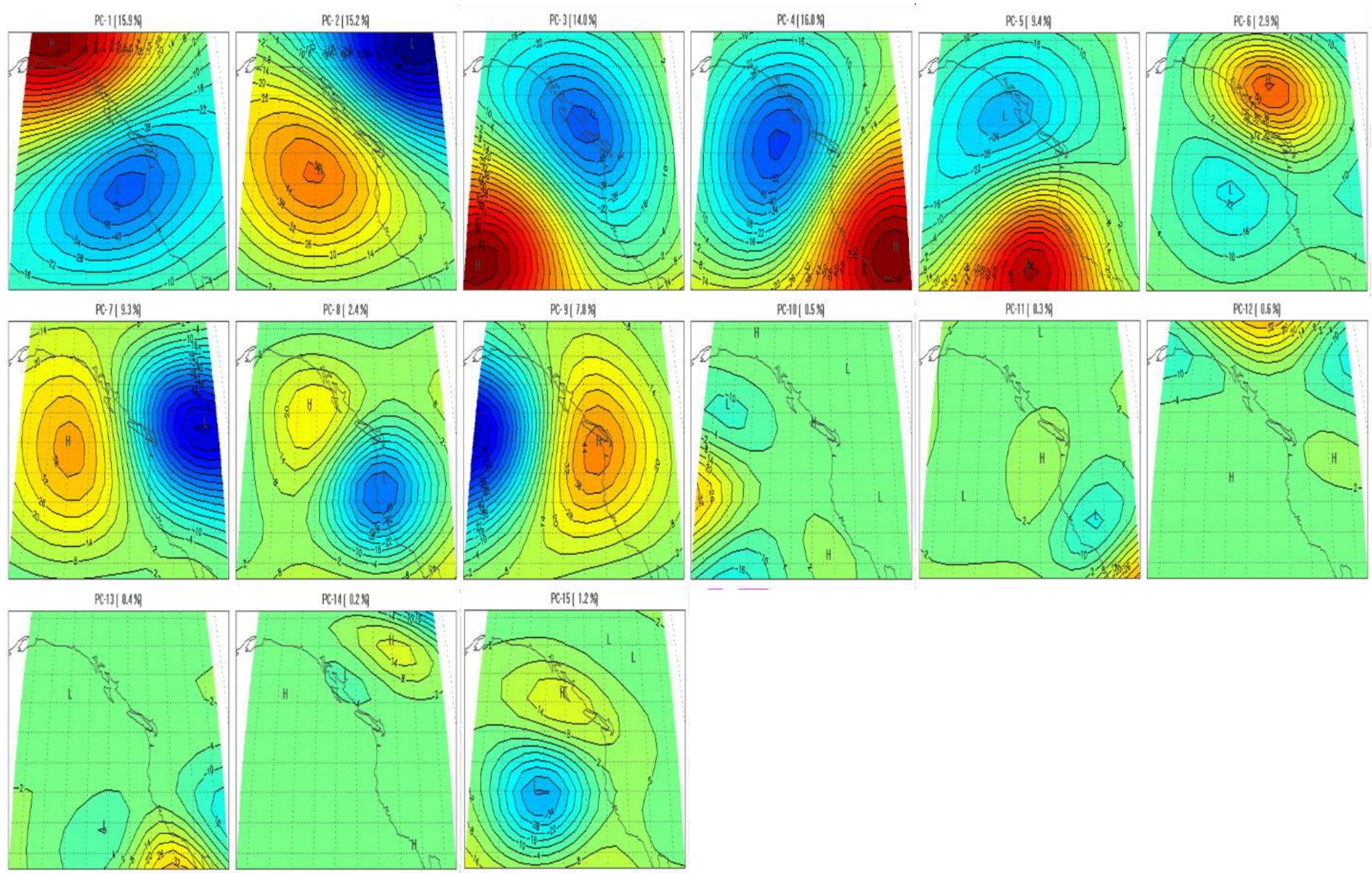

Figure A-4: October-April EOFs of 500 hPa geopotential height anomalies for the period 1950-2015 (hPa).

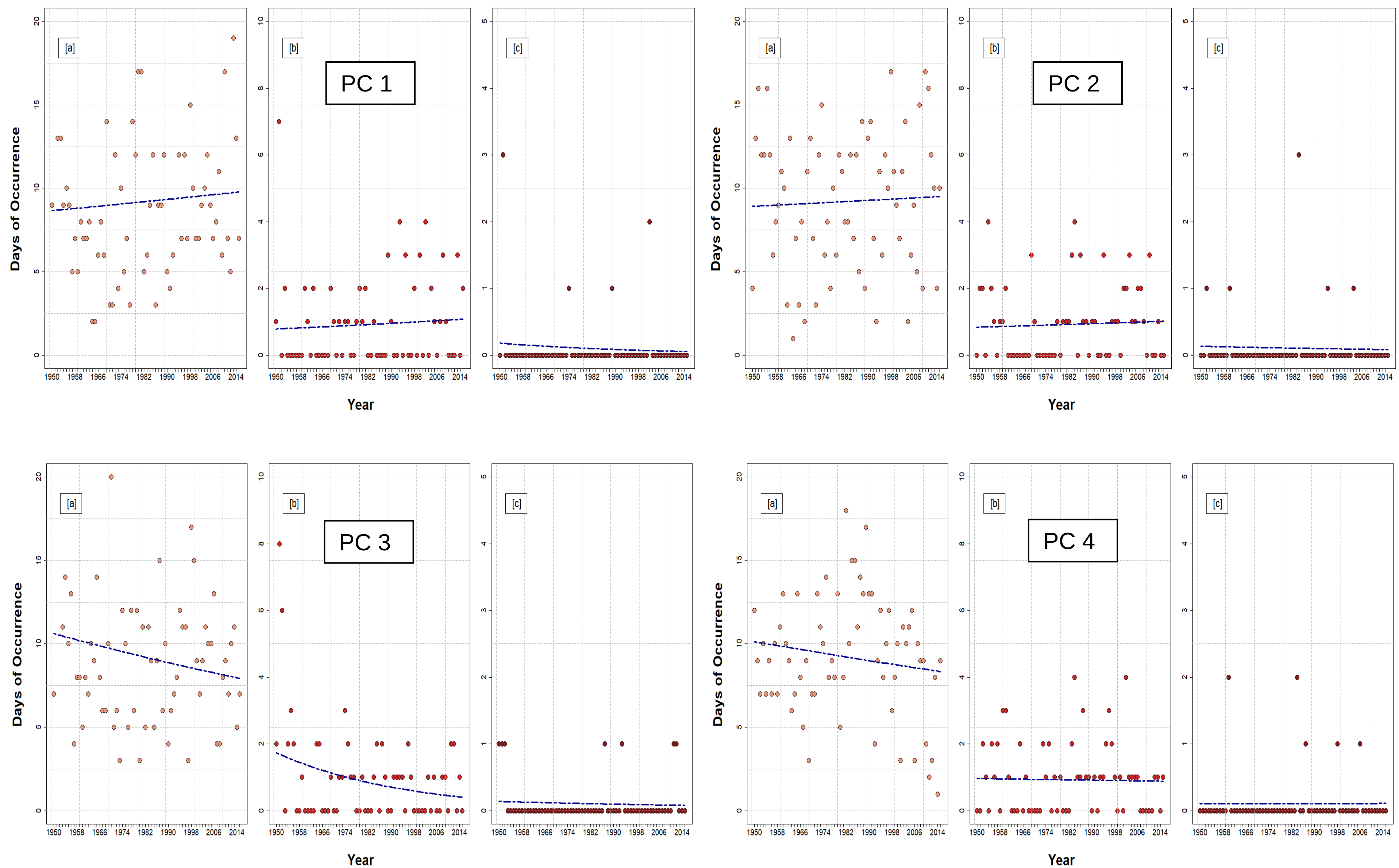

Fig A-12: Logistic trend analysis for counts of SLP PC coefficients greater than a) 90th, b)99th, and c) 99.9th percentile for June-August.

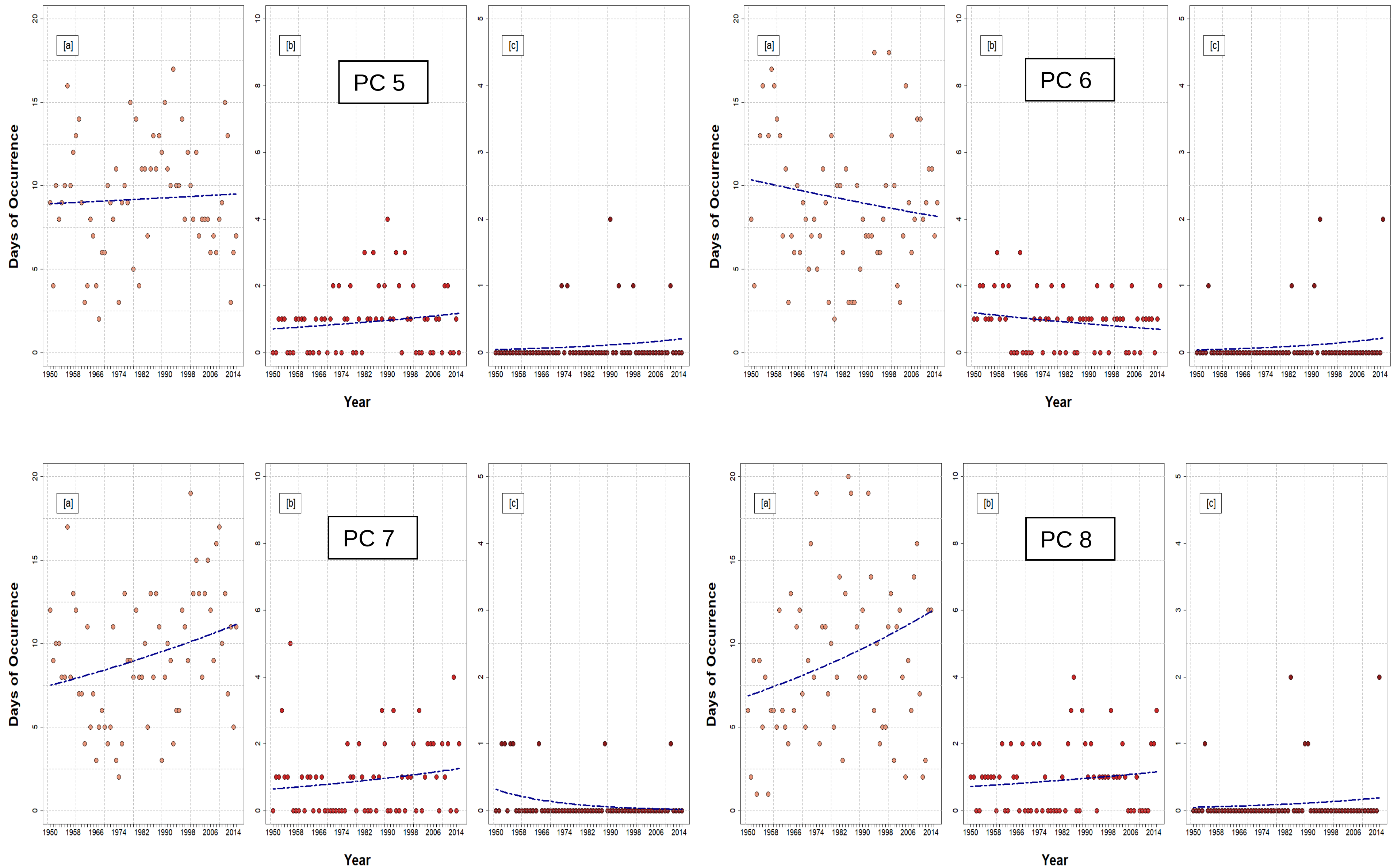

Fig A-6: Logistic trend analysis for counts of SLP PC coefficients greater than a) 90th, b)99th, and c) 99.9th percentile for June-August.

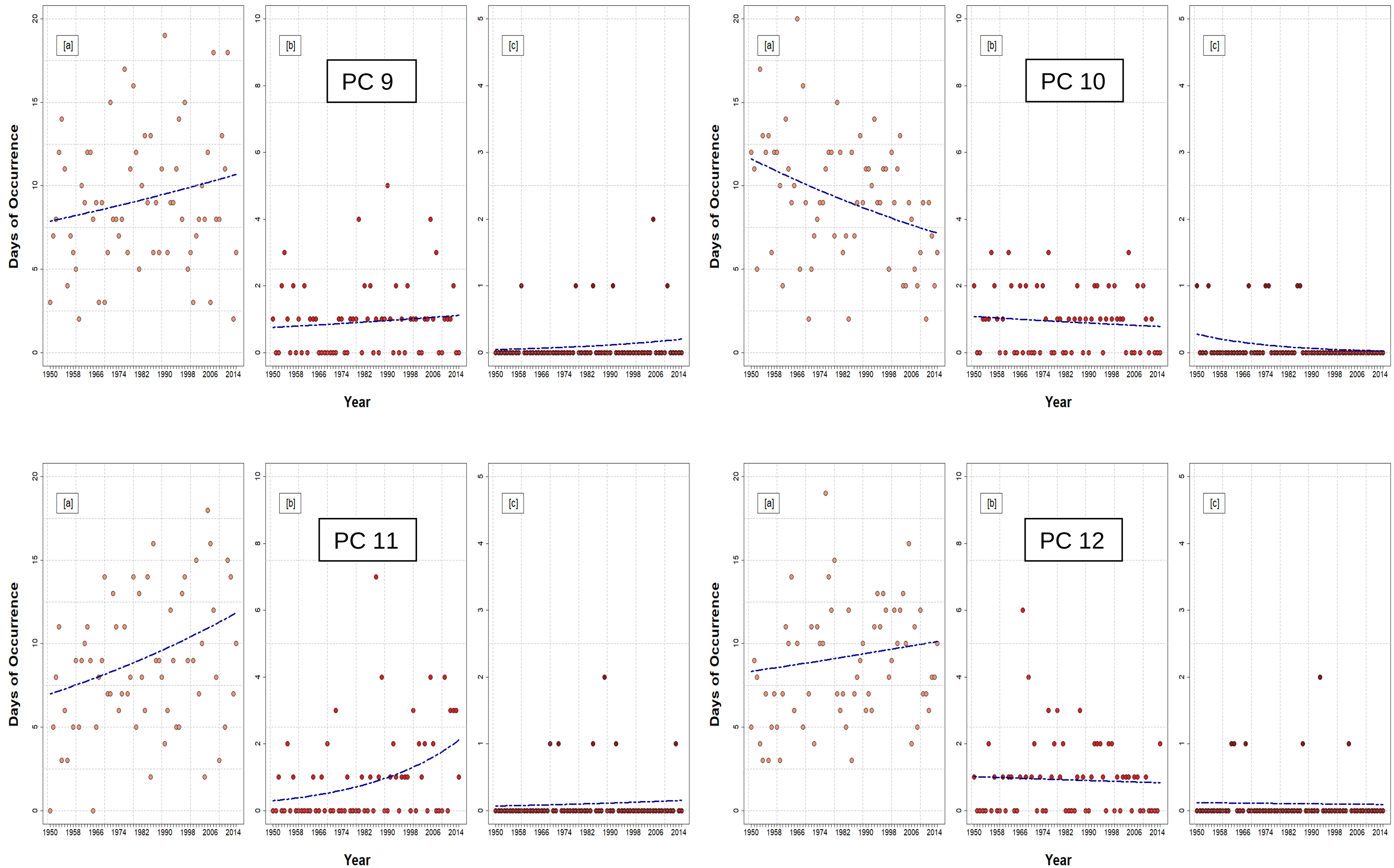

Fig A-7: Logistic trend analysis for counts of SLP PC coefficients greater than a) 90th, b)99th, and c) 99.9th percentile for June-August.

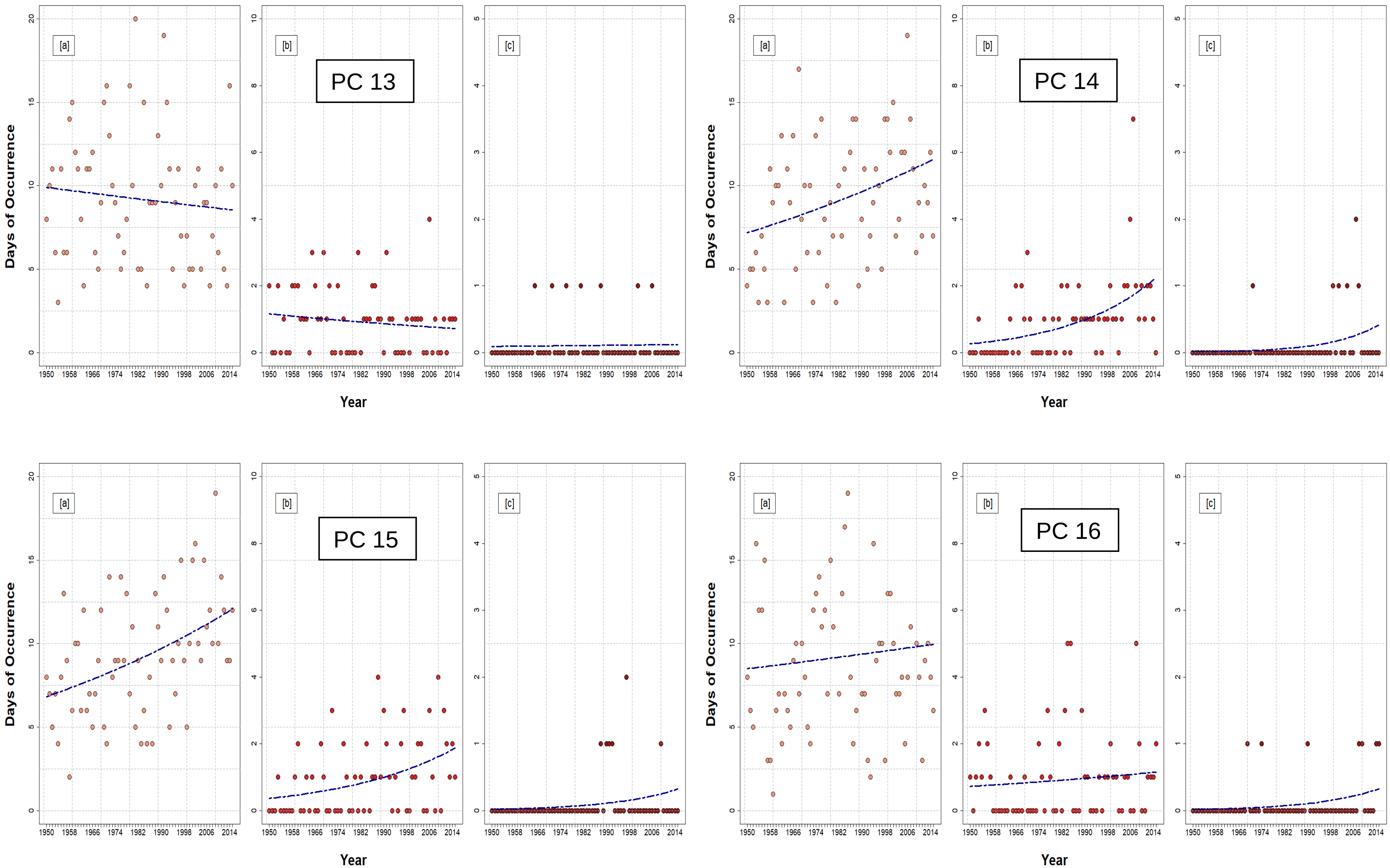

Fig A-8: Logistic trend analysis for counts of SLP PC coefficients greater than a) 90th, b)99th, and c) 99.9th percentile for June-August.

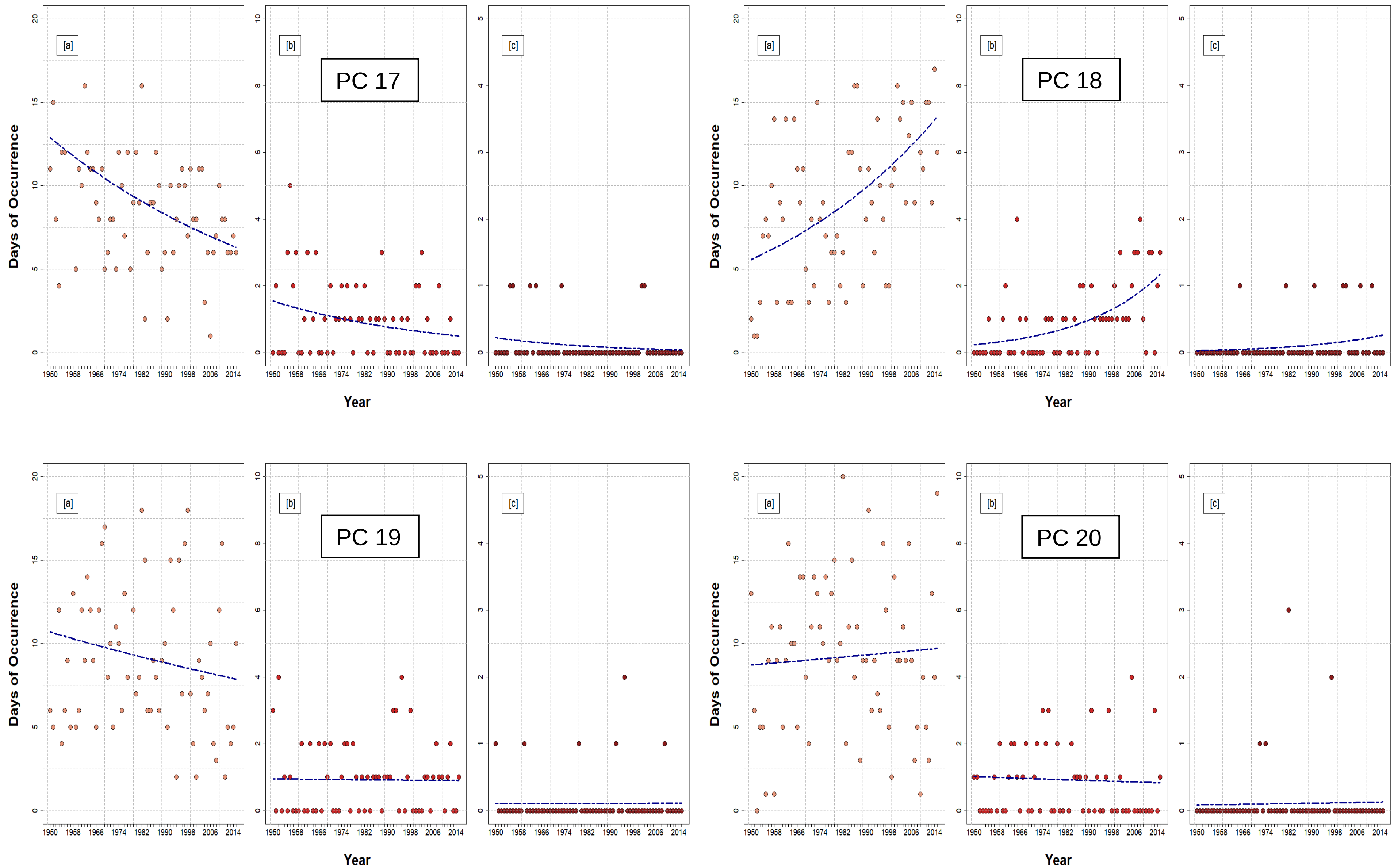

Fig A-9: Logistic trend analysis for counts of SLP PC coefficients greater than a) 90th, b)99th, and c) 99.9th percentile for June-August.

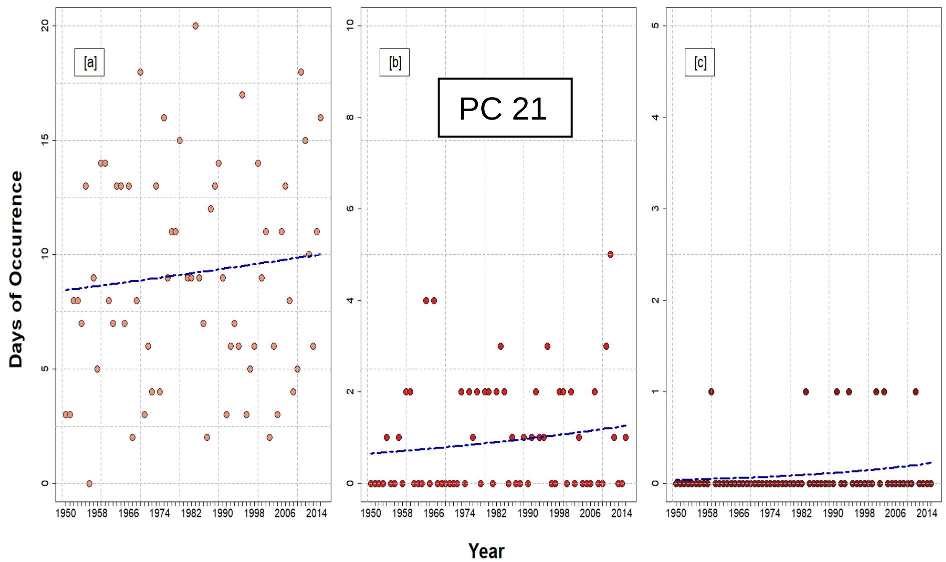

Fig A-10: Logistic trend analysis for counts of SLP PC coefficients greater than a) 90th, b)99th, and c) 99.9th percentile for June-August.

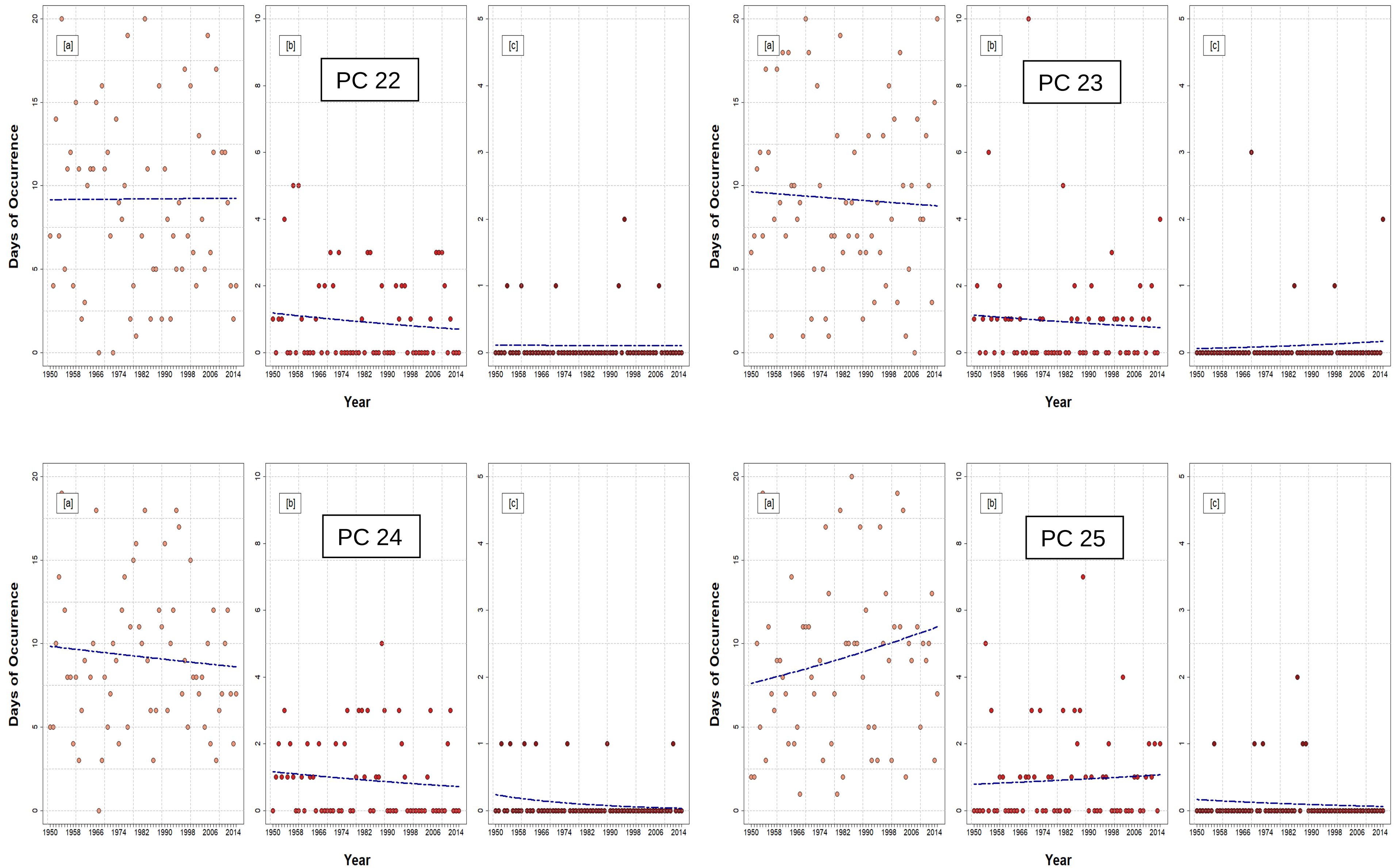

Fig A-11: Logistic trend analysis for counts of 500 geopotential height PC coefficients greater than a) 90th, b)99th, and c) 99.9th percentile for June-

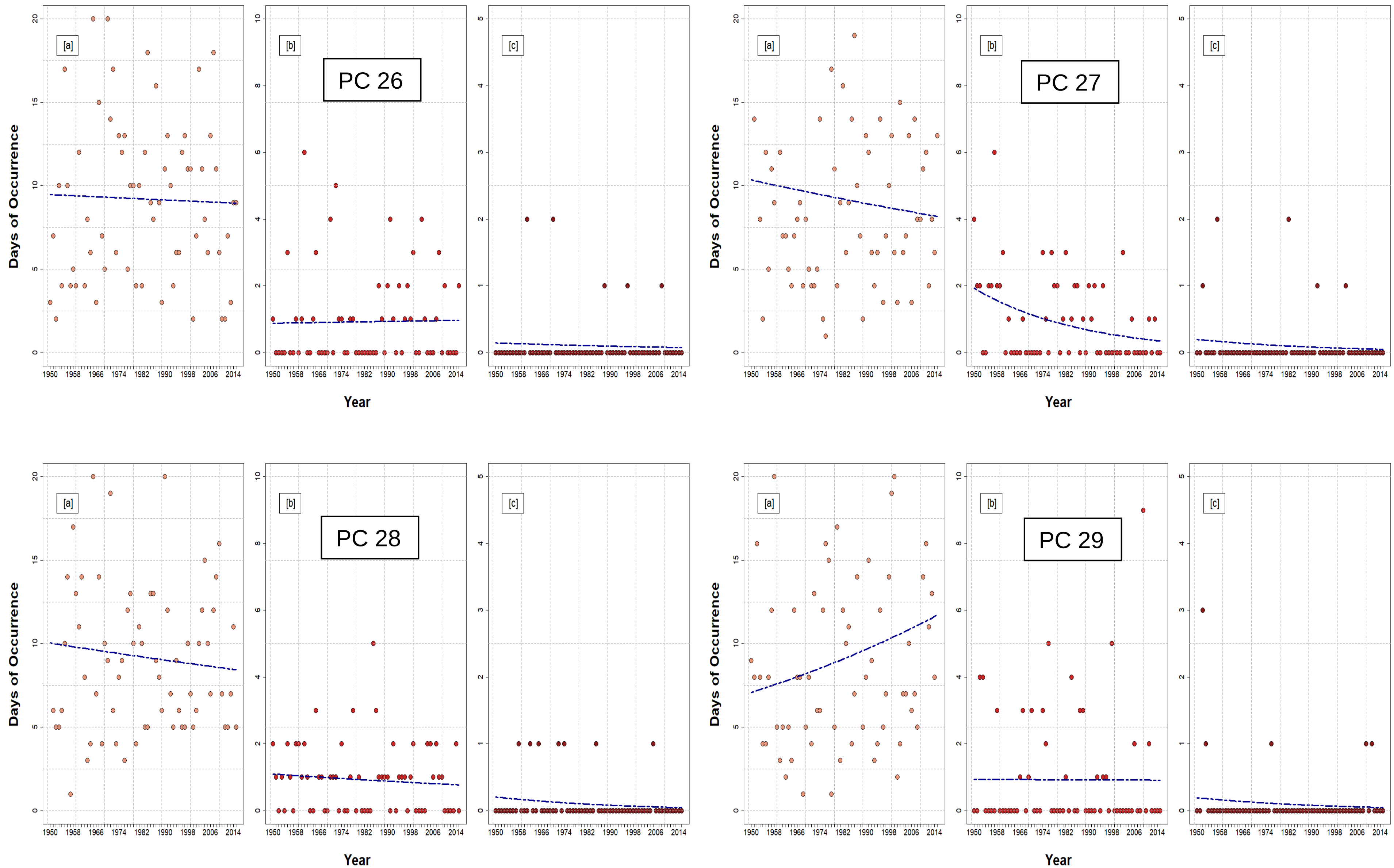

Fig A-12: Logistic trend analysis for counts of 500 geopotential height PC coefficients greater than a) 90th, b)99th, and c) 99.9th percentile for June-

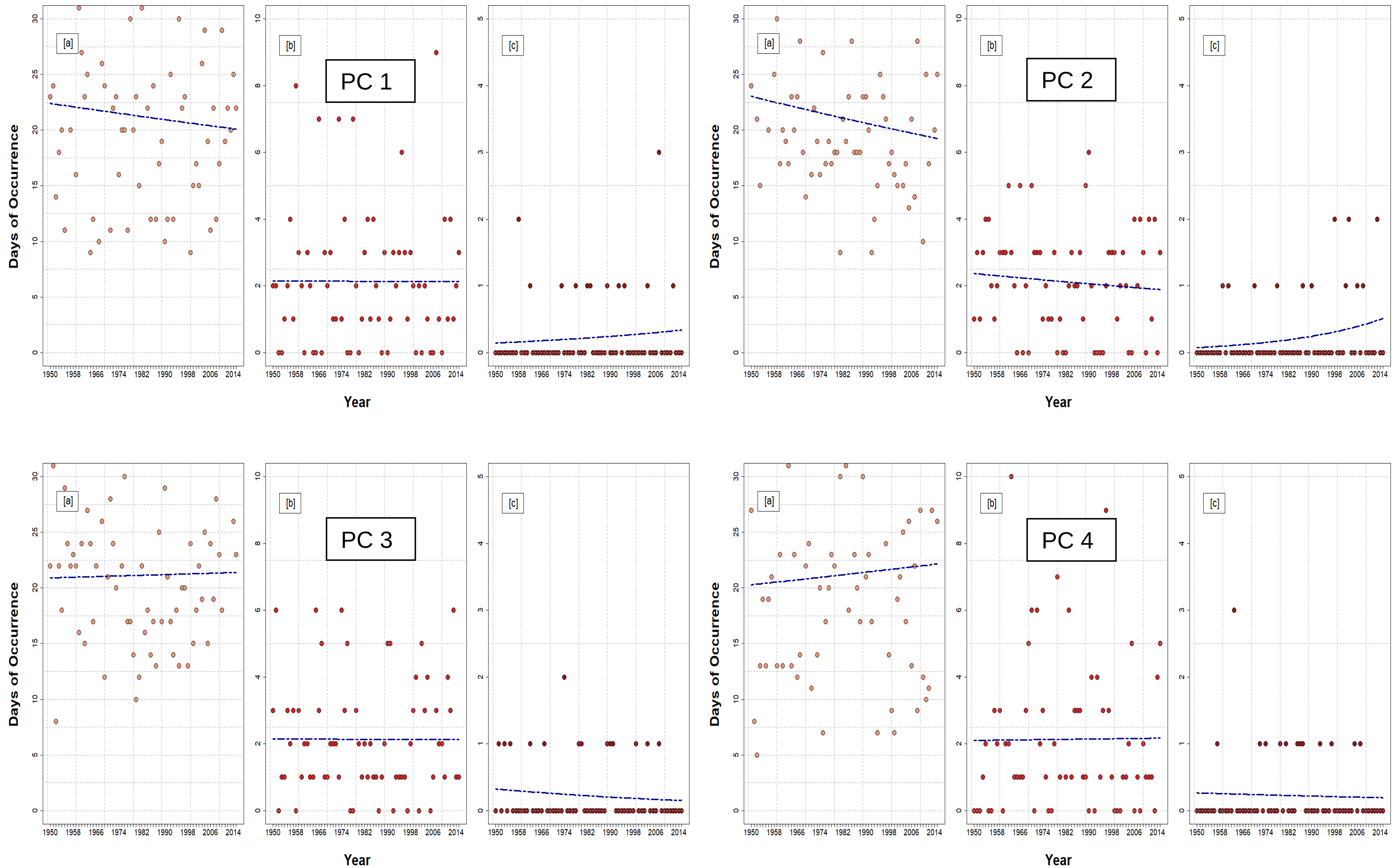

Fig A-13: Logistic trend analysis for counts of SLP PC coefficients greater than a) 90th, b)99th, and c) 99.9th percentile for October-April.

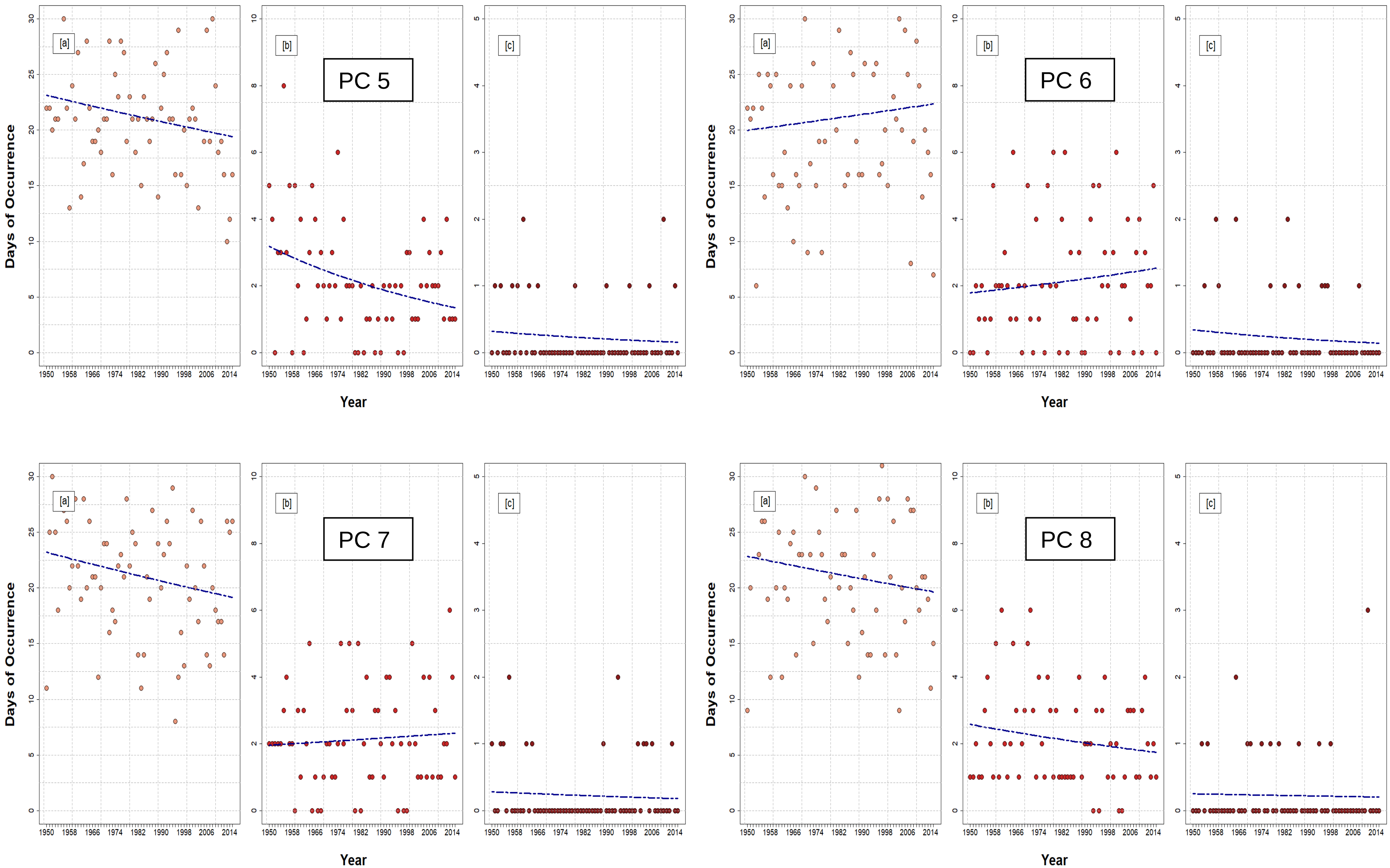

Fig A-14: Logistic trend analysis for counts of SLP PC coefficients greater than a) 90th, b)99th, and c) 99.9th percentile for October-April.

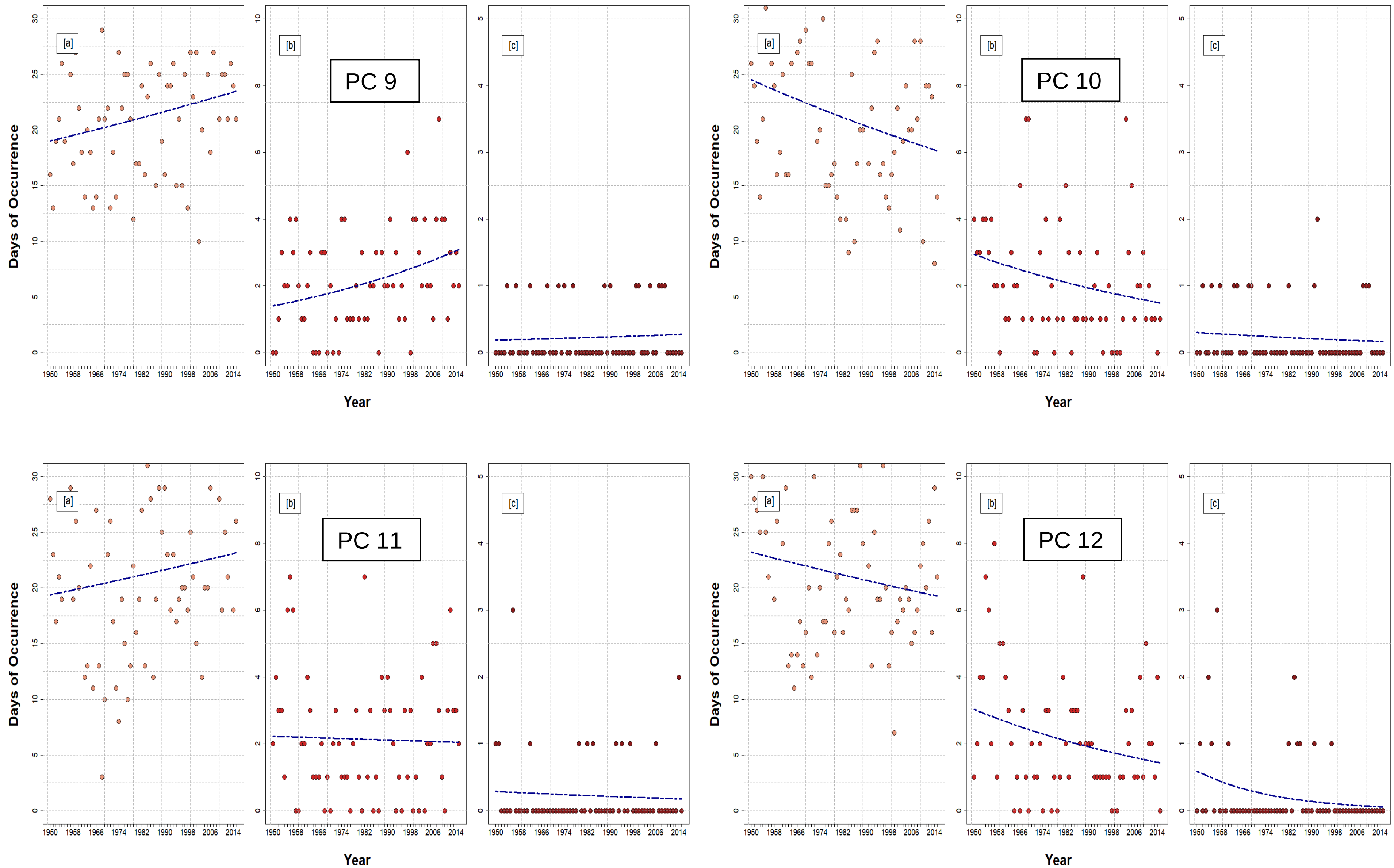

Fig A-15: Logistic trend analysis for counts of SLP PC coefficients greater than a) 90th, b)99th, and c) 99.9th percentile for October-April.

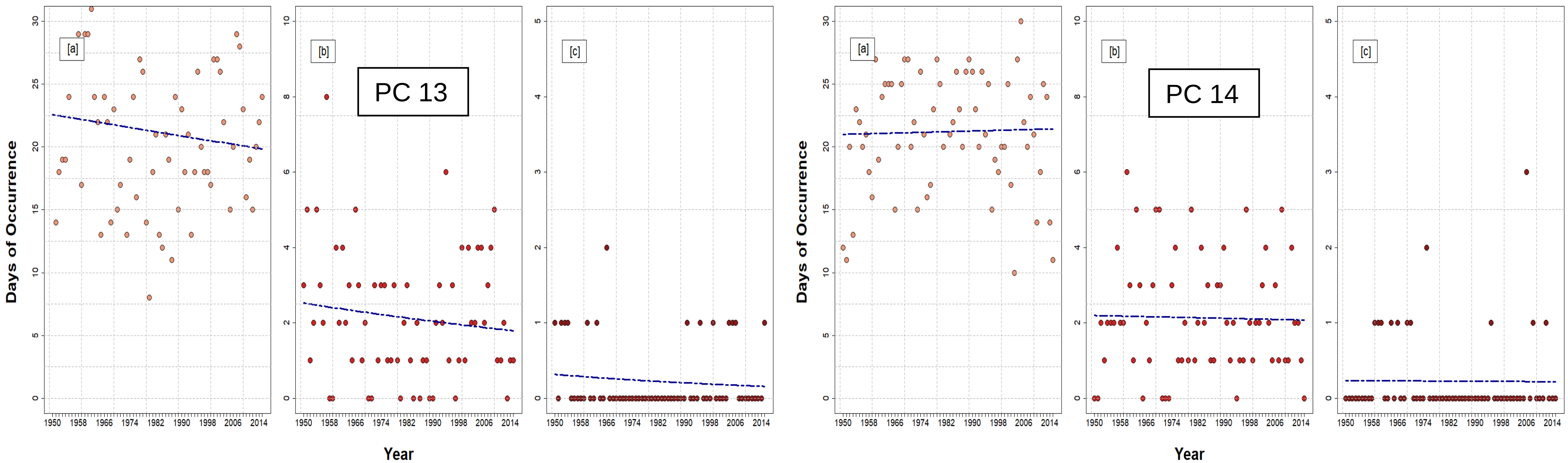

Fig A-16: Logistic trend analysis for counts of SLP PC coefficients greater than a) 90th, b)99th, and c) 99.9th percentile for October-April.

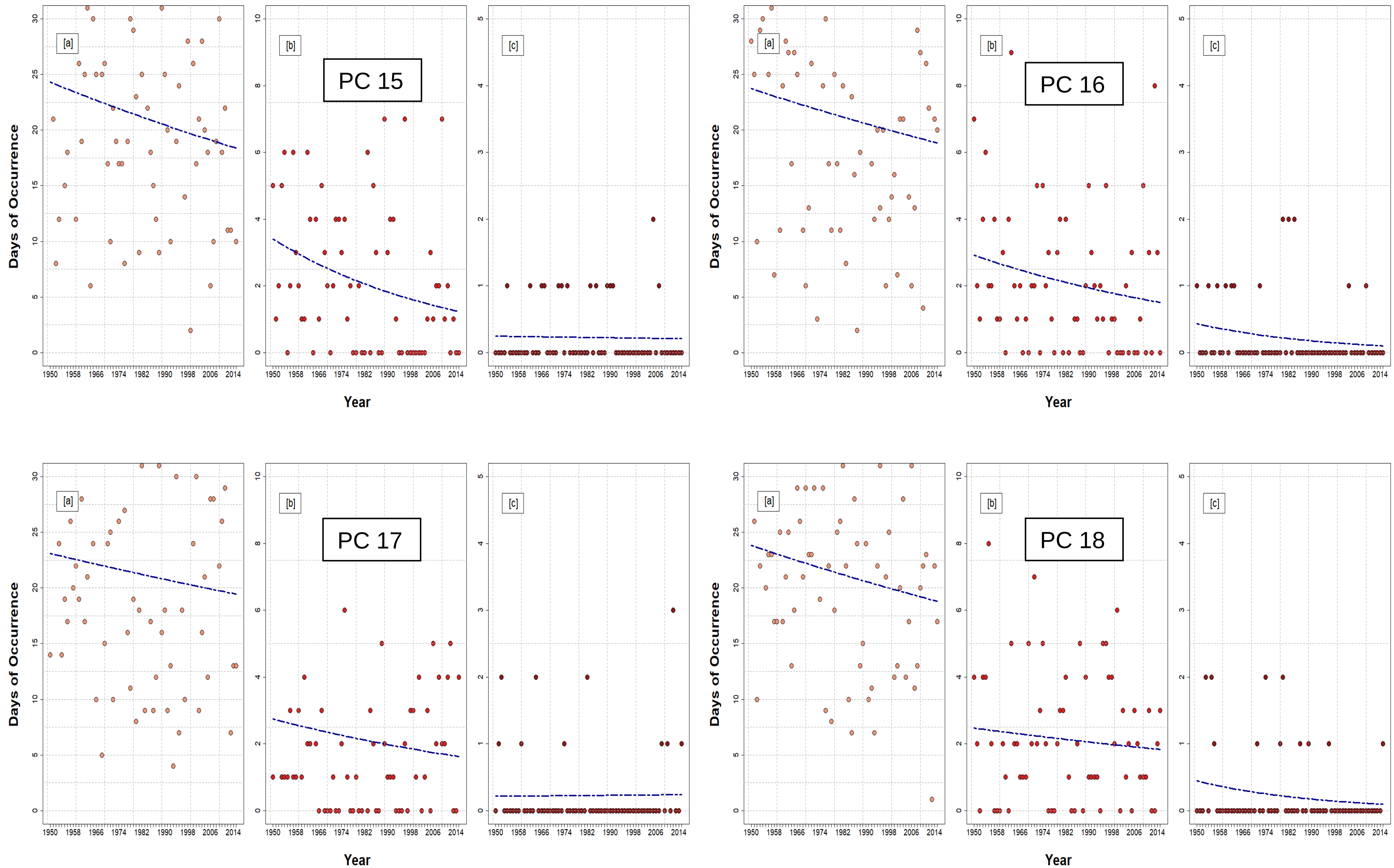

Fig A-17: Logistic trend analysis for counts of 500 geopotential height PC coefficients greater than a) 90th, b)99th, and c) 99.9th percentile for October-April.

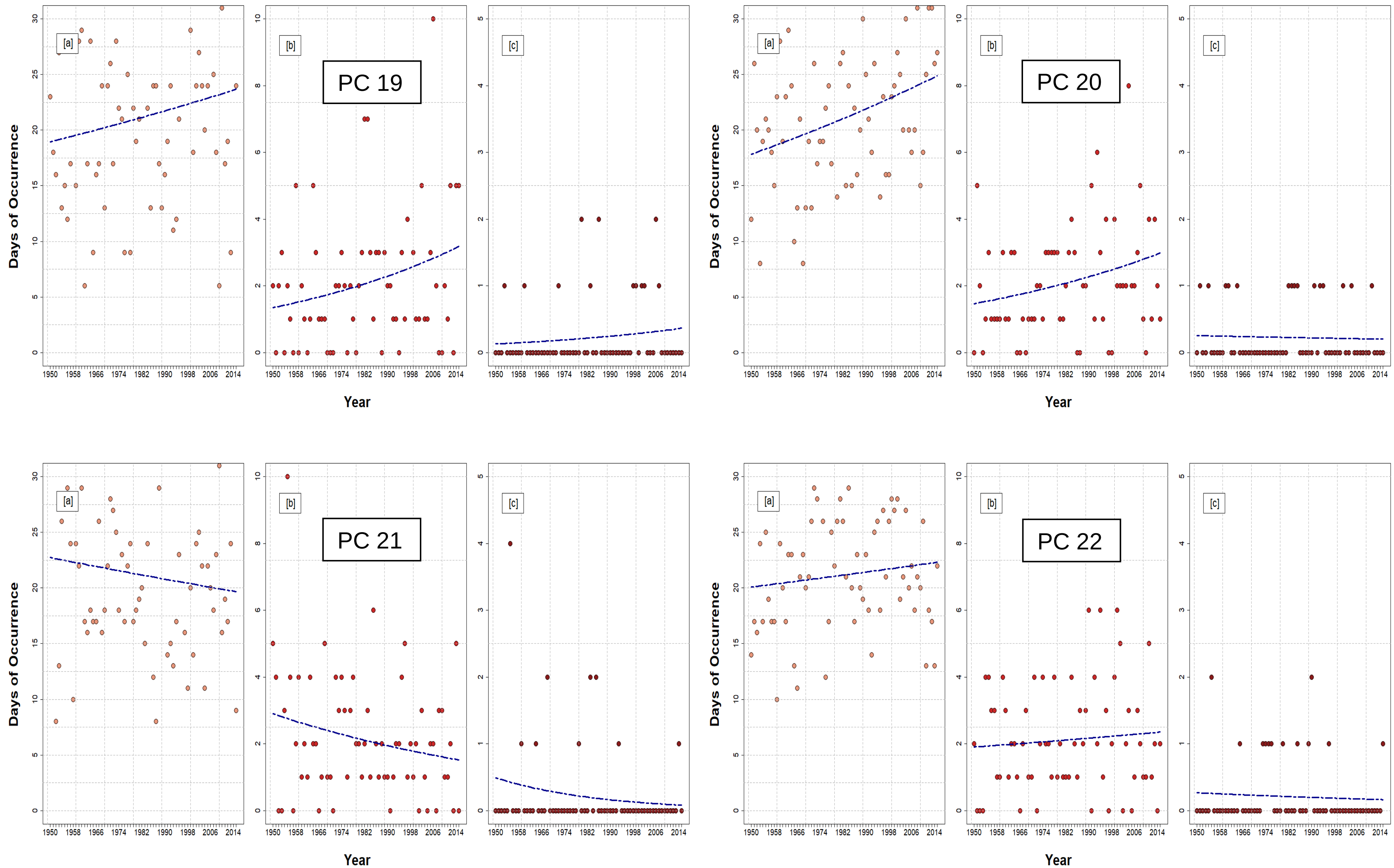

Fig A-18: Logistic trend analysis for counts of 500 geopotential height PC coefficients greater than a) 90th, b)99th, and c) 99.9th percentile for October-April.

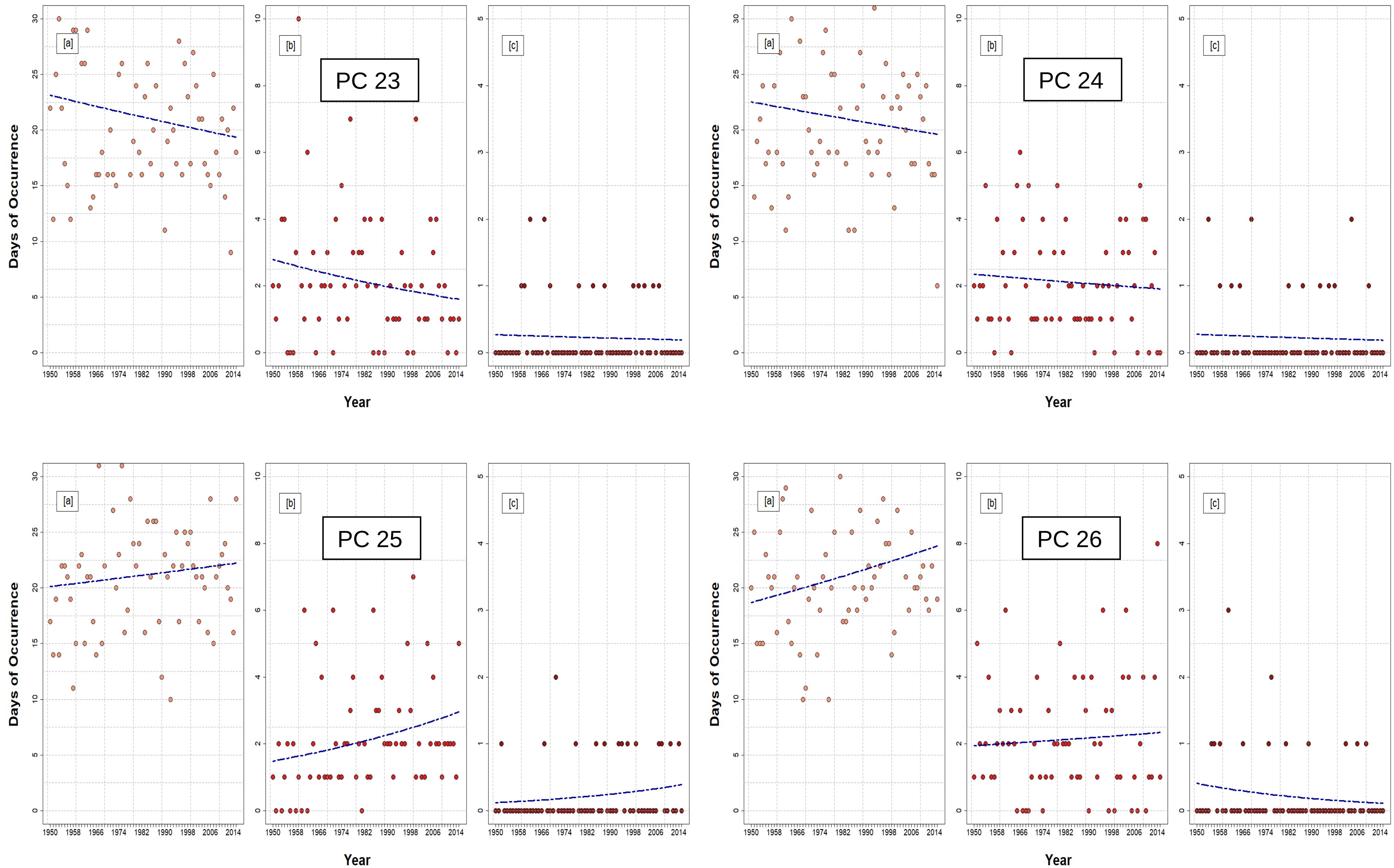

Fig A-19: Logistic trend analysis for counts of 500 geopotential height PC coefficients greater than a) 90th, b)99th, and c) 99.9th percentile for October-April.

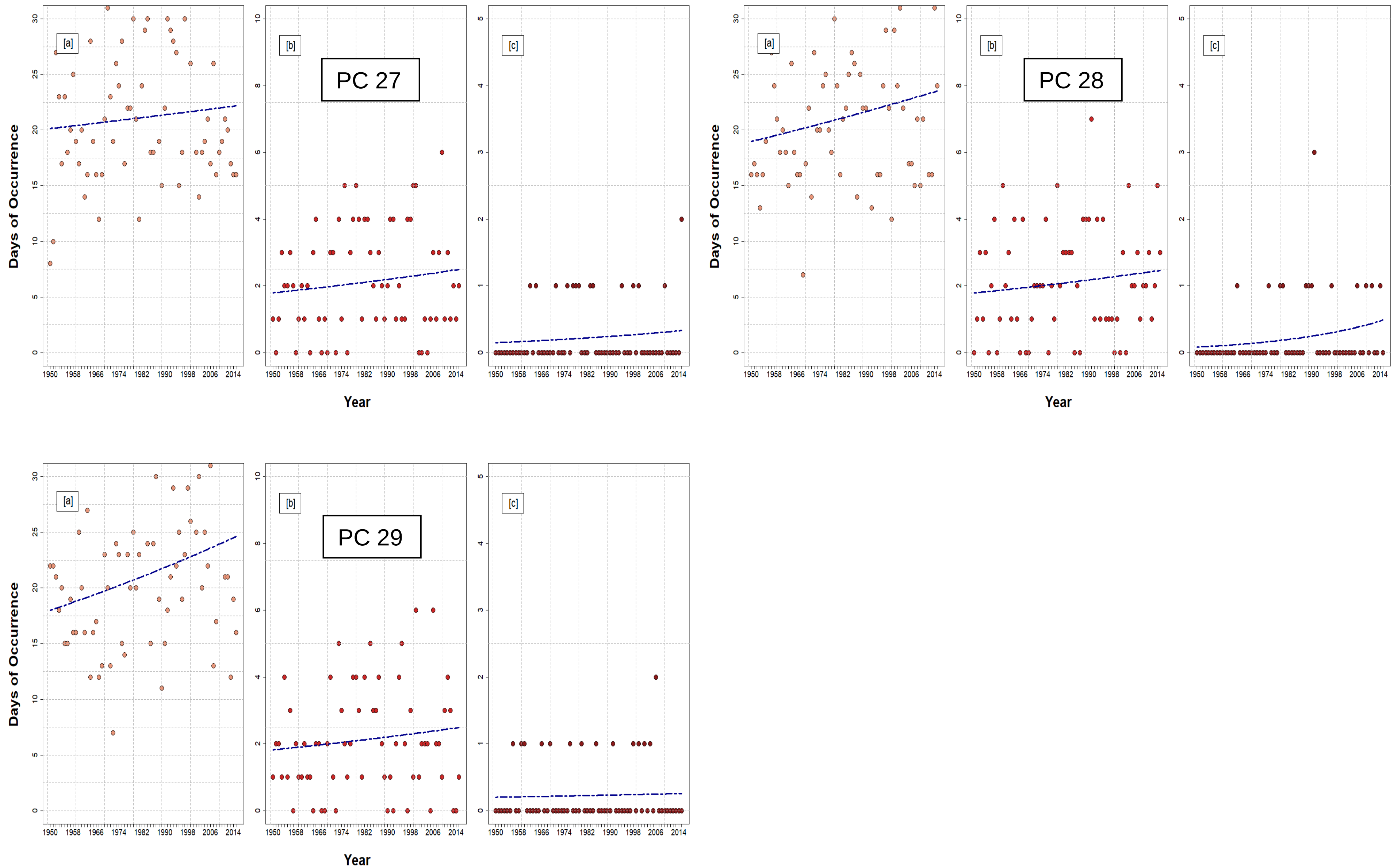

Fig A-20: Logistic trend analysis for counts of 500 geopotential height PC coefficients greater than a) 90th, b)99th, and c) 99.9th percentile for October-April.

APPENDIX B: SUPPLEMENTAL TABLES

This section contains supplemental tables for Chapter 4 including results for logistic trend analysis on the counts of PC coefficients greater than the 90^{th}, 99^{th}, and 99.9^{th} percentiles; and various meteorological parameters associated with extreme wind and wind with antecedent precipitation events.

Table B-1: Logistic regression trend analysis on counts of June-August SLP (1-21), 500 hPa GPH (22-29), April-October SLP (1-14) and 500 hPa GPH (15-29) PC coefficients greater than the 90th, 99th, and 99.9th percentile. Statistically significant values are in bold.

June-August SLP and 500 hPa GPH

PC	Percentile	Odds Ratio	Change in Odds	P-value
1	90.0	1.0018737	1.13	0.58
	99.0	1.0048992	1.37	0.61
	99.9	0.9815638	0.30	0.56
2	90.0	1.0009844	1.06	0.75
	99.0	1.0029674	1.21	0.71
	99.9	0.9928316	0.63	0.79
3	90.0	0.9955435	0.75	0.12
	99.0	**0.9778132**	**0.24**	**0.01**
	99.9	0.9915289	0.58	0.67
4	90.0	0.9970015	0.83	0.23
	99.0	0.9986477	0.92	0.85
	99.9	1.0006699	1.04	0.98
5	90.0	1.0009785	1.06	0.69
	99.0	1.0077654	1.64	0.25
	99.9	1.0236292	4.46	0.31
6	90.0	0.9963277	0.79	0.23
	99.0	0.9917495	0.59	0.22
	99.9	1.0263292	5.28	0.33
7	**90.0**	**1.0086528**	**1.74**	**0.02**
	99.0	1.0073078	1.59	0.28
	99.9	1.0209225	3.76	0.43
8	**90.0**	**1.0061219**	**1.48**	**0.02**
	99.0	1.0102797	1.92	0.18
	99.9	0.9575955	0.06	0.07
9	90.0	1.0046839	1.35	0.11
	99.0	1.0060533	1.47	0.42
	99.9	1.022931	4.27	0.32
10	**90.0**	**0.9925733**	**0.62**	**0**
	99.0	0.995012	0.73	0.46
	99.9	0.9638284	0.09	0.11
11	90.0	**1.008124**	**1.68**	**0.02**
	99.0	**1.030844**	**6.99**	**0**
	99.9	1.0124058	2.20	0.58
12	90.0	1.0029996	1.21	0.32
	99.0	0.9969482	0.82	0.69
	99.9	0.996027	0.78	0.86
13	90.0	0.9977497	0.87	0.41
	99.0	0.9927031	0.63	0.28
	99.9	1.004147	1.30	0.84

14	90.0	**1.0073787**	**1.60**	**0.01**
	99.0	**1.0337543**	**8.37**	**0**
	99.9	**1.0609138**	**44.01**	**0.04**
15	90.0	**1.008806**	**1.75**	**0**
	99.0	**1.0255277**	**5.02**	**0**
	99.9	1.0438178	15.56	0.09
16	90.0	1.002452	1.17	0.47
	99.0	1.0071673	1.58	0.41
	99.9	1.0466984	18.56	0.06
17	90.0	**0.9890737**	**0.50**	**0**
	99.0	**0.9827181**	**0.33**	**0.03**
	99.9	0.9736795	0.18	0.21
18	90.0	**1.0144167**	**2.50**	**0**
	99.0	**1.0360324**	**9.64**	**0**
	99.9	1.0348968	8.98	0.12
19	90.0	0.9953279	0.74	0.14
	99.0	0.9991633	0.95	0.91
	99.9	1.0009754	1.06	0.96
20	90.0	1.0016613	1.11	0.63
	99.0	0.9969865	0.82	0.77
	99.9	1.0063849	1.50	0.84
21	90.0	1.0026296	1.18	0.47
	99.0	1.0101651	1.91	0.26
	99.9	1.0270325	5.51	0.21
22	90.0	1.0001484	1.01	0.97
	99.0	0.9919234	0.60	0.43
	99.9	0.9986216	0.92	0.95
23	90.0	0.9985919	0.91	0.72
	99.0	0.9937499	0.67	0.53
	99.9	1.0159963	2.76	0.62
24	90.0	0.9979381	0.88	0.52
	99.0	0.9925673	0.62	0.41
	99.9	0.9709756	0.15	0.17
25	90.0	1.0056575	1.43	0.14
	99.0	1.0046671	1.35	0.63
	99.9	0.9850993	0.38	0.5
26	90.0	0.9991404	0.95	0.81
	99.0	1.0014414	1.10	0.89
	99.9	0.989943	0.52	0.7
27	90.0	0.9963688	0.79	0.33
	99.0	**0.9739757**	**0.18**	**0**
	99.9	0.9786128	0.25	0.42
28	90.0	0.9973476	0.84	0.41
	99.0	0.9945869	0.71	0.44
	99.9	0.9771767	0.23	0.27

29	90.0	**1.0077787**	**1.64**	**0.04**
	99.0	0.9996149	0.98	0.98
	99.9	0.978187	0.24	0.41

October-April SLP and 500 hPa GPH

PC	Percentile	Odds Ratio	Change in Odds	P-value
1	90.0	0.99832	0.90	0.49
	99.0	0.9998512	0.99	0.98
	99.9	1.0132407	2.32	0.4
2	90.0	0.9972425	0.84	0.17
	99.0	0.9965204	0.80	0.47
	99.9	1.0300851	6.67	0.06
3	90.0	1.0003517	1.02	0.85
	99.0	0.9999139	0.99	0.99
	99.9	0.9882872	0.47	0.39
4	90.0	1.0013626	1.09	0.64
	99.0	1.0004861	1.03	0.95
	99.9	0.9951135	0.73	0.73
5	90.0	1.0017273	1.12	0.47
	99.0	1.0053344	1.41	0.35
	99.9	0.9864914	0.42	0.37
6	90.0	0.9973108	0.84	0.08
	99.0	**0.9868621**	**0.43**	**0**
	99.9	0.9889816	0.49	0.43
7	90.0	0.9970596	0.83	0.07
	99.0	1.0025907	1.18	0.57
	99.9	0.9930524	0.64	0.62
8	90.0	0.9976851	0.86	0.19
	99.0	0.9939734	0.68	0.17
	99.9	0.9967938	0.81	0.84
9	90.0	1.0032538	1.23	0.04
	99.0	1.0122513	2.18	0.01
	99.9	1.0058174	1.45	0.67
10	90.0	**0.9953828**	**0.74**	**0.02**
	99.0	0.9895959	0.51	0.06
	99.9	0.9908936	0.56	0.5
11	90.0	1.0027421	1.19	0.24
	99.0	0.9987036	0.92	0.82
	99.9	0.9924583	0.62	0.62
12	90.0	0.9971464	0.83	0.13
	99.0	0.9885545	0.48	0.03
	99.9	0.9641279	0.10	0.04
13	90.0	0.9980292	0.88	0.3

	99.0	0.9947385	0.71	0.3
	99.9	0.9892212	0.50	0.43
14	90.0	1.0003187	1.02	0.83
	99.0	0.9991451	0.95	0.85
	99.9	0.9990093	0.94	0.95
15	90.0	0.99571	0.76	0.15
	99.0	0.9844598	0.37	0.03
	99.9	0.997522	0.85	0.85
16	90.0	0.996474	0.80	0.31
	99.0	0.9898417	0.52	0.14
	99.9	0.9778617	0.24	0.15
17	90.0	0.9973553	0.84	0.4
	99.0	0.9919046	0.59	0.31
	99.9	1.0016139	1.11	0.93
18	90.0	0.9963708	0.79	0.18
	99.0	0.9953871	0.74	0.44
	99.9	0.9767259	0.22	0.16
19	90.0	1.0034251	1.24	0.16
	99.0	**1.01331**	**2.33**	**0.03**
	99.9	1.0159979	2.76	0.3
20	**90.0**	**1.005137**	**1.39**	**0**
	99.0	1.0109977	2.01	0.03
	99.9	0.996421	0.79	0.79
21	90.0	0.9977803	0.87	0.31
	99.0	0.9901114	0.53	0.06
	99.9	0.9726619	0.17	0.18
22	90.0	1.0016175	1.11	0.29
	99.0	1.0032496	1.23	0.51
	99.9	0.9925213	0.62	0.61
23	90.0	0.9972624	0.84	0.17
	99.0	0.9914986	0.58	0.13
	99.9	0.9947323	0.71	0.7
24	90.0	0.997883	0.87	0.25
	99.0	0.9968254	0.82	0.49
	99.9	0.9940519	0.68	0.69
25	90.0	1.0015327	1.10	0.33
	99.0	**1.0106699**	**1.97**	**0.03**
	99.9	1.0183121	3.19	0.2
26	90.0	1.0036971	1.27	0.02
	99.0	1.0028208	1.20	0.6
	99.9	0.9800292	0.27	0.2
27	90.0	1.0014908	1.10	0.4
	99.0	1.0051087	1.39	0.29
	99.9	1.0124272	2.20	0.37
28	90.0	1.0033	1.23	0.06

	99.0	1.0049718	1.37	0.32
	99.9	1.0277089	5.75	0.07
29	**90.0**	**1.0048296**	**1.36**	**0.01**
	99.0	1.0048185	1.36	0.35
	99.9	1.0037768	1.27	0.78

Table B-2: Various meteorological parameters for wind only events.

Wind Only Events

Date	Maximum Temperature (°C)	Minimum Temperature (°C)	Direction of Maximum Wind Gust (·10°)	Maximum Wind Gust (km/h)	Rain (mm)	Snow (cm)	Precipitation (mm)	Precipitation (PCT)	28 d Antecedent Precipitation (mm)	PCT
1957-11-25	12.2	6.7	29	129	2.5	0.0	2.5	0.72	82.2	0.53
1957-12-23	8.9	5.6	14	100	5.6	0.0	5.6	0.81	112.6	0.68
1958-12-31	11.7	7.8	27	93	2.0	0.0	2.0	0.70	164.2	0.85
1959-11-24	13.9	7.8	27	100	1.8	0.0	1.8	0.69	152.8	0.82
1960-04-13	10.0	4.4	14	95	5.6	0.0	5.6	0.81	51.0	0.33
1961-04-03	10.6	7.2	27	100	0.0	0.0	0.0	0.55	121.2	0.71
1961-04-13	11.7	6.1	27	93	0.0	0.0	0.0	0.55	53.3	0.34
1961-11-01	10.6	1.7	27	109	1.0	0.0	1.0	0.64	129.6	0.75
1961-12-03	7.2	3.3	29	92	1.0	0.0	1.0	0.64	142.5	0.79
1962-10-13	15.0	7.2	14	126	5.6	0.0	5.6	0.81	116.9	0.70
1967-12-05	8.3	2.8	16	93	0.0	0.0	0.0	0.55	138.4	0.77
1972-01-11	3.9	-0.6	29	95	0.3	0.8	1.0	0.64	145.4	0.80
1975-02-20	6.1	0.6	29	92	0.0	0.0	0.0	0.55	138.8	0.77
1975-03-30	8.9	3.9	29	108	0.5	0.0	0.5	0.60	96.0	0.61
1991-12-12	8.4	4.5	30	100	7.2	0.0	7.2	0.85	152.2	0.82
1995-11-17	15.8	10.0	17	91	14.4	0.0	14.4	0.94	143.9	0.79
2002-04-22	11.4	6.2	30	91	0.4	0.0	0.4	0.59	77.4	0.50
2010-04-08	10.1	3.3	29	93	8.2	0.0	8.2	0.87	134.6	0.76
2011-11-11	9.8	2.4	30	100	9.6	0.0	9.6	0.88	55.4	0.36

Table B-3: Various meteorological parameters for wind and precipitation events.

Wind and Antecedent Precipitation

Date	Maximum Temperature (°C)	Minimum Temperature (°C)	Direction of Maximum Wind Gust (·10°)	Maximum Wind Gust (km/h)	Rain (mm)	Snow (cm)	Precipitation (mm)	Precipitation (PCT)	28 d Antecedent Precipitation (mm)	PCT
1955-11-10	8.9	5.6	29	114	0.0	0.0	0.0	0.55	225.1	0.96
1955-11-11	2.8	-4.4	29	109	0.0	0.0	0.0	0.55	223.8	0.96
1960-02-14	8.9	4.4	20	97	14.5	0.0	14.5	0.94	210.0	0.95
1960-02-20	7.2	3.3	27	113	4.3	0.0	4.3	0.78	222.5	0.96
1960-02-21	8.3	1.7	27	105	0.0	0.0	0.0	0.55	225.0	0.96
1961-02-21	10.6	3.9	27	119	12.2	0.0	12.2	0.92	243.4	0.98
1964-01-19	7.8	0.0	23	97	15.5	1.3	16.8	0.95	239.3	0.98
1972-01-02	6.1	-2.2	29	92	0.0	0.0	0.0	0.55	197.5	0.93
1997-03-30	16.7	3.2	15	104	0.2	0.0	0.2	0.56	238.2	0.98
1997-04-03	10.7	4.2	29	100	0.8	0.0	0.8	0.63	189.6	0.91
1999-02-05	6.7	2.4	15	91	6.6	0.0	6.6	0.84	267.8	0.99
2001-12-14	6.1	2.3	29	96	0.0	0.0	0.0	0.55	218.1	0.96
2003-10-28	13.4	8.3	29	95	10.4	0.0	10.4	0.9	237.8	0.97
2006-12-15	8.6	0.3	29	95	6.6	0.0	6.6	0.84	185.8	0.91
2007-01-06	7.9	3.8	29	113	4.0	0.0	4.0	0.77	199.6	0.93
2007-01-09	9.5	0.7	28	98	3.4	0.0	3.4	0.75	215.0	0.95

APPENDIX C: CONTRIBUTIONS FROM AUTHORS

For chapter 6, data for the CTRL and PGW simulations for the period of the July 2009 heatwave were generated by NCAR and the University of Saskatchewan where the simulations were conducted. WRF CTRL and PGW data were provided by the University of Saskatchewan.

Dr. Ronald Stewart provided feedback regarding the content, structure, and formatting of the papers in Chapters 4-6. All other diagrams and analysis were completed by the first author.